Civil Engineering ETDs   Engineering ETDs

2-1-2012

New generation fiber reinforced polymer composites incorporating carbon nanotubes

Eslam Soliman

Follow this and additional works at: https://digitalrepository.unm.edu/ce_etds

Eslam Mohamed Abd El-latif Soliman
Candidate

Department of Civil Engineering
Department

This dissertation is approved, and it is acceptable in quality and form for publication:

Approved by the Dissertation Committee:

Dr. Mahmoud Reda Taha , Chairperson

Dr. Arup Maji

Dr. Yu Lin-Shen

Dr. Marwan Al-Haik

Dr. Thomas Murphey

NEW GENERATION FIBER REINFORCED POLYMER
COMPOSITES INCORPORATING CARBON NANOTUBES

by

ESLAM SOLIMAN

B.S., Assiut University, Assiut, Egypt, 2003

M.S., Lawrence Technological University, Michigan, 2008

DISSERTATION

Submitted in Partial Fulfillment of the

Requirements for the Degree of

Doctor of Philosophy

Engineering

The University of New Mexico

Albuquerque, New Mexico

December, 2011

ii

ACKNOWLEDGEMENTS

PREFACE

The following publications have been co-authored by the Ph.D. student during the course of study. The list includes published articles and others submitted for publications.

Journal Articles

[1] Soliman, E. M., Shyka, M. P. and Reda Taha, M. M. "Ballistic impact of thin woven carbon fabric composites incorporating carbon nanotubes", *International Journal of Impact Engineering*, **In Review**.

[2] Soliman, E. M., Kandil, U. F. and Reda Taha, M. M. "Shear creep of epoxy adhesive incorporating carbon nanotubes at the FRP-concrete interface", *International Journal for Adhesion and Adhesives*, 2011, **Accepted**.

[3] Soliman, E. M., Kandil, U. F. and Reda Taha, M.M. "The significance of carbon nanotubes on styrene butadiene rubber (SBR) and SBR modified mortar", *Materials and Structures*, 2011, **Accepted**.

[4] Soliman, E. M., Al-Haik, M. and Reda Taha, M.M. "On and off-axis tension behaviour of fiber reinforced polymer (FRP) composites incorporating multi-walled carbon nanotubes", *Journal of Composite Materials,* 2011, **Accepted**.

[5] Soliman, E. M., Kandil, U. F. and Reda Taha, M.M. "A new latex modified mortar incorporating carbon nanotubes: preliminary investigations", *Advances on the Use of Polymers in Concrete*, ACI SP-273, 2011.

Conference Articles

[1] Soliman, E., Kandil, U.F., Reda Taha, M.M. "Creep of fiber reinforced polymer-epoxy-concrete interface incorporating carbon nanotubes", *Proceedings of the First Middle East Conference on Smart Monitoring*, Assessment and Rehabilitation of Civil Structures, SMAR 2011, Dubai, UAE, February 2011.

[2] Reinhardt, A., Soliman, E., Sheyka, M., Al-Haik, M., Reda Taha, M.M. "Fracture toughness of hydrated cement using nanoindentation", *CD Proceedings of 7th International Conference on Fracture Mechanics of Concrete and Concrete Structures* (FraMCoS-7), Jeju, South Korea, May 2010.

[3] Dai, J., Soliman, E., Safdari, M., Al-Haik, M., Reda Taha, M. M., "Effect of carbon nanotube growth conditions on strength and stiffness of carbon and glass fiber polymer composites", *51st Structures, Structural Dynamics, and Materials AIAA Conference*, Orlando, FL. April 2010.

[4] Salas, C., Neidigk, S., Soliman, E., Mercer, D. and Reda Taha, M.M., "Creep and relaxation of osteoporotic bones", *CD Proceedings of Annual Conference of Society of Experimental Mechanics,* Albuquerque, NM, June 2009.

In preparation

[1] Soliman, E. M. and Reda Taha, M.M. "Carbon nanotubes for shortening lap splice", *Journal of Composites for Construction,* ASCE.

[2] Soliman, E. M. and Reda Taha, M.M. "Fracture toughness of woven carbon fabric composites reinforced by MWCNTs", *Journal of Composites Part B Engineering, Elsevier*.

NEW GENERATION FIBER REINFORCED POLYMER COMPOSITES INCORPORATING CARBON NANOTUBES

by

Eslam Soliman

B.S., Assiut University, Assiut, Egypt, 2003

M.S., Lawrence Technological University, Michigan, USA, 2008

ABSTRACT

The last five decades observed an increasing use of fiber reinforced polymer (FRP) composites as alternative construction materials for aerospace and infrastructure. The high specific strength of FRP attracted its use as non-corrosive reinforcement. However, FRP materials were characterized with a relatively low ductility and low shear strength compared with steel reinforcement. On the other hand, carbon nanotubes (CNTs) have been introduced in the last decade as a material with minimal defect that is capable of increasing the mechanical properties of polymer matrices.

This dissertation reports experimental investigations on the use of multi-walled carbon nanotubes (MWCNTs) to produce a new generation of FRP composites. The experiments showed significant improvements in the flexure properties of the nanocomposite when functionalized MWCNTs were used. In addition, MWCNTs were used to produce FRP composites in order to examine static, dynamic, and creep behavior. The MWCNTs improved the off-axis tension, off-axis flexure, FRP lap shear joint responses. In addition, they reduced the creep of FRP-concrete interface, enhanced the

fracture toughness, and altered the impact resistance significantly. In general, the MWCNTs are found to affect the behaviour of the FRP composites when matrix failure dominates the behaviour. The improvement in the mechanical response with the addition of low contents of MWCNTs would benefit many industrial and military applications such as strengthening structures using FRP composites, composite pipelines, aircrafts, and armoured vehicles.

TABLE OF CONTENTS

LIST OF FIGURES

xiii

xiv

LIST OF TABLES

CHAPTER 1.   INTRODUCTION

1.1   Problem Statement

The use of fiber reinforced polymer (FRP) composites has increased in last two decades in civil infrastructure, aerospace, and military applications. The distinguished properties of the FRP composites, such as the low weight-to-strength ratio and corrosion resistance, made them excellent materials in structural design. However, there are several shortcomings reported in the mechanical behavior of FRP composites. One of the major challenges is the inter fiber fracture that occurs due to matrix micro-cracking or debonding of fiber-matrix interface. The inter fiber fracture affects the mechanical performance of the composites due to inadequate shear stress transfer among the individual fibers, leading to premature failure of the composite. The delamination of layered composite is widely reported due to lack of interlaminar shear strength (ILSS). The matrix mirco-cracks occur due to transverse or cyclic loading where a noticeable reduction in stiffness is usually observed. In addition, freeze and thaw cycles in aerospace or civil infrastructure cause matrix micro-cracks due to the development of thermal stresses. The thermal stresses occur as a consequence of the difference in coefficient of thermal expansion between the fibers and the surrounding matrix.

The brittleness of FRP composites is also a limiting factor in structural design due to the lack of physical warnings such as yielding and excessive deformations prior to failure. Moreover, appropriate ductility becomes critical parameter in high strain rate events such as blast and impact. Finally, the creep of adhesives at the FRP concrete

1

interface is recently reported by many scientists as a critical challenge in FRP strengthening systems subjected to sustained stresses. The large creep deformations at the interface would cause inappropriate stress transfer to the FRP components. This makes the strengthening system inefficient after several months from installation. Such challenges in the mechanical response of FRP composites resulted in the use of relatively high factor of safety in design. These challenges also become considerable in structural applications where shear strength of composites is crucial.

1.2 Motivation

Nanotechnology has been one of the promising fields in the 21st century for many research areas and applications such as chemistry, material science, and medical treatments. One important branch of this technology is the manufacturing and processing of nanocomposites including ceramic, metal, or polymer matrix nanocomposites. Carbon nanotubes (CNTs) were discovered in 1991 and identified as a very useful material due to their extraordinary mechanical, thermal, and electrical properties. What distinguish their properties is that they are orders of magnitude higher than the standard materials used in construction today. Since their discovery, CNTs have been target for polymer nanocomposite research with outstanding results. Dispersion and interfacial bond are reported as major challenges in manufacturing functional CNTs-polymer nanocomposites. Various techniques were successfully introduced in the last decade to overcome these challenges (Zhu *et al.*, 2003, Geng *et al.*, 2008). However, the use of CNTs in making macro-scale structural elements such as FRP composites is not yet well

2

investigated or totally understood. Therefore, there arises the need for examining the use of CNTs in structural composites.

1.3 Study Objectives

This study aims at giving insight on possible improvements of the mechanical response of FRP composites by incorporating CNTs. The mechanical response of FRP composites includes static, long term, and dynamic behaviors. The improvement in the FRP composite is beneficial to several structural applications. Examples of these applications include reinforced concrete (RC) column retrofit, FRP strands anchors, multi-axially loaded composite laminates, FRP shear studs and FRP bolts, epoxy adhesives for anchors and tie backs, and multi-layered composites subjected to impact and blast. The shear strength of the composites was reported to be a critical design parameter for these applications. In the light of the problem statement, the following objectives were selected:

- Manufacturing and testing of functional CNTs-epoxy nanocomposites including static and dynamic tests.

- Manufacturing and performing static tensile and flexure tests on multi-layered FRP composites laminates incorporating CNTs.

- Examining the significance of CNTs on the lap splice length of the FRP composites in common FRP concrete strengthening systems.

- Investigating the durability of epoxy adhesives with CNTs used in common FRP concrete strengthening systems.

3

- Examining the interlaminar fracture toughness of FRP composites enhanced with CNTs.

- Examining the impact response of FRP composites enhanced with CNTs. The impact test is going to shed light on the effect of CNTs on the high strain rate behavior of FRP composites.

1.4 Dissertation Layout

This research will include testing of CNTs-epoxy nanocomposites and CNTs-FRP composites with the aim of characterizing and understanding the effect of incorporating CNTs. In addition to the introductory Chapter 1, this proposal consists of the following chapters:

Chapter (2): This chapter reports the available literature addressing the shortcomings of FRP composite mechanical response and the advantages of using CNTs in nanocomposites and FRPs.

Chapter (3): This chapter presents the details of several fabrication techniques for manufacturing CNTs-epoxy nanocomposites including the use of pristine and chemically functionalized CNTs. The mechanical characterization of the nanocomposite including flexure, dynamic shear rheometer (DSR), differential scanning calorimetry (DSC), and thermogravemteric analysis (TGA) tests are examined. Morphological investigation is performed by scanning electron microscopy (SEM).

4

Chapter (4): This chapter discusses the on-axis and off-axis tension behavior of CNTs-FRP composites in the light of two approaches. The first approach is performed by growing the CNTs on the macrofibers while the second is performed by producing CNTs-epoxy nanocomposite prior to the fiber impregnation.

Chapter (5): This chapter presents a study on time dependant creep behavior of CNTs-epoxy nanocomposites at FRP concrete interface. Double shear creep specimens are performed and discussed to study the effect of CNTs. In addition, rheological models are developed to predict the creep behavior. The effect of CNTs content on the model parameters is also reported.

Chapter (6): This chapter discusses experimental investigation for FRP lap splices reinforced with CNTs. Single and double lap shear joints are manufactured with epoxy adhesives and tested. The results report the effect of the CNTs on the bond strength and the deformation of the joints.

Chapter (7): This chapter presents fracture toughness tests using double cantilever beams (DCB) to extract mode I fracture toughness of the CNTs-epoxy nanocomposites. In addition, a finite element (FE) simulation is performed to further investigate the delamination growth of the nanocomposites. The effect of CNTs on the governing stress-displacement relationship at the interface is investigated.

Chapter (8): This chapter examines the behavior of woven fabric composite plates under out-of-plane biaxial impact loading. The effect of CNTs on the impact properties such as velocity, energy, and deformations are reported. On and

5

off-axis flexure static tests are performed to further explain the impact test results.

Chapter (9): This chapter summarizes the findings obtained in the previous Chapters. Emphasis is placed on the significance of the research work and the associated limitations. Recommendations are also proposed herein.

CHAPTER 2. LITERATURE REVIEW

2.1 Overview

This chapter starts with an introduction for the FRP composites and their industrial applications. The major challenges on the mechanical behavior of the composites are addressed. These challenges include: 1) the inter fiber fracture due to transverse loads and thermal stresses, 2) Delamination between the composite layers as a result of weak interlaminar shear strength, and 3) the creep of adhesives at the FRP concrete interface. Nanotechnology is introduced as a relatively new field in structural applications. Because of their distinguished properties, emphasis is placed on carbon nanotubes. Various production techniques and chemical treatments of CNTs and their nanocomposites are also discussed. Furthermore, a summary of recent research on the mechanical response of CNTs-FRP composites is reported.

2.2 Fiber Reinforced Polymer Composites

FRP composites are formed by impregnating fibers in resin matrices. Different types of fibers such as carbon, glass and aramid can be used. Resins can be either thermosets or thermoplastics. Polyester, epoxy, and Vinyl ester are thermoset resins while nylon and polyethelene are examples for thermoplastic resins. The role of the fibers in the FRP composites is to carry 70-90% of the load, provide stiffness, thermal stability, and electrical conductivity. The matrix binds individual fibers together to work as one unit, provide shear resistance and ductility (ACI440.2R, 2006, Mazumdar, 2002). FRP

7

composites are manufactured in the industry in several forms such as bars, strands, uni- or multi-directional sheets or pultruded sections. The use of FRP composites has increased in the last few decades due to their outstanding physical and mechanical properties (ACI440.2R, 2006, Hyer, 1997, Mazumdar, 2002). These advantages include:

- High specific strength and specific stiffness in fiber direction (~ 3 to 5 times steel).

- Provide in-service monitoring using embedded fiber optic sensors "Smart Materials".

- Good fatigue strength (up to 90% of the static strength) compared to steel.

- High corrosion resistance.

- Low coefficient of thermal expansion (CTE).

- Good flexibility for producing complex geometries.

- Good flexibility in design such as a laminate with undirectional plies manufactured in a desired stacking sequence.

However, some of the major disadvantages are listed below:

- Expensive: composites cost 8 – 40$/lbs "although cheap when long term maintenance is considered" while steel and aluminum are ~ 1.0$/lbs.

- Temperature resistance is limited by matrix thermal stability.

- Complexity and non-linearity in predicting the failure behavior because of fiber random distribution and multiple failure modes.

8

- Brittle failure, which is a major challenge when structural applications are considered.

- Orthogonality in the mechanical response, which involves weak behavior in transverse direction.

FRP composites are widely used in several civil and military applications. In civil applications, they are used as a construction material in buildings and highway structures. They also have been utilized extensively in aircraft/aerospace, automotive and marine industries. Reinforced concrete (RC) structures designed and constructed in the 1950s-1970s suffered different levels of deterioration in the last two decades. Such structures are currently being externally strengthened using FRP sheets. Internal FRP reinforcement bars and tendons are now replacing the traditional steel reinforcements of RC and prestressed concrete elements especially in corrosive environments. Other civil applications also include the use of pultruded FRP sections in composite decks. Gas pipelines and composite turbine blades for wind mills are other examples for using FRP composites in applications that require long-term durability. Deployable aerospace structures are made from FRP composite with the advantage of being packed in very small volumes, sent and deployed in the space without any structural damage. Sandwich composite panels are also used in military tanks against blasts. The FRPs production rate reached 6.3 Billion dollars in 1999 (Mazumdar, 2002). Transportation and construction applications represented the majority of the FRP production as shown in Figure 1.
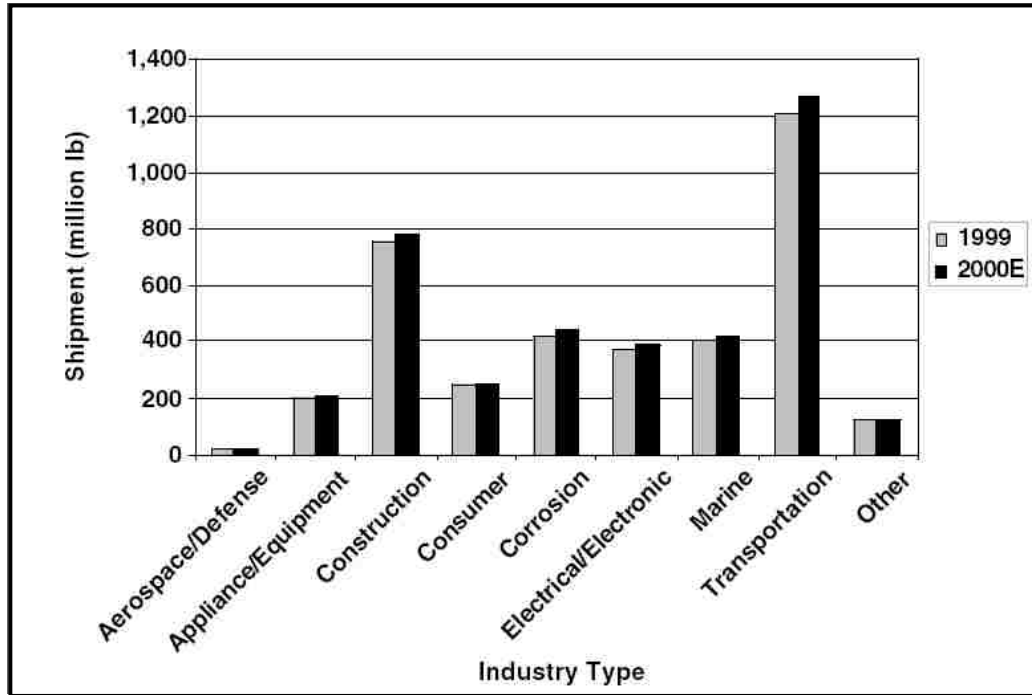
Figure 1. The use of FRP composites in the United States (Mazumdar, 2002)

Although FRPs are widely used in the industry, their strength analysis is very complex and non-linear, especially when multi-layer laminates are considered. Failure behavior of FRPs depends on the loading nature, fabrication quality, and structure of the laminate. Typical failure modes of FRPs include the fiber fracture, matrix fracture, fiber-matrix interface debonding, and delamination between layers in a laminate (Hyer, 1997, Knops, 2008). The fiber fracture is the most desirable failure mechanism in design; however, it occurs in certain conditions such as: the fibers are oriented in the loading direction, and the fabrication is high quality with no fiber "ondulation". The cohesive matrix fracture and adhesive fracture of the fiber/matrix interface are known as inter fiber fracture (Knops, 2008). Figure 2 shows inter fiber fracture of a unidirectional layer in a multi-layer laminate.

10

<div align="center">(a)   (b)</div>
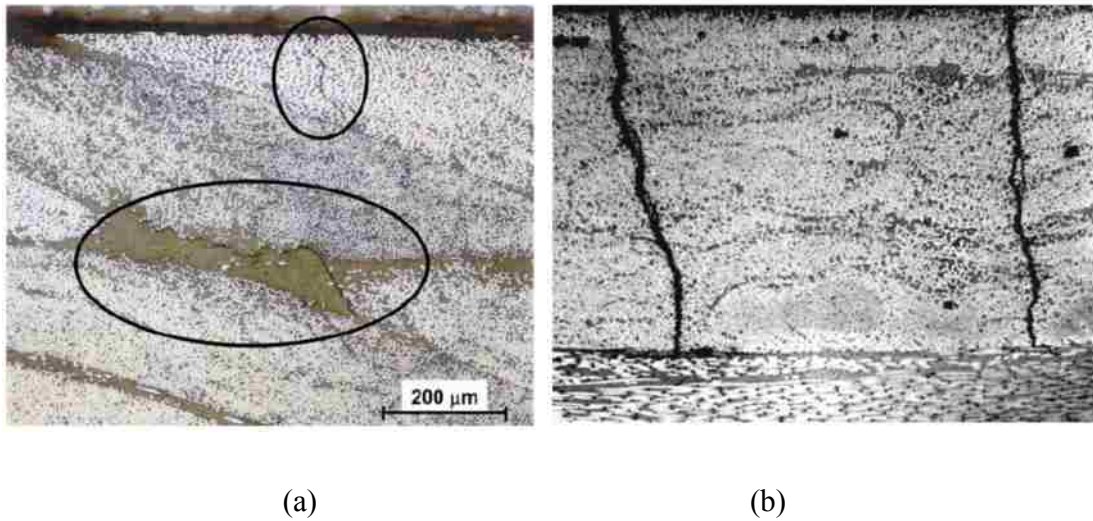
Figure 2. Inter fiber fracture of FRP composite (a) one layer and (b) multiple layers (Knops, 2008)

2.2.1 Inter Fiber Fracture

The inter fiber fracture is a macro-damage starts by matrix micro-cracks occur due to the shrinkage of the matrix during the curing and the differential coefficient of thermal expansion between the fiber and the matrix. Once the FRP is loaded, these micro-cracks propagate through the respective layer to form macro cracks. Micro-cracks are always more prominent in the off-axis loading (Nairn, 2000). The off-axis loading is referred to laminate loaded not parallel to the fiber orientation. If the laminate is one layer, the inter fiber fracture would cause a complete failure of composite. However, if the laminate consists of multiple layers, the interlaminar shear stresses will be re-distributed around the macro-cracks and the laminate will continue carrying the load until failure of the adjacent layers takes place.

Several research groups investigated the failure mechanism of composites. (Hobbiebrunken *et al.*, 2006) performed experimental and numerical studies to investigate the failure behavior of multilayer carbon fiber/epoxy composites. In-situ bending test was performed to continuously observe the progress of the failure with scanning electron microscope (SEM). The normal traction at the fibers matrix interface was found to govern the failure initiation of FRPs when loaded transverse to fiber direction (Figure 3). In the numerical study, micro/macro scales finite element model was performed to investigate the interfacial failure. The same research group extended their numerical investigation to study the effect of the non-uniform distribution of the fibers on the failure and stresses (Hobbiebrunken *et al.*, 2008). Random sequential-addition (RSA) algorithm is used to generate various fibers arrangements within the epoxy matrix. The observations showed that the fiber distribution has significant effect on the interfacial strength of a unit cell. In addition, there is significant difference between the irregular arrays and the periodic arrays. (Kelly & Hallstrom, 2005) investigated the failure of composite laminate subjected to transverse load. The damage was found to initiate at 20-30% of the ultimate strength with interlaminar shear cracks at the matrix. The interlaminar shear cracks propagate to form a network of cracks.

(Katerelos *et al.*, 2008) studied the effect of matrix cracking on the behavior of cross-plies and unbalanced symmetric GFRP laminates under in-plane tension. The longitudinal stiffness obtained by experiments was compared to the predicted values using equivalent constraint model (ECM) which takes into account reduction in stiffness due to matrix cracking. The experimental stiffness was obtained by laser Raman spectroscopy (LSR). The good agreement between the theoretical and predicted stiffness

12

indicates the effectiveness of using ECM in predicting the degradation of stiffness in composites loaded off-axis. (Knops & Bogle, 2006) investigated the gradual failure of composites due to the inter fiber fracture. The authors raised a controversial discussion regarding which approach should be used in describing the degradation model, which describes the stiffness loss due to inter fiber fracture. Three approaches were discussed; fracture mechanics, damage mechanics, and phenomenological model. The authors suggested the phenomenological model by (Puck & Schurmann, 1998) to be the best for describing a degradation model. (Rebiere & Gamby, 2008) proposed an energy approach to describe the initiation of damage in composites. Their analyses were based on computing the strain energy release rate for three different matrix damage mechanisms: transverse cracks, longitudinal cracks, and delamination and identifying which mechanism governs.
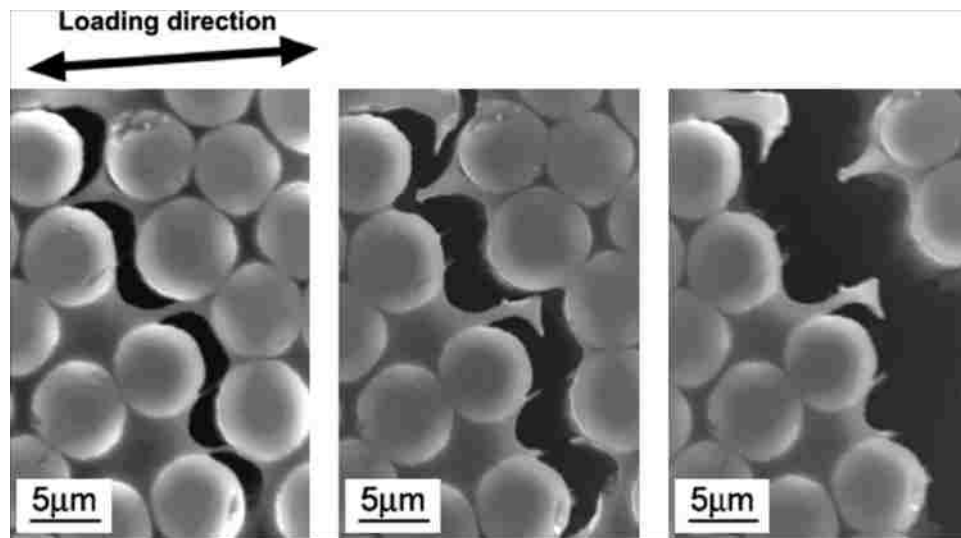
Figure 3. SEM images for fiber-matrix debonding crack initiation and propagation in CFRP composites (Hobbiebrunken et al., 2006)

2.2.2   Delamination and Debonding

Delamination is separation between the individual layers or plies in FRP laminate due to out-of-plane tensile stresses and/or interlaminar shear stresses. It represents lack of shear strength of matrix in between the individual layers or plies. FRP layer here is multiple FRP plies that have the same fiber orientation. In many occasions, inter fiber fracture propagates to the layers boundaries and initiates the delamination (Figure 4). Delamination also occurs more frequently in regions with geometrical discontinuity. Many efforts were directed in modeling the delamination phenomenon of FRPs. Basic assumption made in most of these modeled is called effective modulus theory (EMT). In the EMT, it is assumed that composite consists of multiple layers and the delamination occurs at their interfaces. However, in reality the interfaces represent a thin layer of matrix with relatively low stiffness and strength (Pagano & Schoeppner, 2000).

Figure 4. Delamination of composite laminates (Pagano & Schoeppner, 2000)

(Xiao *et al.*, 2007) studied the failure behavior of multi-layer S2 GFRP plates under quasi-static punching shear load experimentally and numerically. They observed that the delamination and fiber fracture in tension are the dominant failure mechanisms. The authors used the finite element software package LS-DYNA® for numerical analysis.

14

They calibrated the material properties of the element type MAT 162 using the response of part of the experimental results and used these parameters to predict and verify the rest of the experiments. Overall, the predicted failure behavior was in a good agreement with the experiments. Figure 5 shows comparison between the experimental and numerical failure behavior at different penetration levels. (Ye, 1989) investigated the use of two types of matrices in enhancing the resistance to the FRPs delamination growth under quasi-tension test. The two types of matrices were 648/BF3 MEA (mono-ethyl-amine) and 634/DDS epoxy resins. The author proved that the epoxy resin 648/BF3 MEA with relatively high ductility improved the resistance to delamination of FRPs twice the other type. Furthermore, Ye developed a simple energy release rate approach to describe the delamination phenomenon by constructing delamination resistance curve similar to the crack resistance R-curves. The model showed a good agreement to the experiments.
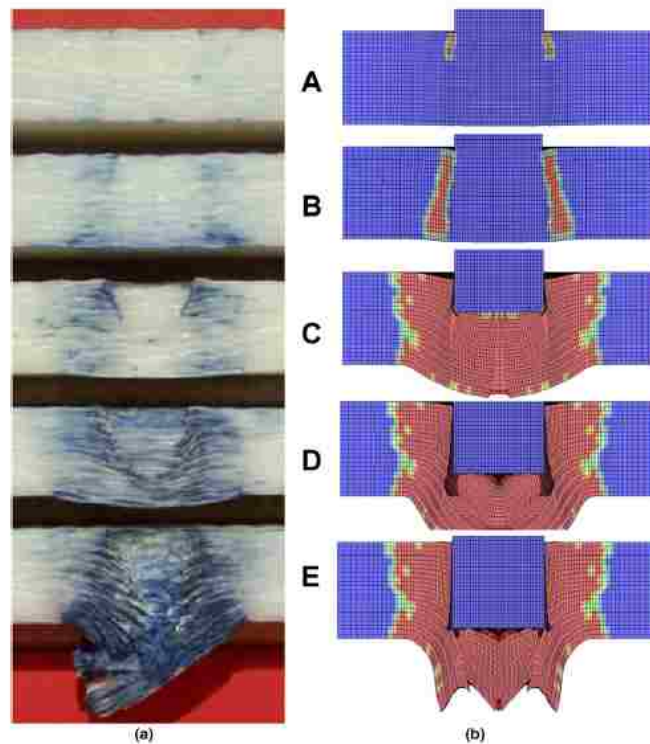
Figure 5. Fiber tensile/shear failure at different punch displacements for 25.4 mm span (a) Experiment: A-0.7 mm, B-1.27, C-3.39, D-5.71, E-22.86. (b) Simulation: A-0.6 mm, B-1.20, C-4.80, D-9.00, E-14.00 (Xiao et al., 2007)

(Aslan & Sahin, 2009) conducted experimental investigation to study the effect of delamination sizes on the buckling behavior of GFRP composites. They introduced the delamination by placing 100 µm polytetrafluoroethylene (PTFE) film during the fabrication of the composites. They also developed finite element model (FEM) using ANSYS 11[®] to predict the delamination behavior. The results show that the location and the area of the delaminations affect the buckling and the compressive failure loads significantly. (Tamuzs *et al.*, 2003) developed experimental setup based on double cantilever beam (DCB) technique to examine the effect of low percentages of transverse

16

fibers (translaminar reinforcement) on the delamination resistance of 3-D woven carbon and glass fiber composites. The energy release rate was computed and R-curves are developed. The experiment showed that the transverse reinforcement did not delay the crack initiation. However, the crack propagation resistance increased significantly at the steady-state propagation when transverse reinforcements were provided.

Furthermore, several researchers introduced cohesive zone model (CZM) as interface elements to describe the delamination of composite laminates especially for DCB. (Chandra, 2002) provided comprehensive evaluation of using CZM in describing the crack propagation for various composite materials. The author emphasized on the difficulty of assuming or extracting the appropriate interfacial properties even when experimental data is available. Depending on the composite material, it is important to use the correct form (exponential or bilinear) of CZM in order to obtain useful results. (Wang, 2007) used CZM to describe the behavior of FRP-concrete interface under mixed mode loading. New unified traction separation model was introduced. The new model shows good agreement in the crack initiation and propagation with the experimental studies. (Hu *et al.*, 2008) proposed a new CZM, known as adaptive cohesive model (ACM), which includes pre-softening zone ahead of the existing softening zone with relatively higher stiffness and strength. The proposed model overcomes the convergence problems usually associated with the use of CZM especially when coarse mesh is used.

2.2.3 Failure Theories

Because of the complexity and non-uniformity of the FRP behavior, a lot of effort was directed in the FRP composite field to develop various failure theories. The big

17

challenges structural engineers usually face when designing FRP structures are because of the lack of analytical tools that describes the FRP behavior to a reasonable or reliable level. Therefore, a "Make and Test" approach combined with appropriate safety factors is the common practice in FRP design. To further understand the failure behavior, a very useful and comprehensive study, known as the world wide failure exercise (WWFE), was introduced by (Hinton *et al.*, 2004). The WWFE is a comprehensive international activity organized to improve the foundation of the design theories or improve the prediction of the deformations and the failures of FRP composites. The study includes the research work of more than thirty experts from six countries on the field of FRP composites. The idea of this exercise is to develop sufficient experimental database, evaluate various failure theories, and produce appropriate recommendations for structural engineers to follow during the design and construction of various FRP components.

In this assessment, 19 failure theories with various approaches were examined. Some of them are based on interactive failure theories such as Tsai-Wu. Other theories are based on physical failure of composite components such as fiber or matrix failures. Industrial and standard code approaches such as US Mil Handbook and UK BS 4994 are also evaluated in that report. Commercial finite element software packages such as ABAQUS®, ANSYS®, and DYNA3D® are examined. Statistical prediction of failure was also considered. The final chapter in the book represents a useful and comprehensive guide for using various theories in predicting different characteristics in the FRP behavior. Some of these characteristics are accurately predictable by several theories. For instance, Puck, Cunte or Tsai theories can be used together to describe the strength of unidirectional laminate under combined loading. On the contrary, all failure theories

18

failed to predict many characteristics such as the initial strength of multidirectional laminate. Although there is sufficient data available for design guides, yet no failure theories are implemented effectively for design.

2.2.4   Creep of FRP Strengthened Structures

Retrofitting and strengthening of existing reinforced or prestressed concrete structures have been a rapidly growing area in civil engineering in the last few decades. Two reasons caused the researchers to develop advanced techniques for strengthening; 1) infrastructure designed in the 1950s-70s are now experiencing serious deterioration due to aging and serving in harsh environments and 2) the development of various design codes to allow higher load-carrying capacities requires increasing the strength of existing structure even if they are adequate. One of the excellent techniques developed over years are strengthening using fiber reinforced polymer (FRP) composites due to their high strength-to-weight ratio and good durability. Researchers and designers reported many successful field applications where FRP was used successfully in new structures (Nanni, 2000) or in strengthening of existing structures (Reda Taha et al., 2003).

However, in many occasions this technique experiences premature failure due to lack of shear transfer at the FRP-concrete interface and leads to debonding. Furthermore, creep of viscoelastic adhesives at the interface was reported recently in many investigations to be problematic when FRP strengthening systems aim to resist sustained loads (Taha et al., 2010). Recent experiments by (Taha et al., 2010) on full-scale RC beams showed that creep of the epoxy adhesive can result in off-loading the FRP strips and thus late cracking of concrete. The double lap shear test, proposed by the Japanese

19

Concrete Institute, is examined by (Ferrier & Hamelin, 2002) to study the creep behavior of FRP-concrete interface as a function of time and temperature and estimate the corresponding rheological model parameters. (Feng et al., 2005) studied creep behavior of structural adhesives using accelerated creep tests. They concluded that the long-term creep behavior of the epoxy structural adhesives can be reliably predicted using a set of short term accelerated creep tests.

(Benyoucef et al., 2007) developed a closed form solution to describe shear creep and shrinkage of adhesives at the FRP-concrete interface. From their theoretical approach, they found that edge interfacial stresses decrease as the thickness of the adhesive increases. It was also observed that creep of adhesives increases the bond length of the FRP significantly (Wu & Diab, 2007). (Meshgin et al., 2009) performed extensive study to examine the effect of different parameters on the creep response of epoxy at the FRP-concrete interface using double shear test. It was found that the epoxy thickness, curing time, and load level affect significantly the shear creep. In addition, (Majda & Skrodzewicz, 2009) examined the creep of epoxy adhesive under tension and developed rheological models. They showed that stress level has significant impact on creep model parameters. Furthermore, (Hamed & Bradford, 2010) found that creep results in developing significant shear and normal stresses in the adhesives at the edges. Recently, (Ferrier et al., 2011) examined time-temperature principle on epoxy adhesives with various glass-transition temperatures subjected to shear loading. They concluded that shear modulus decreases due to creep and the creep behavior is correlated to the glass transition temperature of epoxy.

2.3 Nanotechnology

The definition of the nanotechnology involves controlling or manipulating materials and creating devices and structures at the nano scale in order to enhance material functions and characteristics, leading to considerable energy savings and environmental load reduction. It also involves studying and understanding the fundamental principles of molecules and structures with at least one dimension between 1-100 nm (Gasman, 2006). The first one to shed the light on the Nanotechnology was Richard Feynman, Nobel Prize winner in physics 1965 in his famous talk entitled "There's plenty of room at the bottom" (Feynman, 1992). There are a lot of promising directions and opportunities for the field of Nanotechnology in industry and business. Most of these opportunities are oriented towards mechanical, electrical, and medical applications. General examples of the mechanical applications are listed below (Gasman, 2006):

- Aerospace industry such as nanocoating of aircraft components.

- Automotive industry such as using nanocrystalline ceramic liners and silicon nitride in building engine cylinders and ball bearings respectively.

- Building materials such as aerogels, insulations, and smart windows.

In addition to the mechanical applications, electrical applications include batteries with aerogels for separator plates, Televisions/monitors with enhanced CRTs resolution using nano materials and nano electro mechanical systems (NEMS) devices. Medical applications involve nano engineered materials to replace lost or damaged tissues. There are two approaches in the design and manufacturing processes at the nano-level, top-down and bottom-up approaches. The top-down approach involves processing the desired

21

macro-materials and structures using special tools in order to create the nano-level features. Famous example of this is the processing of semi-conductors to manufacture smaller chips. The use of more advanced tools allows manufacturing smaller chips and therefore achieves higher restoring capacity and better performance. On the other hand, the bottom-up approach involves creating and processing the desired molecules at the nano level (molecules) in order to obtain a functional micro and macro-structures. Example of this approach is the fabrication and processing of nanocomposites (Gasman, 2006).

Nanocomposite or nanomaterial is an advanced branch of material science. A general definition of nanocomposites, reported by (Shaffer & Sandler, 2007), is a multi-phase or composite material where at least one of the dimensions of one of its constituent is in the nanometer size scale. This definition implies the synthesis of composite with two or more different materials with different properties in order to obtain a distinctive micro or macro-properties including mechanical, electrical, thermal properties. Polymer, ceramics, or metallic matrix composites are the famous types of nano composites investigated by researchers and produced in the industry. Several reinforcing nano particles are introduced for the polymer nanocomposites in the literature such as carbon nanotubes, rubber, clay, and silicate.

2.4   Carbon Nanotubes

Beside the carbon nanotubes, carbon based structure are found in many forms such as Diamond, graphite, and fullerene. Diamond has crystalline structure where sp^3 hybridized carbon atoms are bonded to four others in a tetrahedral arrangements. The

22

crystalline structure gives the diamond its unique properties specifically the hardness. Planer sheets of sp^2 hybridized carbon atoms boneded together in a hexagonal network create graphite structures. Each carbon atom in the graphite structure is bonded only to three others. Fullerene is a spherical or soccer ball like structure with sp^2 hybridized carbon atoms. Figure 6 shows the various types of carbon structures (O'Connell, 2006). Carbon nanotubes can be visualized by concentrically rolled single graphene sheet or multiple sheets to form tubular structures with sp^2 hybridized carbon atoms similar to fullerene. In terms of length scale, carbon nanotubes represent the intersection or the transition between fullerene family and the traditional carbon fibers as shown in Figure 7.
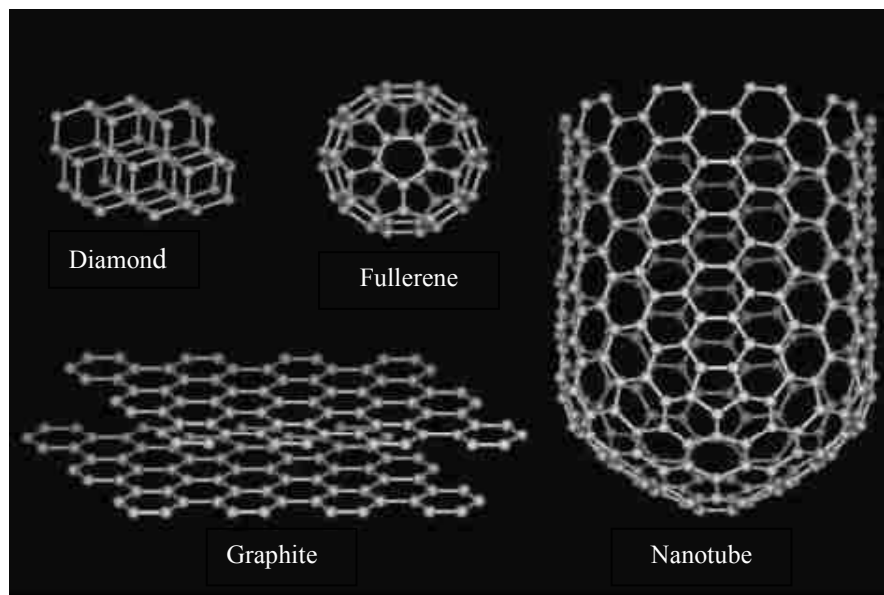
Figure 6. Carbon based structures adapted from (O'Connell, 2006)
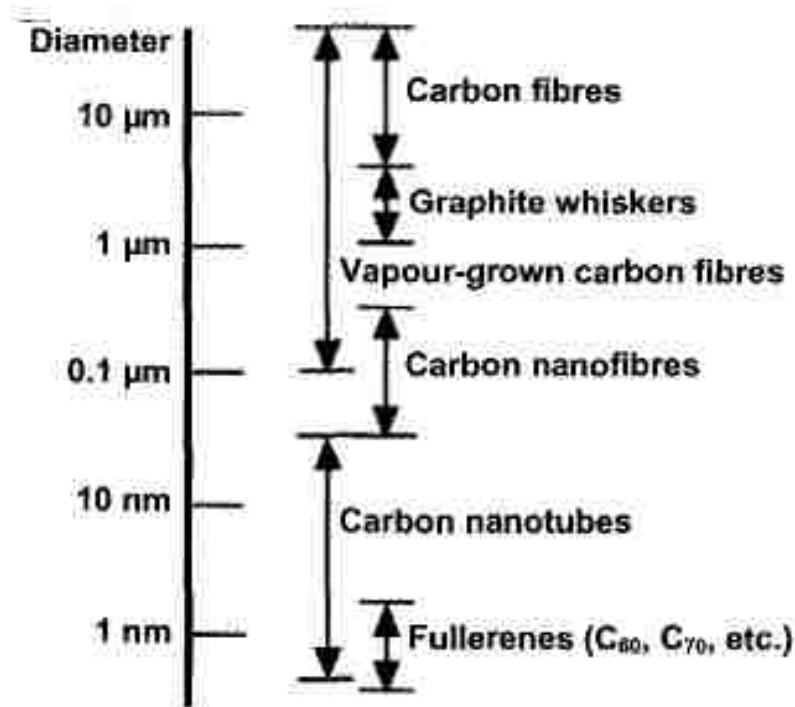
Figure 7. Comparison between various carbon fiberous structures (Shaffer & Sandler, 2007)

CNTs were first introduced in 1991 by Iijima when he found tubular structures of carbon at the nano scale (Iijima, 1991). The first CNTs found consisted of multiple shells of graphitic structure and were known later as Multi-walled carbon nanotubes (MWCNTs). Approximately two years later, Iijima discovered single graphitic shell CNTs which were later called as Single-Walled Carbon nanotubes (SWCNTs) (Iijima & Ichihashi, 1993). Although Iijima was credited for the discovery of the nanotubes, there are earlier reports in the literature about the nanotubes. Roger Bacon reported troublesome carbon nanowhiskers under SEM investigation when he used electric arc method to produce graphite whiskers (Bacon, 1960). Later, Endo imaged the nanotubes using high-resolution transmission electron microscope (HRTEM) and reported the

24

synthesis of tubular carbon structure using hydrocarbon decomposition (Oberlin et al., 1976).

The orientation of rolling a graphene sheet determines the structure or the geometrical properties of the SWCNTs (Loiseau *et al.*, 2006). The rolling orientation can be characterized by describing a unit vector on the graphene sheet as shown in Figure 8. Similarly, the unit vector can be described using a pair of integers (n,m). This pair defines the so-called the chiral vector $\vec{C}$ which can be computed by

$$\vec{C} = n\vec{a}_1 + m\vec{a}_2 \tag{2.1}$$

where $\vec{a}_1$ and $\vec{a}_2$ are constants equal in length and called graphene basis. C represents the circumference of nanotubes and describes implicitly another parameter called the chiral angle θ where

$$\theta = \arctan\left(\sqrt{3}m / (2n + m)\right) \tag{2.2}$$

The unit cell is defined by $\vec{C}$ and $\vec{T}$ where $\vec{T}$ is given perpendicular to $\vec{C}$ in the longitudinal axis of the nanotube and it is also a function of m and n. The unit cell is repeated in the direction of $\vec{T}$ to form the nanotubes. Based on the chiral parameters, many unique structures of the nanotubes exist. Examples of this structure are presented in Figure 9 (O'Connell, 2006). Armchair structure is formed when n equals m while zigzag like structure is formed when n or m is zero.

25
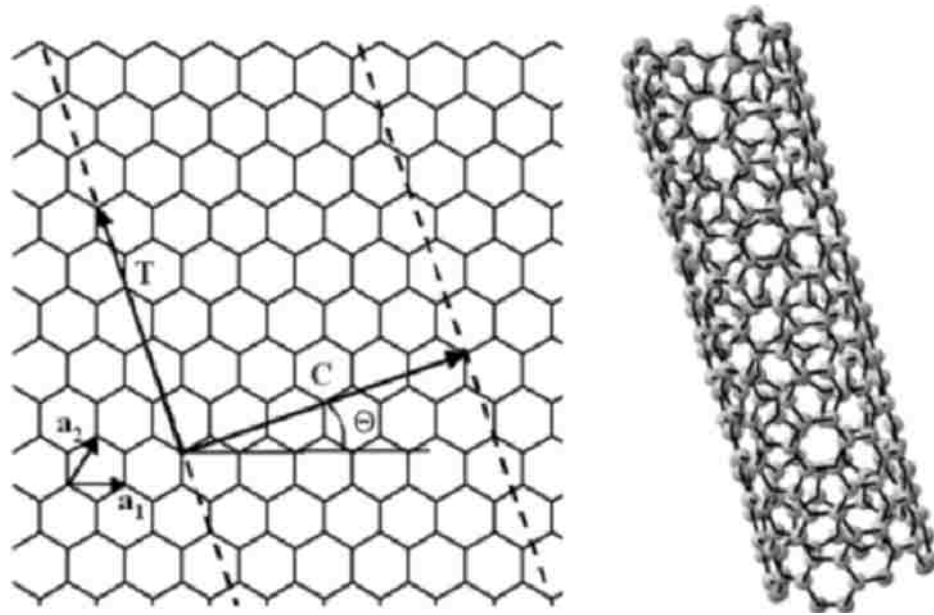
Figure 8. Construction of carbon nanotube from graphene sheet (O'Connell, 2006)

Armchair: n = m

Zigzag: (n,0)

Chiral: (n,m) m≠0
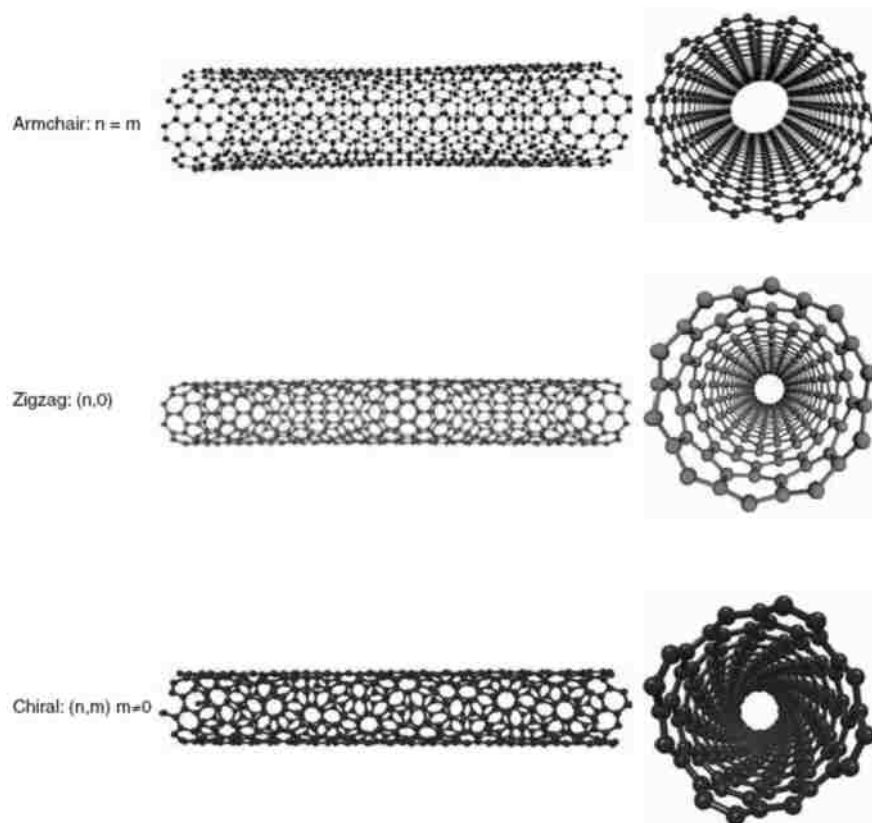
Figure 9. Special geometries of the nanotubes (O'Connell, 2006)

26

Several methods were developed over the last two decades to produce CNTs. The synthesis of CNTs is usually performed providing the required energy to break the graphite feedstock and produce the nanotubes. This process is performed under specific conditions of inert atmosphere with high pressure and temperature. This energy can take the form of electrical, light, heat/chemical energies such as the arc discharge, laser ablation, and chemical vapor deposition (CVD) techniques. In most cases, metallic catalyst is required for the synthesis or growth process. Ijima first used arc discharge method to synthesize MWCNTs (Iijima, 1991). In this method, a low-voltage (~12 to 25 V), high current (50 to 120 amps) power supply is used to produce an arc across a 1-mm gap between two graphite electrodes 5 to 20 mm in diameter. The synthesis is performed under the atmosphere of inert gas such as Helium or Argon at a pressure of 100 to 1000 Torr. The MWCNTs are formed on the cathode. The laser ablation technique produces large quantities of SWCNTs (Thess et al., 1996). This technique uses pulse or continuous laser waves stroke a graphite source and a cobalt/nickel metal catalyst in a 1200°C quartz furnace under pressure of 500 Torr. In the CVD method, the carbon source is a hydrocarbon gas flow that is directed to metallic catalyst placed in a furnace with medium temperature (550-1200°C). Other techniques provide heat/chemical energy include flame synthesis and Plasma Enhanced CVD (O'Connell, 2006).

Since their discovery at 1991, scientists spent a lot of effort to investigate various properties of CNTs and to develop methods for increasing the production capacity. As per 2006, the worldwide production of single and multi-walled CNTs reached 7 and 300 tons/year respectively (Eklund et al., 2007). China, USA, Korea, and Japan are among the countries that produce the highest capacities of CNTs. In 1992, only nine papers were

published relevant to the CNTs. The number of publications exceeded 10,000 papers by 2006 with a big portion related to CNTs-polymer composites. The big effort spent on the CNTs research is attributed to their distinguished mechanical, electrical, and thermal properties. Table 1 presents a comparison of the mechanical properties between CNTs and other materials. The mechanical properties of CNTs are one or more order of magnitude higher than the other materials. Typically, the price of SWCNTs is approximately \$500/gm while the price of MWCNT \$10/gm (O'Connell, 2006). The price of SWCNTs is much higher than the MWCNTs because of the cost of the synthesis process. In spite of being relatively expensive, the significantly low volume of CNTs used in polymer composites (typically less than 3%) makes small addition to cost. Moreover, the cost of large quantities showed to be much cheaper than the above noted cost.

Table 1. Mechanical properties of different materials (Eklund et al., 2007)

Material	Young's Modulus (GPa)	Tensile Strength (GPa)	Density (g.cm^{-3})
SWCNT	~1000	~100-200	~0.7-1.7
High tensile steel	210	1.3	7.8
Toray carbon fibers	230	3.5	1.75
Kevlar	60	3.6	1.44
Glass fibers	22	3.4	2.6

The only route to scale up the production capacities of the CNTs is through successful industrial applications. Currently, there are limited applications for the CNTs with the majority being the mechanical and electrical applications (Eklund et al., 2007).

28

The mechanical applications include polymer, metal and ceramic matrix composites for improving strength, toughness, and stiffness and thin film composite coatings. Examples of electro-mechanical applications include scanning probe tips, compliant interconnects, and contact devices for MEMS devices. Other promising applications in the optical, electrical, or medical fields include electrodes and additives for batteries, single tip electron guns for SEM and TEM systems, and cancer cell targeted radiation absorbers.

2.5   CNTs-Polymer Composites

Although great portion of CNTs research is directed to the production and performance of CNTs-polymer nanocomposites, yet the behavior is not well understood. The aim of incorporating stiff nano reinforcement in the soft polymers is to enhance their mechanical response. Conceptually, once the nanocomposite is loaded, the matrix transfers the load via shear to the CNTs. The large length-to-diameter (aspect) ratio of the CNTs would provide sufficient interfacial area for the load transfer and subsequently the CNTs compensate for the low modulus of the soft matrix, leading to an enhanced mechanical response for the nanocomposite.

Several types of polymers were used along with the CNTs to fabricate enhanced nanocomposites including thermosets, elastomeric, and thermoplastic polymers. In this dissertation, emphasis is placed on thermosetting polymers. Although incorporating the CNTs in polymer matrix seems to enhance the mechanical properties, three challenges are addressed by (Advani & Fan, 2007) while processing the nanocomposites as follows:

(1) Uniform dispersion of CNTs within the polymer matrix is necessary to obtain homogenous nanocomposites. The good dispersion would guarantee the

29

maximum surface area of the CNTs for the composite action between the CNTs and polymer to take place.

(2) Creation of strong interfacial bond between the CNTs and the polymer matrix through various types of chemical treatments. The interfacial bond will not only enhance the chemical interaction between the two materials, but also helps obtaining a good dispersion.

(3) Alignment or orientation of CNTs using mechanical, electrical and magnetic fields.

Over the years, many techniques were developed to overcome the aforementioned challenges. Mechanical or magnetic stirring, extruder, and ultrasonic agitation are the most popular mechanisms used to exfoliate the CNTs agglomerations and improve the dispersion. Surface functionalization is also used to improve the interfacial bond between the polymers and the CNTs. Different types of functionalizations are addressed in the following section.

2.6   Functionalization of Carbon Nanotubes

2.6.1   Surfactant Treatment of CNTs

The surfactant treatment is also known as non-covalent functionalization. The addition of surfactants was found to improve the dispersion of CNTs in polymers and water. The surfactant in this case works as dispersing or coupling agent for the nanotubes in the epoxy resin. There are many types of surfactants addressed in the literature. These types include anionic, non-anionic, and cationic surfactants (Sahoo et al., 2010).

Common surfactants used with CNTs are polyoxyethylene octyl phenyl ether (Triton-X100), sodium dodecylbenzene sulfonate (SDS), hexadecyltrimethylammonium bromide (CTAB), sodium dodecylbenzene sulfonate (NADDBS), and Polyoxyethylene 8 lauryl (C12EO8) (Islam et al., 2003). Figure 10 shows various surfactants' adsorption on nanotubes surface.
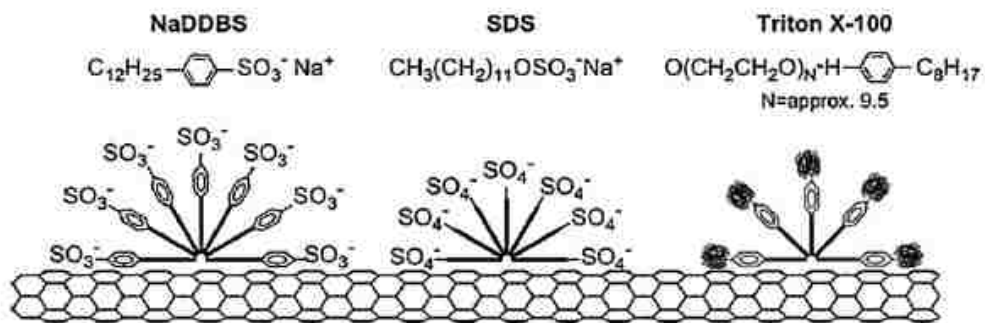
Figure 10. Adsorption of surfactant on CNTs surface (Islam et al., 2003)

The use of surfactant provides a non-covalent chemical interaction through coulombic attraction between the nanotubes and the surrounding matrix. This interaction takes place due to the surfactant bridging action between the incompatible hydrophilic polymers and hydrophobic nanotubes. The bridging effect is achieved because surfactants comprise of two parts: the hydrophilic region of the molecule or the polar head group; and the hydrophobic region or the tail group that usually consists of one or few hydrocarbon chains. The non-polar tail of the surfactant tends to get attracted to the CNTs surface creating non-reactive functional groups while the polar part interact with the polymer chains through Hydrogen bond. As a result, they overcome the incompatibility between the hydrophobic surface of the CNTs and the hydrophilic epoxy

31

resin. In addition, the dispersibility of CNTs increases via the electrostatic repulsion between the surfactant.

The distinct structural feature of a surfactant originates from its "duality". Surfactants are classified according to the charge of their head groups, thus cationic, anionic, nonionic or zwitterionic are known. The uniform dispersion of CNTs in polymer matrices showed the ability to alter polymer microstructure and enhance thermal stability of polymers such as Poly methyl methacrylate (PMMA) (Alexandre & Dubois, 2000, Coleman et al., 2006, Lau et al., 2006). (Fukushima et al., 2003) reported a strong physical interaction with the π electrons of the nanotubes with ionic liquids. The exfoliation of MWCNTs in the polymer composites depends on the Hydrophilic-Lipophilic balance (HLB) of the used surfactants. This is because; the best result has been obtained with a combination of electrostatic (anionic surfactant) and steric (nonionic surfactant) stabilization (Tillier et al., 2003).

The HLB value represents the tendency of an emulsifier (surfactant) to act as an oil-soluble or as a water-soluble type of emulsifier (Becher, 1966). It can be determined by calculating values for the different regions of the molecule, as described by Griffin in (Davies, 1957, Griffin, 1949, Griffin, 1954). Griffin's method that is applicable for non-ionic surfactants is described in 1954 as follows:

$$HLB = 20\left(\frac{M_h}{M}\right) \tag{2.3}$$

where M_h is the molecular mass of the hydrophilic portion of the molecule, and M is the molecular mass of the whole molecule, giving a result on an arbitrary scale of 0 to 20. A low HLB, e.g. 1–9, indicates an oil soluble substance, while a high HLB, e.g. 11–20,

suggests a water-soluble compound. Lipophilic emulsifiers are typically nonionic, such as sorbitan trioleate (HLB = 1.8) or propylene glycol monolaurate (HLB = 4.5), as well as the saturated and unsaturated fatty acids such as palmetic acid. On the other hand, hydrophilic emulsifiers are typically ionic, such as soaps of alkyl or aryl sulfuric acids, e.g. sodium lauryl sulfate or sodium dodecyl sulfate, or soaps of alkyl or aryl sulfonic acids, e.g. sodium dodecyl benzene sulfonate (HLB = 11.7). Moreover, for nonionic surfactants, the HLB value is also related to the ethoxylation level of the surfactant, namely the ethylene oxide content, which represents the water-soluble portion of the surfactant molecule. Consequently, more ethylene oxide units lead to a higher water-solubility and a higher HLB value.

In this dissertation, emphasis is placed on surfactants compatible with epoxy resins. In this context, (Gong et al., 2000) examined the use of Polyoxyethylene 8 lauryl (C12EO8) surfactant with MWCNTs in epoxy composites. The major findings from the study was that the addition of 1.0% wt. of nanotubes along with surfactant increased the glass transition temperature (Tg) and storage modulus (G') drastically. However, the addition of nanotubes alone yielded moderate or limited enhancement in G' and Tg by 26 and 40% respectively. Furthermore, the addition of surfactant alone resulted in a noticeable reduction in G' and no effect on Tg. The scanning electron microscope (SEM) micrographs revealed better dispersion for the nanotubes when surfactant is used. (Geng et al., 2008) investigated the effect of Triton X100 surfactant treatment on the thermal, mechanical, and electrical properties of CNTs epoxy nanocomposites. It was reported that the addition of 0.1% wt. surfactant treated CNTs increased storage modulus, flexural strength, flexural stiffness and glass transition temperature significantly. The

33

improvement is attributed to the improvement in the interfacial bond between the nanotubes and the surrounding polymer.

2.6.2 CNTs' Covalent Functionalization

The covalent functionalization on the other hand involves impregnating function groups on the surface of the nanotubes. The functional groups have two roles. The first function is it helps the dispersion of the CNTs due to the positive or negative charge that counteract the van der Waal interaction. The second function is that it chemically reacts with the epoxy components (either the resin or the hardener) forming a strong covalent chemical bond which increases the interfacial bond considerably (Advani & Fan, 2007). One of the earliest functionalization process is reported by (Zhu et al., 2003) who used mixture of sulfuric, nitric, and hydrochloric acids to attach carboxyl (COOH) groups at the ends of SWCNTs. They also performed fluorination in order to attach fluorine (F) functional groups on the sidewalls of the nanotubes. The carboxyl groups are expected to react with the resin while the fluorine groups are expected to react with the hardener, thus the interfacial bond increases. Figure 11 shows a schematic for the covalent functionalization process.

34
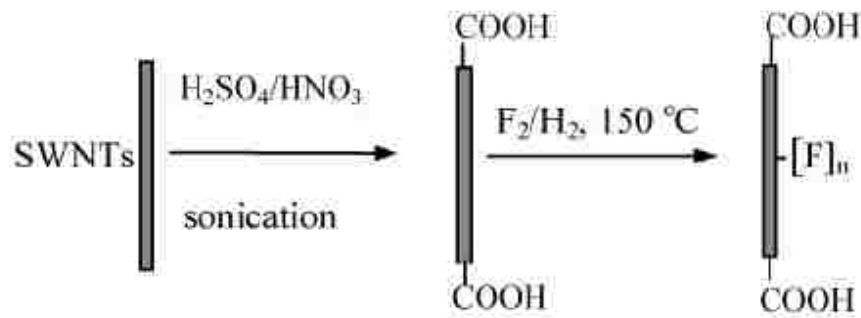
(a) Attachment of functional groups

(b) Carboxyl groups react with resin
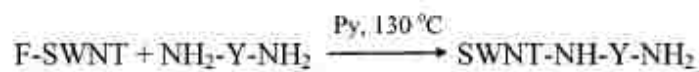
(c) Fluorine groups react with hardener

Figure 11. Covalent functionalization (Zhu et al., 2003)

Since the discovery of the CNTs functionalization process in 2003, many scientists directed their effort to examine the behavior and the capability of various functional groups in enhancing the CNTs-polymer nanocomposites. Examples of other functionalizations include UV/ozone treatment or plasmas (Seo et al., 2005, Sham & Kim, 2006) amine (Gabriel et al., 2006, Sham & Kim, 2006) , silane (Ma et al., 2006) and fluorine treatments (Lee et al., 2003). The functionalized CNTs have been found to enhance the mechanical response of CNTs-epoxy nanocomposites. For example, solution

35

mixing 1.0% wt flourinated SWCNTs increased the tensile strength and Young's modulus by 18 and 30% respectively (Zhu et al., 2003). In addition, simple mixing of 6.0% wt oxidized MWCNTs reduced the tensile strength by 25% and increased the Young's modulus by 32% (Breton et al., 2004). Moreover, shear mixing of 0.5% wt NH2-modified double walled carbon nanotubes (DWCNTs) increased the tensile strength, Young's modulus, and toughness by 10%, 15%, and 45% respectively (Gojny et al., 2005). Furthermore, solvent mixing of 0.25 % wt Copolymer modified MWCNTs increased the tensile strength and Young's modulus by 50% (Li et al., 2004). It seems that the functionalized CNTs mechanical enhancement is very sensitive to the chemical process, type and content of CNTs.

In general, the two approaches of functionalizations were found to be effective in improving the mechanical response of CNTs-polymer nanocomposites. The major advantages and disadvantages of the two approaches are as follows:

1) The non-covalent functionalization are particularly attractive because the physical adsorption seldom damages the structure of CNTs, nor disturbs the inherent π-bonds of CNTs and thus maintains the intrinsic properties of the individual nanotubes un-affected (Gong et al., 2000, Grossiord *et al.*, 2006, Kim *et al.*, 2007, Vaisman *et al.*, 2006). On the contrary, the covalent functinaliozation is aggressive especially the oxidation process using mixture of concentrated acids (Kim *et al.*, 2005, Park *et al.*, 2005), thus they generate structural defects deteriorating the intrinsic properties of CNTs.

2) The strong bond, created by the covalent functionalization, enhances significantly the mechanical response due to the distinguished stress transfer between the

36

relatively soft polymers and the stiff nanotubes. The non-covalent interaction between the surfactant and the nanotubes has moderate effect in enhancing the interfacial bond achieved by the non-covalent bond. This can be noticed from the range of mechanical enhancement both approaches could achieve for the same type of polymer.

2.7   CNTs-FRP Composites

Few articles have addressed the use of CNTs to enhance the mechanical properties of composites in the last decade. However, these studies showed good enhancements in mechanical response when CNTs-epoxy nanocomposites are used in the fabrication of FRP composite. For instance, (Qiu et al., 2007) examined the tensile and shear behavior of glass fiber reinforced polymer (GFRP) composites. With 1.0% by weight functionalized MWCNTs, they reported 14% and 5% increase in on-axis tensile and shear strengths respectively. They also reported a 20% and 8% increase in Young's and short beam moduli. (Seyhan et al., 2008) investigated mode I & II fracture toughness of GFRP composites using double cantilever beam (DCB) test. They observed 8% increase in mode II fracture toughness when 0.1% wt functionalized MWCNTs were added.

Compressive shear tests were performed to determine the interlaminar shear strength (ILSS) of glass woven fabric composites with different dispersion techniques. The statistical analysis showed no enhancement in ILSS due to the addition of 0.5% by weight MWCNTs (Chandrasekaran et al., 2010). The surfactant treatment of as-received and functionalized MWCNTs was used to improve the electrical resistance and

37

mechanical response of GFRP composites. The use of surfactant with CNTs improved the on-axis tensile and impact response (Yesil et al., 2010). A major conclusion can be drawn from most of the above investigations is that MWCNTs might produce a slight increase in the on-axis strength and stiffness of FRP composites (< 10%). This limited enhancement cannot justify the use of CNTs with an expected increase in cost of composite fabrication.

2.8   Summary

Although fiber reinforced polymer (FRP) composites have been widely used in many civilians and military applications, there exist many shortcomings on their structural behavior. The inter fiber fracture due to transverse, fatigue loadings, and thermal stresses is addressed as a major problem that causes the initiation and propagation of micro cracks. Furthermore, creep of adhesive's bond lines is recognized recently as a major challenge when reinforced or prestressed concrete structures are strengthened against sustained loads. On the other hand, the use of CNTs in polymer nanocomposites increased rapidly in the last few years as one of the promising applications of Nanotechnology. Recent studies showed a good improvement in the mechanical response of FRP composites when CNTs are incorporated. However, these studies are limited to few mechanical tests and CNTs content.   Therefore, further investigations on static, long term, and dynamic behavior of FRP composites incorporating CNTs are required.

CHAPTER 3. CNTS-EPOXY NANOCOMPOSITE: FABRICATION AND CHARACTERIZATION

3.1 Overview

This chapter presents detailed investigation on the fabrication and testing of CNTs-epoxy nanocomposites, which are used for further investigations with FRP in the subsequent chapters. In particular, various approaches including physical and chemical treatments of CNTs are described. Mechanical characterization was performed to extract various mechanical properties through flexure and dynamic shear rheometer (DSR) tests. Thermal analyses are also performed using differential scanning calorimetry (DSC) and thermo gravimetric analysis (TGA). Furthermore, the microstructure of the nanocomposites is investigating via scanning electron microscope (SEM). Therefore, this chapter is divided to two main sections. The first section reports the treatment of CNTs in epoxy while the second section reports the mechanical, thermal, microstructure characterization of the produced CNTs-epoxy nanocomposite.

3.2 CNTs Treatment in Epoxy

This section deals with various approaches implemented to fabricate different CNTs-epoxy nanocomposites. The main goal from introducing several fabrication approaches is to evaluate the mechanical properties of the CNTs-epoxy nanocomposite produced by each approach and investigate their effect on the FRP mechanical performance. The major difficulties usually arise when fabricating the CNTs-epoxy nanocomposite is to

39

overcome the formation of agglomerated CNTs which reduce the mechanical properties of the nanocomposite. In general, two methods are introduced in the following sections: physical and chemical methods. The physical method is performed by mixing the CNTs as received in the epoxy resin and is denoted as "Pristine". The chemical methods include performing non-covalent or covalent functionalization while processing the CNTs in the epoxy resin.

The CNTs used in this study were supplied by Cheap Tubes, Inc. Based on the manufacturer's specifications, the CNTs were multi-walled with outer diameter (OD) of 20-30 nm, inner diameter (ID) of 5-10 nm, length of 10-30 µm, and aspect ratio of 500 to 1000. The bulk density of the MWCNTs is 0.21 gm/cm^3 and the specific surface area is 110 m^2/gm. The nanotubes are manufactured using catalytic chemical vapor deposition (CCVD) technique with purity greater than 95% by weight. Table 2 shows elemental analysis of the MWCNTs.

Table 2. Elemental Analysis of MWCNTs (Ohama, 1995)

Component	Content (%)
C	98.35
CI	0.45
Fe	0.26
Ni	0.94

The epoxy used in fabrication of the nanocomposite is EPOTUF® 37-127 epoxy system supplied by U.S. Composites, Inc. The epoxy resin is diluted liquid based on Bisphenol-A contains Diglycidyl ether (DGEBPA) while the hardener is aliphatic Amine.

40

The epoxy resin is low viscosity 100% reactive diluted liquid based on Bisphenol-A containing glycidyl ether. The resin viscosity at room temperature is 600 cps. The hardener is Aliphatic Amine EPOTUF® 37-614. The resin to hardener mixing ratio is 2:1, pot life is 30-45 minute at 26.7 ºC, setting time is 5-6 hours, and curing time of 24-28 hours. The tensile strength and elongation at failure are 68.9 MPa and 2.5% respectively. The chemical structures for the resin and the hardener are shown in Figure 12.
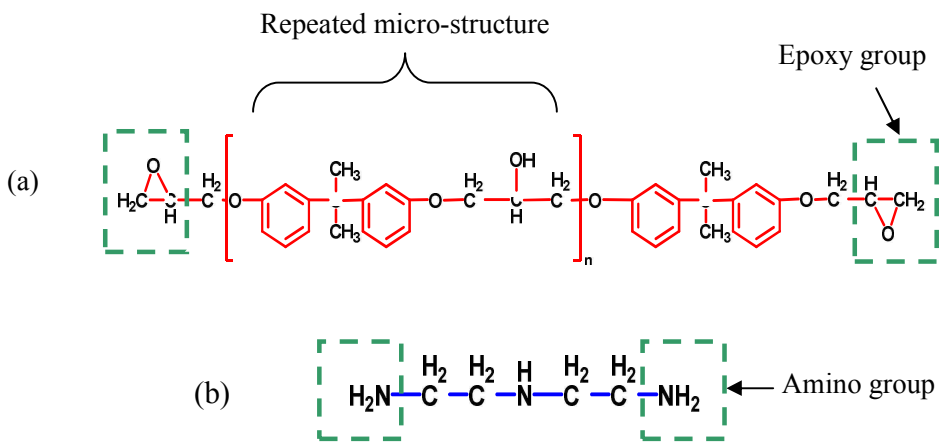
Figure 12. Chemical structure of the epoxy system (a) resin and (b) hardener

3.2.1 Physical Approach

This approach involves incorporating the pristine CNTs into the epoxy resin using ultrasonic agitation and magnetic stirring. Ultrasonic waves are sound waves transmitted at frequencies generally beyond the range of human hearing. The ultrasonic bath used in the process is supplied by Misonix, Inc. with a tank capacity and maximum input power 0.5 gal and 80 Watt, respectively. It is also operating at frequency of 40 kHz.

The ultrasonication mechanism is explained in Figure 13. During the sonication, the sound waves from the transducer radiate through the solution in the tank causing alternating high and low pressures. During the low-pressure stage, millions of

41

microscopic bubbles form and grow for a process known as "cavitation". During the high-pressure stage, the bubbles collapse or implode releasing enormous amounts of energy (Misonix®). The magnetic stirring was performed using 610-HPS standard hot plate stirrer supplied by VWR International. The hot plate operates on temperature range of 30 to 500°C and magnetic speed range of 60-1600 rpm. The ceramic top plate provides even heating surface and good chemical-resistant. The microprocessor control in the hot plate regulates heat and speed to accuracy within ± 2%.
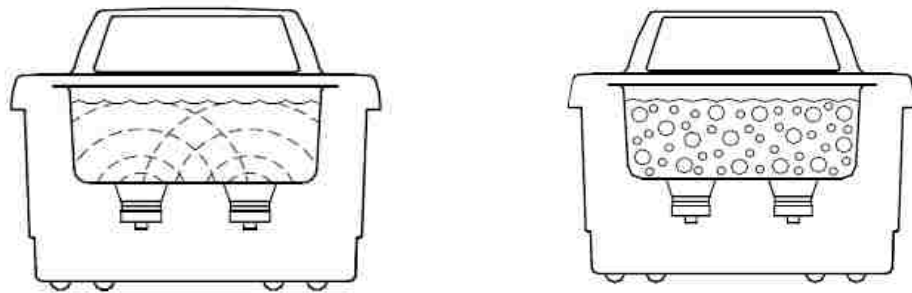
    (a) Transducers radiate ultra sonic waves   (b) Low pressure stage induces bubbles
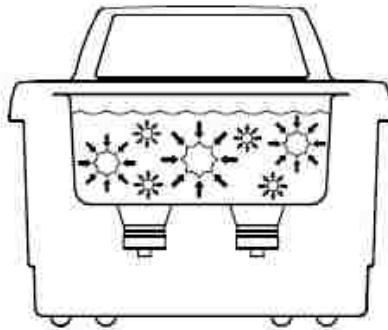
(c) High pressure stage collapsing the bubbles and releasing the energy
Figure 13. Mechanism of ultrasonic bath in dispersion process (Misonix®)

In this study, the dispersion was performed by adding the required CNTs content to the epoxy resin. The CNTs contents of 0.45, 0.9, and 1.35 gm were added to 60 gm epoxy resin to obtain CNTs percentages of 0.5, 1.0, and 1.5% by weight of epoxy. The

42

CNTs-resin mixture was sonicated in the ultrasonic bath for 1.0 hour at room temperature (Figure 14). Magnetic stirring was then applied to the dispersion for 30 minutes followed by 15 minutes sonication. Thirty grams of hardener was added to the CNTs-resin composite with 5 minute mechanical stirring and the nanocomposite is ready to use.

3.2.2   Chemical Approach

The chemical approaches are introduced at this study to examine the improvement of the fabrication and the mechanical response of the CNTs-epoxy composite. These approaches provide the solution of many challenges arise when CNTs are physically dispersed in the epoxy. The chemical approach consists of three categories: non-covalent, covalent, and combined functionalization. The term "functionalization" implies introducing functional groups on the surface of the CNTs to improve the chemical interaction between the CNTs and the surrounding epoxy matrix.

Figure 14. Ultrasonication of CNTs in epoxy resin

3.2.2.1 Non-Covalent Functionalization

There are two types of non-covalent functionalization introduced in the literature: surfactant assistance and polymer wrapping. In this study, we will examine the use of

43

surfactant assistance in fabricating the CNTs-epoxy nanocomposite. The well-known non-ionic surfactant Triton X-100 is used [molecular formula is $C_{14}H_{22}O(C_2H_4O)_n$]. Triton X-100 has specific gravity of 1.065 at 25°C, effective molarity of 1.7 M, viscosity of 240 cps at 25°C, hydrophilic-lipophilic balance (HLB) value of 13.5, and critical micelle concentration (CMC) of 0.2 mM. Triton X-100 consists of a hydrophilic polyethylene oxide group (on average it has 9.5 ethylene oxide units) and a hydrophobic hydrocarbon lipophilic group.

The hydrophobic group (non-polar tail) of the surfactant attracts to the CNTs surface creating non-reactive functional groups on the surface of the nanotubes. These functional groups improve the dispersibility of CNTs by inducing electrostatic repulsion among functional groups, which disentangle the individual nanotubes. On the other hand, the hydrophilic group provides the chemical compatibility with the epoxy matrix. Another major advantage of using the surfactant is that it does not affect the surface of the nanotubes, therefore maintains the structure and strength of the CNTs. Figure 15 shows the chemical structure of Triton X-100 and Figure 16 shows schematically the the CNTs dispersion mechanism via non-ionic surfactant.

An important phenomenon would occur with the addition of relatively large amount of surfactant to solutions is the formation of micelles of surfactant which are small colloidal particles. When micelles form, the surfactant solution behaves as a micro-heterogeneous medium (Dominguez *et al.*, 1997). Schematic of surfactant micelles are shown in Figure 17. The formation of micelles is associated with a critical concentration known as critical micelle concentration (CMC). The value of the CMC can be determined by the abrupt change in the slope of the physical properties of the surfactant solution with

respect to the surfactant concentration such as surface tension. The CMC is measured by the concentration of the surfactant in the dispersion media (solvent in this case). It can be noted that the surfactant content should exceed CMC in order to introduce strong steric repulsive forces among the nanotubes and it should not also be very large to avoid the plasticizing effect of surfactant with low molecular weight. The concentration, in terms of number of moles per liter, can be obtained using the following Eqns:

Concentration = Number of moles/volume   in Mol/liter   (3.1)

Number of moles = weight/molecular weight   in Mol   (3.2)

Given that the molecular weight of Triton X-100 is 625 gm/mole and the CMC is 0.2 mM, the equivalent weight which achieves the CMC per liter of solvent is 0.125 mg. A choice is made after (Geng et al., 2008) for using a concentration of 10 CMC to produce the surfactant treated CNTs-epoxy nanocomposites.
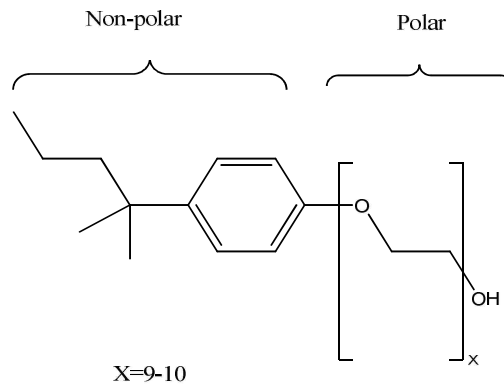
(a)

(b)

Figure 15. Triton X-100 (a) chemical structure and (b) 3-D model

A 0.5% CNTs-epoxy nanocomposite was produced by adding 500 mL methanol (solvent) to 0.5 g MWCNTs and sonicating the mixture for 30 minutes. 0.3 g of the non-ionic surfactant Triton X-100 was added with 2 hours sonications. Epoxy resin of 120 g was heated to 75°C under magnetic stirring using the hot plate and added to the CNTs-solvent-surfactant dispersion. The mixture was sonicated for 1.0 hour at 60°C and vacummed overnight to remove the solvent. The vacuum pump used is Edwards RV3 supplied by Ideal Vacuum Products, Inc. with motor power of 300 Watt. The pump operates at speed of 60 Hz and can maintain pressure of 1.5×10^{-3} Torr. 60 g of hardner

46

was applied to the CNTs-surfactant-resin composite with 5 minute mechanical stirring and the nanocomposite is ready to use.
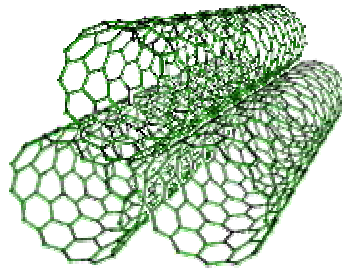
(a) CNTs agglomeration
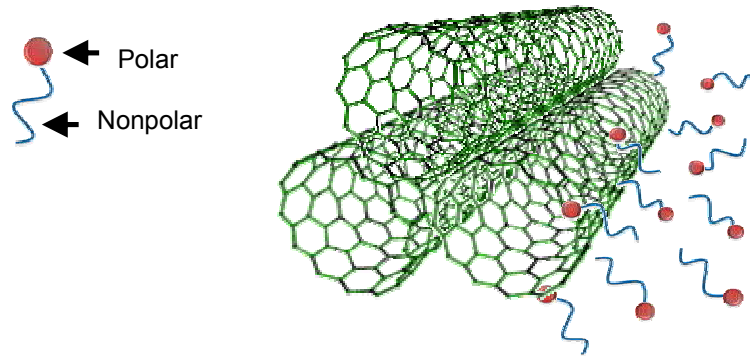
(b) CNTs + Surfactant
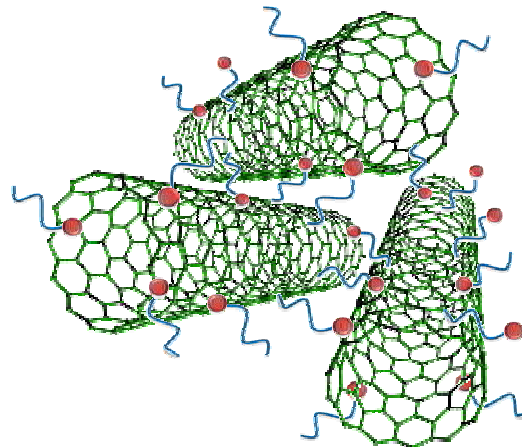
(c) Dispersed CNTs

Figure 16. CNTs-surfactant mechanisms

47
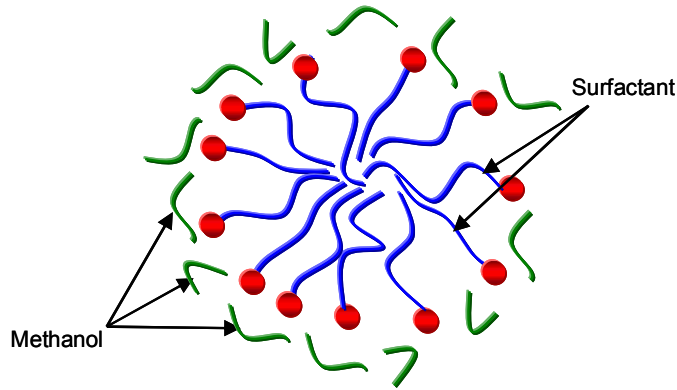
Figure 17. Schematic of surfactant micelles formed in methanol

3.2.2.2 Covalent Functionalization

The main advantage of performing the covalent surface functionalization is to introduce functional groups on the surface of the nanotubes. These functional groups react with the epoxy resin or the hardener to form a strong covalent chemical bond. The covalent bond improves the interfacial bond or load transfer between the nanotubes and the epoxy matrix. However, the covalent functionalization process in many occasions is aggressive and causes severe damage to the structure of the nanotubes. There are many types of functional groups introduced in the literature such as carboxyl (COOH) and hydroxyl (OH) groups. In this study, functionalization with carboxyl groups is examined using non-organic and organic acids.

(i) Functionalization using non-organic acids

Two types of non-organic acid functionalized CNTs are examined. In the first type, commercial MWCNTs, supplied by Cheaptubes, Inc. and functionalized with carboxyl (COOH) groups, are processed in epoxy. The COOH-MWCNTs were added

48

first to the resin with 1.0 hour sonication at 40°C. In order to ensure chemical reaction between the functional groups on the surface of the nanotubes and the resin chains, the dispersed mixture was stirred for 2.0 hour at 80°C. The hardener was added after cooling the resin and the epoxy-MWCNTs were ready to use. <u>In the second type</u>, the functionalization process was performed on pristine MWCNTs supplied by Cheaptubes, Inc. The covalent surface functionalization with non-organic acids was performed using sulfuric (H_2SO_4), nitric (HNO_3), and hydrochloric (HCL) acids. The functionalization process was performed after (Osorio *et al.*, 2008) by first preparing acidic mixture of H_2SO_4:HNO_3 (3:1). The CNTs were sonicated with the mixture for 4 hours and upheld for 15 hours and stirred afterwards for 40 minutes at 140 °C. Then, hydrochloric acid was added to the solution. Subsequently, this solution was neutralized with ammonium hydroxide (NH_4OH) and filtered with a 0.22 µm cellulose acetate membrane (Figure 18-a). The CNTs were washed several times using deionized water until the pH 5.5 was reached. The functionalized CNTs were dried over night under vacuum. The major challenge from the functionalization process is to get rid of the salt produced from the neutralization process which mixes well with the functionalized CNTs.

In general, the functionalization process results in CNTs with chemically bonded carboxylic groups (COOH). When CNTs are added to the resin, these functional groups bond chemically to the resin, thus create strong connection between the CNTs and the resin. In order to apply the functionalized CNTs to the resin, they were sonicated in methanol for 2 hours and the dispersion was sonicated with the resin afterwards. The CNTs-methanol-resin dispersion was vacuumed to remove the methanol (Figure 18-b). The hardener was added to the CNTs-resin mix and the epoxy was used to produce the

49

CNT-epoxy nanocomposite. Figure 19 and Figure 20 show schematics for the functionalization process and the microstructure of the CNTs-epoxy nanocomposites. In this dissertation, the results of mechanical and thermal responses obtained using the first type (the commercial functionalized MWCNTs) are presented in the results section.

Figure 18. Filtration of functionalized CNTs
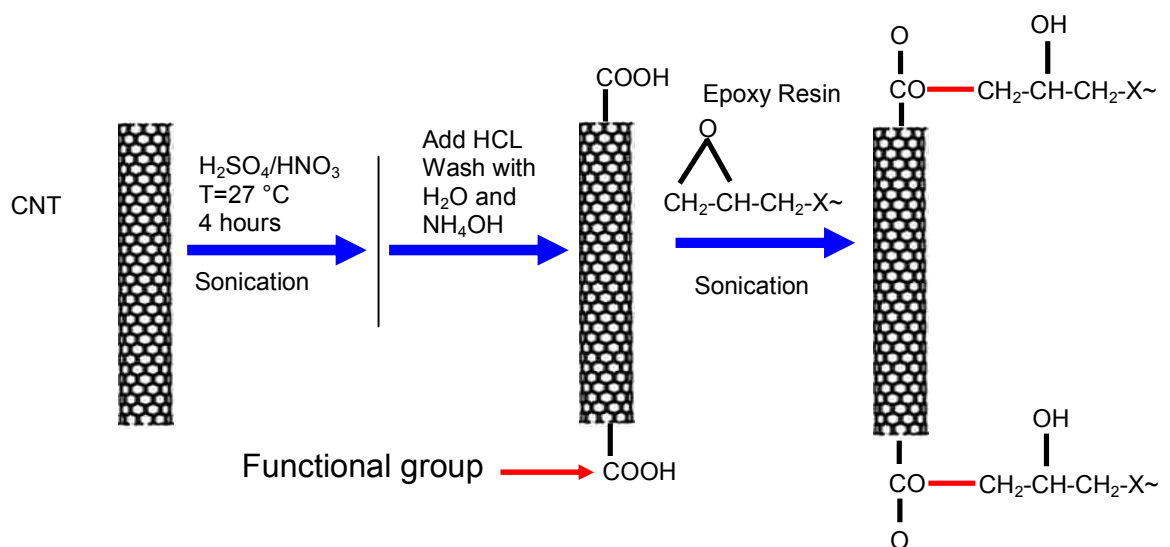
Figure 19. Surface functionalization of CNTs using non-organic acids
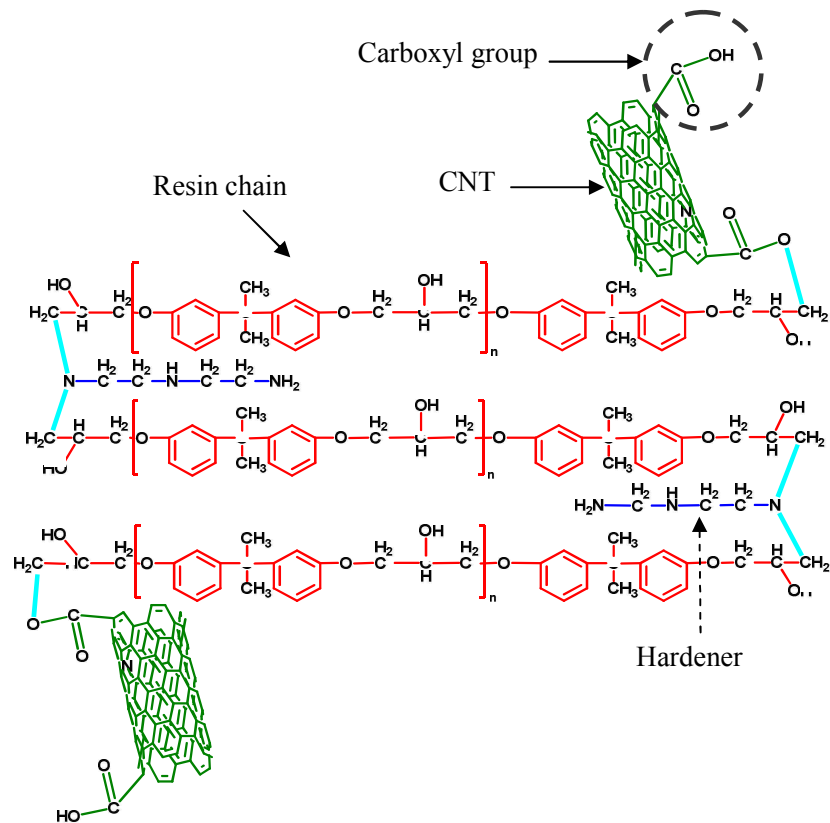
Figure 20. Schematic for the microstructure of CNTs-epoxy nanocomposite

(ii) Functionalization using organic acids

The organic acid functionalization was performed after (Khan *et al.*, 2010) using oleic acid [$CH_3(CH_2)_7CH=CH(CH_2)_7COOH$]. The advantage of this method of covalent functionalization is that it is less aggressive than the functionalization performed with the non-organic acid mixture. The oleic acid has a week C=C bond and carboxyl group (-COOH) (Figure 21). The C=C bond is expected to break under high level of supplied energy and heat and would result in attachment of functional groups on the surface of the nanotubes. In order to obtain 0.5% functionalized CNTs-epoxy nanocomposite, 0.9 g CNTs are added to 200 mL methanol with sonication for 30 minutes. 5 mL oleic acid was

51

added to the CNTs-methanol dispersion and the mixture is stirred for 1 hour and sonicated for 30 minutes afterwards. 50 mL ammonium hydroxide is then applied with 6 hours magnetic stirring at 50°C. The dispersion was left to dry overnight at 50°C and the dried functionalized CNTs were obtained.
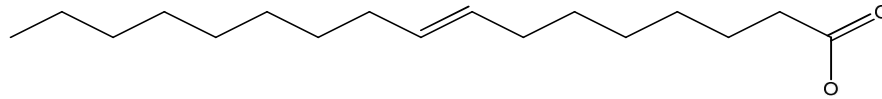
(a)

(b)

Figure 21. Oleic acid (a) chemical structure and (b) 3-D model

(iii) Combined non-covalent and covalent functionalization

In this technique, the non-covalent and covalent functionalizations were combined to produce the CNTs-epoxy nanocomposite similar to (Khan et al., 2010). The main idea was to ultilize the effectivness of the non-covalent functionalization in dispersing the nanotubes and the covalent functionalization in improving the interfacial bond between the nanotubes and the surrounding matrix. In this case, Triton X-100 is used to perform the non-covalent functionalization while oleic acid is used to perform the covalent functionalization.

The functionalization was performed by adding 0.9 g CNTs to 300 mL and sonicate for 30 minutes. 0.9 g Triton X-100 surfactant was added to the dispersion with 2.0 hours sonication and the mixture was left overnight. 5 mL oleic acid was added to the supernatant of CNTs dispersion, which is expected to be free from catalytic impurities and aggregates. The mixture was sonicated for 30 minutes and stirred for 1 hour. 50 mL of ammonia solution was added with magnetic stirring at 60°C for 4 hours. The solution was left overnight and then washed with water:methanol (1:1) solution. The foamy portion on the top of the solution was removed and the rest was dried overnight at 70°C.

3.3 Mechanical Characterization of CNTs-Epoxy Nanocomposite

Two tests were performed on different types of epoxy produced with CNTs: flexure and dynamic shear rheometer tests. The two tests were performed on epoxy prisms. In order to cast the epoxy prism, the hardener was applied to the CNTs-resin composite with 5 minute mechanical stirring. Steel molds were sealed using Cyanoacrylate glue and mechanical clamps (Figure 22). The CNTs-epoxy nanocomposites were cast in the steel molds using syringe pump to avoid the formation of air bubbles. The CNTs-epoxy specimens were demold after two days and cured for 10 days before they are tested.

53
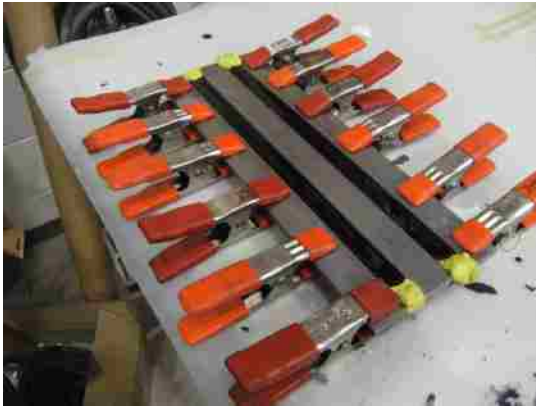
| (a) Epoxy cast in steel molds | (b) CNTs-epoxy prisms ready for testing |

Figure 22. Preparation of CNTs-epoxy prisms

3.3.1 Procedures and Test Setup

3.3.1.1 Flexure Test

There are two ASTM standards which deal with determining the flexure properties of unreinforced or reinforced plastics: (ASTMD790, 2010, ASTMD6272, 2010). The major difference between the two tests is that (ASTMD790, 2010) is concerned with three-point bending test while (ASTMD6272, 2010) is concerned with four-point bending test. In this study, the four-point bending ASTM standard is used. In this test, a prism of the produced CNTs-epoxy nanocomposite is rested on two supports and loaded by displacement-controlled mode at two points located at one third of the span. The dimensions of the prisms and the test setup are shown in Figure 23 and Figure 24, respectively. It is recommended by ASTM standard that the span-to-depth ratio to be at least 1:16. The displacement rate or the motion of the crosshead is estimated so that a maximum flexure strain of 0.01 mm/mm is induced at the outer fibers using the following equation (ASTMD6272, 2010).

54

$$R = 0.185ZL^2 / d \tag{3.3}$$

where (R) is the rate of crosshead motion in mm/minute, (Z) is the rate of straining of outer fibers (0.01), (L) is the supporting span, and (d) is the depth of the epoxy prism.

In many occasions, the flexure specimens do not fail because of the excessive deformation of polymers. For this regard, the ASTM suggested the termination of the flexure test by the occurrence of one of two events, either rupture of the flexure specimens or a maximum strain at the outer fiber of 0.05 mm/mm is reached. The reason for the 5.0% strain limit is to avoid the excessive deformations and predict the mechanical properties using formula that are based on small deformation theory. From the load-displacement response, the flexure stress (S) and flexure strain (r) at any load level are computed as follows (ASTMD6272, 2010):

$$S = PL / bd^2 \tag{3.4}$$

$$r = 4.70Dd / L^2 \tag{3.5}$$

where (P) is the applied load, (b) is the prism width, and (D) is the deflection. In addition, the toughness for each specimen is calculated to be the area under stress-strain curve up to 5% strain and the tangent modulus of elasticity in bending (E_B) is computed as follows (ASTMD6272, 2010):

$$E_B = 0.21L^3 m / bd^3 \tag{3.6}$$

where (m) is the initial slope of the load-displacement curve (obtained from 0 to 1.0% strain).

55
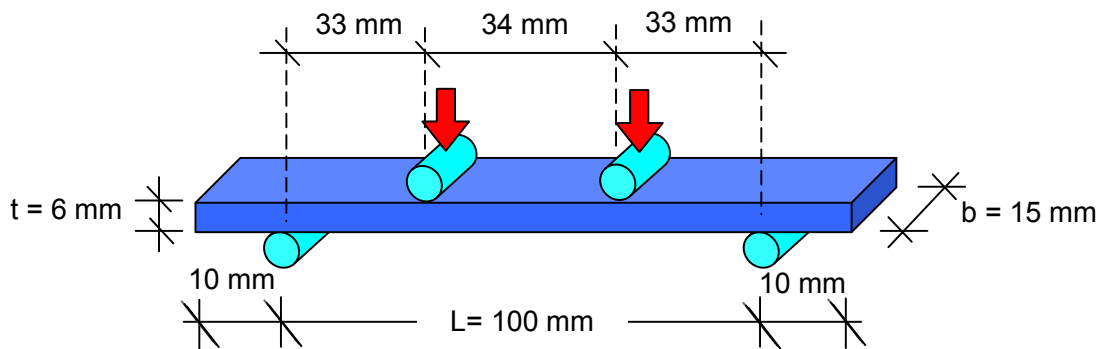
Figure 23. Dimensions of CNTs-epoxy beams

(a) Test setup   (b) Deflected shape

Figure 24. Flexure test setup and deformation

3.3.1.2 Dynamic Shear Rheometer (DSR) Test

The dynamic shear rheometer (DSR) test is performed to measure the viscoelastic properties of the CNTs-epoxy nanocomposites. This test is widely used in testing asphalt binders (ASTMD7175, 2008), however; it can be applied for any viscoelastic materials such as polymers. During the test, a known torque or shear stress is applied and the corresponding shear strain is measured. Depending on the test protocol, various viscoelastic properties can be obtained. The testing machine was physica MCR-301 rheometer supplied by Anton Paar, Inc. Figure 25 and Figure 26 shows the DSR test setup and specimens respectively.

56

In this study, two test protocols were applied to the CNTs-epoxy nanocomposites specimens. <u>The first test protocol</u> is conducted by applying constant torque of 100 mN/m for a short period of 150 second and is used to determine the creep compliance. <u>The second test protocol</u> is performed by applying oscillating torque of 100 mN/m with angular frequency ranges from 0.1-10 rad/sec (0.0159 to 1.59 Hz). Complex, storage, loss shear moduli, phase angle, and complex compliance are various mechanical properties obtained based on the oscillation response. Four specimens were examined in this study. They are neat epoxy and epoxy with 0.5, 1.0, and 1.5 % pristine CNTs. Figure 27 shows the three test protocols.
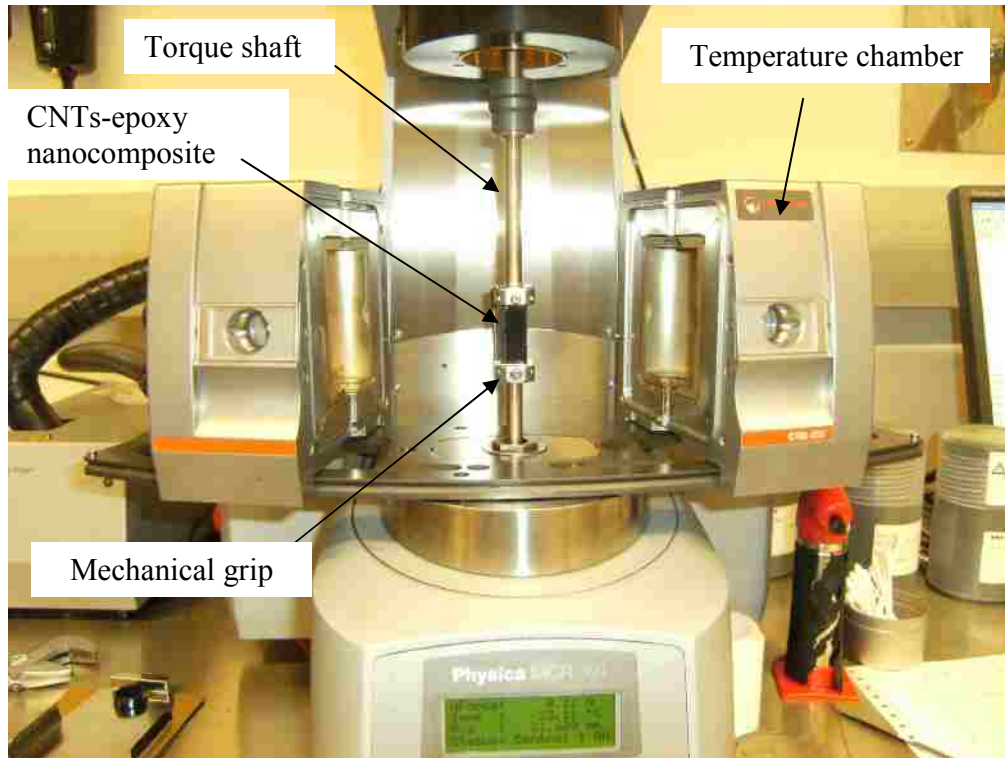
Figure 25. DSR test setup

(a)	(b)	(c)
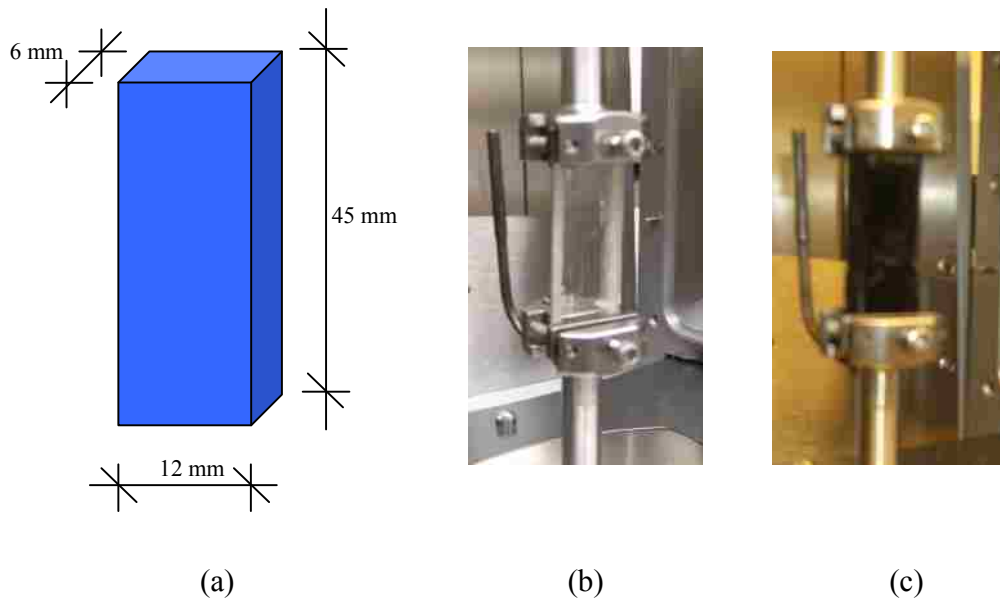
Figure 26. DSR specimen (a) dimensions, (b) Neat epoxy and (c) Epoxy with 0.5 %

pristine CNTs
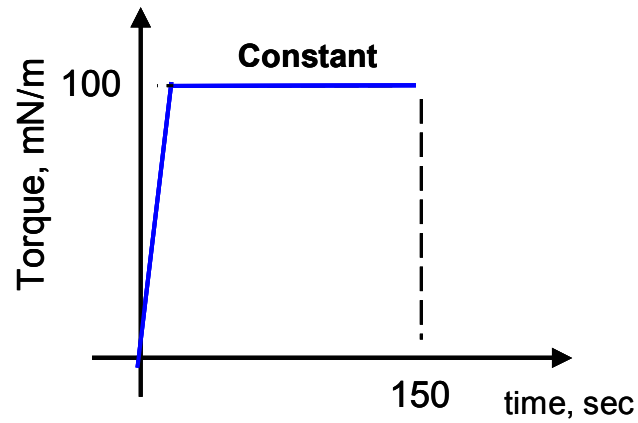
(a) Creep test
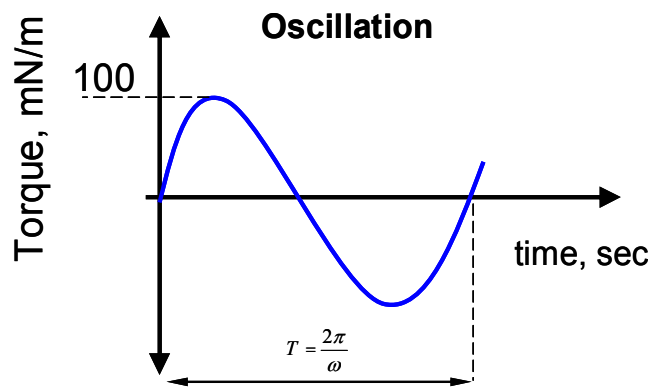
(b) Dynamic test

Figure 27. DSR test protocols

The major goal of performing the ramp or static loading is to obtain the static shear modulus (G) for specimens with various CNTs content. The shear modulus is obtained by computing the slope of shear stress (τ) and shear strain (γ) relationship. Another reason of performing the static shear test first is to ensure that the shear response of epoxy specimens stays within the linear elastic region under the applied torque level. The linearity of the response is important in the subsequent creep and dynamic tests for determining linear visco-elastic properties. The maximum shear stress for rectangular section is computed as follows:

$$\tau = \frac{M}{\alpha_1 bc^2} \qquad (3.7)$$

where (*M*) is the applied torque [100 mN/m], (*b*) is the long side of the cross-section [12 mm], (c) is the short side of the cross-section [6 mm], and (α_1) is a constant depends on the ratio (b/c) [0.246]. The deflection angle (θ) is measured using the shaft torque and the resulting shear strain and is computed as:

$$\gamma = \theta \frac{c}{L} \frac{\beta}{\alpha_1} \qquad (3.8)$$

where (*L*) is the length of the specimen [45 mm] and (β) is a constant depends on the ratio (b/c) [0.229].

The creep behavior of the CNTs-epoxy nanocomposite was investigated by conducting short-period creep test. In this test, constant shear stress (τ_o) was applied through constant torque and the shear strain [$\gamma(t)$] was computed from equation (3.8) at different time steps and the creep compliance [$J(t)$] was computed as follows (Findley *et al.*, 1989):

$$J(t) = \frac{\gamma(t)}{\tau_o} \qquad (3.9)$$

where (*t*) is the time. In order to remove the effect of initial elastic compliance [$J(0)$], the creep compliance is normalized with respect to the initial compliance as shown below (Findley et al., 1989).

$$J_n(t) = \frac{J(t)}{J(0)} \qquad (3.10)$$

60

The static and creep tests usually provide information about the mechanical response for relatively moderate to long period. However, in order to extract more information about the mechanical response at very short period, the dynamic test is recommended (Findley et al., 1989). The aim of conducting the oscillating test is to examine the dynamic response of the CNTs-epoxy nanocomposites. In this test, oscillating torque [$M(t,\omega)$] is applied with an amplitude (M_o) of 100 mN/m and the resulting shear stress [$\tau(t,\omega)$] with an amplitude of (τ_o), shear strain [$\gamma(t,\omega)$] with an amplitude of (γ_o), and a time lag (Δt) between the two responses are obtained from (Findley et al., 1989) (Figure 28) and equations (3.11 to 3.13).

$$M(t,\omega) = M_o \cos \omega t \tag{3.11}$$

$$\tau(t,\omega) = \tau_o e^{i\omega t} = \tau_o (\cos \omega t + i \sin \omega t) \tag{3.12}$$

$$\gamma(t,\omega) = \gamma_o e^{i(\omega t - \delta)} = \tau_o [\cos(\omega t - \delta) + i \sin(\omega t - \delta)] \tag{3.13}$$

where ($\omega = 2\pi f$) is the angular frequency in rad./sec, ($i = \sqrt{-1}$) represents the imaginary axis of the complex variables, and (δ) is the phase angle.

61
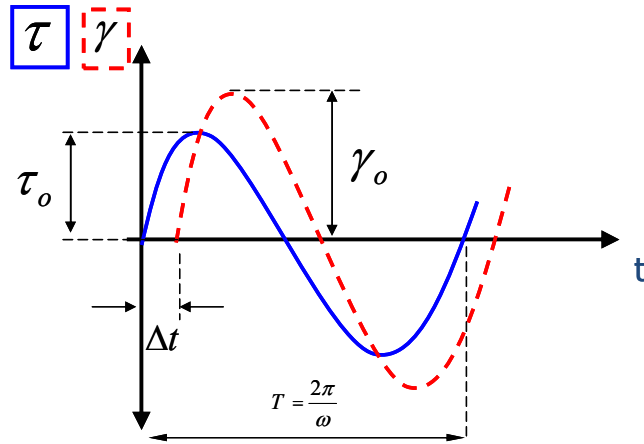
Figure 28. Shear stress and shear strain responses of the oscillation test

The phase angle or the loss angle is a function of the internal friction of the material. A phase angle of 0° represents ideal elastic behavior while phase angle of 90° represents ideal viscous behavior. The relationship between the phase angle and the time lag (Δt) between the applied stress and the corresponding strain is described by equation (3.14) (Findley et al., 1989).

$$\delta = \omega \Delta t \tag{3.14}$$

Three moduli are computed from the dynamic response. The <u>complex shear modulus (G^*)</u> which is an indicator to the resistance to dynamic shear loading including both elastic and viscous resistance. It can be obtained from the ratio between the shear stress amplitude (τ_o) and shear strain amplitudes (γ_o) as shown in equation (3.15). The <u>storage shear modulus (G')</u> which is associated with energy storage and release during periodic deformation. In another way, (G') represents the elastic component of the complex modulus and is obtained using equation (3.16). In addition, the <u>loss modulus (G'')</u> is associated with the dissipation of energy and its transformation into heat. It

62

represents the viscous component of the complex modulus and is obtained using equation (3.17). The ratio of the loss modulus (G'') to the storage modulus (G') is known as the mechanical loss and is a function of the phase angle (equation 3.18). The complex creep compliance (J^*) can be given by equation (3.19) and it represents the inverse of the complex modulus from a mechanical point of view (Findley et al., 1989).

$$G* = \frac{\tau_o}{\gamma_o} e^{i\delta} = \frac{\tau_o}{\gamma_o}(\cos\delta + i\sin\delta) \qquad (3.15)$$

$$G' = G*\cos\delta \qquad (3.16)$$

$$G'' = G*\sin\delta \qquad (3.17)$$

$$Tan\delta = \frac{G''}{G'} \qquad (3.18)$$

$$J* = \frac{\gamma_o}{\tau_o} e^{i\delta} = \frac{\gamma_o}{\tau_o}(\cos\delta + i\sin\delta) \qquad (3.19)$$

3.4   Thermal Characterization of CNTs-Epoxy Nanocomposite

TGA and DSC used to examine the thermal stability of different nanocomposites using TGA/DSC model SDT Q600 instrument. The TGA is a thermal test that measures the weight loss of a material due to increase in temperature. On the other hand, the DSC is performed to investigate the heat required to increase the temperature of various CNTs-epoxy nanocomposites measured by the heat flow. The heat flow represents the amount of heat absorbed by the tested material. The change in the heat flow with the increase in temperature occurs due to the change of the heat capacity of the material. A positive heat flow represents an endothermic process where the material absorbs heat while undergoing phase transition. A negative heat flow represents an exothermic process

63

where the material gives away heat. The CNTs-epoxy nanocomposite samples are loaded in a high precision balance with platinum pans and placed in a small electrically heated oven with a thermocouple to accurately measure the temperature. The atmosphere may be purged with an inert gas of nitrogen flow (60 ml/min) on a high-resolution Thermobalance of the TGA/DSC (model SDT Q600) instrument. The resolution for the instrument is $0.001°C$. The heating rate was $10^{o}C$/min. and the final temperature was $1000^{o}C$.

3.3.2   Results and Discussion

3.3.2.1   Flexure Test

In this section, the results of the flexure test with respect to different mechanical properties such as ultimate strength, tangent modulus, and toughness are discussed. All flexure specimens did not rupture up to a strain limit of 5% is reached. Therefore, the test was terminated at 5% strain limit and all other the mechanical properties were obtained. The results are presented in two categories: the first category is concerned with the effect of CNTs treatment in epoxy. This category includes treatment of 1.0 % CNTs by dispersion (D), surfactant assistance (S), covalent functionalizion using non-organic acid (F), and combined covalent and non-covalent functionalization (C). The second category is concerned with the CNTs content in epoxy. Three percentages of pristine CNTs are examined: 0.5, 1.0, and 1.5%.

Figure 29 shows flexure stress-strain curves for various CNTs treatment in epoxy nanocomposites. It can be noted that the pristine CNTs did not improve the stress strain behavior while the functionalized CNTs yielded significant improvements. On the contrary, the surfactant and combined functionalization have adverse effects on the

64

stress-strain response. These results are further presented in details in Figure 30, Figure 31, and Figure 32. The functionalized CNTs improved the strength by 42%. Limited enhancement of 1% in ultimate strength is observed with dispersed CNTs while the strength is reduced by 25 and 17% in the case of surfactant assistant and combined treatment respectively.

In addition, the tangent modulus increased by 29 and 40% in the case of pristine and functionalized CNTs respectively while it decreased by 14 and 25% in the case of surfactant assistance and combined treatment respectively. Similarly, 9 and 47% enhancements in toughness is observed with pristine and functionalized CNTs while 21 and 20% reduction in toughness was observed with surfactant assistant and combined treatment respectively. From previous observation, it can be understood that the surfactant treatment with Triton X-100 has adverse effect on the mechanical behavior of the CNTs-epoxy nanocomposite. In addition, the functionalization enhanced the mechanical properties significantly as expected due to the improvement the interfacial bond. Further investigations on the chemical treatments with other surfactants techniques are recommended.
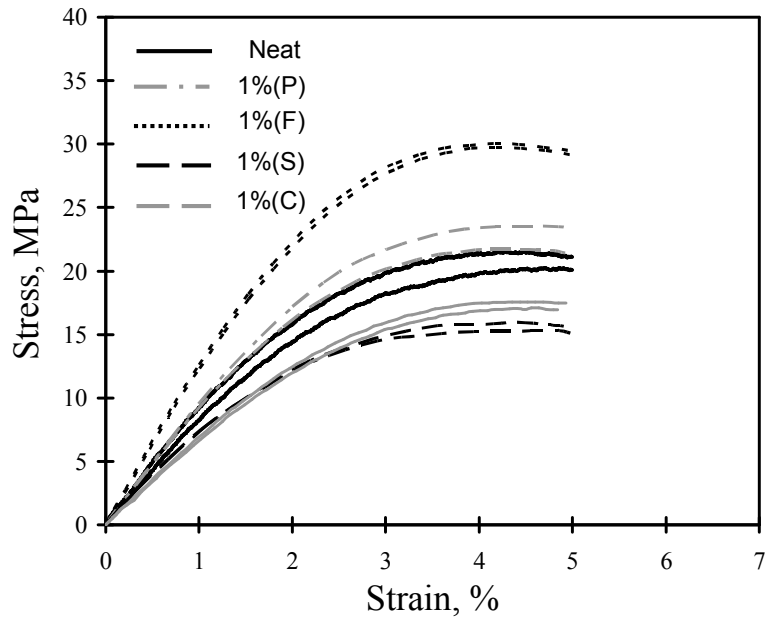
Figure 29. Flexure stress-strain curve for CNTs-epoxy nanocomposites with various CNTs treatments
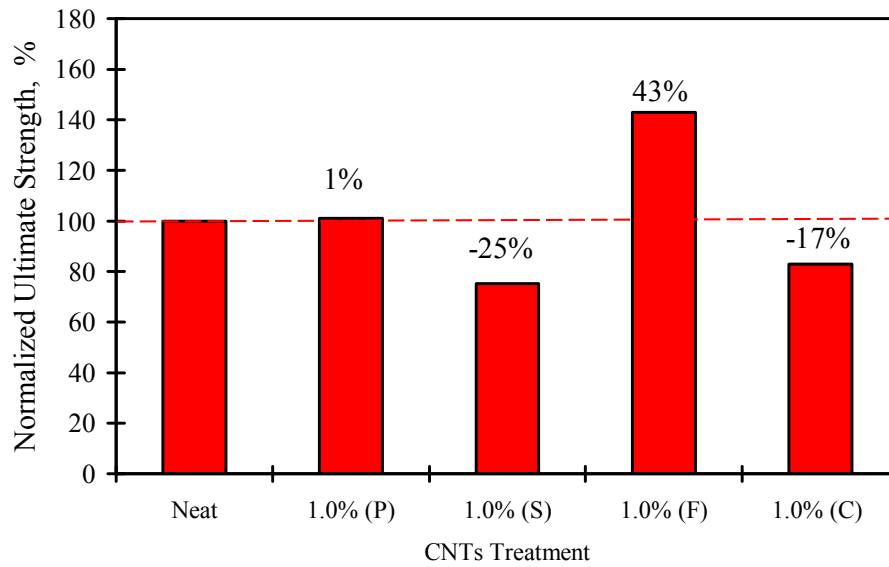
Figure 30. Flexure strength for CNTs-epoxy nanocomposites with various CNTs treatments

66
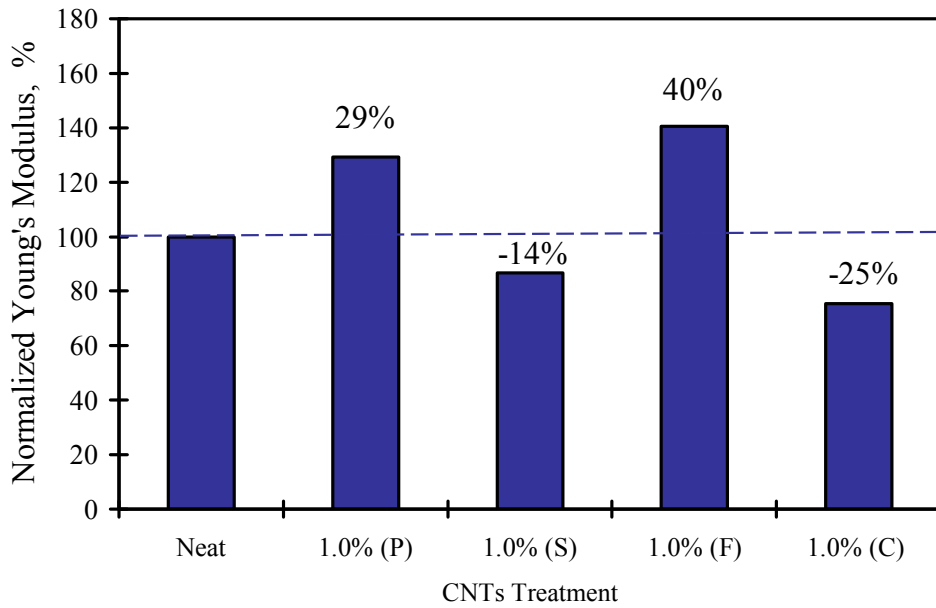
Figure 31. Tangent modulus for CNTs-epoxy nanocomposites with various CNTs treatments
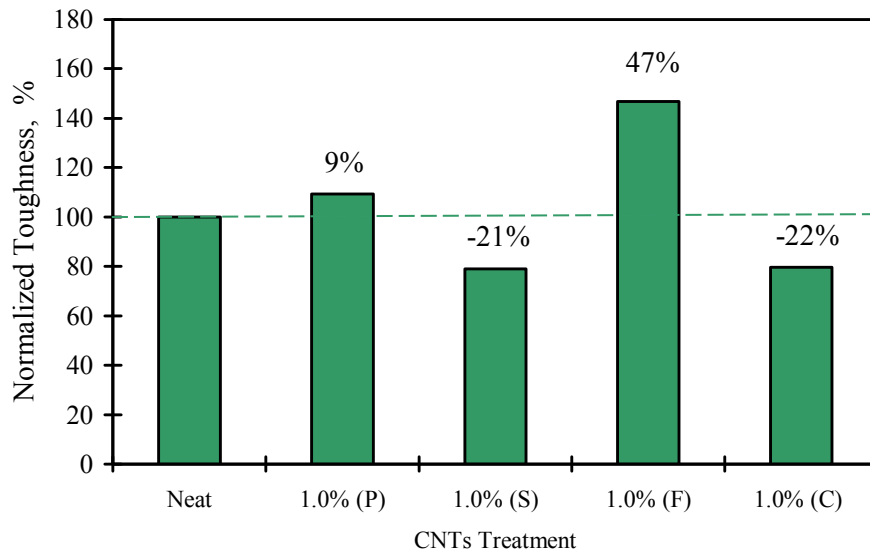
Figure 32. Toughness for CNTs-epoxy nanocomposites with various CNTs treatments

67

Figure 33 and Figure 34 show flexure stress-strain curve for various pristine and functionalized CNTs contents in epoxy nanocomposites, respectively. In general, all the percentages of pristine CNTs yielded moderate improvements in stress strain behavior while the functionalized CNTs enhanced the mechanical properties significantly. For instance, the average enhancement in ultimate strength was improved by 11 and 43% in the case pristine and functionalized CNTs respectively as shown in Figure 35. Similarly, 29 and 36% average enhancements in Young's modulus are observed with the pristine and functionalized CNTs contents (Figure 36). Average toughness is also increased by 10 and 48% as shown in Figure 37. Therefore, there are enhancements in flexural properties in epoxy with pristine CNTs, however the average enhancements are limited to about 15% while they reached 50% when functionalized CNTs are used. The functionalized CNTs outperformed the pristine CNTs due to the strong covalent interfacial bond between the CNTs and the surrounding matrix. In general, the case of 0.1 pristine CNTs out-performed the cases of 0.5, 1.0 and 1.5% pristine CNTs. Moreover, the case of 0.5% functionalized CNTs out performed 0.1 and 1.0%. This observation can be attributed to the difficulties in dispersing higher contents of CNTs.
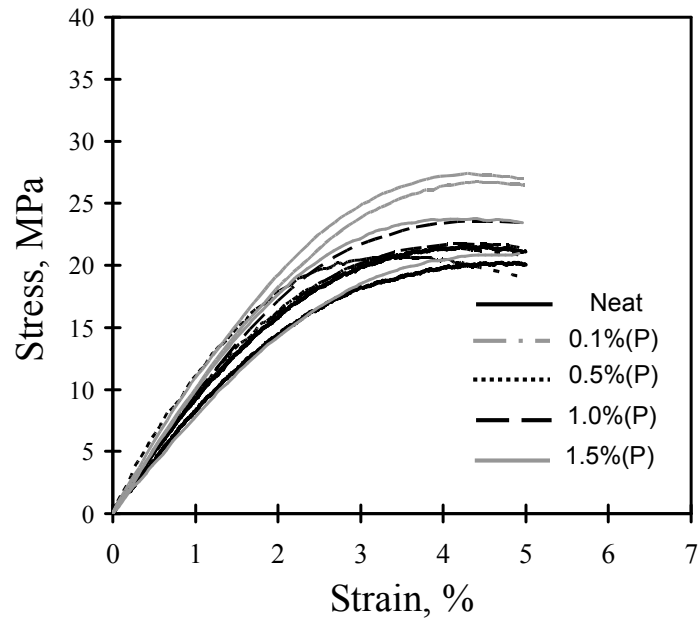
Figure 33. Flexure stress-strain curve for pristine CNTs-epoxy nanocomposites with various CNTs contents
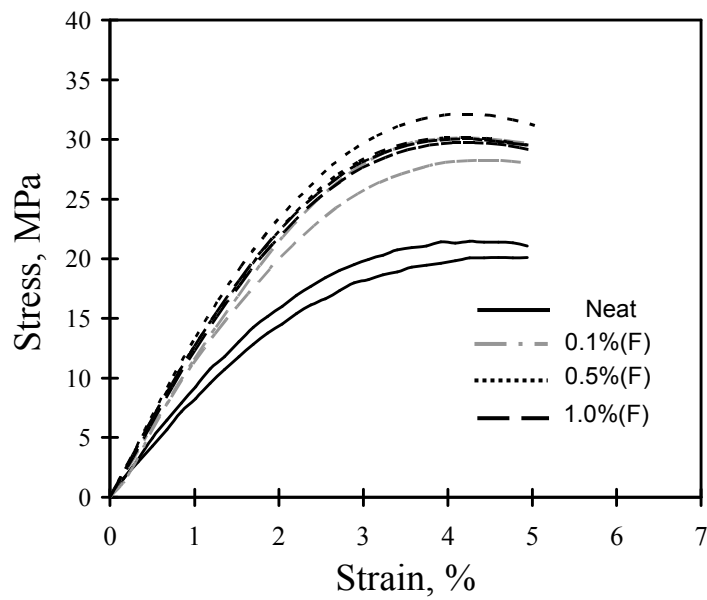
Figure 34. Flexure stress-strain curve for functionalized CNTs-epoxy nanocomposites with various CNTs contents

69
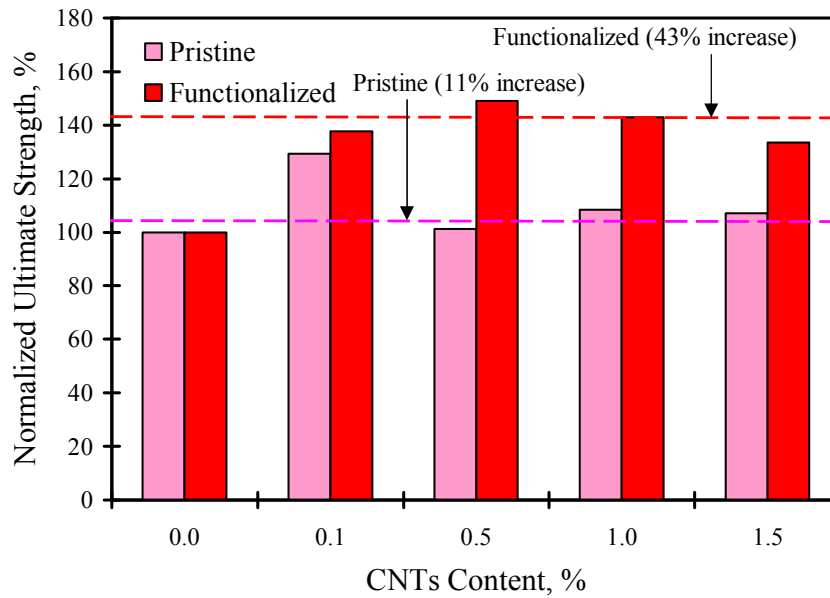
Figure 35. Ultimate strength for pristine and functionalized CNTs-epoxy nanocomposites with various CNTs contents
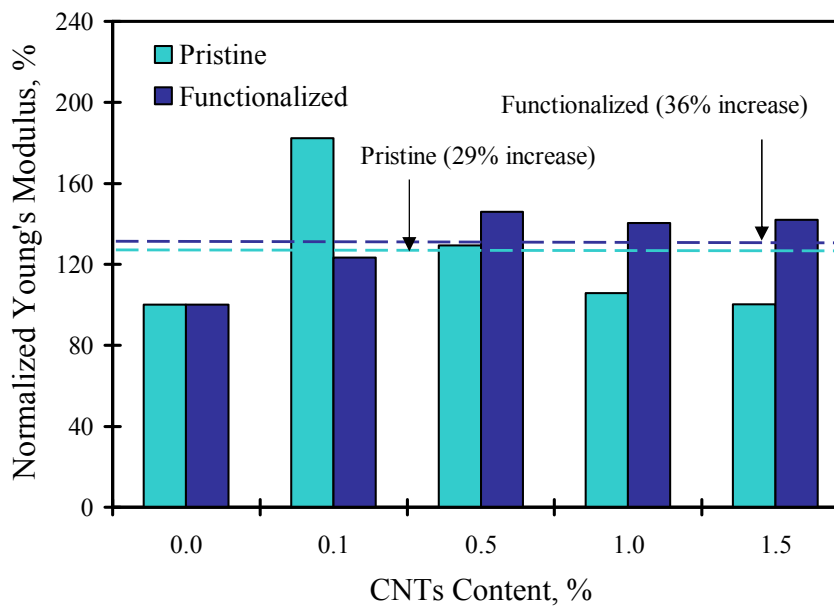
Figure 36. Tangent modulus for pristine and functionalized CNTs-epoxy nanocomposites with various CNTs content
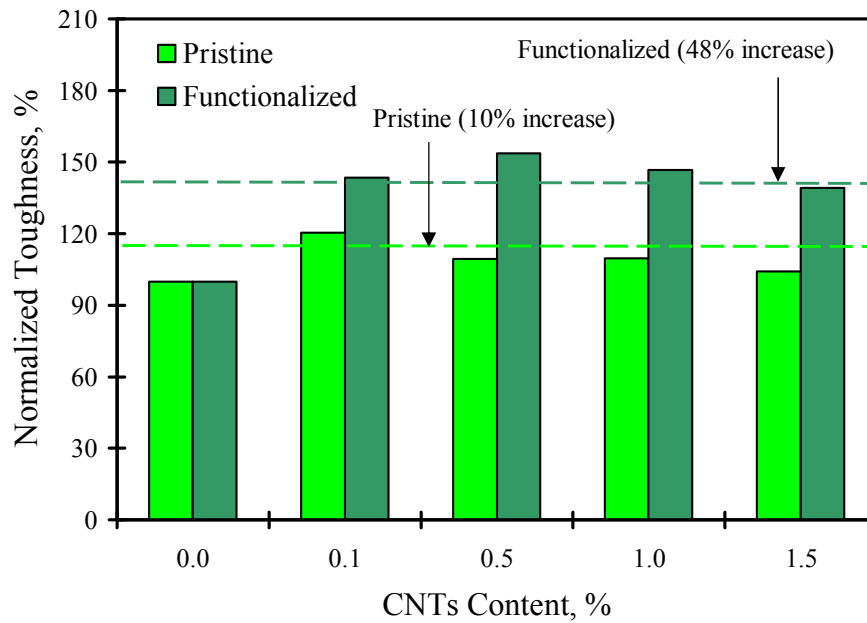
Figure 37. Toughness for pristine and functionalized CNTs-epoxy nanocomposites with various CNTs content

3.3.2.2 Dynamic Shear Rheometer (DSR) Test

Figure 38 shows the normalized creep compliance for various pristine CNTs contents. It is noted that the addition of pristine CNTs has limited effect on creep behavior. The addition of 0.5% pristine CNTs reduced the creep compliance by 3% while 1.5% pristine CNTs increased the creep compliance by 5%. The difference is therefore insignificant and within the statistical variation of the experiments. The trend of adding various percentages of pristine CNTs is shown in Figure 39 with second order polynomial curve fitting and a value of (R^2) equal to 0.99 was obtained. In general, the trend of CNTs improvement in creep loading is similar to that of the static loading.

71
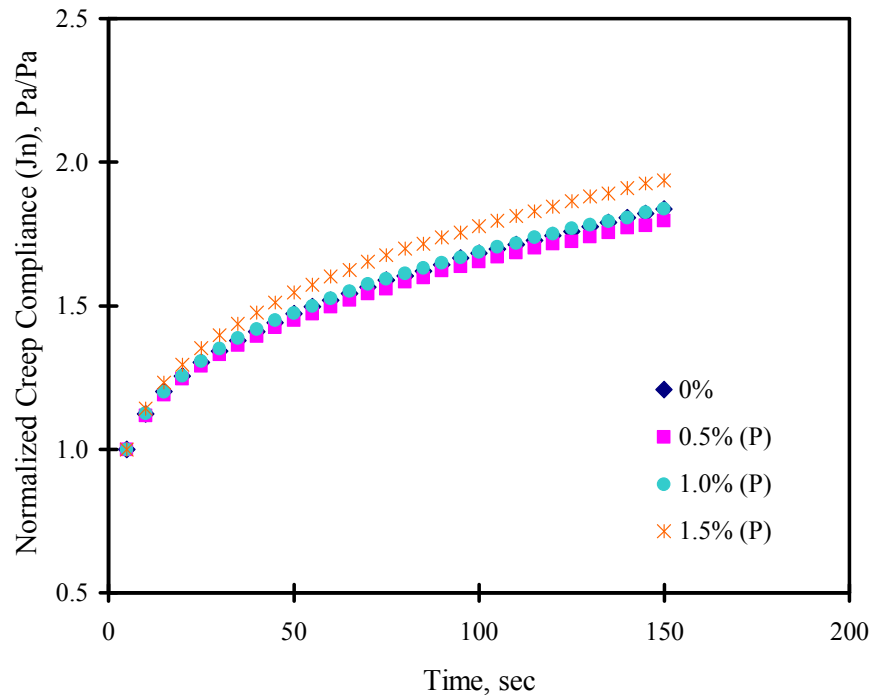
Figure 38. Normalized creep compliance for CNTs-epoxy nanocomposite with various CNTs content
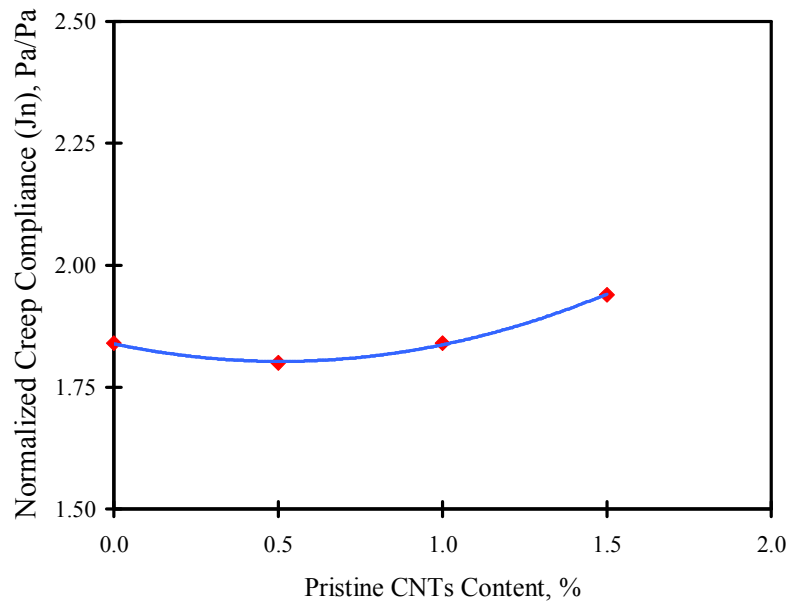
Figure 39. Comparison of normalized creep compliance after 150 seconds

72

The variation of storage modulus (G') with angular frequency and CNTs content are shown in Figure 40 and Figure 41 respectively. As the angular frequency increased from 0.1 to 10 rad./sec (0.0159 to 1.59 Hz), the storage modulus (G') increased by 60 to 90%. The improvement in storage modulus verifies that the dynamic resistance is usually higher than the static one. Furthermore, the addition of different percentages of CNTs increased the storage modulus [energy storage] (G'). The case of 1.0% CNTs out performed all the other cases. The average increase over the frequency domain was 23, 42, and 35% due to the addition of 0.5, 1.0, and 1.5% CNTs respectively. Since the loading level is within the elastic region, the case of 1.0% CNTs seem to provide more elastic resistance to deformations than other cases. Furthermore, unlike the storage modulus (G'), loss modulus (G'') reduced by 14 to 18% as the angular frequency increased from 0.1 to 10 rad/sec (Figure 42). In addition, loss modulus [energy dissipation] did not exhibit significant change among different CNTs contents (Figure 43). Additional investigations are needed to study the effect of different types of CNTs on loss modulus (G'').
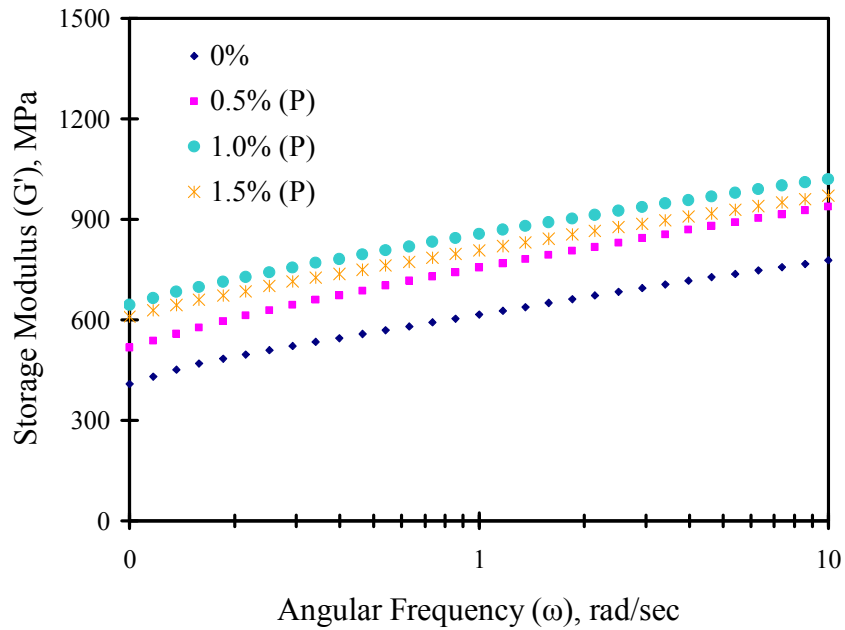
Figure 40. Storage modulus with various angular frequencies
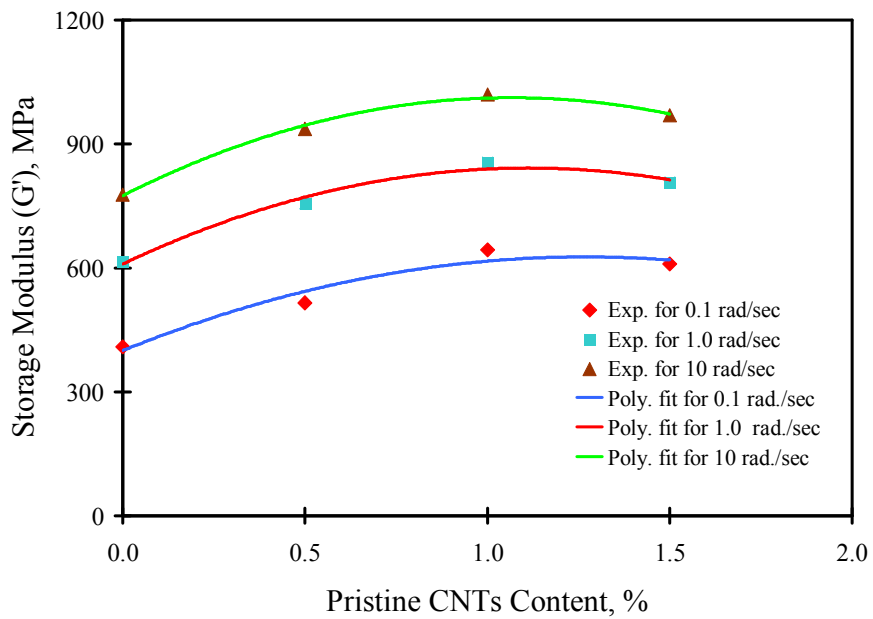
Figure 41. Variation of storage modulus with different CNTs contents

74
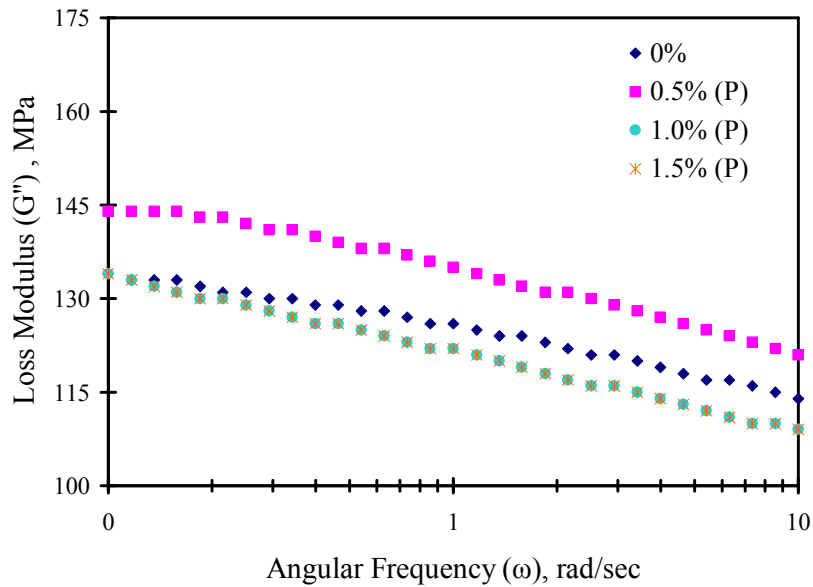
Figure 42. Loss modulus with various angular frequencies
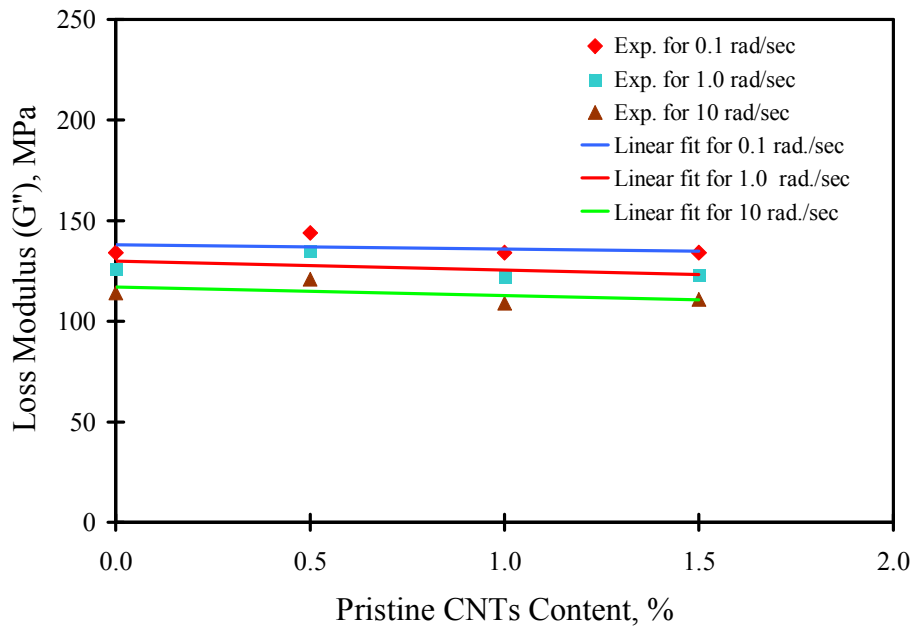
Figure 43. Variation of loss modulus with different CNTs contents

Given the response of the storage and loss moduli, one can predict the response of

the complex modulus (G^*) and the phase angle. Since the storage modulus (G')

75

increased with the addition of pristine CNTs and the loss modulus (G'') did not change significantly, it is expected that the complex modulus (G^*) response to follow the response of the storage modulus (Figure 44 and Figure 45). As the angular frequency increased from 0.1 to 10 rad./sec. (0.0159 to 1.59 Hz), the complex modulus increased by 56 to 82%. Furthermore, increasing CNTs content increased the complex modulus (G^*). Again, the case of 1.0% CNTs out performed all the other cases. The average increase over the frequency domain was 22, 40, and 31% due to the addition of 0.5, 1.0, and 1.5% CNTs respectively.
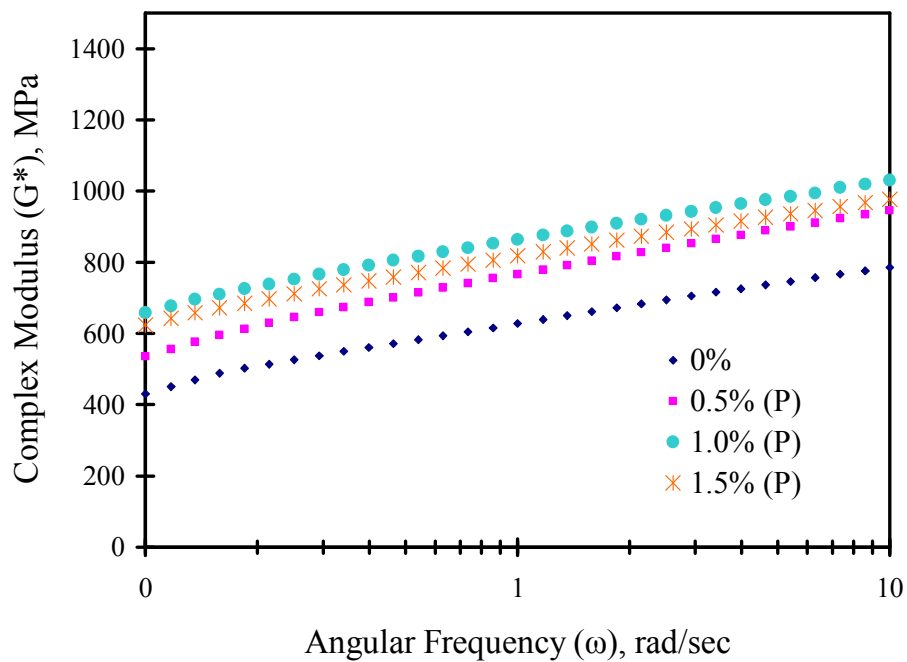
Figure 44. Complex modulus with various angular frequencies
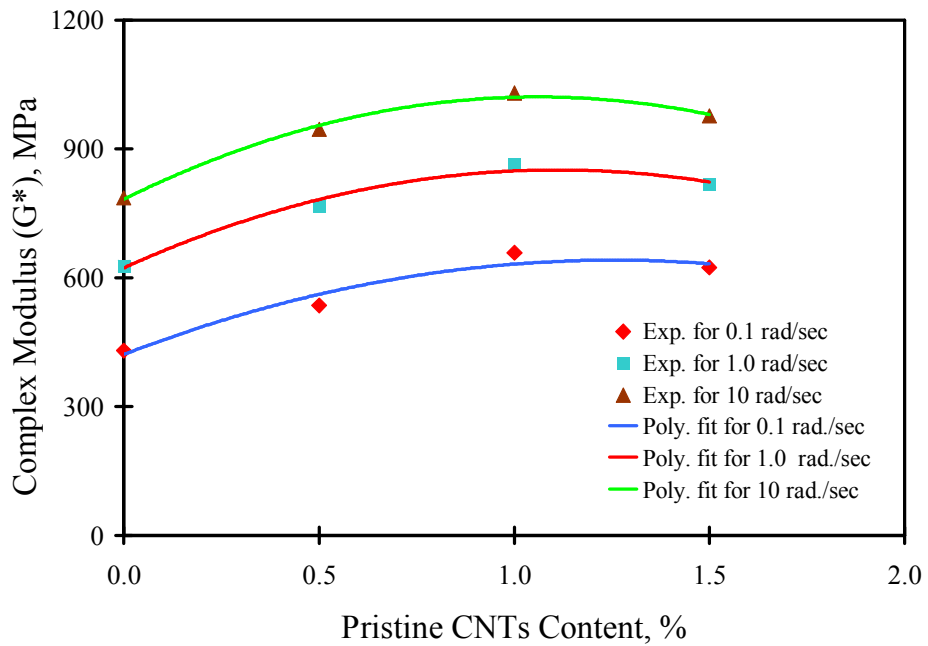
Figure 45. Variation of complex modulus with different CNTs contents

.

The phase angle (δ) was reduced significantly ($\approx$ 50%) as the angular frequency (ω) increased from 0.1 to 10 rad/sec (0.0159 to 1.59 Hz). The reduction in phase angle (δ) at high angular frequencies indicates less viscous behavior to elastic response ratio (Figure 46). The increase in storage modulus with the addition of pristine CNTs decreased the phase angle (δ) (Figure 47). The average decrease over the frequency domain was 12, 31, and 26% due to the addition of 0.5, 1.0, and 1.5% CNTs respectively. The relationship between the storage, loss, and complex moduli, and the phase angle with the addition of pristine CNTs can be described schematically as shown in Figure 48. The addition of CNTs strengthened the behavior by enhancing the elastic response represented by storage modulus (G') and maintaining the same viscous response

77

represented by loss modulus (G''). This effect resulted in an increase in complex modulus (G^*) and a decrease in phase angle (δ).
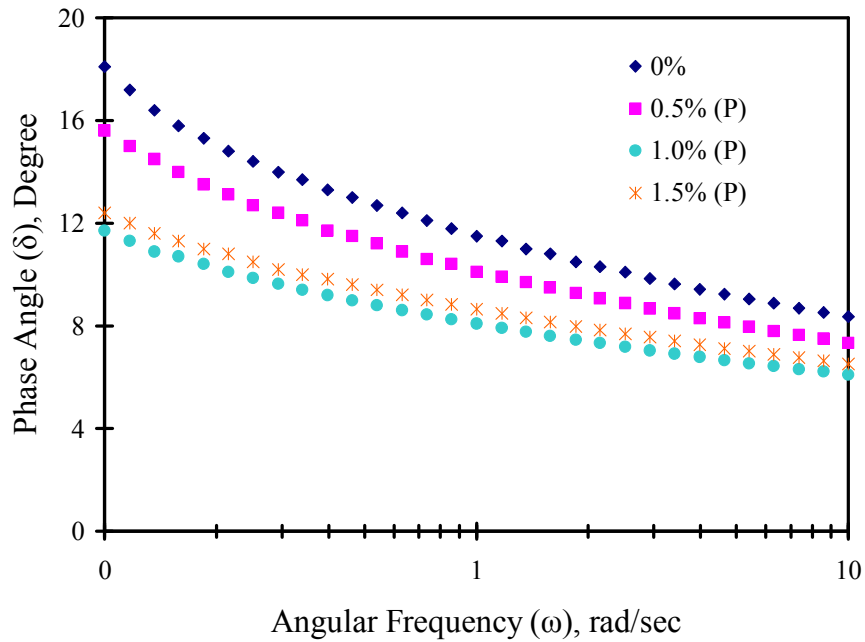
Figure 46. Phase angle with various angular frequencies
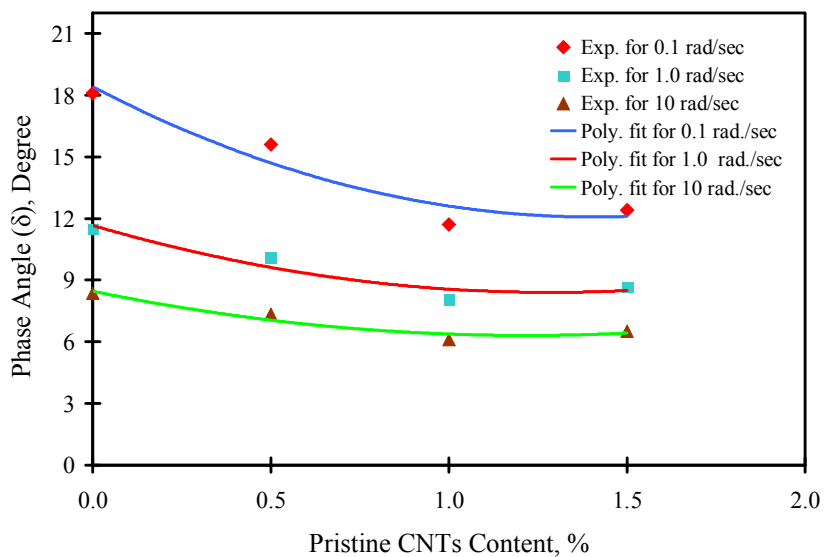
Figure 47. Variation of phase angle with different CNTs contents

78
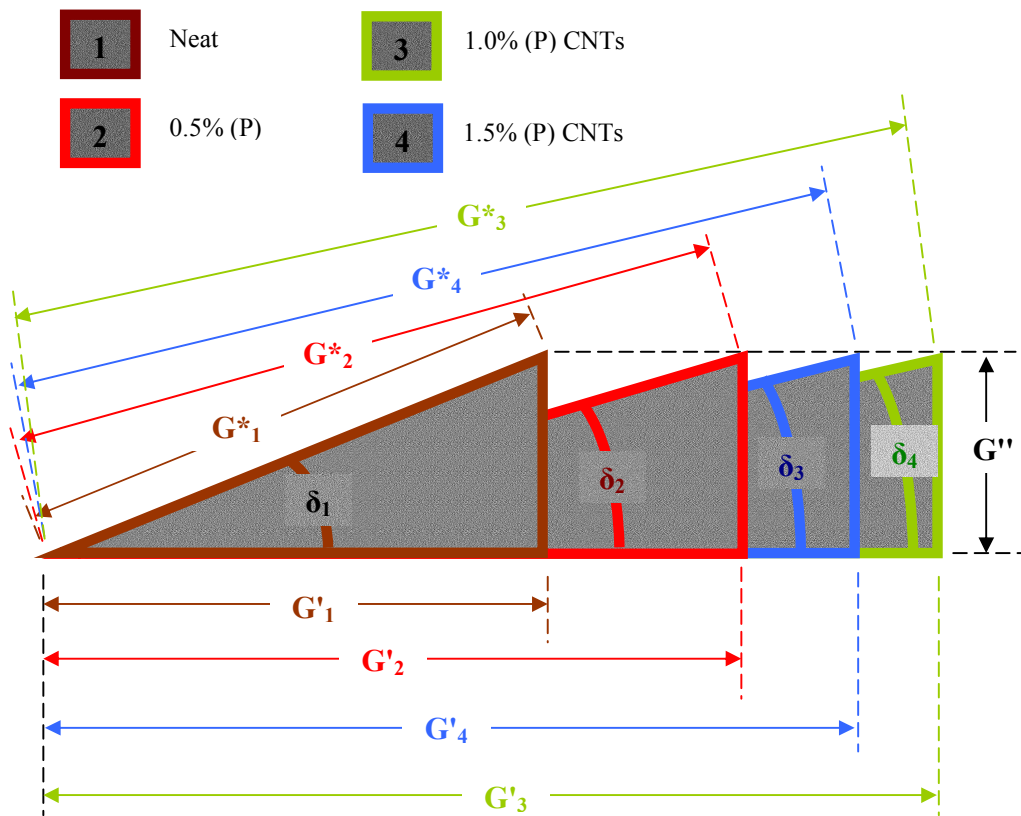
Figure 48. Variation of phase angle with different CNTs contents

It is well known that the complex modulus and the complex creep compliance are reciprocal. Therefore, given the behavior of complex modulus, the behavior of complex creep compliance can be predicted. In general, the complex creep compliance reduced with the increase in pristine CNTs content and the increase in angular frequency. Since the highest complex modulus was obtained by the addition of 1.0% pristine CNTs, the lowest complex creep compliance was also achieved with the same CNTs content as shown in Figure 49 and Figure 50. The average decrease in complex compliance was 18, 28, and 24% with the addition of 0.5, 1.0, and 1.5% respectively. In addition, the increase in angular frequency from 0.1 to 10 rad./sec. resulted in a 35 to 45 % decrease in complex

79

compliance. It is obvious that CNTs content of 1.0% can produce a significant reduction of complex creep compliance of epoxy.
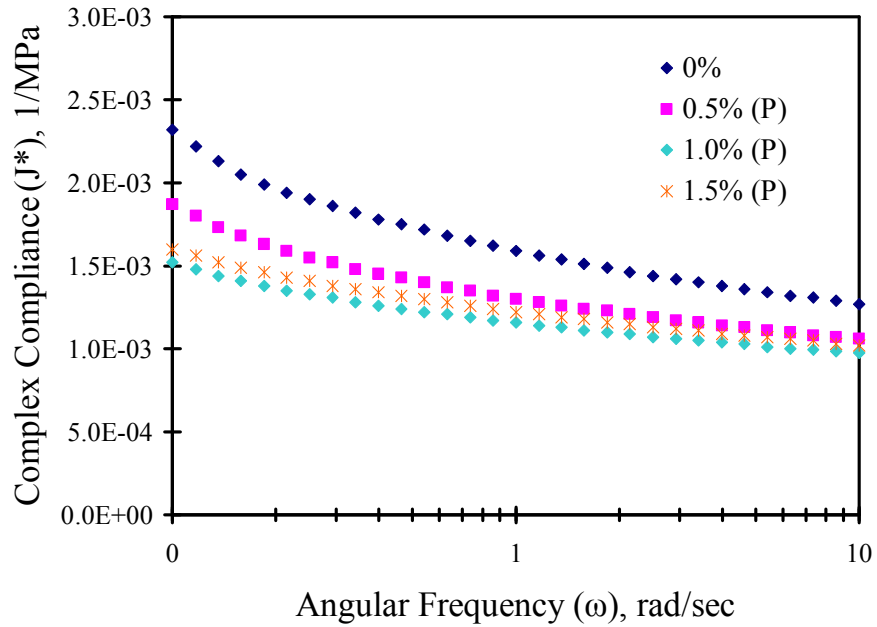
Figure 49. Complex creep compliance for various CNTs contents and angular frequencies
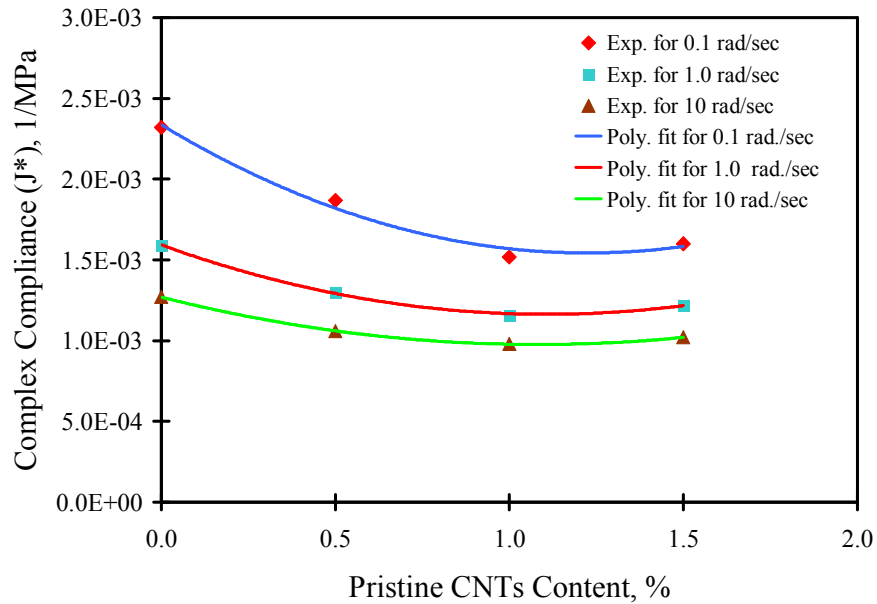
Figure 50. Variation of complex creep compliance with different CNTs contents

3.3.2.3 Differential Scanning Calorimetry (DSC) Test

Figure 51 show the plots for the normalized heat flow as a function of the temperature for different types of treated 1.0% CNTs-epoxy nanocomposites as well as pristine nanotubes. The hear flow is normalized with respect to the weight of the samples. The figure shows that all the nanocomposites underwent endothermic process when heated. Moreover, Figure 52 shows close view of different nanocomposites. For comparison purpose, the heat flow values at 200°C are reported and compared for various nanocomposites. The normalized heat flows at 200°C were 4.85, 1.75, 0.83, 0.64, and 0.62 mW/mg corresponding to functionalized (F), Surfactant treated (S), Neat (N) and Pristine (P) MWCNTs-epoxy nanocomposites. The individual nanotubes absorb the largest amount of heat followed by the functionalized MWCNTs-epoxy nanocomposites. The heat flow of the surfactant treated MWCNTs-epoxy nanocomposites indicates the

81

solvent molecules in the nanocomposites are fully evaporated. This observation also leads to the assumption that the degradation of the flexure properties of surfactant treated CNTs-epoxy nanocomposites is likely due to the relatively large content of surfactant.
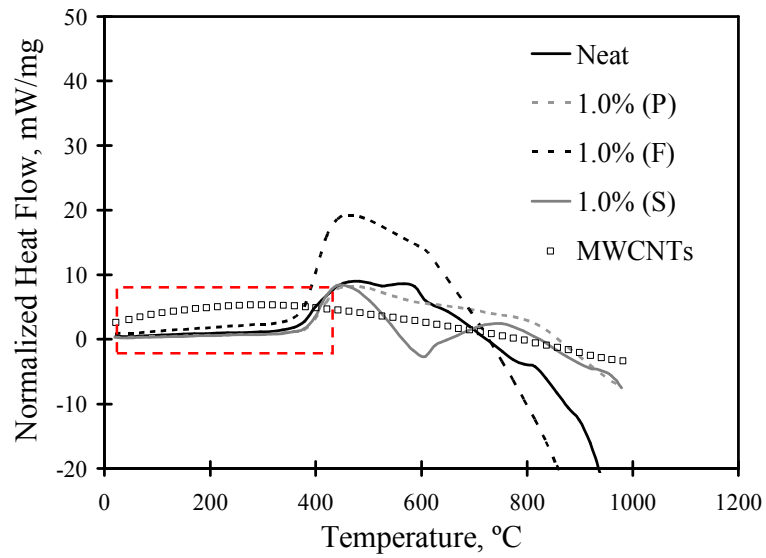
Figure 51. DSC results for various MWCNTs-epoxy nanocomposites
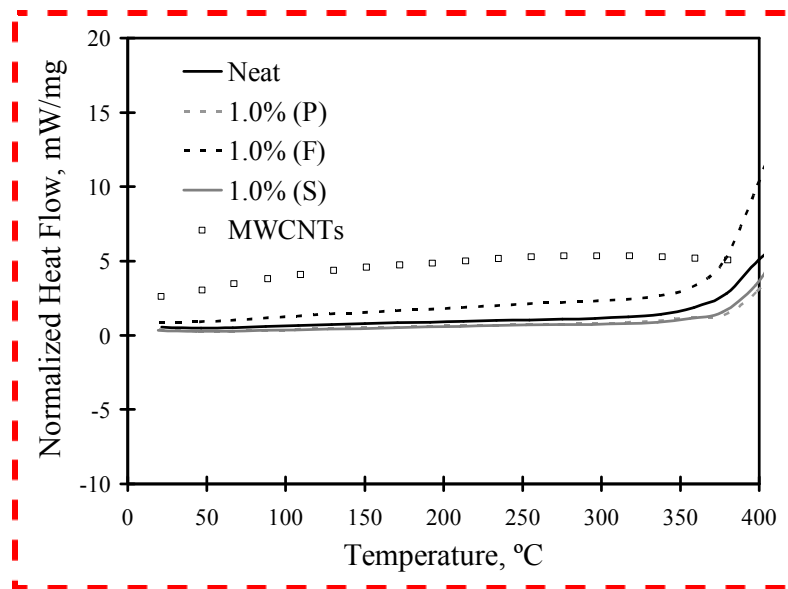
Figure 52. Close view of DSC test results

82

3.3.2.4 Thermogravemetric Analysis (TGA) Test

Figure 53 shows the TGA plots for the 1.0% CNTs-epoxy nanocomposites with various treatments. The temperature (T-50), at which 50% of the weight diminishes, is also reported and compared (Figure 54). The nanotubes showed outstanding thermal stability and T-50 was not observed within the examined range. T-50 for the neat, as-received pristine (P), functionalized (F), and surfactant treated (S) MWCNTs-epoxy nanocomposites were 367, 367.7, 374.2, and 365.8°C respectively. Since, the nanotubes have high thermal stability; it is expected to enhance the thermal stability for the neat epoxy matrix. However, the surfactant treated (S) case showed 1.2°C drop in T-50, which demonstrates lower thermal stability than what was expected. The above explanation of the significance of surfactant functionalizing with 10 CMC extends to the thermal characteristics of epoxy. More investigations are needed for surfactant treated CNTs in epoxy composites. Previous investigation by Soliman et al. for the significance of MWCNTs surfactant treatment on polymer concrete show significant improvement in mechanical properties (Soliman *et al.*, 2011d, Soliman *et al.*, 2011b). The pristine (P) case exhibited no increase in the T-50. Furthermore, the functionalized (F) case showed 7.2°C increase in T-50 due to the strong interfacial bond between the nanotubes and the epoxy matrix. The TGA observations confirmed the results obtained from the DSC and flexure tests regarding the absence of the solvent molecules within the nanocomposites.
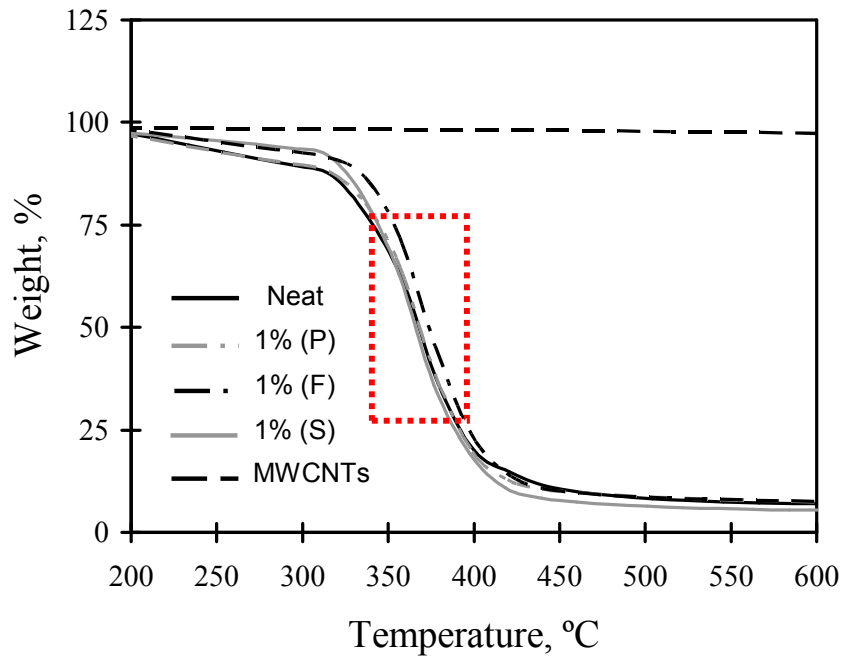
Figure 53. TGA results for various treatments of MWCNTs-epoxy nanocomposites
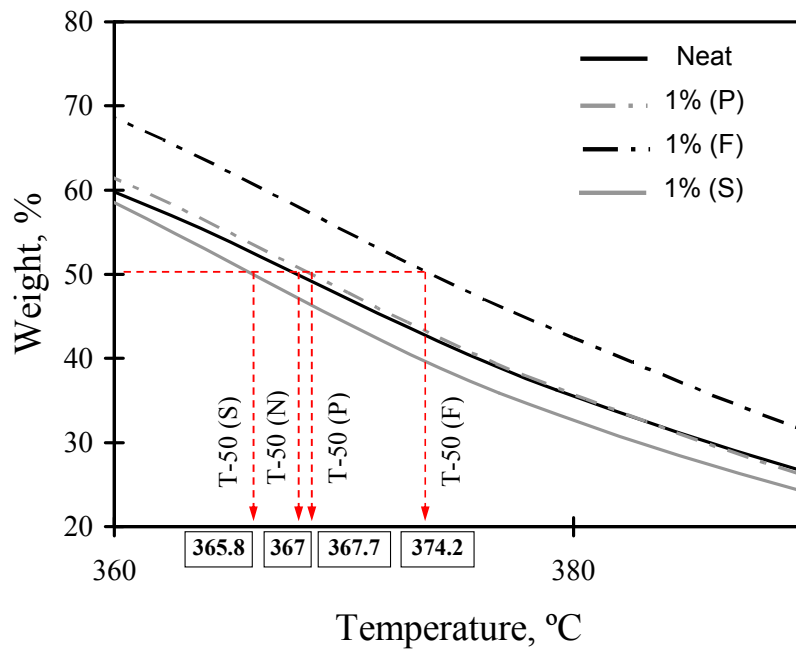
Figure 54. T-50 for various treatments of MWCNTs-epoxy nanocomposites

84

Figure 55 and Figure 56 show the TGA and T-50 for pristine CNTs-epoxy nanocomposites with various CNTs contents. In general, noticeable increases in T-50 were observed with the addition of pristine and functionalized CNTs. The increase in T-50 for the 0.1, 0.5, 1.0, and 1.5% pristine CNTs-epoxy nanocomposites were 6.9, 5.1, 0.3, and 1.1°C respectively. It is noted that the highest increase in T-50 was observed with 0.1% pristine CNTs. This might be attributed to the difficulties of dispersing large contents of CNTs and obtaining uniform microstructure. In addition, the functionalized CNTs increased the T-50 for the epoxy (Figure 57 and Figure 58). The increase in T-50 for the 0.1, 0.5, 1.0, and 1.5% pristine CNTs-epoxy nanocomposites were 5.8, 8.1, 5.5, and 3°C respectively. Similar to the pristine case, the increases in T-50 associated with 0.1 and 0.5% CNTs were higher than that of the large CNTs contents. Moreover, the increase in T-50 with the functionalized case was higher than that of the pristine case. This is attributed to the strong interfacial bond with the use of functionalized CNTs. The above results show the effect of adding CNTs on enhancing the thermal stability of CNTs-epoxy nanocomposites.
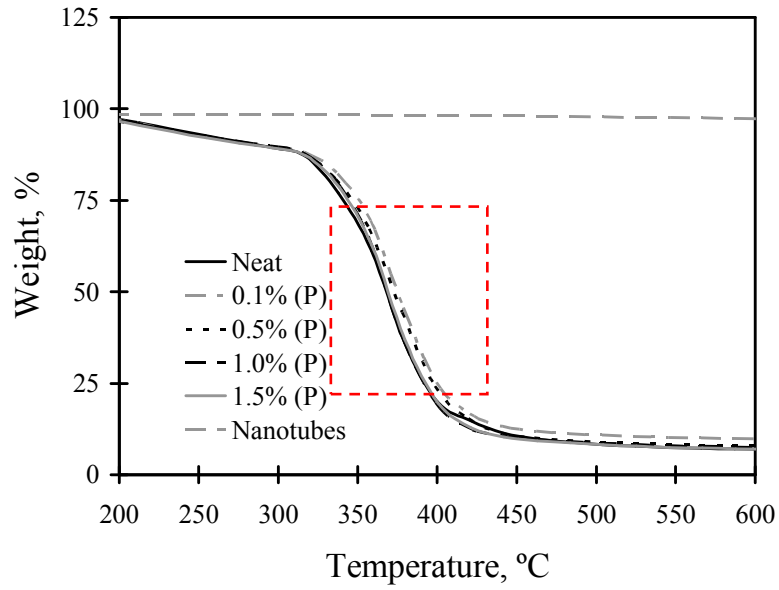
Figure 55. TGA results for pristine MWCNTs-epoxy nanocomposites
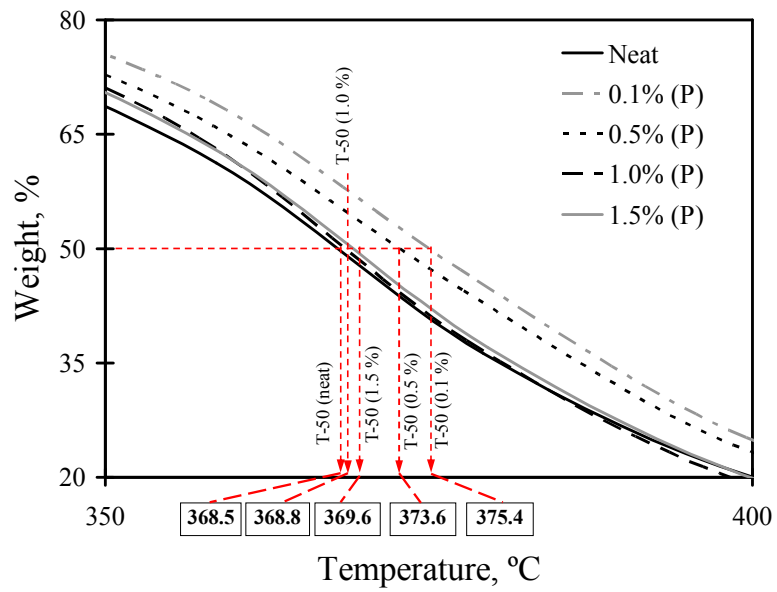
Figure 56. T-50 for pristine MWCNTs-epoxy nanocomposites

86
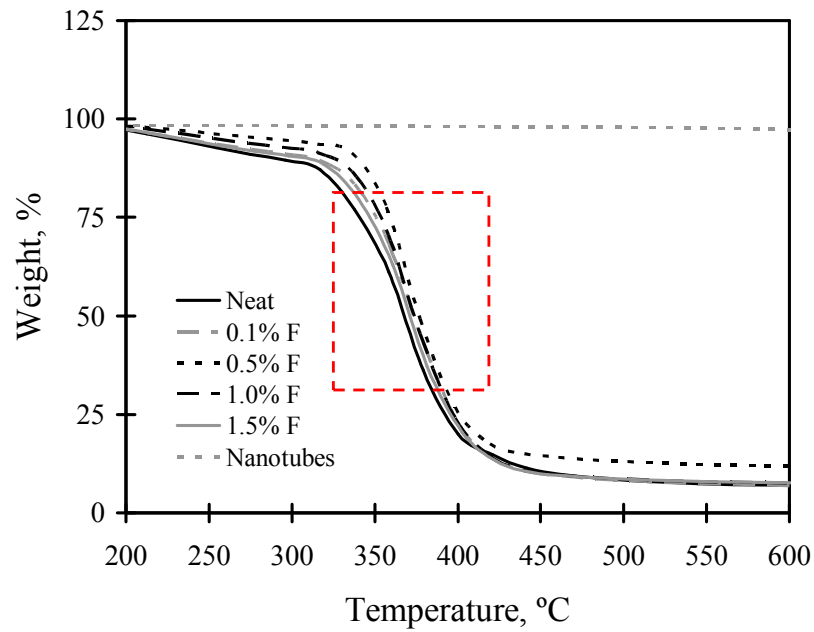
Figure 57. TGA results for functionalized MWCNTs-epoxy nanocomposites
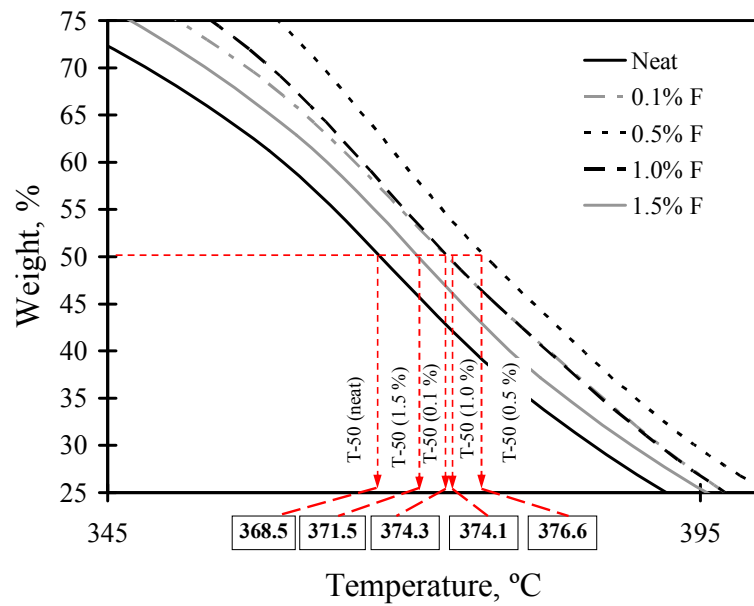
Figure 58. T-50 for functionalized MWCNTs-epoxy nanocomposites

3.3.2.5 Scanning Electron Microscope (SEM) Investigation

SEM images for neat (N), pristine (P), functionalized (F), surfactant treated (S) MWCNTs-epoxy nanocomposites as shown in Figure 59 to Figure 62. The figure shows SEM images with different length scales. The comparison between the neat epoxy SEM images (Figure 59) and pristine or functionalized MWCNTs-epoxy nanocomposites SEM images (Figure 60 and Figure 61) shows that MWCNTs appear as bright spots randomly distributed within the epoxy matrix. The diameter of the bright features in the close view 1 μm SEM images is less than 50 nm and with agreement to the nanotubes diameter specified by the manufacturers. Moreover, it can be noted that the intensity of the bright features increases as the percent of MWCNTs increases.

The use of loadings of 0.5 % for pristine and functionalized MWCNTs seem to be fairly dispersed in the epoxy matrix as shown in Figure 60 (a) and Figure 61 (a). However, formation of MWCNTs agglomerations in the epoxy matrix is observed with the use of 1.5% loading Figure 60 (b) and Figure 61 (b). This observation indicates that the use of ultrasonic bath accompanied by magnetic stirring might not be efficient when large contents of MWCNTs are incorporated. No unique difference in dispersion is observed between the pristine and functionalized MWCNTs images (Figure 60 and Figure 61). Unlike the pristine and functionalized MWCNTs, it is quite difficult to identify the nanotubes in the case of surfactant treated MWCNTs [Figure 62]. In addition, it is suggested that large regions of surfactant micelles (appears as dark areas) seem to form in the case of surfactant treated MWCNTs-epoxy nanocomposites. Therefore, it is expected that these regions enclose the nanotubes interacted with the surfactant. The relatively large content of surfactant used here (10 CMC) resulted in the formation of

www.manaraa.com

large micelles which adversely affected the mechanical performance of the nanocomposites as observed in the flexure test.
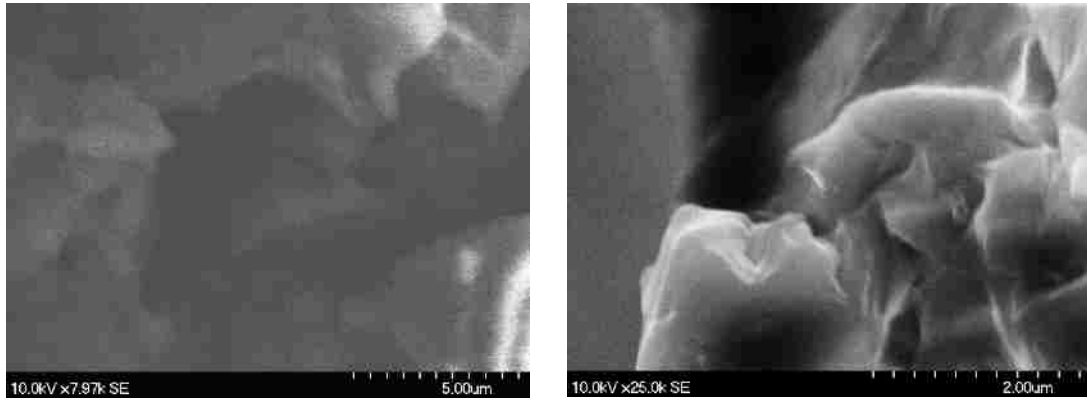
Figure 59. 5 and 2 µm SEM images for neat epoxy
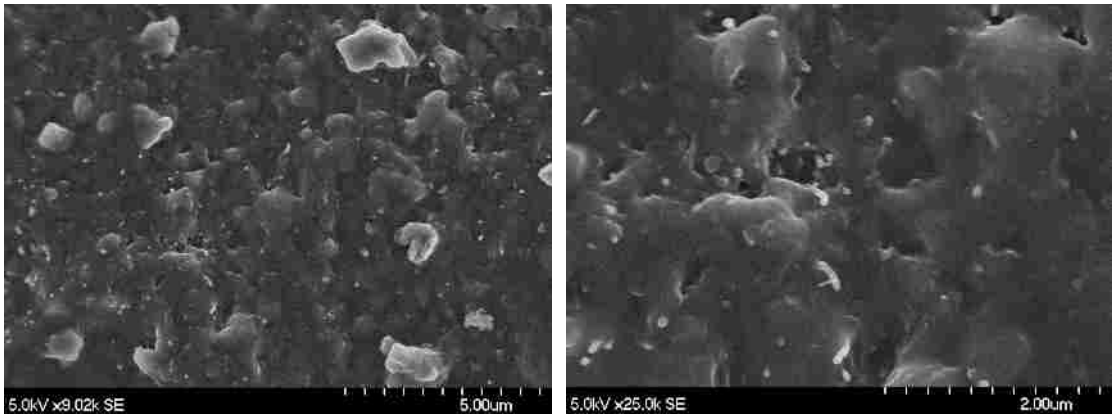
(a) 5 and 2 µm images for 0.5% MWCNTs
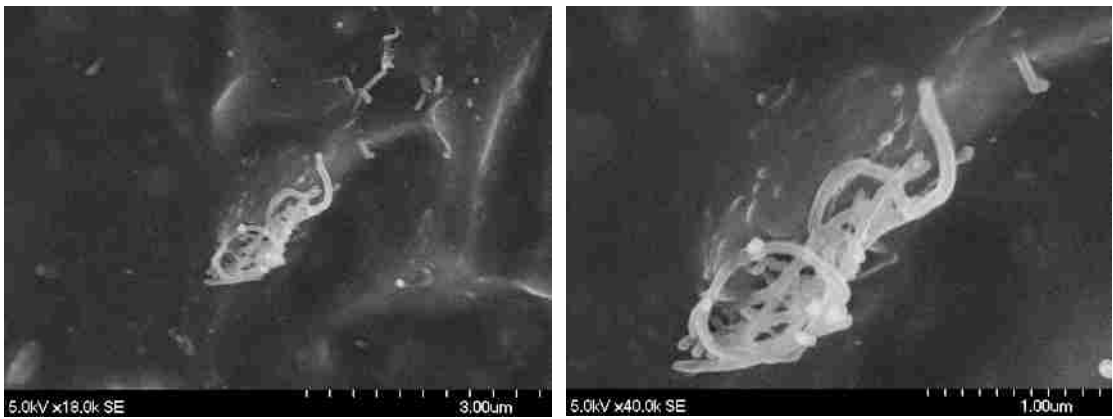
(b) 5 and 2 µm images for 1.5% MWCNTs

Figure 60. SEM images for pristine MWCNT-epoxy nanocomposites

90
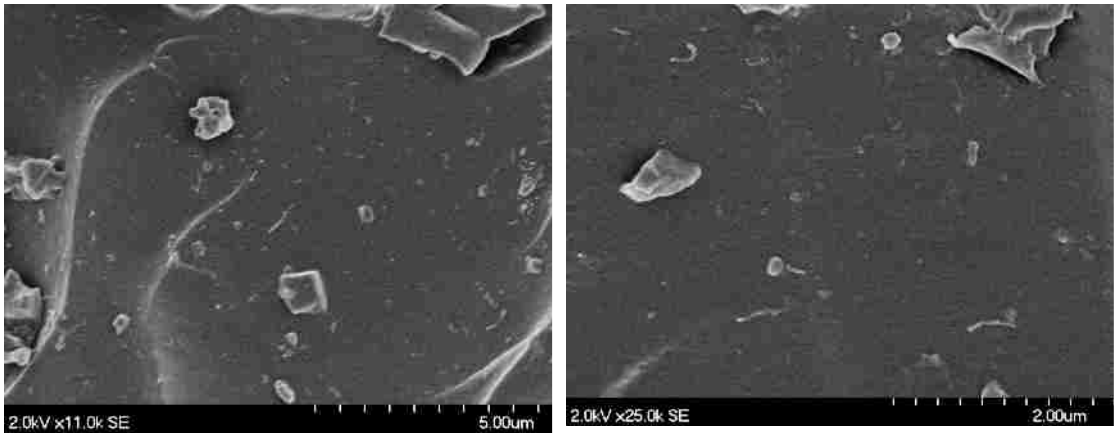
(a) 5 and 2 µm images for 0.5% MWCNTs
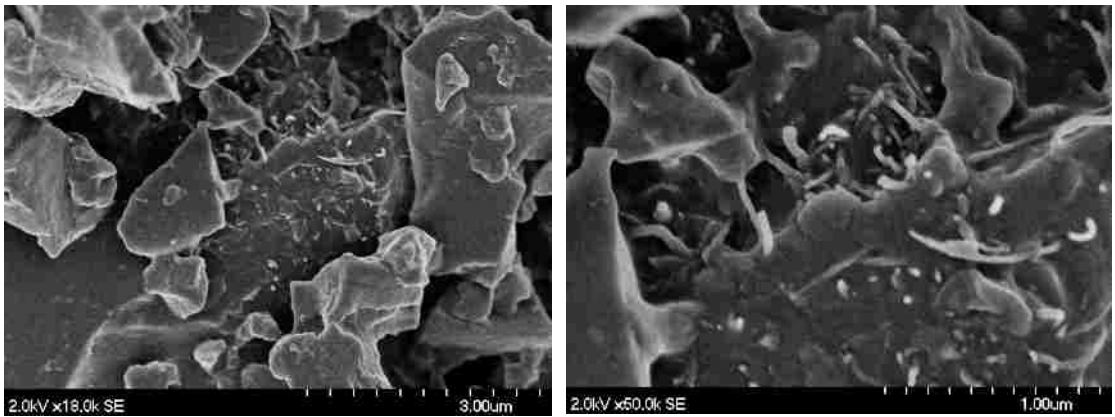
(b) 5 and 2 µm images for 1.5% MWCNTs

Figure 61. SEM images for functionalized MWCNT-epoxy nanocomposites
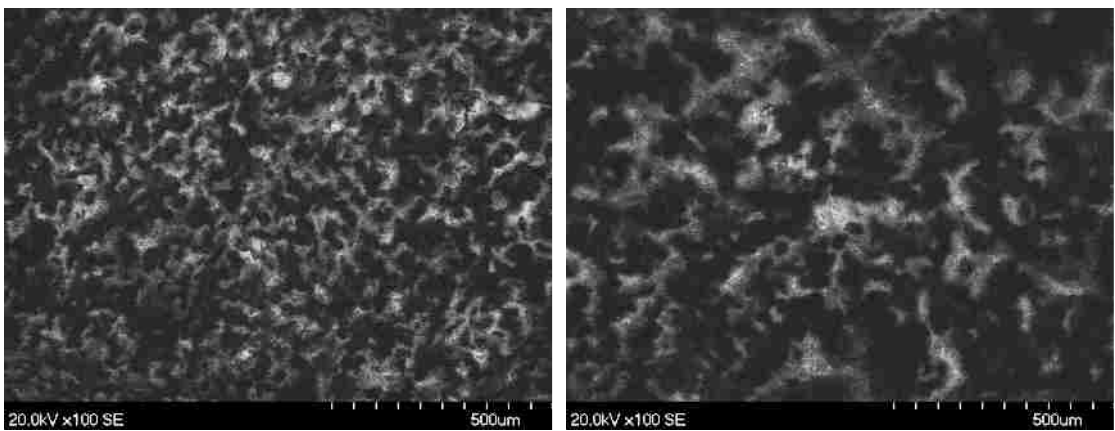
Figure 62. SEM images for surfactant treated MWCNT-epoxy nanocomposites

91

3.5 Summary

In this chapter, several methods of processing MWCNTs-epoxy nanocomposite were introduced. These techniques were examined by two mechanical tests: Flexure and dynamic shear rheometer tests. Several mechanical properties were extracted such as flexure strength, modulus of elasticity in bending, flexure toughness, phase angle, creep compliance, complex modulus, and complex compliance. In general, it was observed that the addition of functionalized MWCNTs can enhance the mechanical properties of epoxy while limited improvements in mechanical properties are observed with pristine MWCNTs. However, other techniques, such as chemical treatment with surfactant, yielded reduction in the mechanical properties. Thermal analyses and SEM suggested that the main reason of such reduction is attributed to the large contents of surfactant added to the nanocomposites. The large contents would form micelles of surfactant which therefore affected the mechanical properties adversely. Moreover, the addition of large contents of CNTs seems to limit or have adverse effect on the mechanical performance. This might be attributed to the difficulties in obtaining a uniform dispersion for large contents of MWCNTs as observed in the SEM images.

CHAPTER 4.   TENSION BEHAVIOR OF CNTS-FRP COMPOSITES

4.1   Introduction

In this chapter, tension and in-plane shear behavior of woven fabric CNTs-epoxy composites are investigated. The manufacturing of woven fabric composites was performed using vacuum assisted hand lay-up technique. Two approaches of incorporating CNTs in FRP are studied. The first approach was performed by growing CNTs prior to the manufacturing of the composite using graphitic structure by design (GSD) approach. In this approach, both glass and carbon fiber composites are examined. Second approach was performed by incorporating the CNTs in epoxy using various methods discussed in Chapter 3. The tensile and in-plane shear behaviors are examined through on and off-axis tension tests.

4.2   CNTs Mechanism in FRP Composites

The main goal of incorporating CNTs in FRP composites is to minimize or eliminate the occurrence of inter fiber fracture (IFF). The IFF involves two mechanisms of failure. The first mechanism is the debonding between the fibers and the surrounding matrix due to weak interfacial bond strength. The second mechanism involves tensile and shear cracking of the matrix. Based on the two failure mechanisms, two methods of incorporating CNTs are examined. In first method, carbon nanotubes (CNTs) and carbon nano filaments (CNFs) are grown on the surface of the carbon or glass macro-fibers using

93

graphic structure by design (GSD) technique. The growth process is performed by loading 1.0% Nickel as catalyst on the fibers surface using incipient wetness impregnation technique. This technique is expected to improve the interfacial bond strength between the macro-fibers and the surrounding matrix, thus limits the initiation of FRP micro-cracks. In the second method, various techniques discussed in Chapter 3 are performed to produce CNT-epoxy nanocomposites during the FRP manufacturing. The tensile and shear response of FRPs under tension are examined. This technique is expected to limit the propagation of micro-cracks within the epoxy matrix, thus increases the ductility of the FRP response. Schematics for the two approached are demonstrated in Figure 63. The FRP fabrication technique is described in Appendix A.
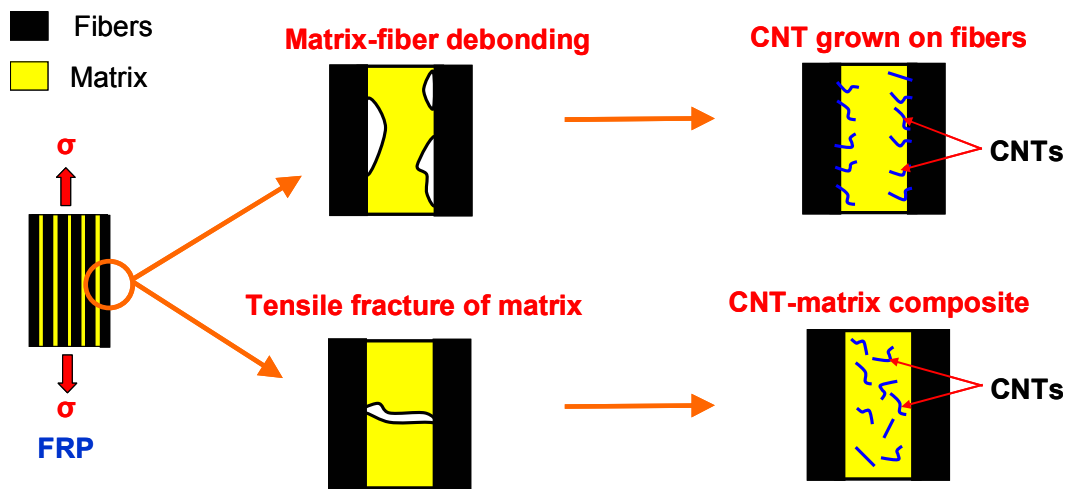
Figure 63. CNTs hypothetical mechanisms in FRP composites

4.3 CNTs Grown on Macro-Fibers

In order to grow carbon nanotubes and carbon nanofilaments on the surface of the carbon or glass fibers, the state-of-the-art technique named "Graphitic Structures by

Design (GSD)" is used. This method was reported by (Phillips *et al.*, 2006) who showed that different graphitic structures can be grown under different conditions and thus graphitic structures can be grown 'by design'. There are two advantages of this method: 1) The growth process can be performed in relatively low temperatures (i.e. 550ºC) and atmospheric pressure unlike other methods and 2) Basic laboratory equipment and tools (small furnace, gas bottles, etc.) can be used to accomplish various steps during the growth process. The proposed GSD process consists of four main steps: (i) removal of the sizing from the surface of the carbon fiber, (ii) 'activation by burning' to form nucleation sites for a metal catalyst to adhere to, (iii) loading of the metal and (iv) synthesis of the CNTs/CNFs on the fabric surface. The following sections discuss the experimental procedures of the synthesis of CNFs on carbon fibers and glass fibers and provide initial results of the mechanical behavior of the hybrid composites produced via GSD technique.

4.3.1 Growth Process of Carbon Nanotubes

Several 127×152 mm size carbon and glass fiber woven fabrics sheets were prepared for the growth process. The carbon fiber fabric used is 5.4 oz plain weave pan-based 3k tow size, 0.254 mm thick while the glass fiber used is 4 oz plain weave E-glass with thickness of 0.15 mm. The average diameters of the fibers are around 8 microns for the carbon fiber and 15 microns for the fiber glass respectively. In order to expose the actual surface of the carbon fiber, it is necessary to remove the sizing from the carbon fiber sheets. Specifically, the sheets were heated in an air environment under 500 ºC or 250 ºC for one hour to decompose the sizing, soaked in acetone for 1.0 hour to dissolve

95

the sizing from the fibers, and then followed with an ethyl alcohol rinse. Finally, the sheets were air dried for 1.0 hour at 100 ºC.

A catalyst was prepared by incipient wetness impregnation of aqueous solutions of metal salt (Luhrs *et al.*, 2009). In this study, $Ni(NO_3)_2 \cdot 6H_2O$ (supplied by Aldrich) was used as a metal source with the loading amount of Nickel adjusted to 1.0 wt. % for all the catalyzed samples. After the samples underwent drop by drop incipient wetting via a syringe pump, they were dried in an oven at 100 ºC overnight and then calcined at 250 ºC under a N_2 (106 sccm) atmosphere for 4 hours to decompose the nickel salt. The synthesis of the carbon nanotubes was carried out in a Lindberg Heavy-Duty (one-zone) furnace (diameter and length of the horizontal reactor were 2 inch and 12 inch respectively). The samples were inserted into the center of the reactor where an inert gas (N_2) was introduced at a flow rate of 600 sccm for 20 minutes while the temperature was being raised to 550 ºC. A reduction took place in 50 sccm diluted hydrogen by nitrogen ($N_2:H_2=90:10$, v/v) for 1 hour at 550 ºC to reduce the already calcinated metallic oxide particles to pure nickel.

The diluted hydrogen was then replaced by 600 sccm N_2 flow for 20 minutes when the reactor was heated to 700 ºC. Then the N_2 flow was reduced to 300 sccm. Meanwhile, 30 sccm ethylene (chemically pure) and 50 sccm diluted hydrogen ($N_2:H_2=90:10$, v/v) were introduced for 2 hours to deposit the carbon nanofilaments on the fiber sheets. The carbon nanotubes and CNTs/CNFs grown on the fiber sheets were analyzed by scanning electron microscopy (SEM) (Hitachi S5200 Nano SEM) and high-resolution transmission electron microscope (HRTEM). Figure 64 and Figure 65 show SEM micrographs of CNTs/CNFs growth on carbon fiber sheets and glass fiber sheets

96

respectively. Both figures show the fiber microstructure with burning at 500 ^{o}C and 250 ^{o}C. Figure 66 and Figure 67 show HRTEM micrographs of CNTs/CNFs growth on carbon fiber sheets and glass fiber sheets respectively. Both figures show the fiber microstructure with burning at 500 ^{o}C and 250 ^{o}C.
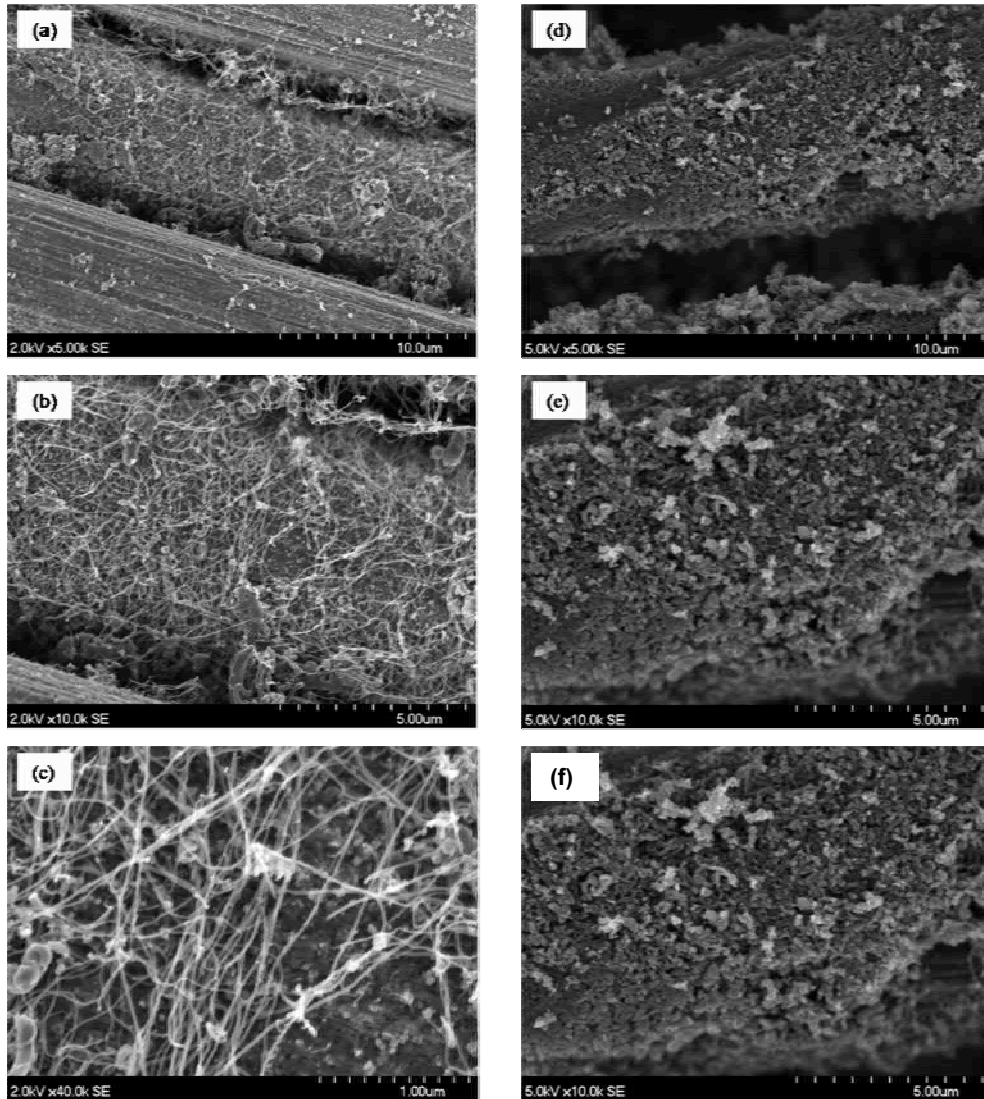
Figure 64. SEM of CNTs/CNFs on carbon fiber sheets burn at 500 ^{o}C (a-c) and at 250 ^{o}C (d-f)

Figure 65. SEM of CNTs/CNFs on glass fiber sheets burn at 500 °C (a-c) and at 250 °C (d-f)
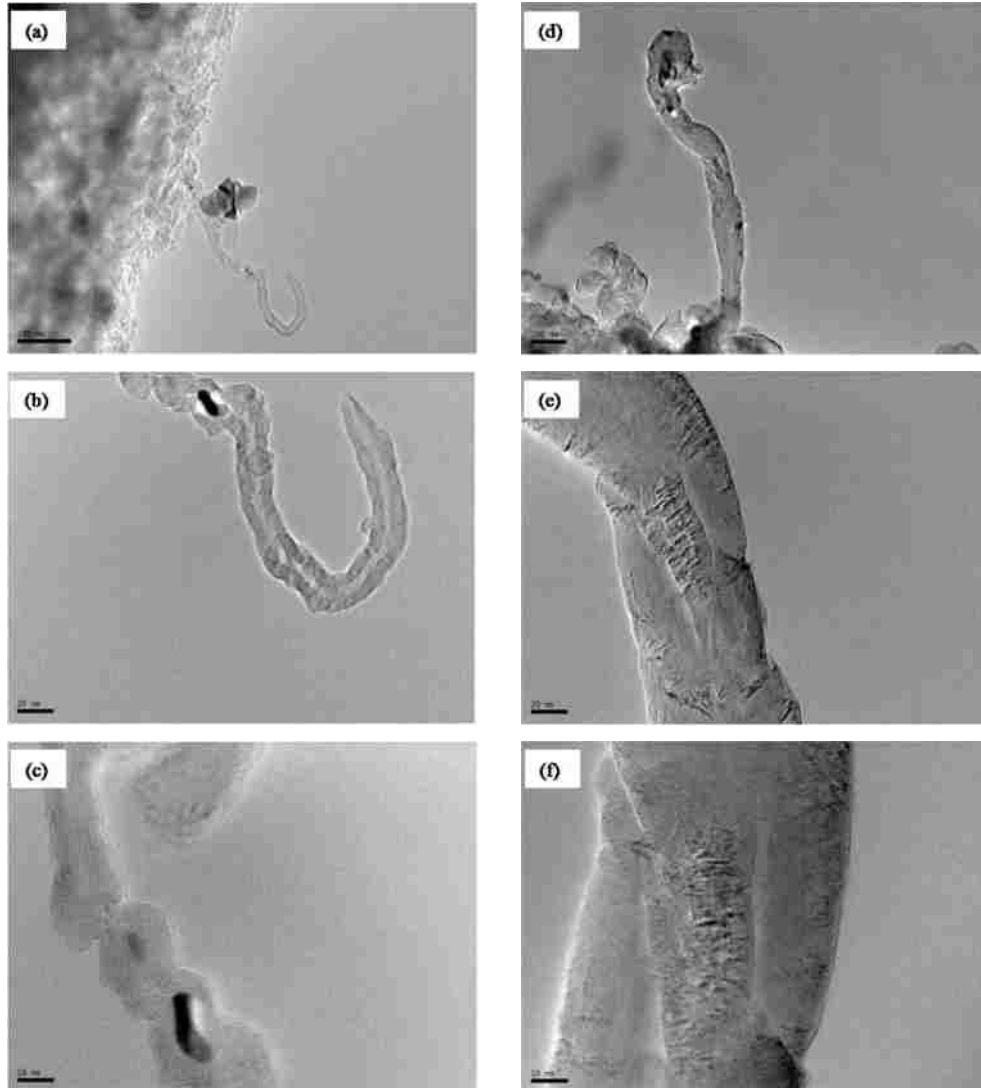
Figure 66. TEM of CNTs/CNFs on carbon fiber sheets burn at 500 ºC (a-c) and at 250 ºC (d-f)
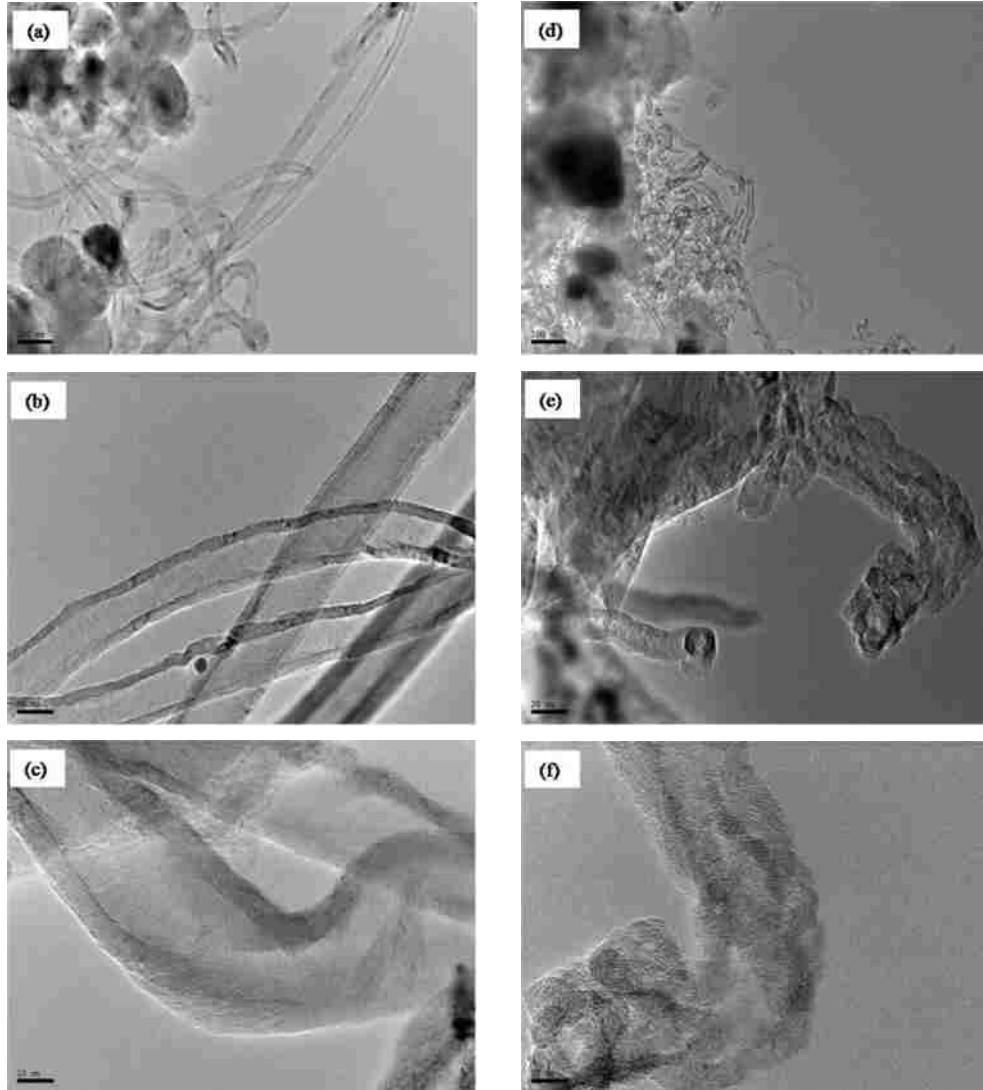
Figure 67. HRTEM of CNTs/CNFs on glass fiber sheets burn at 500 ºC (a-c) and at 250 ºC (d-f)

4.3.2 Composite Fabrication and Testing Plan

The FRP composite plates were fabricated using vacuum assisted hand lay-up technique. The carbon fiber fabric used is 5.4 oz plain weave 3k tow size, 0.254 mm thick while the glass fiber used is 4 oz plain weave E-glass with thickness of 0.15 mm. Only two fabric layers were used to manufacture each specimen in order to minimize the potential of any inconsistency that might arise during the fabrication and to investigate the effect of CNTs addition on the interlaminar shear strength between the two layers. The tension specimens were prepared using tapered G10 ends to allow uniform pressure distribution on the specimen at the grips location and to prevent slip and possible failure at the grips. The fabricated carbon fiber reinforced polymer (CFRP) and glass fiber reinforced polymer (GFRP) composite plates are shown in Figure 68.

All parameters examined in the experimental plan are summarized in Figure 69. Three groups of fabrics were examined; group (a): the original fabrics wihout any processing, group (b): the fabrics with the sizing removed and group (c): the fabrics with the sizing removed and CNTs growth. These groups were manufactured and tested for each set. Two temperatures were examined for removing the sizing, 250 ºC and 500 ºC. Four sets were examined by alternating the two temperatures and the two types of fibers. The CNTs/CNFs growth was performed using Nickel at 700 ºC. Five specimens were manufactured from each group and tension tests were performed. The effect of fabrication parameters on the tensile strength of the CNTs-carbon and CNTs-glass FRP fabrics was examined. The test specimens were left to cure for 24 hours and then were attached in the tension testing frame as shown in Figure 70. The tension test was

101

performed in accordance with (ASTMD3039/D3039M, 2008) and the load and displacement of the specimens were recorded using a standard data acquisition system.
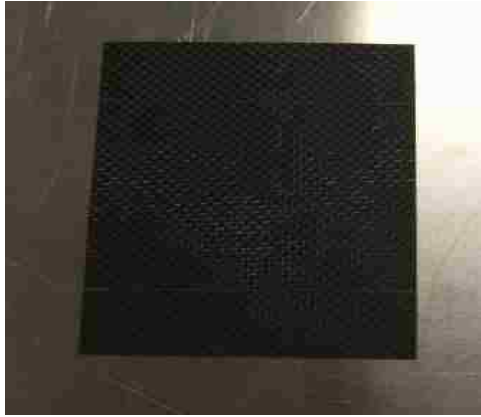
(a) Carbon   (b) Glass

(c) Tabbing the ends using G-10 fiber glass

Figure 68. Manufacturing of carbon and glass fiber reinforced polymers
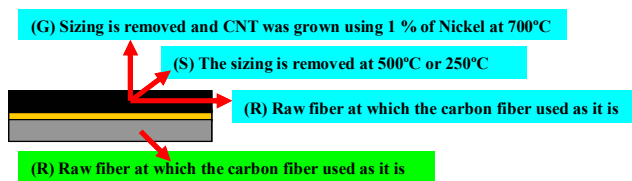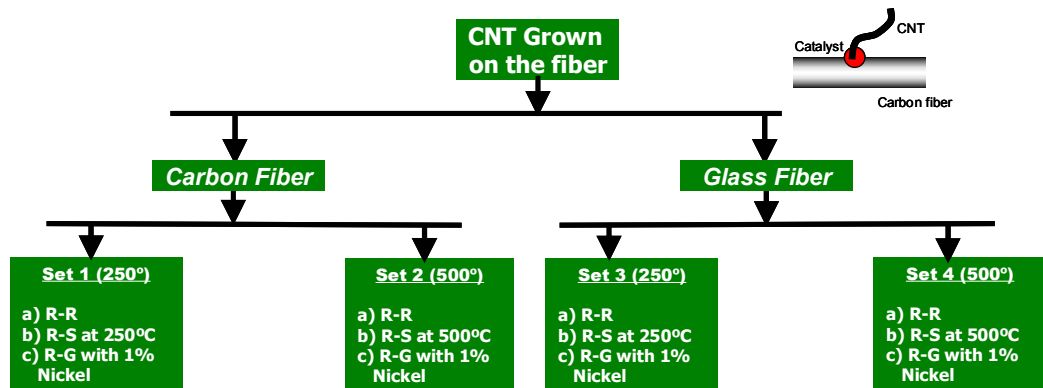
Figure 69. Experimental plan to examine the significance of CNTs-composite fabrication process on the tensile strength
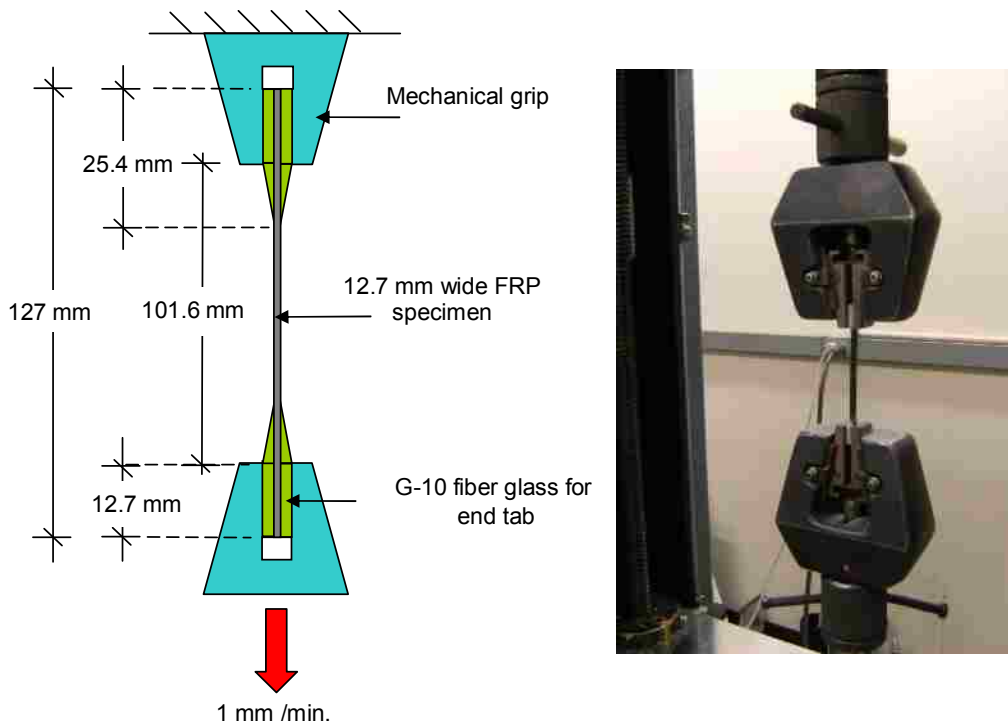
Figure 70. Tension test for FRP composites

4.3.3   Results and Discussions

The effect of three parameters on the tensile behavior of FRP is examined in this study. They are fiber type, sizing removal temperature, and growth of nanotubes. Figure 71 shows a comparison for the stress-strain curves of the carbon and glass fiber composites. The average ultimate tensile strengths without any treatment (R-R) were 390 and 82.7 MPa for carbon and glass fibers respectively. Similarly, after the growth of CNTs at 250ºC (R-G), the average ultimate strengths of CFRP and GFRP were 297.12 and 67.20 MPa respectively. These results show that the carbon fiber ultimate strength is approximately five times that of the glass fibers. The CFRP composite has showed stiffness and strain at failure about 50-70% higher than that of the GFRP composites.

The effect of temperature level of the sizing removal can be deduced from Figure 72. The average ultimate tensile strengths for the sizing removal (R-S) at 250 ºC were 424.7 and 85.8 MPa for carbon and glass fibers respectively while they were 291.6 and 68.11 MPa for the sizing removal (R-S) at 500 ºC. The results here show that the carbon fiber experienced a slight increase in the average ultimate strength (9%) in the case of 250 ºC while the strength decreased by 25% in the case of 500 ºC. In the case of glass fibers, the average ultimate strength decreased by 37% and 50% in the case of 250 ºC and 500 ºC respectively. It is worth noting that the strength reduction was always accompanied with a reduction in strain at failure in both carbon and glass fiber composites.

The increase of the carbon fiber strength with sizing removal at 250 $^{\circ}$C might be attributed to an enhanced frictional/bond strength between the carbon fiber surface and the epoxy matrix upon the removal of the sizing coatings. However, it is obvious that

104

temperatures higher than 250 ^{o}C such as the case of sizing removal at 500 ^{o}C might have an adverse effect and result in damaging the fiber material leading to a reduced composite strength. It can also be observed that glass fiber is much more sensitive to such thermal treatment than carbon fibers with strength loss at both 250 ^{o}C and 500 ^{o}C. Damage at growth might be attributed to the existence of Oxygen. Therefore, the removal of Oxygen during the preprocessing and growth process might be necessary. Finally, no significant effect of either sizing removal or CNTs/CNFs growth can be observed on the carbon or glass fiber composite stiffness. This may indicate that damage due to thermal treatment is a surface damage of the fiber materials that does not allow for development of good bond with the matrix.
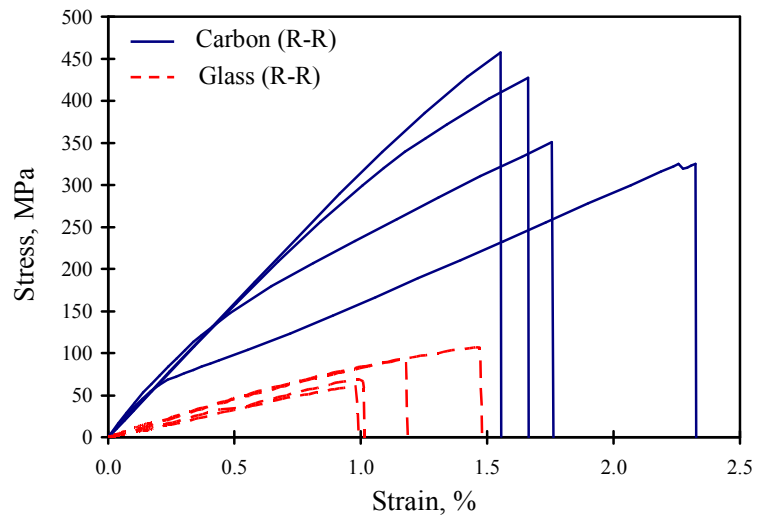
(a) Raw fibers
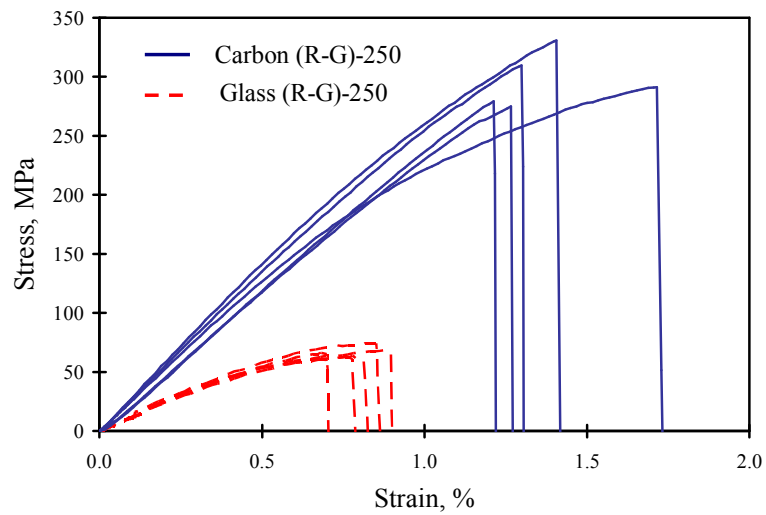
(b) After sizing removal

Figure 71. Comparison between the carbon and glass fiber composites
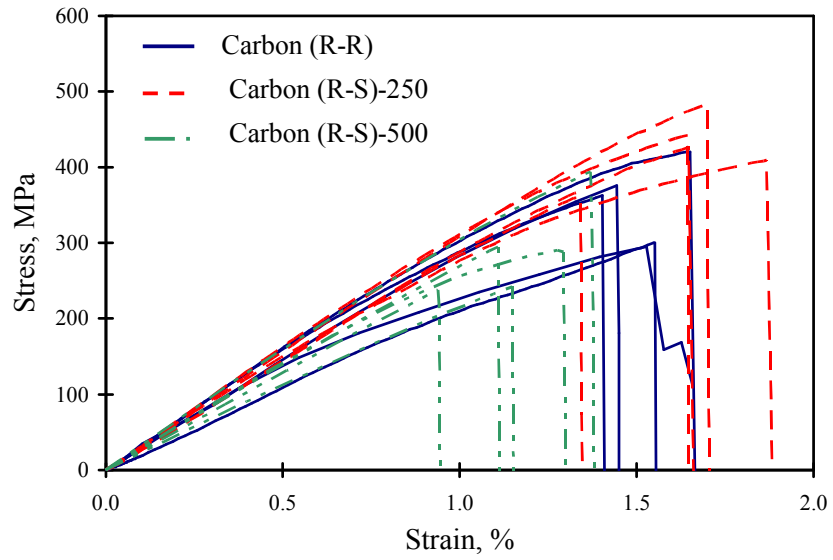
(a) CFRP
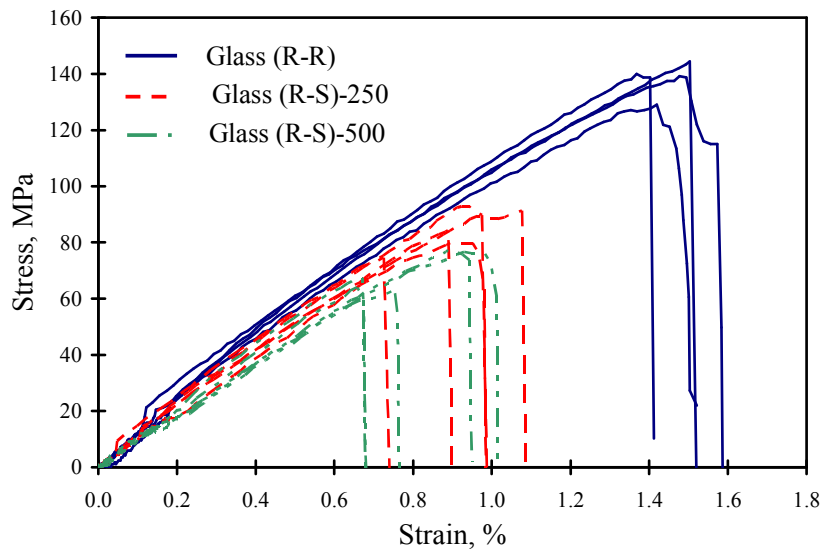
(b) GFRP

Figure 72. Effect of sizing removal temperature on final strength of composites

107

Figure 73 shows that the growth of the CNTs/CNFs decreases the ultimate strength further. For example, the average ultimate strength for the carbon fibers with sizing removal at 500 ºC decreased by 26% after growing carbon nanotubes. Similarly, the average ultimate strength of glass fibers with sizing removal at 250 ºC decreased by 25%. This loss of strength after growth might be explained by the further damage anticipated in the fiber during growth at 700 ^{o}C. SEM investigation of fracture surfaces for the carbon fiber composites with and without CNTs/CNFs growth was performed. Figure 74 and 4.16 show the fracture surface at different growth conditions. No significant difference between the fracture surfaces was observed under the SEM that can be correlated to the fabrication process. However, sizing material melt down can be observed in both Figure 74-(b) and Figure 75-(b). While the SEM micrographs do not show a major difference between sizing removal using 250 ^{o}C and 500 ^{o}C, it is obvious from the results that temperatures as high as 500 ^{o}C will have an adverse effect on the fiber itself. Moreover, it can be deduced that fiber damage took place during the growth process resulting in a significant loss of composite strength. It is therefore obvious that successful growth of CNTs/CNFs CFRP or GFRP composites will require preparing growth conditions to occur at low temperature to prevent fiber damage (i.e. as low as 250 ºC for the CFRP and much lower than 250ºC for the GFRP).

108
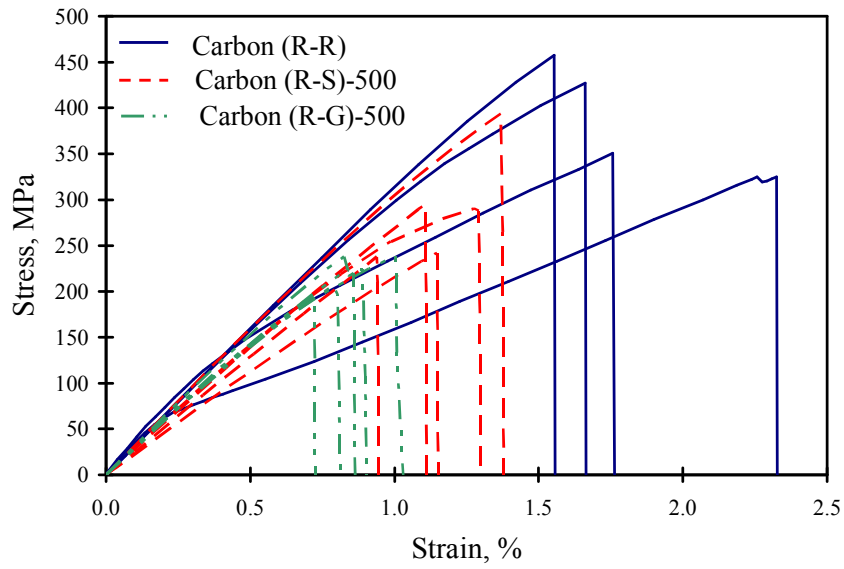
(a) CFRP
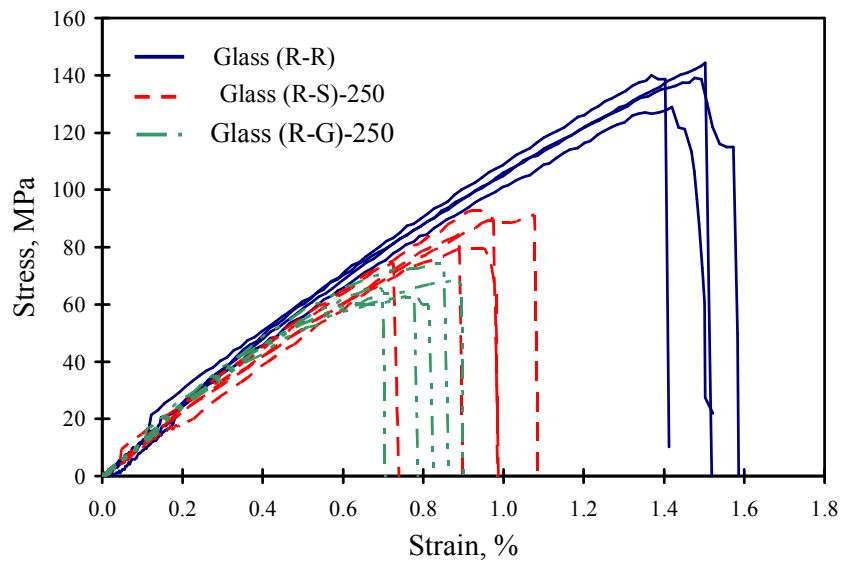
(b) GFRP

Figure 73. Effect of carbon nanotubes growth on the tensile strength of composite

109

(a)

(b)

(c)
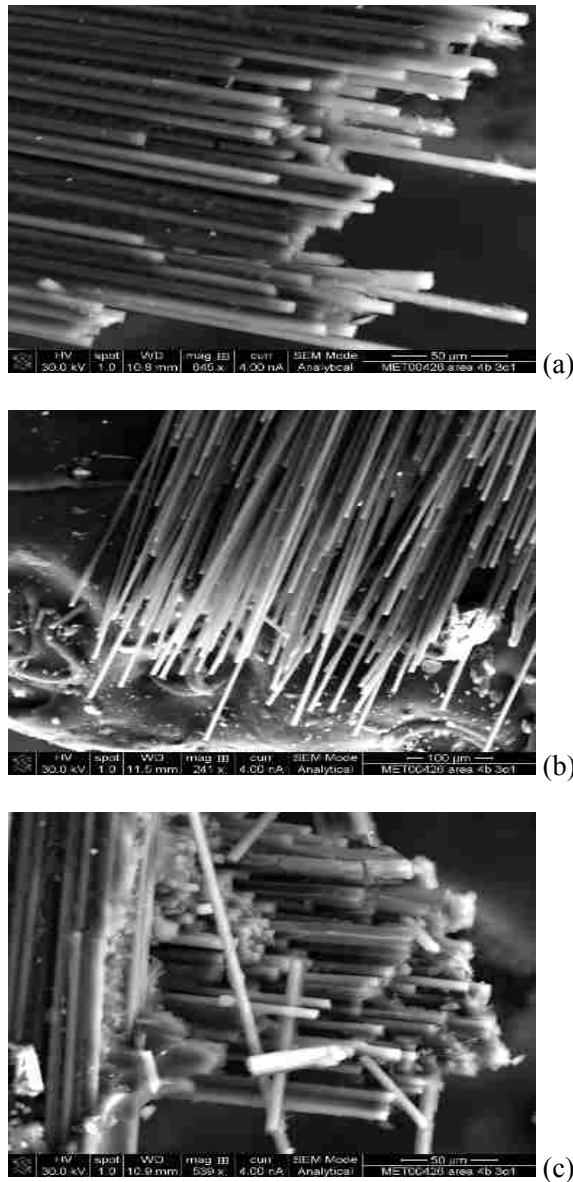
Figure 74. SEM micrographs showing composite fracture surface of (a) raw fibers from specimens (R-R), (b) after sizing removal at 250 ^{o}C from specimens (R-S) and (c) after sizing removal at 250 ^{o}C and growth at 700 ^{o}C of CNTs/CNFs from specimens (R-G)

110

(b)

(c)
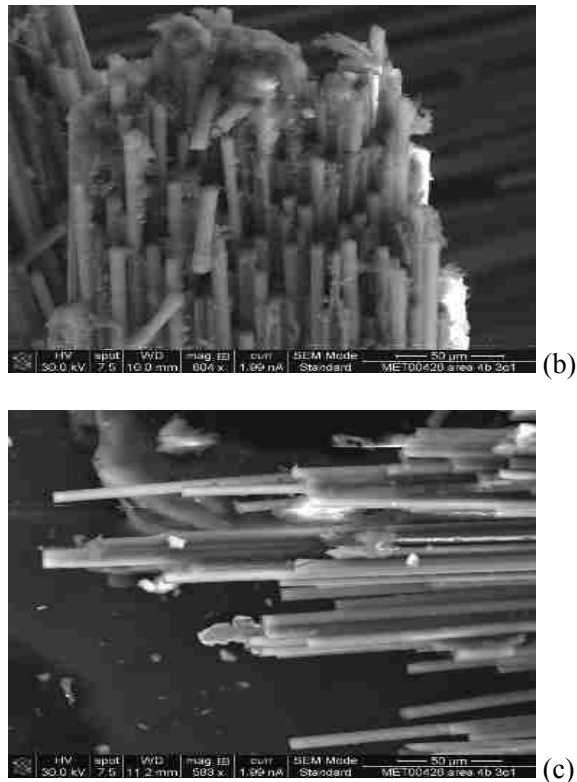
Figure 75. SEM micrographs showing composite fracture surface of (a) raw fibers from specimens (R-R), (b) after sizing removal at 500 ^{o}C from specimens (R-S) and (c) after sizing removal at 500 ^{o}C and growth at 700 ^{o}C of CNTs/CNFs from specimens (R-G)

4.4 CNTs-Fiber Reinforced Epoxy Composites

In this section, the microstructure of FRP composites is altered by incorporating CNTs in the epoxy matrix prior to composite fabrication. A new class of CFRP composites is produced using MWCNTs. The effect of adding CNTs on the strength, strain and toughness of CFRP composite is examined. We believe that CNTs can significantly enhance the shear capacity of the polymer matrix, thus improving the mechanical response of the FRP composites. It is important to emphasize that there are

111

other factors can affect the mechanical properties of FRP such as the CNTs type, content and aspect ratio. These factors were identified as the most important ones affecting the ability of CNTs to enhance the mechanical properties of polymer matrices (Kim *et al.*, 2006). This is because of the fact that these factors directly affect the interfacial bond strength, which in its turn is essential for efficient stress transfer from the weak polymer matrix to the strong CNTs.

4.4.1 On-Axis versus Off-Axis Tension Tests

According to ASTM standards, there are two tension tests for FRP composites; on and off-axis tests. The on-axis tests involves testing FRP coupons on the fiber direction (ASTMD3039/D3039M, 2008) while the off-axis test involves testing the FRP coupons at a 45° angle with respect to the fiber direction according to (ASTMD3518/D3518M, 2007) standards. This observation can be explained by looking at the effect of fiber orientation on the stress-strain behavior of woven fabric. A fundamental article by (Naik et al., 1991) can shed the light of the failure behavior of woven fabric composites. Particularly, Figure 76 represents the stress-strain response for woven fabric composite with various fiber orientations. It is noted that the fiber orientation has significant effect on the tensile response. 0 and 90° corresponds to the highest ultimate strength and lowest failure strain while 45° is opposite in response. This response is attributed to the fact that on-axis test (0° or 90°) depends significantly on the fiber response while off-axis test (45°) depends significantly on the matrix response. Typically, the reduction in elastic modulus with loading represents the intensity of the matrix damage under tensile stresses (Figure 77). In the case of on-axis test, the change in elastic modulus is small thus; the

112

associated matrix damage is also small. However, in the case of off-axis test, the change in elastic modulus is large leading to a significant damage in matrix before failure occurs.

The stress-strain response can be further understood through Figure 78, which shows the variation of ultimate strength with various fiber orientations. In this figure, the steep ascent of the ultimate strength of fiber orientation relation near 0 and 90° shows the significant impact of fiber orientation at that zone. However, the gradual ascent at fiber orientation of 45° represents very little effect of fiber orientation on the stress-strain response. In fact, the response of other tensile properties such as Young's modulus, strain at failure, and toughness would follow same profile or trend as the ultimate strength response. Given the manufacturing method, weaving of fibers is expected to occur. Even small weaves would influence the stress-strain response significantly if composites are tested on-axis and thus lead to shear failure in some occasions. However, the previous results of the on-axis tension test can be compared in condition that all specimens where manufactured using same method. In summary, the best zone to design in plane shear test for woven fabric composites is 45° rather than 0 or 90°. Therefore, in order to examine the shear behavior of woven fabric composite, off-axis tension test would be more reliable test for the following reasons:

1) The effect of fiber orientation is minimal in the middle region where fiber orientation between 30 and 60° while it is maximum at the end regions near 0° and 90°. Given the manufacturing method using hand lay-up technique with simple laboratory tools, it is expected that small weaving of fibers would occur resulting in large influence on the tensile response.

113

2)   The matrix damage associated with the off-axis test is very significant when compared to the on-axis test. Therefore, matrix effect on the tensile behavior of woven fabric composite can be truly examined through off-axis test.
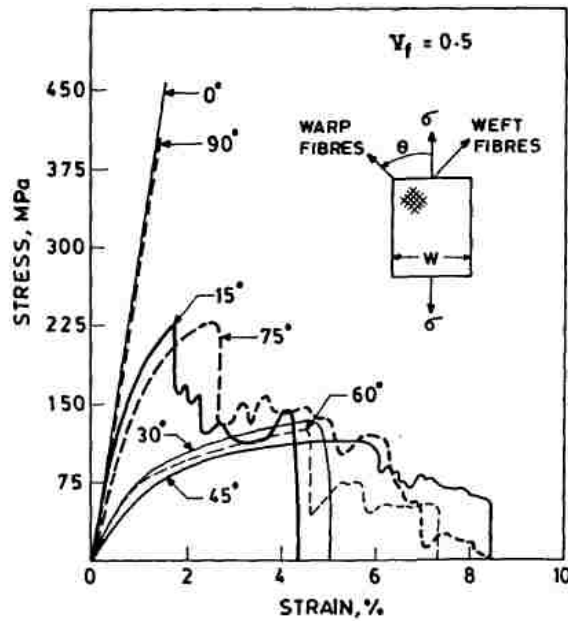
Figure 76. Stress-strain response of woven fabric composite with various fiber orientations (Naik et al., 1991)
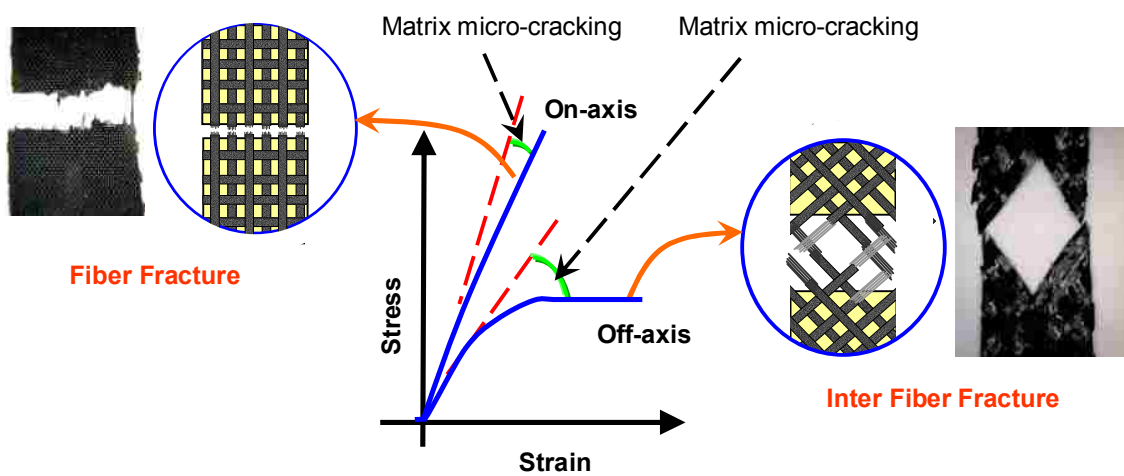
Figure 77. Stress strain behaviour for on and off-axis tests
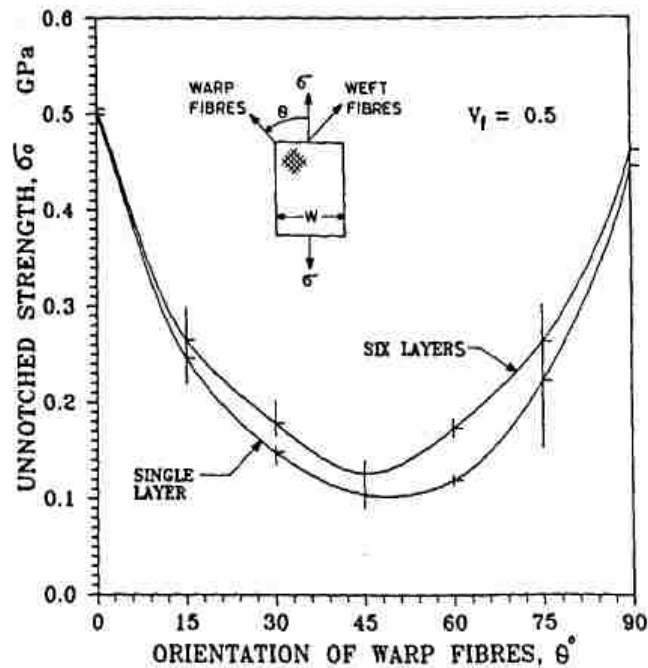
Figure 78. Effect of fiber orientations in ultimate strength of woven fabric composites (Naik et al., 1991)

4.4.2 Fabrication and Test Procedures

Four different types of treated epoxies were produced to fabricate the carbon woven composites in this study. The first type was neat epoxy prepared by mixing the resin with the hardener and applying the mixture directly to the carbon fabric during the impregnation process. The second type was prepared by reinforcing the epoxy with pristine MWCNTs. The third type was prepared by reinforcing the epoxy with surfactant treated MWCNTs. The fourth type was prepared by reinforcing the epoxy with functionalized COOH-MWCNTs.

The off-axis tension test, where the loading direction was oriented at a 45° angle with respect to the fiber direction, was carried out according to (ASTMD3518/D3518M,

115

2007) standards. In this test, it is intended to examine the in-plane shear behavior of the CFRP composites. To compare the different types of MWCNTs on the off-axis tension strength, only 1.0% CNTs by weight was examined and the different types of treated MWCNTs were compared with the reference case (neat epoxy). Five specimens were examined in each test as recommended by (ASTMD3039/D3039M, 2008). After analyzing the results, investigations of the pristine (P) and functionalized (F) MWCNTs were expanded for a wide range of MWCNTs contents of 0.1, 0.5, 1.0, and 1.5 % by weight of epoxy. Off-axis tension testing was performed for these four MWCNTs contents. Moreover, on-axis tension test was performed, where the loading was oriented at the same direction as the fibers following (ASTMD3039/D3039M, 2008) standards. In the on-axis tension test, the pristine (P) and functionalized (F) MWCNTs were examined with various contents including 0.1, 0.5, 1.0, and 1.5 % by weight. To further explain the experimental observations, the flexure behavior of various MWCNTs-epoxy nanocomposites was tested in four-point bending according to ASTM D 6272-10 standards. Figure 79 and Figure 80 show schematic for experimental plan and Figure 81 the fabricated CFRP composites respectively.

116
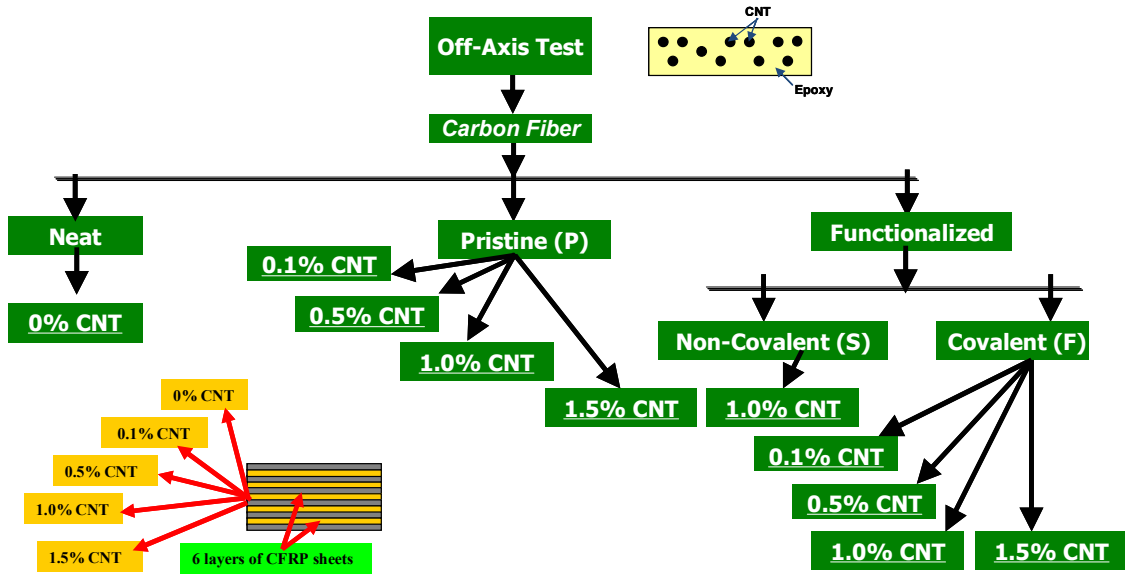
Figure 79. Schematic for experimental plan for off-axis tension test
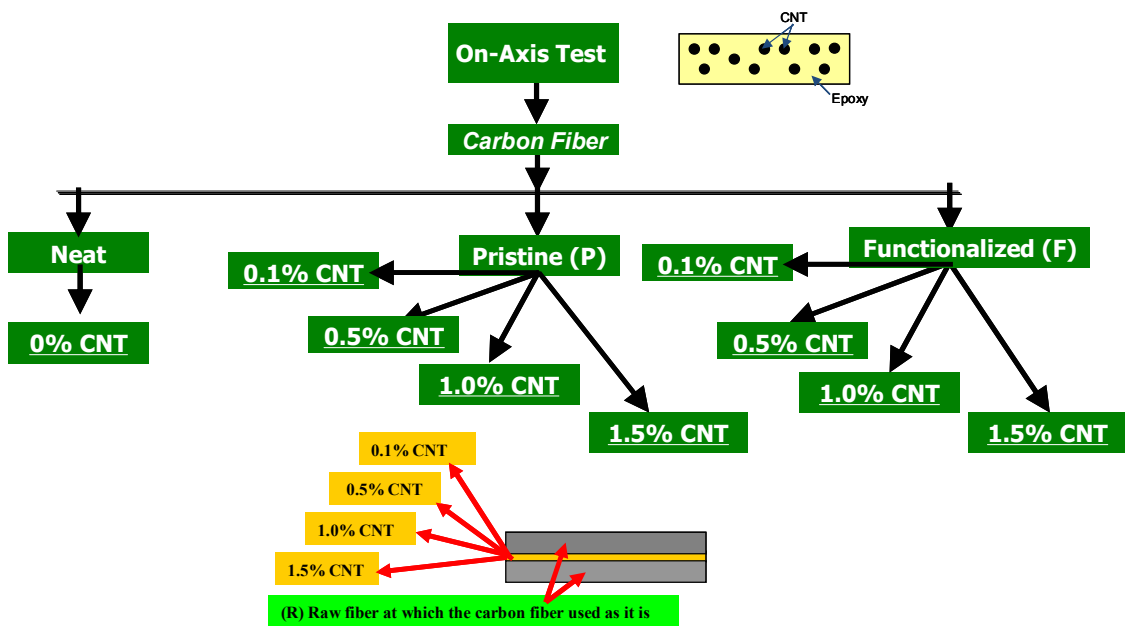
Figure 80. Schematic for experimental plan for on-axis tension test
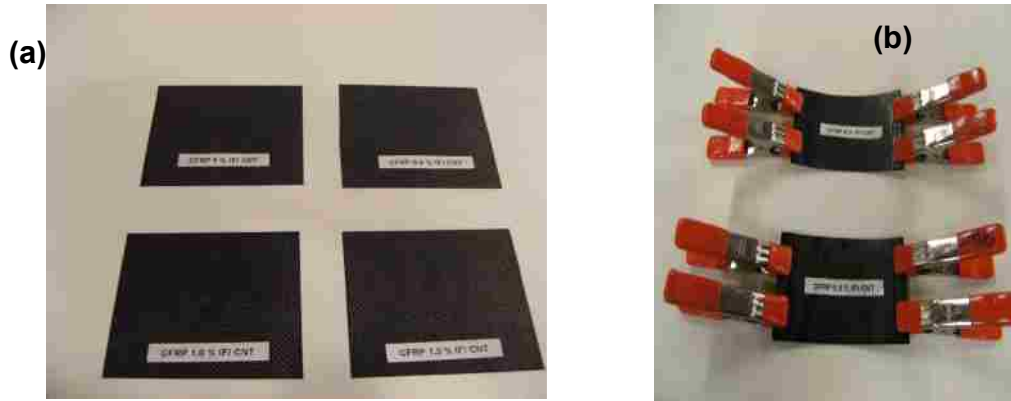
Figure 81. Fabrication of CFRP composite laminates (a) Fabricated CFRP composite coupons and (b) Attachment of end tabs

Each CFRP composite was cut into 127 ± 2.5 mm long, 12.5 ± 1.5 mm wide coupons and tested according to ASTM D3039 testing standards. This ASTM standard involves tested FRP composites to obtain various tensile properties. It is important to report that this ASTM involves testing composite with the fibers oriented in the loading direction (On-axis test). At least five coupons were tested from each composite. Tension and flexure tests were performed on the coupons using MTS® Bionix servo hydraulic system with mechanical grips (Figure 82). The machine has a load capacity of 25 kN and a maximum stroke of 152.4 mm. In each test, load, displacement, and strain were measured and recorded.

The strain was measured by contact extensometer attached to the coupons with gauge length of 25.4 mm. The extensometer has range of +50% and -20% strain that is much higher than failure strains typically observed in FRP composites. The sampling rate for all the experiments was 50 Hz and the data was collected by FlexStar MTS® 793 data acquisition system. For each coupon, the stress-strain relation was obtained. The tensile

118

strength, Young's modulus, failure strain, and toughness were then computed and evaluated. Statistical analyses were performed on these results and the statistical significance of difference between the specimens was evaluated using the student t-test assuming 85% levels of significance.

(a)   (b)
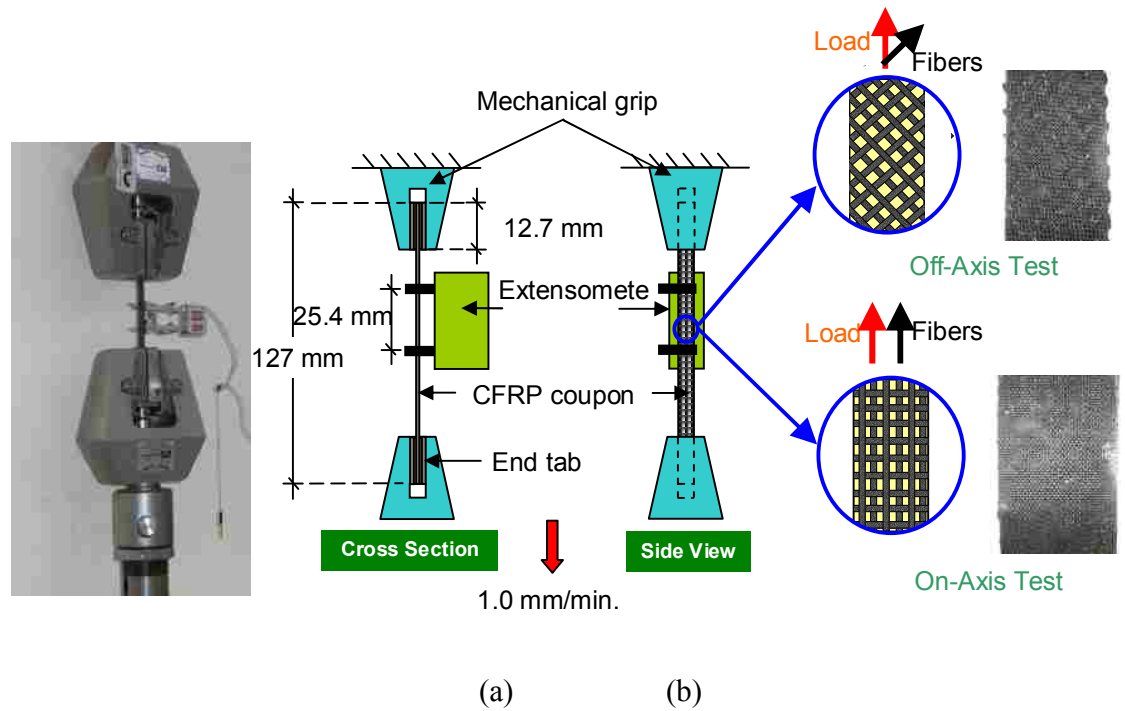
Figure 82. Tension test of CFRP composite (a) Contact extensometer attached to CFRP coupons and (b) Schematic for the test setup

The axial stress (σ) is computed at any load level using equation (1) as follows:

$$\sigma = \frac{P}{A} \tag{4.1}$$

where (P) is the applied load and (A) is the cross-sectional area. The axial strain is computed as a function of the specimen extension (ΔL) and the gage length (L) as follows:

119

$$\varepsilon = \frac{\Delta L}{L} \tag{4.2}$$

The extension is measure by either the machine or the extensometer. The gage length for the extensometer was 25.4 mm. Toughness is found by computing the area under the stress-strain curve using Simpson's rule. The modulus of elasticity (E) was computed as per ASTM D3039 by fitting the tensile chord modulus within 1000 and 3000 micro-strain range to linear regression curve as follows:

$$E = \frac{\Delta \sigma}{\Delta \varepsilon} \tag{4.3}$$

4.4.3 Results and Discussions

4.4.3.1 Off-Axis Test

All coupons exhibited similar failure behavior. The failure behavior was associated with matrix cracking and no fiber fracture occured. Complete delamination was observed at the failure zone between the six layers. The stress-strain responses for various techniques for chemical treatments of CNTs are presented in Figure 83. Clearly, the surfactant treatment reduces the stress-strain response for FRP significantly. This effect confirms the flexural response of surfactant treated CNTs, which was reported earlier in Chapter 3. On the other hand, the pristine CNTs increase the strain capacity while the functionalization treatment increases the strength and strain capacity.

These results are further discussed in the bar charts in Figure 84, Figure 85, and Figure 86 here the ultimate strength, failure strain, and toughness for various CNTs treatments are normalized with respect to the neat case. The bar charts show 20, 19, and

120

50% increase in ultimate strength, failure strain, and toughness in the 1.0% functionalized CNTs case. A 29% increase in strain capacity was also observed in the pristine case. On the contrary, the ultimate strength and toughness in the case of surfactant treatment are reduced by 23 and 24% respectively. Based on the thermal analyses and SEM images reported in the Chapter 3, the degradation in the case of surfactant treatment is attributed to the formation of micelles of surfactant. The micelles are expected to isolate the nanotubes from the surrounding polymer matrix and causes phase separation in the microstructure of the nanocomposite. The phase separation degrades the mechanical properties in the nanocomposites. In general, the highest improvements in mechanical response are observed at the failure strain. The improvement in failure strain might be attributed to the increase in fracture toughness near the failure. The CNTs bridge the micro-cracks leading to higher fracture toughness. Therefore, performing a fracture toughness test could be useful at that point. Furthermore, the enhancements in the ultimate strength are attributed to the strong interfacial bond between the CNTs and the matrix.
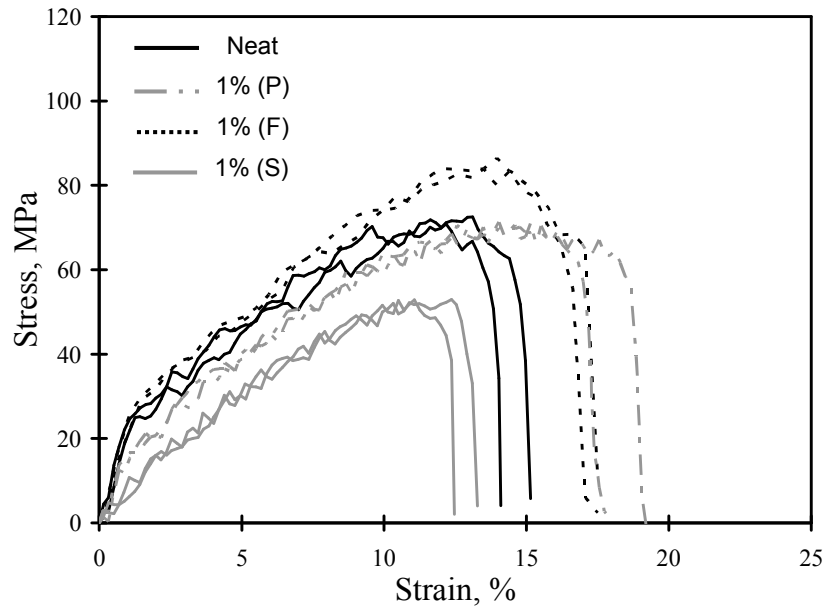
Figure 83. Stress-strain relationships for CFRP off-axis composite coupons for various chemical treatments of 1.0% MWCNTs-epoxy nanocomposites
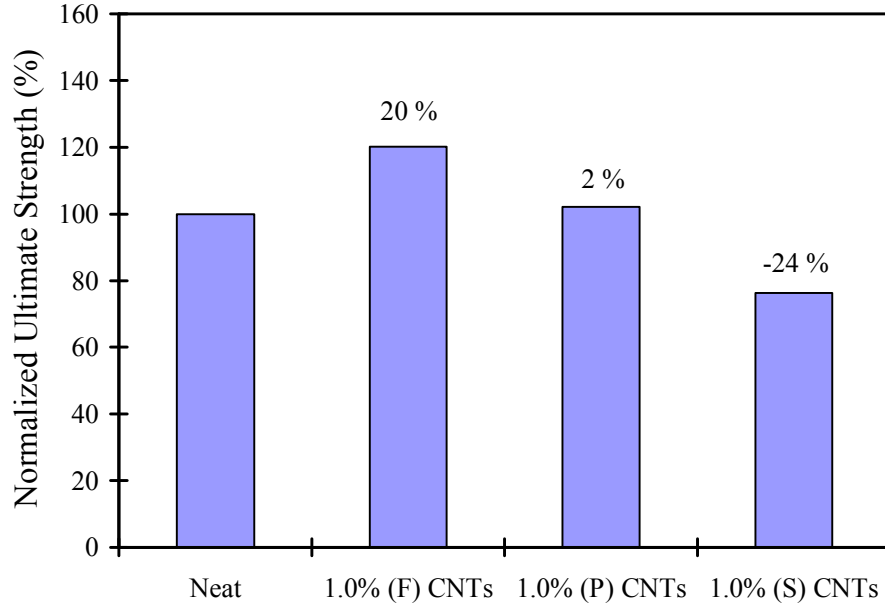
Figure 84. Ultimate strength of woven fabric composites with various chemical treatments of 1.0% MWCNTs-epoxy nanocomposites

122
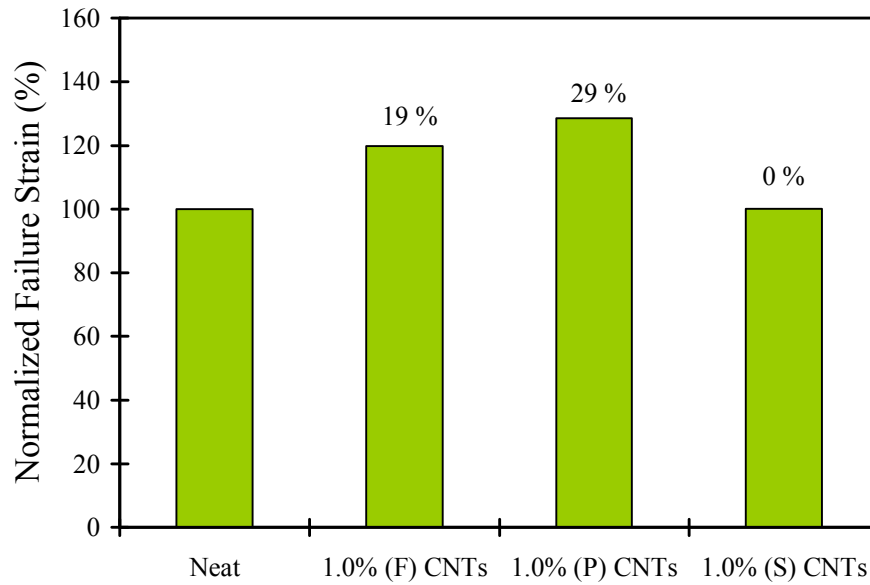
Figure 85. Failure strain of woven fabric composites with various chemical treatments of 1.0% MWCNTs-epoxy nanocomposites
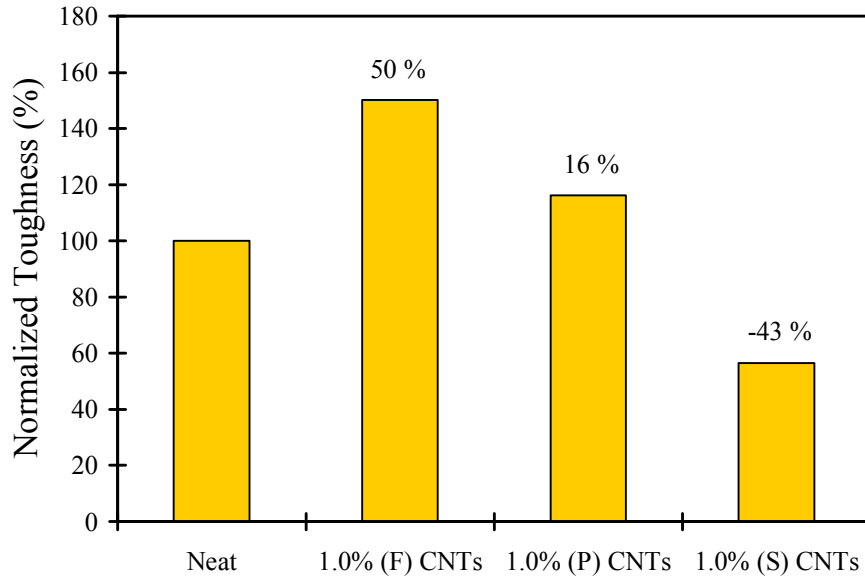
Figure 86. Toughness of woven fabric composites with various chemical treatments of 1.0% MWCNTs-epoxy nanocomposites

123

Figure 87 shows the stress-strain response for the pristine (P) MWCNTs case with various MWCNTs loadings. In addition, statistical analyses for the off-axis test for pristine CNTs FRP composites are presented in Table 3. From Figure 87, it is noted that the pristine (P) MWCNTs had significant effect on the failure strain. For example, the strain increase due to the addition of 0.1, 0.5, 1.0, and 1.5% were 13, 18, 28, and 30% respectively. The highest increase in failure strain is associated with the highest CNTs loadings. The enhancement in failure strains can be attributed to the increase in fracture toughness which might be attributed to the ability of CNTs to provide some crack bridging effect within the matrix at the nanoscale and thus enabling the epoxy matrix to continue carrying loads after cracking. In addition, limited increase in ultimate strength is observed with the highest enhancement of 10% associated with 0.5% MWCNTs. The limited enhancement in strength is attributed to the weak interfacial bond between the nanotubes and the surrounding matrix when the nanotubes were dispersed in the epoxy matrix. Moreover, the moderate improvement in toughness is mainly due to the enhancements in failure strain.

The functionalized (F) MWCNTs cases exhibited significant enhancements in ultimate strength, failure strain, and toughness as shown in the stress strain response (Figure 88). In addition, statistical analyses for the off-axis test for functionalized CNTs FRP composites are presented in Table 3. 20 and 39% increase in ultimate strength were achieved by adding 1.0 and 1.5 % respectively. Also, 20 and 50% increase in failure strains were achieved with the same MWCNTs contents. The toughness enhancement reached 121% with 1.5 % functionalized MWCNTs. The role of functionalization in increasing the interfacial bond between the nanotubes and the epoxy matrix and enhance

124

the tensile response is evident. However, the enhancement in Young's modulus of elasticity is limited to 20% as observed in the case of 1.0% (F).

The tensile properties of the pristine (P) and functionalized (F) CNTs FRP composites are compared in Figure 89 to Figure 91 and in Table 3. The average enhancements in ultimate strength for the pristine and functionalized cases were 2 and 17% respectively (Figure 89). These improvements in ultimate strength reflect the effect of surface functionalization on the mechanical response. The average improvements in strain capacity for the pristine and functionalized cases are 22 and 20% respectively. Both techniques showed similar improvements with respect to the failure strain as a result of the crack bridging effect. The average toughness enhancements reached 14 and 50% for the pristine and functionalized cases respectively.
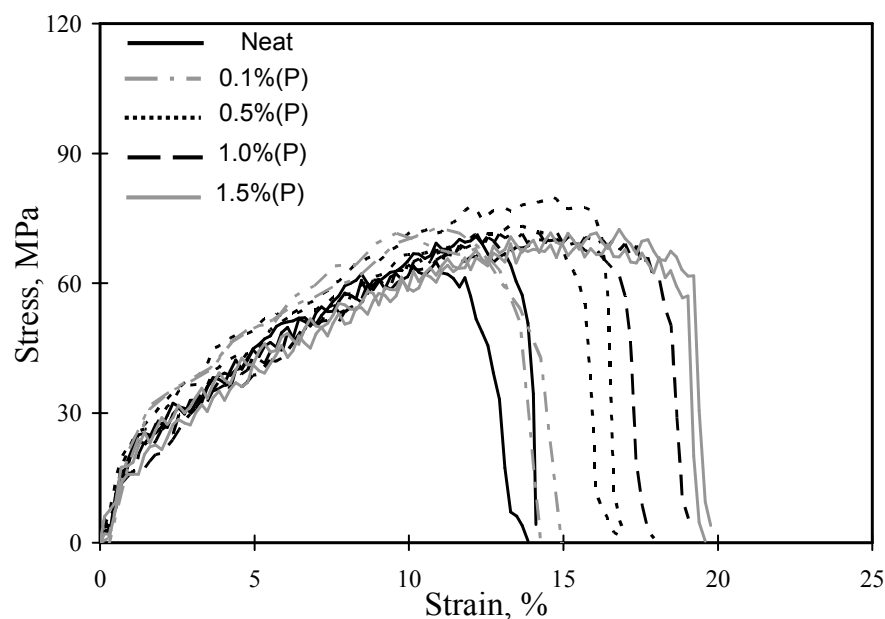
Figure 87. Stress-strain relationships for CFRP off-axis composite coupons with various pristine MWCNTs contents
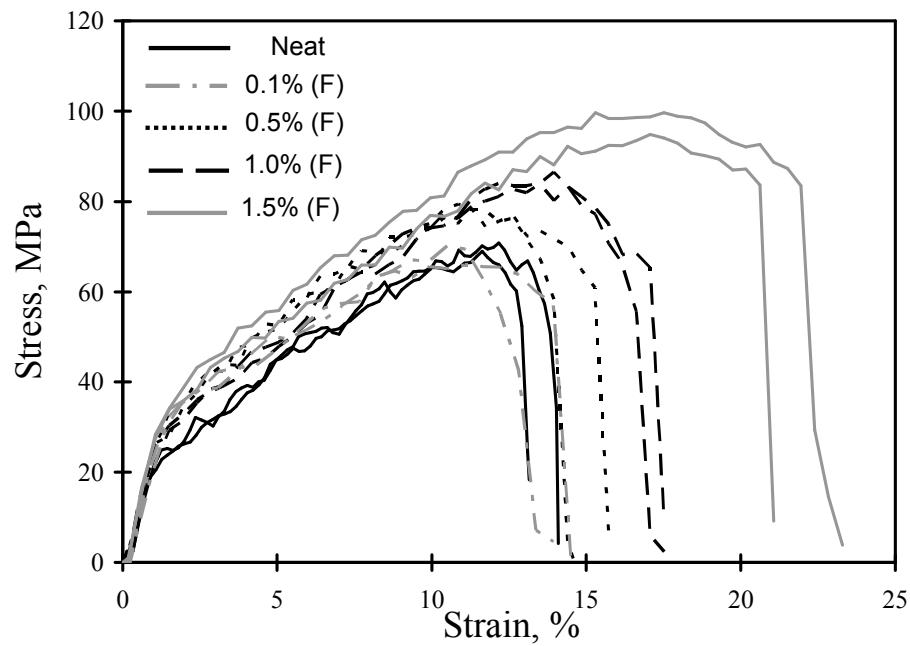
Figure 88. Stress-strain relationships for CFRP off-axis composite coupons with various functionalized MWCNTs contents
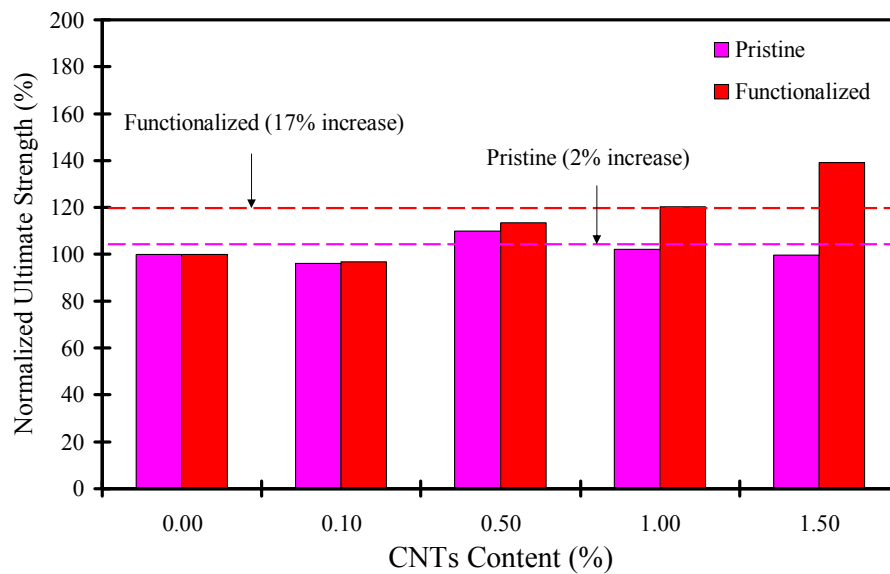
Figure 89. Off-axis ultimate strength of woven fabric composites for pristine and functionalized CNTs

126
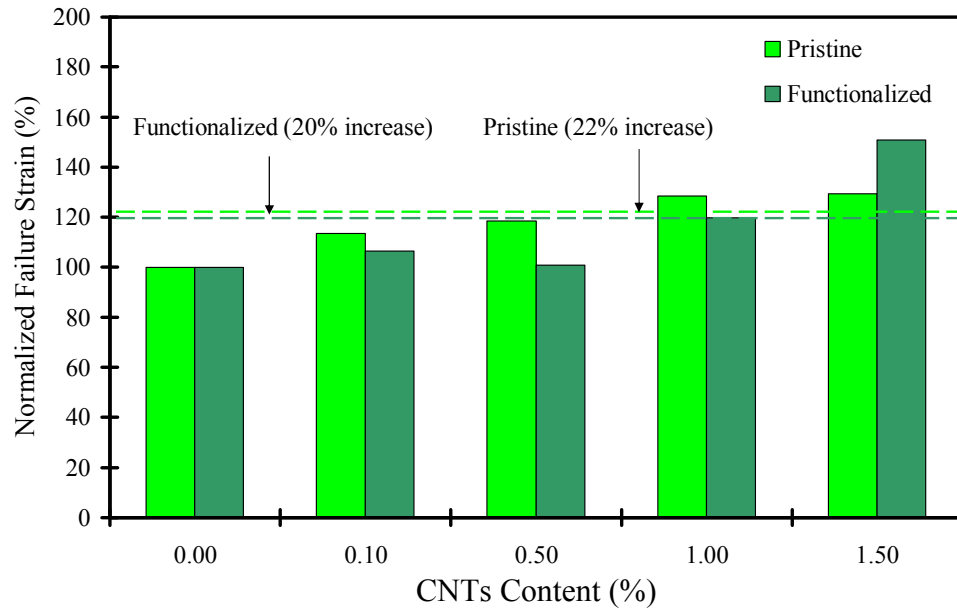
Figure 90. Off-axis failure strain of woven fabric composites for pristine and functionalized CNTs
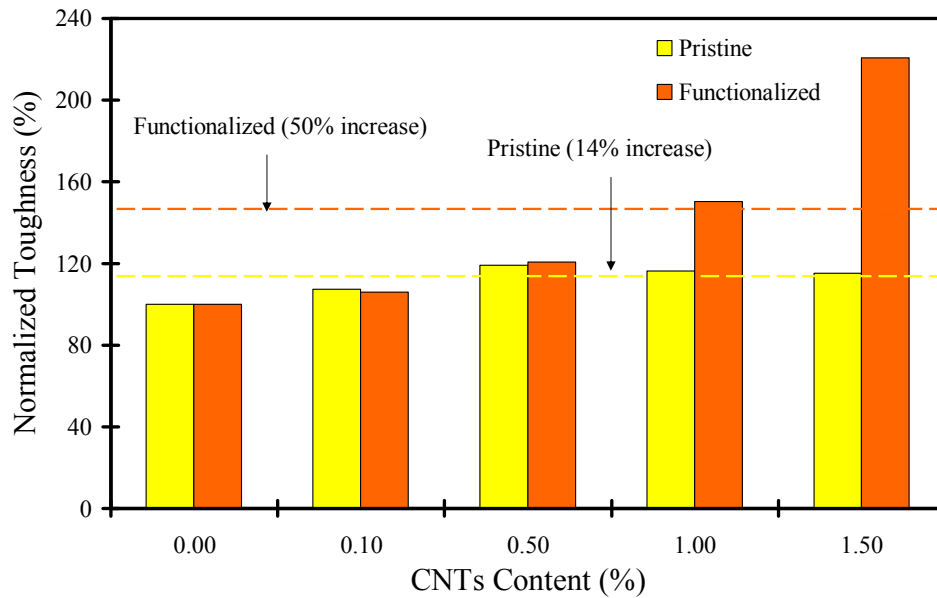
Figure 91. Off-axis toughness of woven fabric composites for pristine and functionalized CNTs

127

Table 3. Statistical analyses for off-axis test coupons

		Young's modulus, GPa	Ultimate strength, MPa	Failure strain, %	Toughness, MPa
Neat	Mean	3.86	69.8	14.45	6.67
	COV, %†	21.7	4.1	6.9	10.6
0.1% (P*)	Mean	3.74	66.9	16.4	7.17
	COV, %	15.1	9.5	5.5	7.6
	% Increase‡	-3	-4	13	7
0.5% (P)	Mean	4.29	76.6	17.12	7.94
	COV, %	21.2	6.2	3.9	8.1
	% Increase	11	10	18	19
1.0% (P)	Mean	3.54	71.2	18.57	7.76
	COV, %	27.7	4.3	4.9	5.8
	% Increase	-8	2	28	16
1.5% (P)	Mean	3.63	69.6	18.70	7.69
	COV, %	25.3	4	5	6.9
	% Increase	-6	-0.3	30	15
0.1% (F**)	Mean	4.56	67.4	15.39	7.07
	COV, %	20.2	4.3	7	5.3
	% Increase	18	-3	6	6
0.5% (F)	Mean	4.35	79.1	14.57	8.04
	COV, %	18.6	3.8	6.1	8.9
	% Increase	13	13	1	21
1.0% (F)	Mean	4.63	83.8	17.31	10.03
	COV, %	15.9	2.2	4.3	7.5
	% Increase	20	20	20	50
1.5% (F)	Mean	3.85	97.1	21.81	14.72
	COV, %	23.6	3.9	5.7	9.8
	% Increase	-0.3	39	51	121

*P: Pristine, **F: Functionalized, †COV: coefficient of variation, ‡% Increase: percentage of increase

4.4.3.2 On-Axis Test

Figure 92 and Figure 93 show the on-axis stress-strain behaviour of pristine (P) and functionalized (F) MWCNTs and the statistical analyses for both cases are reported in Table 4. Statistical analyses for on-axis test coupons. The fibers dominated the tensile behaviour of the tested coupons when it is loaded in the fibers direction. Failure occurred due to fiber fracture. In general, no significant improvements in on-axis tensile properties were observed as oppose to the off-axis properties. A toughness increase of 20 and 29%

128

were observed in the case of 0.5 and 1.0% (F) MWCNTs. Also, a toughness increase of 6 and 5% in the case of 0.1 and 1.0% (P) MWCNTs. Although increases in toughness are observed in some cases, decreases in toughness of 17 and 2% are also observed in other cases [0.5% (P) and 1.0% (F) MWCNTs]. Similarly, the ultimate strength increased by 7, 10, 14, and 12% in the cases of 1.0% (P), 1.5% (P), 0.1% (F), and 0.5% (F) MWCNTs respectively. On the other hand, the ultimate strength decreased by 2, 11, and 1% in the case of 0.1% (P), 0.5% (P), and 1.0% (F) MWCNTs respectively. Same observations can be applied to other properties such as Young's modulus and failure strain. The change in mechanical properties in the on-axis test due to the addition of either pristine or functionalized CNTs is limited compared to the off-axis test. In addition, the changes are in the positive and negative side. The above observations lead us to the fact that the epoxy matrix with various CNTs loadings and treatments did not affect the mechanical response of the on-axis test as oppose to the off-axis test.

Furthermore, Figure 94 to Figure 97 show a comparison between the pristine and functionalized cases with various CNTs content in terms of Young's modulus, ultimate strength, failure strain, and toughness. It can be noted the functionalization did not have effect in improving the mechanical response of the on-axis tension test. The nature of the failure for the on-axis test (fiber fracture without damage in the matrix) dominated the mechanical response. In addition, Young's modulus of CFRP coupons is typically dominated by the Young's modulus of carbon fibers rather than the epoxy matrix especially when loaded in the fiber direction. Therefore, the addition of CNTs also did not affect the Young's modulus because of the significant difference in Young's modulus between the continuous macrofibers and the epoxy matrix.

129
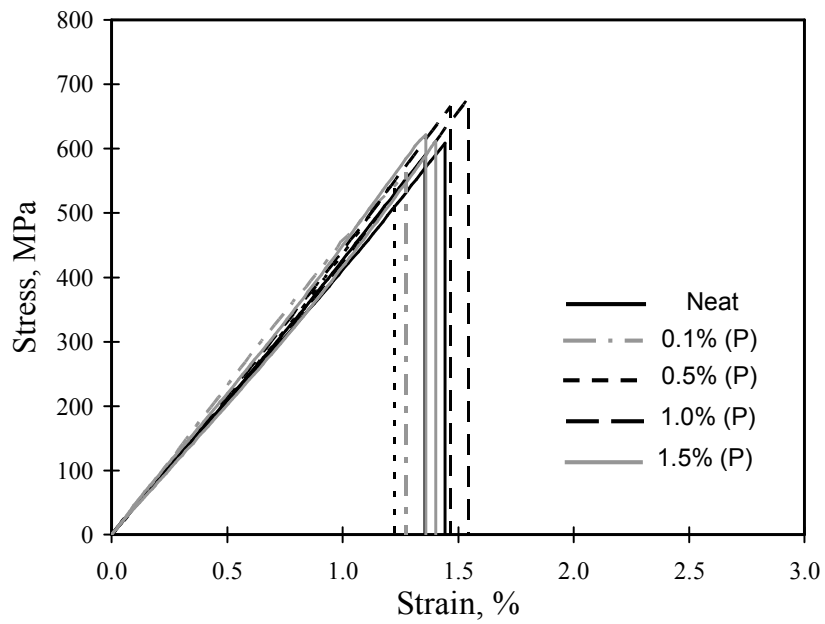
Figure 92. Stress-strain relationships for CFRP on-axis composite coupons with various dispersed MWCNTs contents
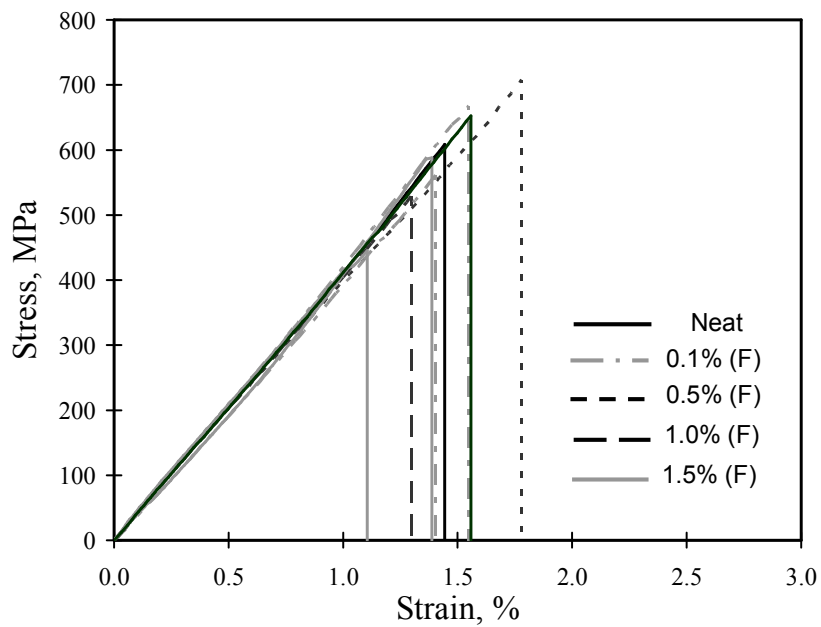
Figure 93. Stress-strain relationships for CFRP on-axis composite coupons with various functionalized MWCNTs contents

130
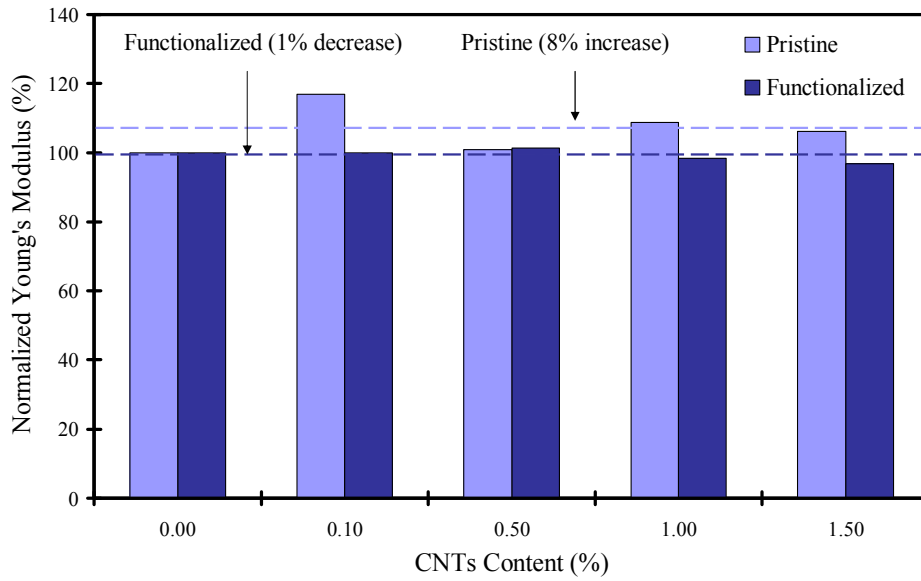
Figure 94. On-axis Young's modulus of woven fabric composites for dispersed and functionalized CNTs
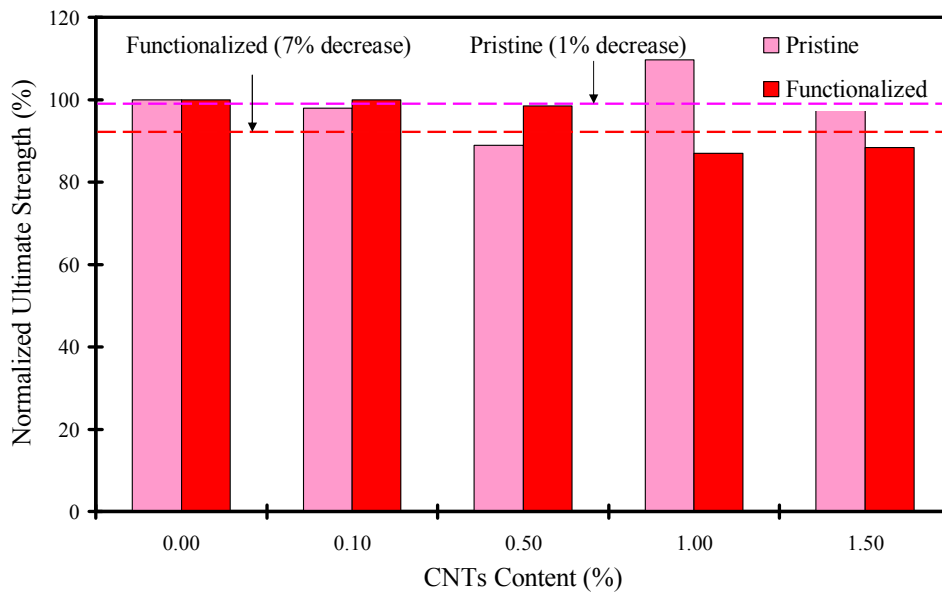
Figure 95. On-axis ultimate strength of woven fabric composites for dispersed and functionalized CNTs

131
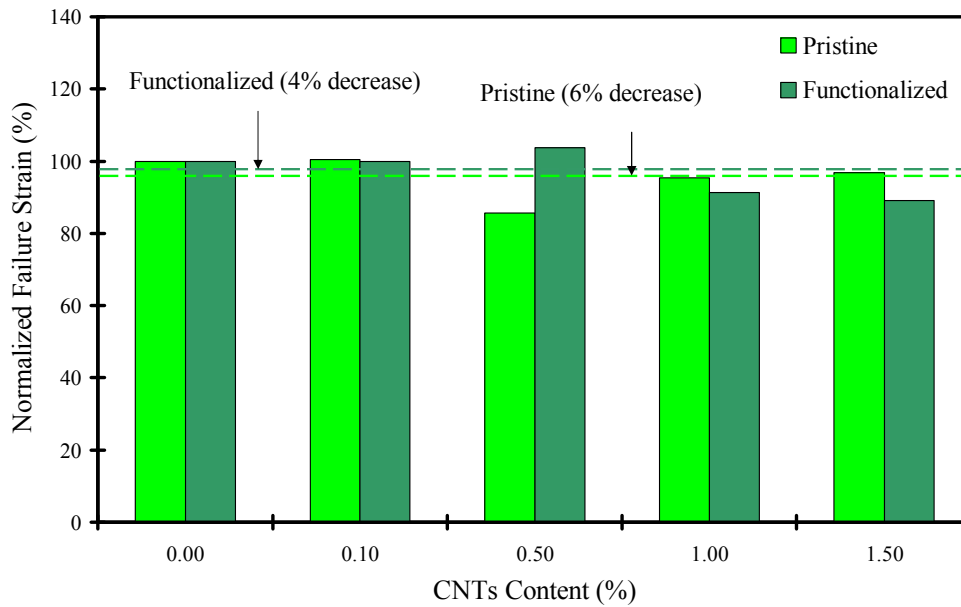
Figure 96. On-axis failure strain of woven fabric composites for dispersed and functionalized CNTs
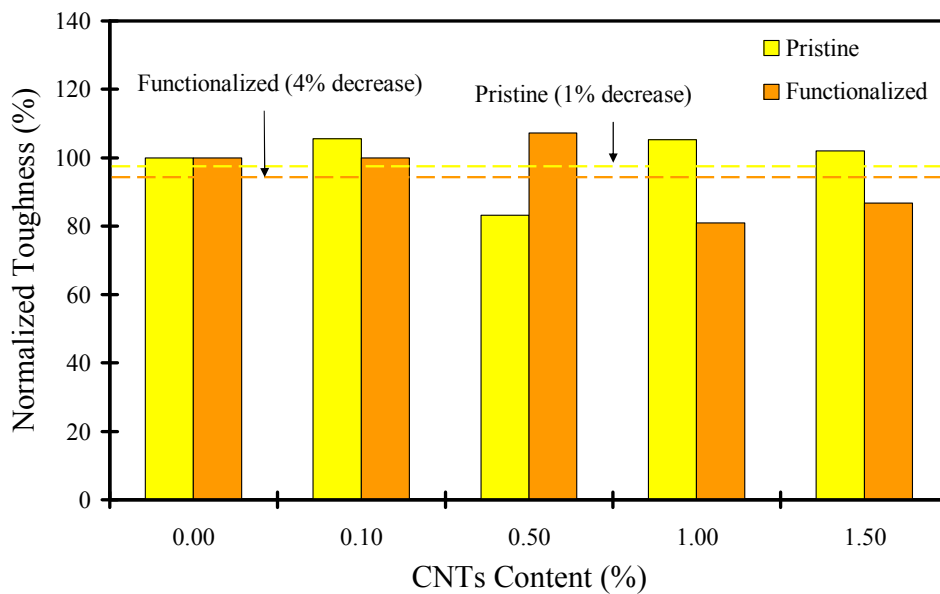
Figure 97. On-axis toughness of woven fabric composites for dispersed and functionalized CNTs

132

Table 4. Statistical analyses for on-axis test coupons

		Young's modulus, GPa	Ultimate strength, MPa	Failure strain, %	Toughness, MPa
Neat	Mean	40	554	1.38	3.8
	COV, %†	7	6.6	8.2	14.7
0.1% (P*)	Mean	47	543	1.39	4.02
	COV, %	14.3	3.8	12	12.6
	% Increase‡	17	-2	0	6
0.5% (P)	Mean	41	493	1.18	3.16
	COV, %	4.4	16.9	12.2	19.5
	% Increase	1	-11	-14	-17
1.0% (P)	Mean	44	607	1.32	4
	COV, %	6	10	12.4	22.2
	% Increase	9	10	-5	5
1.5% (P)	Mean	43	591	1.34	3.88
	COV, %	6.9	5.2	5.9	8.8
	% Increase	6	7	-3	2
0.1% (F**)	Mean	40	630	1.50	4.58
	COV, %	6	7.5	10.3	13.9
	% Increase	-1.5	14	9	20
0.5% (F)	Mean	40	620	1.59	4.91
	COV, %	4.4	15.3	19.2	29.1
	% Increase	-0.1	12	13	29
1.0% (F)	Mean	39	548	1.37	3.71
	COV, %	6	9.3	6.7	16.2
	% Increase	-3	-1	-1	-2
1.5% (F)	Mean	38	556	1.34	3.97
	COV, %	6.8	19.5	20.5	28.7
	% Increase	-5	0	-3	4

*D: Dispersed, **F: Functionalized, †COV: coefficient of variation, ‡% Increase: percentage of increase

4.5   Summary

Two approaches of incorporating CNTs in FRP composites were examined in this chapter. They are 1) Growing CNTs on macro-fibers and 2) Reinforcing epoxy with CNTs. In the CNTs growth experiment, the sizing removal and growth typically result in reducing CFRP and GFRP strength. Little effect on the material stiffness was observed, but a reduction of the ultimate strength and strain at failure was observed. Of special interest was the significance of sizing removal at 250 ºC where a slight increase in the

133

composite strength was observed. The removal of Oxygen during the preprocessing and growth process seems necessary to limit damage in the composite materials. This research work is published in 2010 (Dai *et al.*, 2010).

In the CNTs reinforcing epoxy study, the tensile behaviour of the on and off-axis pristine and functionalized MWCNTs composite coupons is examined with various contents. A significant enhancement in the mechanical properties can be achieved in the off-axis tensile behaviour of FRP incorporating the functionalized MWCNTs. However, no effect of the MWCNTs was observed when the composite coupons were loaded on-axis. The pristine MWCNTs were shown to enhance the failure strain only while the functionalized MWCNTs were shown to enhance the ultimate shear strength and failure strain. With 1.5% functionalized MWCNTs epoxy FRP composites, strength and strain increase of 39 and 51% were achieved. This enhancement is due to the strong interfacial bond between the nanotubes and epoxy matrix. Flexure and TGA tests of MWCNTs-epoxy nanocomposites confirmed that the strong interfacial bond in the functionalized MWCNTs could improve the flexure strength and thermal stability of the nanocomposites. The reported enhancement in the shear strength of the FRP composite can provide excellent enhancement to many applications of FRP composites governed by weak shear strength confirmed by delamination as discussed above. The research work is accepted for publication in 2011 (Soliman *et al.*, 2011f).

134

CHAPTER 5.   CREEP BEHAVIOR OF CNTS-EPOXY NANOCOMPOSITE AT THE FRP-CONCRETE INTERFACE

5.1   Introduction

Previous studies reported in the literature showed significant creep deformation of epoxy when used to bond FRP sheets to concrete structure against sustained loads. This observation applies to reinforced or prestressed concrete strengthened against dead loads. In this Chapter, double shear tests were performed on FRP sheets bonded to concrete blocks using CNTs-epoxy nanocomposites. Various contents of pristine and functionalized CNTs by weight were examined including 0.1, 0.5, 1.0, and 1.5%. The CNTs were dispersed in the epoxy matrix, tested, and compared to the case of using neat epoxy. The Chapter is divided into two sections. The first section presents the experimental methods and their respective results. The second section presents a rheological modelling for the experimental investigation.

5.2   Experimental Methods

The double lap shear test was used to evaluate creep of epoxy with CNTs at the concrete-epoxy interface. The double lap shear test specimen consisted of two carbon fiber reinforced polymer (CFRP) composite laminates bonded to two sides of two concrete blocks using controlled thickness epoxy adhesive as shown in Figure 98. The concrete blocks were loaded in tension to induce shear stresses at the four epoxy joints.

135

The applied load (P) induces shear stress of 25% of the ultimate shear strength of the epoxy. DEMEC (gauge) points were bonded to the concrete blocks and were used to measure the deformation of two shear joints in the loading direction. Unidirectional CFRP laminates were chosen in order to ensure minimal creep response of the FRP when loaded in the fiber direction. In addition, concrete blocks were cured for 7 days and left to dry for 21 days before being used in the experiments. The axial stress in concrete during experiments did not exceed 0.36 MPa (less than 10% of the tensile strength of concrete). Therefore, creep and shrinkage of concrete during the experiment was expected to be negligible compared with epoxy creep. By neglecting creep and shrinkage of concrete and creep of the CFRP laminate and ignoring the deformation through epoxy thickness, epoxy shear strain γ(t) per joint can be computed as:

$$\gamma(t) = \frac{\Delta L(t)}{h}$$

(5.1)

where (h) is the epoxy thickness and (t) is the time. In addition, the shear stress (τ) acting on every shear joint can be computed as follows:

$$\tau = \frac{P}{2A}$$

(5.2)

where (A) is the area of one shear joint. The creep compliance of the epoxy is computed as follows:

$$J(t) = \frac{\gamma(t)}{\tau}$$

(5.3)

The normalized creep compliance $J_n(t)$ of epoxy is also computed relative to the elastic deformation using:

136

$$J_n(t) = \frac{J(t)}{J(0)}$$

(5.4)

where J(0) is the initial elastic compliance. The major idea from computing the normalized creep compliance is to exclude the effect of initial elastic deformation on the long-term behavior.
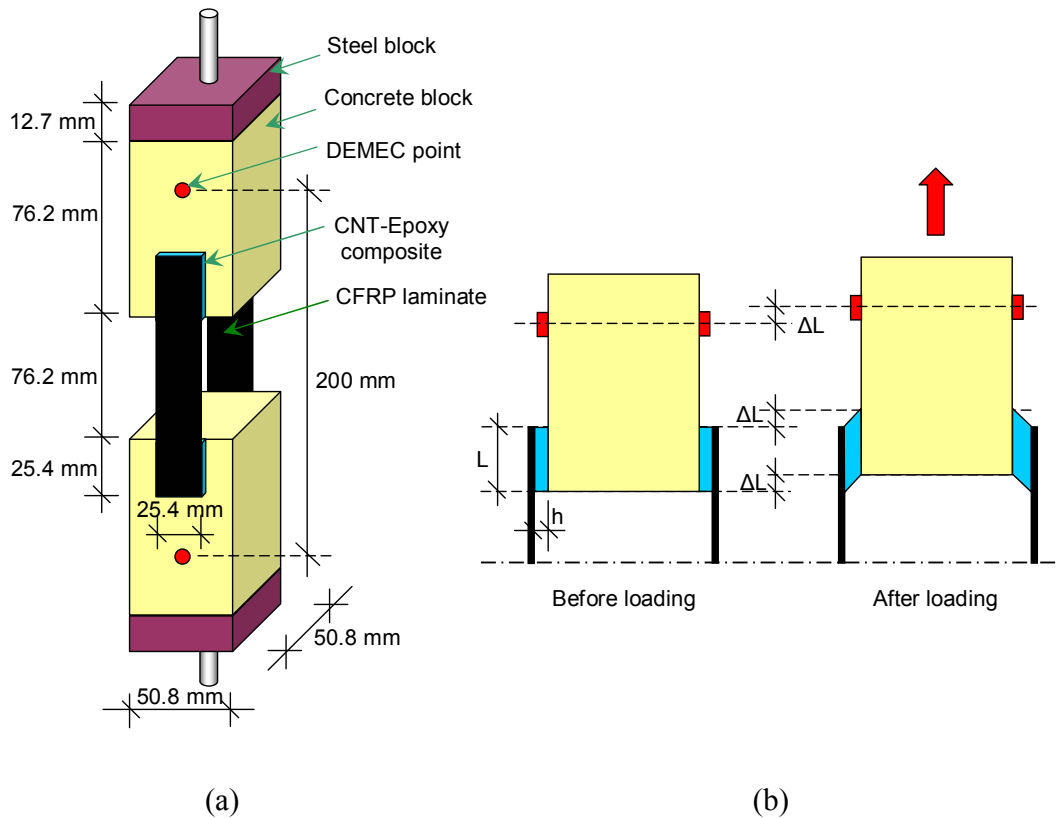
Figure 98. Schematic of the double lap shear specimen (a) dimensions and (b) deformation

5.2.1 Material Properties

Table 5 shows the mix proportion by weight of the concrete substrates used in all experiments. The chosen concrete mix has a 28-day compressive strength of 42 MPa similar to most concrete used nowadays in construction of reinforced or prestressed

137

concrete elements. The MWCNTs and the epoxy system are similar to those used in the previous chapters. The low viscosity of the resin facilitates incorporating the CNTs during the fabrication process and provides reasonable level of deformations in order to obtain accurate creep measurements. CFRPs composites were supplied by Graphtek LLC Company. The CFRPs were 1.1 mm thick uni-directional CFRP strips fabricated using 33 million pounds per square inch (m.s.i) carbon and Vinylester resin. The unidirectional strips are chosen in order to ensure their limited creep response when loaded in the fiber direction. Density, tensile strength and flexural strength of the CFRP laminates are 1.49 g/cm^3, 2689 MPa, and 1875.4 MPa, respectively.

Table 5. Concrete mix proportions for concrete blocks used as substrate for FRP

Water (kg/m^3)	150
Cement (kg/m^3)	360
Class F Fly Ash (kg/m^3)	90
Fine Aggregate (kg/m^3)	920
Coarse Aggregate (kg/m^3)	809
Superplasticizer (mL/m^3)	7650
7 day compressive strength (MPa)	34.6 ± 2.2
28 day compressive strength (MPa)	42.6 ± 3.0

5.2.2 Fabrication and Testing

In order to examine the creep of FRP-concrete interface, four different double shear specimens were fabricated and tested under sustained load. The first specimen was fabricated with neat epoxy without CNTs while the other three were fabricated with

138

CNT-epoxy composites with various CNTs loadings. Three percentages of CNTs by weight of epoxy were examined: 0.5, 1.0, and 1.5%. 50.8 × 50.8 × 76.2 mm concrete blocks were cast and cured in water bath for one week. After wet curing, the concrete was dry cured for three weeks in order to enable the shrinkage strains to take place. Steel blocks with dimensions of 50.8 × 50.8 × 12.5 mm were bonded to the ends of the concrete blocks using 105 West System® thick epoxy resin with 206 hardener and cured for one week. The strength of the 105 epoxy system is four times the EPOTUF® 37-127 epoxy system used in the shear joint to avoid any potential failure of the steel block-concrete interface during the creep experiment. In addition to the creep specimens, similar specimen with neat epoxy was fabricated and tested to failure to obtain the ultimate shear strength of the shear joint. Also, single lap shear specimen is fabricated to examine the ultimate strength on the FRP-FRP interface. The single lap shear joint dimensions were 12.7 × 25.4 mm.

The CNTs-epoxy nanocomposites were prepared and cast on 25.4 × 25.4 mm shear joint. 0.71 ± 0.035 mm diameter class VI soda-lime glass beads supplied by Mo-Sci Corporation were used to control the epoxy thickness as recommended by ASTM standards (ASTMD5868, 2008). Glass beads with volume fraction of 0.5% were added to the concrete surface and the CNTs epoxy composites was applied afterwards by syringe pump to minimize the air voids at the shear joint. A pressure of 34 kPa was applied after placing the CFRPs composite over the epoxy shear joint and the excess of epoxy was carefully removed. Figure 99 shows various steps of fabricating the double lap shear specimens. The shear joint was cured for 10 days before applying the sustained load for one month. DEMEC strain gauges supplied by Mayes Instruments, Ltd were installed

139

using a reference bar and dial gage is used to obtain strain measurements during the creep experiment (Figure 100).

(a) Steel blocks attached to concrete substrates

(b) Casting of CNT-epoxy composite on concrete

(c) Placement of CFRP sheet on the shear joint

(d) Curing of epoxy composite under steel weight

Figure 99. Fabrication of double lap shear specimens

The ultimate shear strength test was performed using MTS® Bionix servo hydraulic system (Figure 101). The double shear specimen was loaded to failure by displacement control mode with loading rate of 0.5 mm/minute and stress-strain response was obtained. Figure 102 shows the loading frame of the creep experiments. The frame

140

consists of applying the sustained loads through steel weights. The applied load was measured using load cell (Figure 103-a) and the load level of 934 ± 22 N was maintained. This load level induces shear stress of 724 ± 17 kPa at each shear joint which corresponds to 25% of the ultimate shear strength. A system of steel hooks and chains were used in transferring the load to the double shear specimens to avoid inducing any eccentricities. The creep experiments were performed under controlled environment of relative humidity (RH) of 60% and temperature of 23 °C. Figure 103-b shows the four creep specimens attached to the loading frames.

Figure 100. Reference bar and dial gauge used to install and measure DEMEC points

(a) Ultimate test setup for double lap shear specimen

(a) Ultimate test setup for single lap shear specimen

Figure 101. Creep experiment performed on four specimens
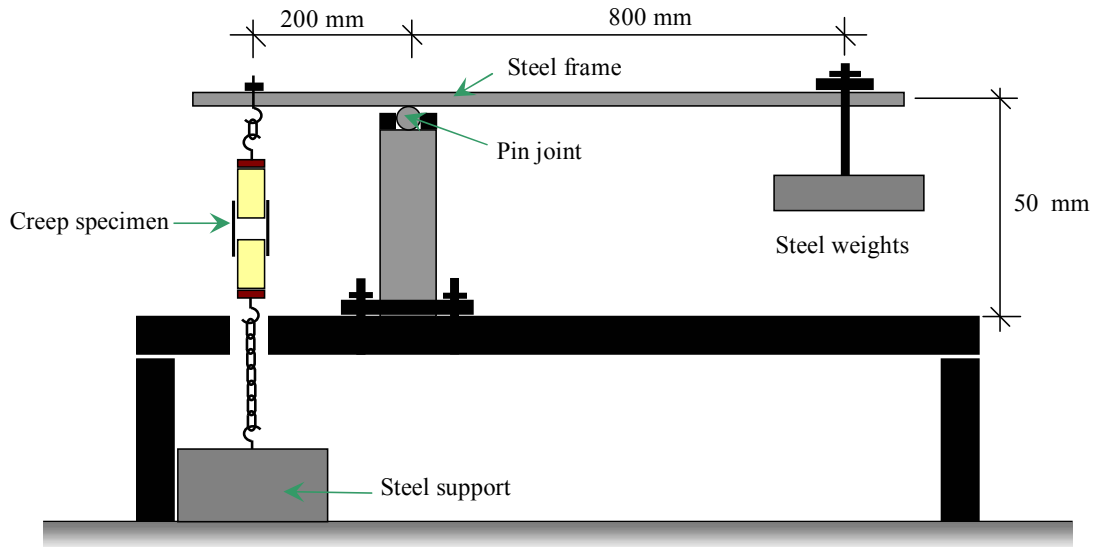
Figure 102. Schematic of creep test setup

(a) Load cell attached to determine creep load   (b) Four creep specimens loaded

Figure 103. Creep experiment performed on four specimens

5.3 Rheological Modeling

Rheological models have been widely used to simulate the behavior of viscoelastic materials such as polymer, concrete, and masonry due to their simplicity and practicality. They provide a tool for understanding the physical phenomena including the instantaneous and time-dependant deformations. In addition, the modularity of rheological models allows development of different models by means of different arrangements and combinations of springs and dashpots. During the last decade, many researchers have used rheological models to describe epoxy adhesives' behavior at the FRP-concrete interface (Ferrier & Hamelin, 2002, Meshgin et al., 2009, Wu & Diab, 2007). In this study, the effect of incorporating MWCNTs into epoxy adhesives is considered. Several rheological models are considered and all but two are ruled out. The effect of MWCNTs is included implicitly in the parameters of the model.

Figure 104 shows some basic rheological models developed to describe the behavior of viscoelastic materials. Maxwell [Figure 104 (a)] and Kelvin [Figure 104 (b)] are two-parameter models which consist of springs and dashpots connected in series and parallel

respectively. The two-parameter models are inefficient in predicting the creep behavior of adhesives because of their lack of simulating some basic phenomena. For example, the Maxwell model fails in simulating a decreased creep strain rate under constant stress while the Kelvin model fails in simulating the instantaneous deformations (Findley et al., 1989). On the other hand, four-parameter models such as Burgers [Figure 104 (g)] are abundant in describing the creep behavior of polymers. Three-parameter models such as Ross [Figure 104 (c)], Modified Maxwell (MM) [Figure 104 (d)], and other models [Figure 104 (e) and Figure 104 (f)] have a sufficient number of parameters to predict the behavior. Models Figure 104 (e) and Figure 104 (f) can be excluded because of their lack of instantaneous deformation. Therefore, two models are considered in this study; Ross [Figure 104 (c)] and Modified Maxwell (MM) [Figure 104 (d)] models. The long-term strain $\varepsilon(t)$ under sustained stress σ_0 for the two models can be described as follows:

$$\varepsilon(t) = \frac{\sigma_0}{R_1} + \frac{\sigma_0}{R_2}\left[1 - \exp\left(\frac{-tR_2}{\mu_2}\right)\right] \text{ for Ross model} \tag{5.5}$$

$$\varepsilon(t) = \frac{\sigma_0}{R_2} - \left(\frac{\sigma_0}{R_2} - \varepsilon_0\right)\exp\left[\frac{-t}{\mu_2\left(1 + R_2/R_1\right)}\right] \text{ for MM model} \tag{5.6}$$

where R_1 and R_2 are elastic moduli coefficients, ε_0 is the instantaneous strain, and μ_2 is the viscosity coefficient. Given the strain formula and by following similar procedures as in section 5.2, the normalized creep compliances are computed as in Eqns. 5.7 and 5.8 [(Findley et al., 1989), Appendix B].

$$J_n(t) = \frac{1}{\varepsilon_0}\left[\frac{\sigma_0}{R_1} + \frac{\sigma_0}{R_2}\left(1 - \exp\left[\frac{-tR_2}{\mu_2}\right]\right)\right] \text{ for Ross model} \tag{5.7}$$

$$J_n(t) = \frac{1}{\varepsilon_0}\left[\frac{\sigma_0}{R_2} - \left(\frac{\sigma_0}{R_2} - \varepsilon_0\right)\exp\left(\frac{-t}{\mu_2\left(1 + R_2/R_1\right)}\right)\right] \text{ for MM model} \tag{5.8}$$

144

In addition, Ross and MM models are evaluated by computing the root mean square prediction error *RMSE* between the predicted and the experimental data (Eqn. 5.9).

$$RMSE = \sqrt{\sum_{i=1}^{N} \frac{\left(J_{ni}^{\exp} - J_{ni}^{\mathrm{pred}}\right)^2}{N}} \tag{5.9}$$

where N is the number of creep data points, $J_{ni}^{\exp}$ is the normalized creep compliance for the ith experimental data point, and J_{ni}^{pred} is the normalized creep compliance for the ith predicted data point. It is important to note that the classical Ross and MM models might be able to simulate creep behavior of neat epoxy, but they cannot represent the significance of MWCNTs on creep of epoxy. Therefore, in order to represent the significance of MWCNTs loadings, we suggest modifying both models to account for the MWCNTs loading (weight fraction) $\alpha = \dfrac{\text{weight of CNTs}}{\text{weight of epoxy}}$. The new Ross and MM models are denoted as MWCNT-Ross and MWCNT-MM respectively. In these models, the elastic moduli coefficients R_1 and R_2 as well as the viscosity coefficient μ_2 are presented as a function of the MWCNTs loading α.

145
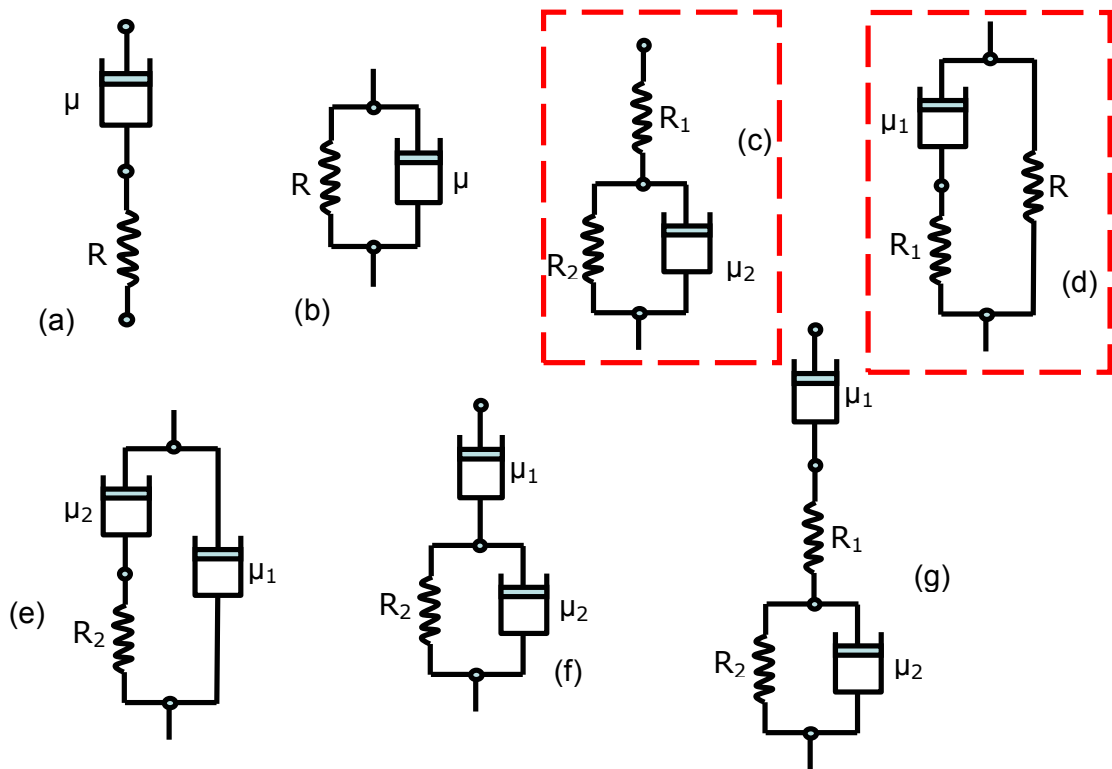
Figure 104. Various combinations of rheological models with (a-b) two parameters (c-f) three parameters and (g) four parameters

5.4 Results and Discussions

5.4.1 Experiments

Figure 105 shows the failure of ultimate shear strength test specimens. It can be noted that the double lap shear test exhibited shear failure in the concrete substrate. Therefore, the ultimate strength obtained using the double shear test is misleading. On the other hand, the single lap shear test, in which the failure occurred at the FRP-FRP interface, is considered more accurate in estimating the ultimate shear strength. This observation is supported by the load-displacement response for the two cases for the same epoxy interfacial area (645.16 mm^2) is plotted as shown in Figure 106. The estimated ultimate strength from the double and single lap shear joints are 2521 and 2822

146

kPa, respectively. A choice was made afterwards for the creep shear stress to be 25 % of the ultimate strength.
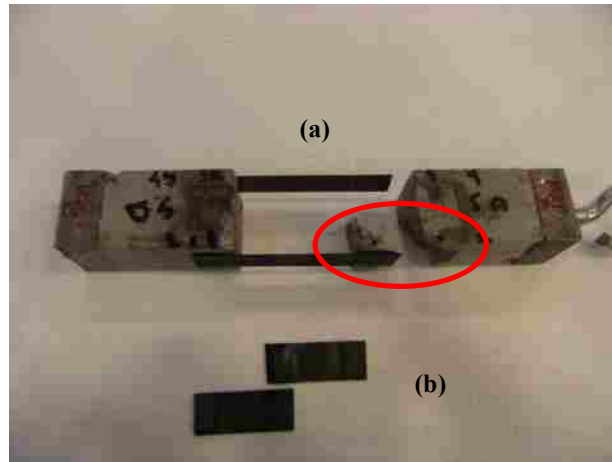
Figure 105. Failure of lap shear joints (a) double lap and (b) single lap
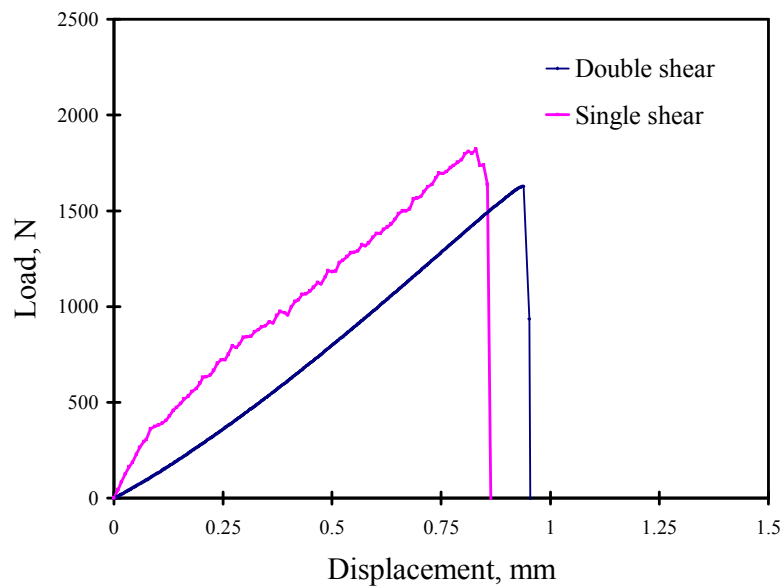
Figure 106. Load displacement responses for ultimate shear tests

The shear strains per one lap shear joint for pristine and functionalized MWCNTs are shown in Figure 107 and Figure 108 respectively. Elastic shear strains of 0.17, 0.12,

147

0.11, 0.20, and 0.21% were exhibited by neat, 0.1, 0.5, 1.0, and 1.5% pristine MWCNTs-epoxy composites respectively. This observation demonstrates that the highest elastic shear modulus was obtained in the case of 0.5% pristine MWCNTs while the lowest was obtained in the 1.5% pristine MWCNTs. In the case of functionalized MWCNTs, the elastic shear strains were 0.18, 0.10, 0.12, and 0.13% for the cases of 0.1, 0.5, 1.0, and 1.5% MWCNTs respectively. The average elastic shear strains in the case of functionalized MWCNTs were less than that of the pristine MWCNTs which indicates higher elastic shear modulus in the functionalized case. Moreover, the shear strains after 1.0 month of monitoring were 0.87, 0.72, 0.57, 1.04, and 1.03% with the addition of 0, 0.1, 0.5, 1.0, and 1.5% pristine MWCNTs respectively. The shear strains for 0.1, 0.5, 1.0, and 1.5% functionaized MWCNTs were 0.42, 0.39, 0.38, and 0.35 % respectively. The shear strains show that the functionalized MWCNTs reduced the shear deformation of the epoxy adhesive at the interface immediately and after one month of loading.

The normalized creep compliances were computed and plotted with time in Figure 109 and Figure 110 for the pristine and functionalized MWCNTs-epoxy nanocomposites. In general, the addition of pristine CNTs had limited effect on the normalized creep compliances as oppose to the functionalized MWCNTs. The normalized creep compliances after one month were 5, 5.61, 5.38, 5.61, and 5.02 for the cases of 0, 0.1, 0.5, 1.0, and 1.5% pristine CNTs respectively. In addition, the normalized creep compliances after one month were 5, 2.31, 3.93, 3, and 2.63 for the cases of 0, 0.1, 0.5, 1.0, and 1.5% functionalized MWCNTs respectively. The case of 0.1% functionalized CNTs had the largest drop in creep compliance among all cases and the creep compliance reduced by 46%. This is attributed to the fact that the low loadings of

CNTs are easier to disperse in epoxy matrix and to obtain a uniform microstructure. As the CNTs content increases, difficulties in dispersion arise due to the formation of CNTs agglomerations. The interfacial bond seem to be a critical parameter in long term shear deformation of adhesives at the interface since the functionalized CNTs significantly outperformed the pristine CNTs (Figure 111). The average increase in normalized creep compliance with pristine CNTs was 8 % while the average decrease was 40 % in the case of functionalized CNTs. It is obvious that functionalized CNTs can reduce creep of epoxy at the FRP-concrete interface significantly.
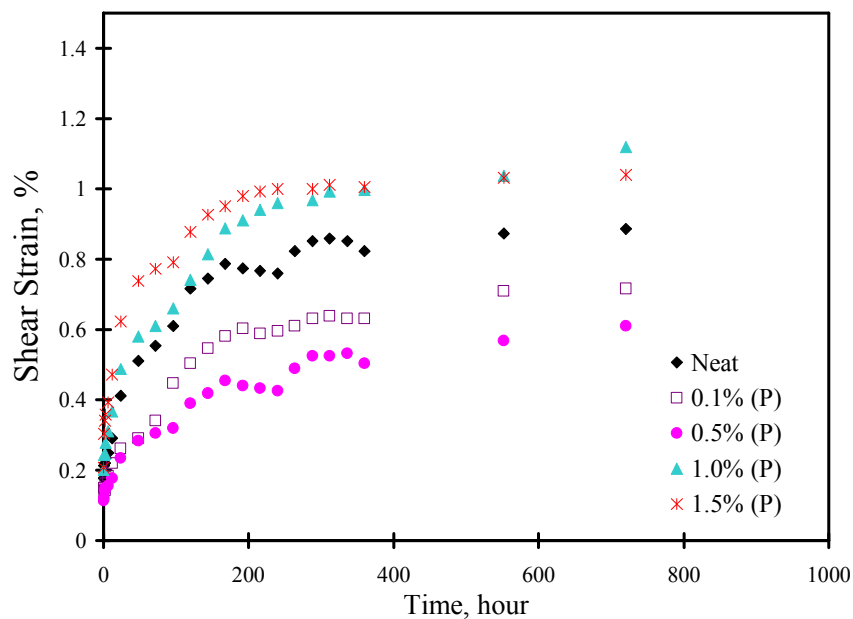
Figure 107. Shear strain of FRP-concrete interface with pristine CNTs percentages

149
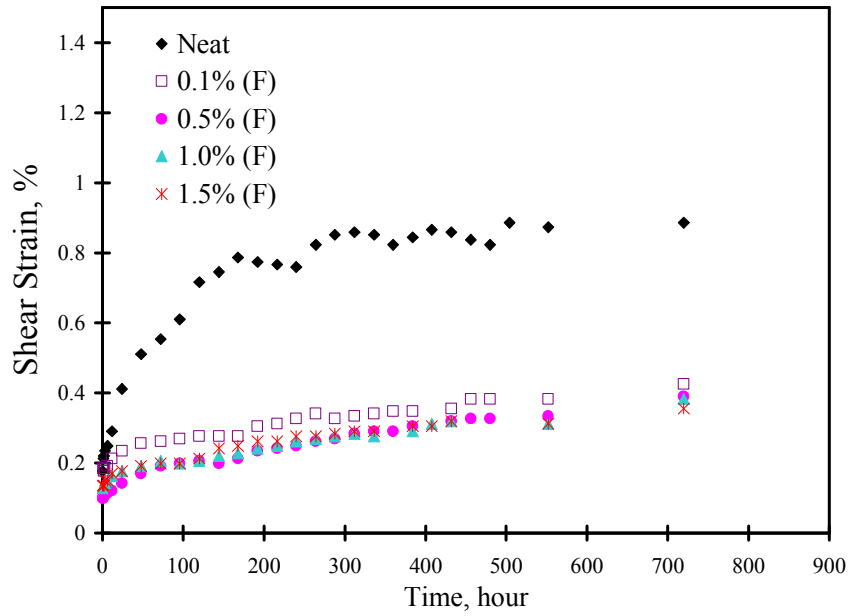
Figure 108. Shear strain of FRP-concrete interface with functionalized CNTs percentages
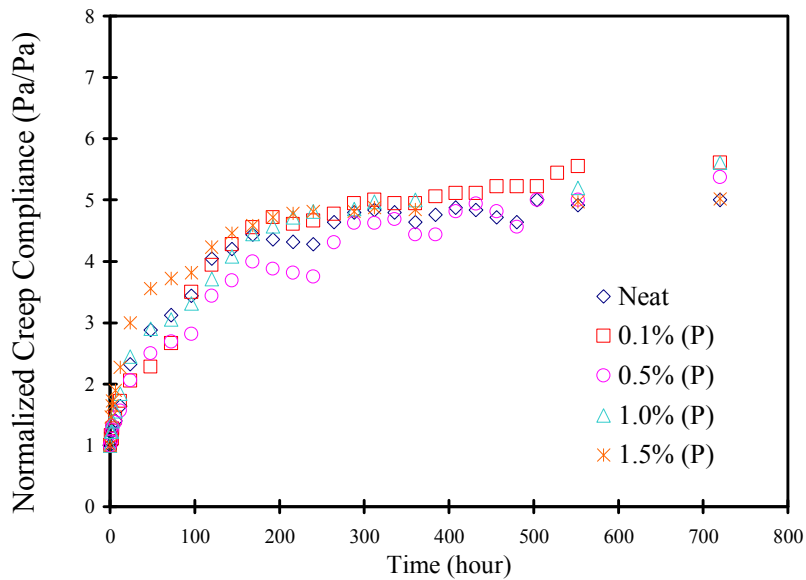
Figure 109. Normalized creep compliance of FRP-concrete interface with pristine CNTs-epoxy nanocomposites

150
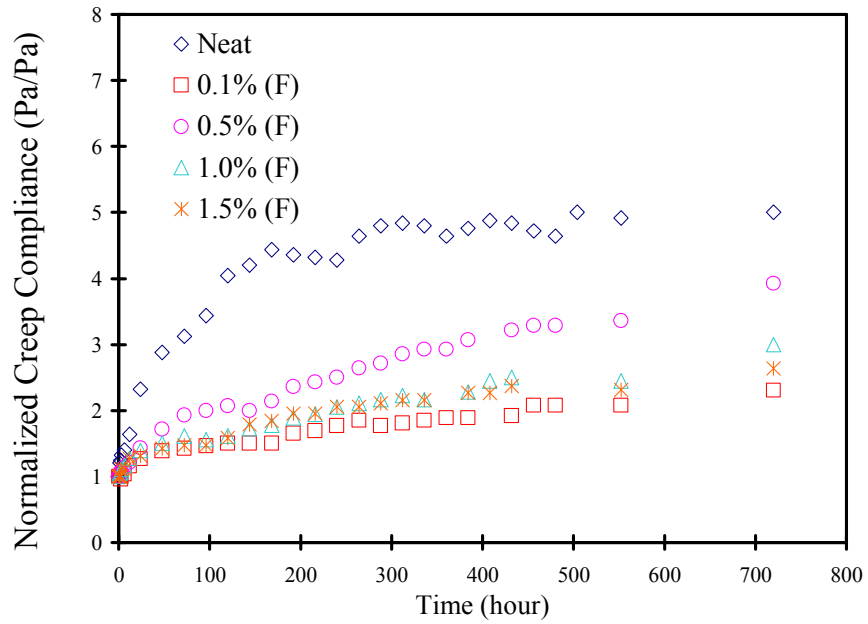
Figure 110. Normalized creep compliance of FRP-concrete interface with

functionalized CNTs-epoxy nanocomposites
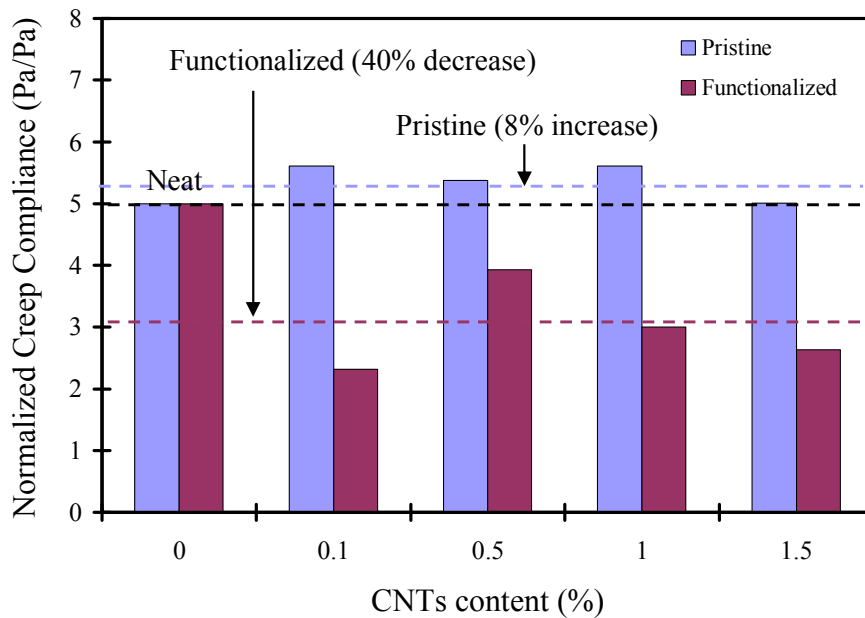
Figure 111. Comparison between the pristine and functionalized CNTs in terms of

normalized creep compliance of FRP-concrete interface

151

5.4.2 Rheological Models

Since there was no significant effect of pristine MWCNTs on the creep behavior of epoxy, only the specimens with functionalized MWCNTs reinforced epoxy nanocomposite were simulated with rheological models. Figure 112 and Figure 113 depict MWCNT-Ross and MWCNT-MM rheological models fitting curves for various functionalized MWCNTs loadings. As shown in the figures, the two models are capable of predicting creep compliance of MWCNTs reinforced epoxy nanocomposite with small *RMSE*. The relatively small *RMSE* values for the two models indicate that three parameters are sufficient in describing the shear creep behavior of functionalized MWCNTS reinforced epoxy nanocomposite at the FRP-concrete interface. The average *RMSEs* for the MWCNT-Ross and MWCNT-MM models were 0.094 and 0.111 respectively. This indicates that MWCNT-Ross model slightly outperformed MWCNT-MM model in predicting shear creep behavior of epoxy at the FRP-concrete interface when functionalized MWCNTSs are incorporated.

Figure 114 and Figure 115 show the effect of various functionalized MWCNTs loadings on MWCNT-Ross and MWCNT-MM models respectively. The elastic moduli for the springs in Figure 114(a) and Figure 115(a) for the two models increased with the addition of the functionalized MWCNTs. However, the shape of the increase differs from each elastic modulus and each model. For instance, the elastic moduli R_1 and R_2 for MWCNT-Ross model varies with the functionalized MWCNTs content according to third-order polynomial functions as shown in Eqns. 9 and 10. On the other hand, the elastic modulus R_1 for MWCNT-MM varies according to second order polynomial function (Eqn. 5.12). Moreover, by separating the neat epoxy $(\alpha = 0)$ data point, it can be

152

noticed that the elastic modulus R_2 varies linearly with the MWCNTs content (Eqn. 5.13).

MWCNT-Ross model

$$R_1 = 639.3\,(\alpha)^3 - 1737.9\,(\alpha)^2 + 1287.6\,(\alpha) + 294.8 \text{ in MPa} \tag{5.10}$$

$$R_2 = 599.2\,(\alpha)^3 - 1579.1\,(\alpha)^2 + 1075.8\,(\alpha) + 144.4 \text{ in MPa} \tag{5.11}$$

MWCNT-MM model

$$R_1 = 135.5\,(\alpha)^2 - 209.3\,(\alpha) + 174.3 \text{ in MPa} \tag{5.12}$$

$$R_2 = \begin{cases} R_2 = 80 \text{ in MPa for } \alpha \leq 0.1 \\ \\ R_2 = 23.95\,(\alpha) + 162.3 \text{ in MPa for } \alpha > 0.1 \end{cases} \tag{5.13}$$

More emphasis is placed on studying the effect of adding functionalized MWCNTs on the viscosity coefficients μ_2 for the dashpot due to their importance on the viscous and long-term behavior of epoxy. In the case of MWCNT-Ross model, the coefficient of viscosity increased in average by 900% due to adding functionalized MWCNTs, while 200% average increase was observed in the case of MWCNT-MM model [Figure 114(b) and Figure 115(b)]. The coefficient of viscosity μ_2 also varied with the loading, α, of the functionalized MWCNTs in the epoxy. Eqns. (5.14) and (5.15) describe the relation as second- and third-order polynomials for the MWCNT-Ross and MWCNT-MM models respectively. From these results, it is obvious that the effect of functionalized MWCNTs on creep of epoxy at the FRP-concrete interfaces can be modeled by means of rheological models. These established relationships between the

153

rheological model parameters and the MWCNTs loading α are useful for numerical analysis of FRP-concrete interface.

MWCNT-Ross model

$$\mu_2 = -99.4\,(\alpha)^2 + 180.5\,(\alpha) + 35.5 \ \text{in GPa.sec} \tag{5.14}$$

MWCNT-MM model

$$\mu_2 = 168.5(\alpha)^3 - 467.3\,(\alpha)^2 + 345.7\,(\alpha) + 63.4 \ \text{in MPa.sec} \tag{5.15}$$

Finally, it is worth noting that an early 2011 quick market survey showed that with the use of large amount of MWCNTs in the production of epoxy adhesives, in the order of metric tons, the price of MWCNTs will have a limited impact on total composite cost. For instance, the cost of adding 0.1-1.0% MWCNTs functionalized MWCNTs to epoxy represents a cost increase of 20-30% of the current epoxy cost. This is believed to be a very small cost given the pronounced effect of functionalized MWCNTs on limiting the creep of epoxy adhesives at the FRP-concrete interface.
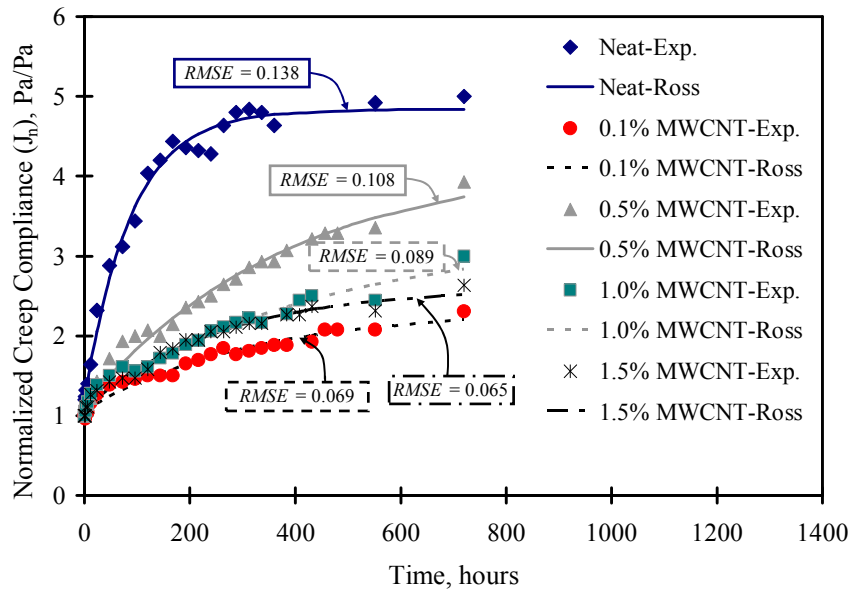
Figure 112. Fitting of normalized creep compliance data for functionalized MWCNTs with Ross model
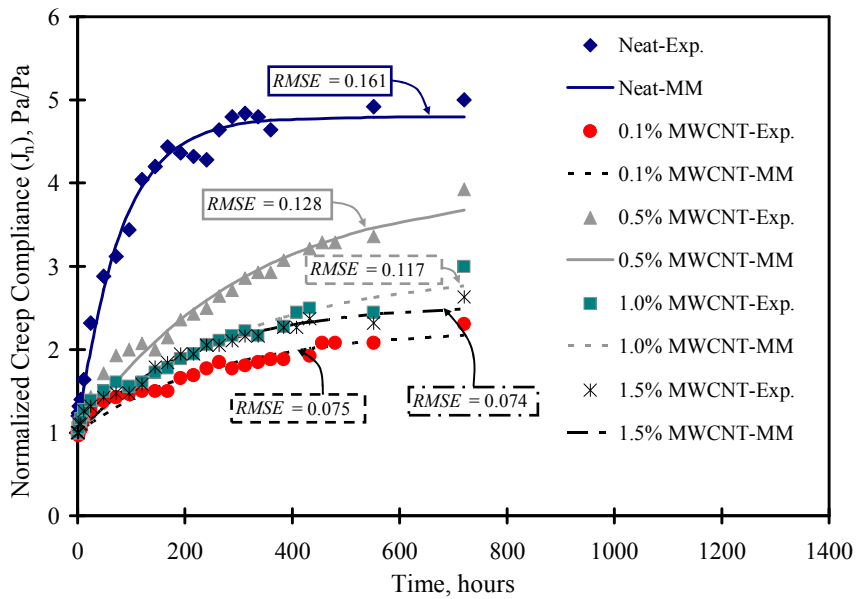
Figure 113. Fitting of normalized creep compliance data for functionalized MWCNTs with Modified Maxwell (MM) model
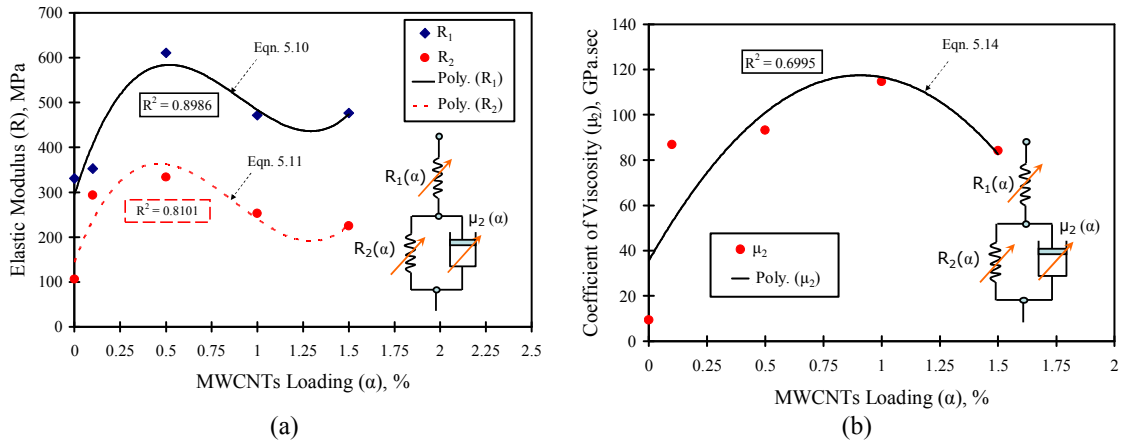
Figure 114. Effect of MWCNTs on MWCNT-Ross model parameters: (a) Elastic Moduli and (b) Viscosity Coefficient
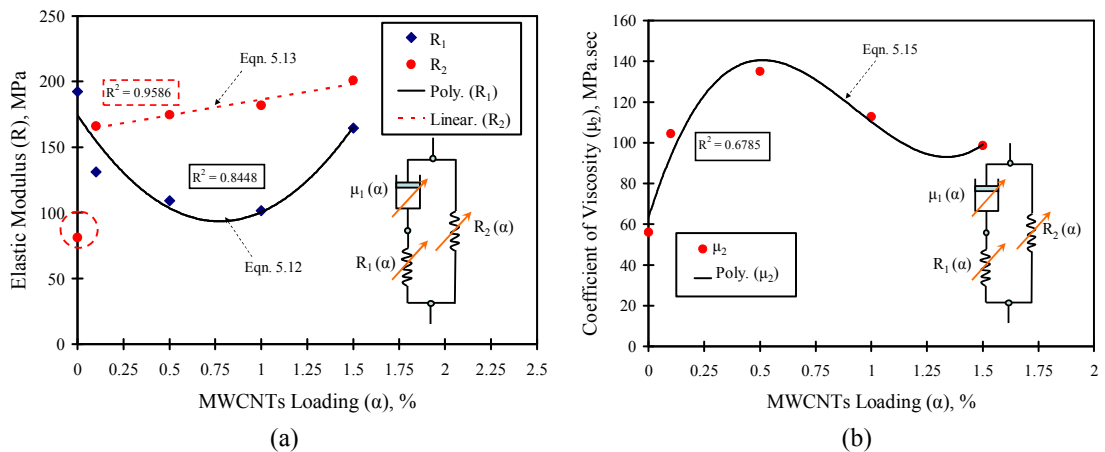
Figure 115. Effect of MWCNTs on MWCNT-MM model parameters: (a) Elastic Moduli and (b) Viscosity Coefficient

5.5   Summary

Creep experiments of FRP-epoxy-concrete interfaces were performed on double lap shear test specimens. The effect of incorporating various contents of pristine and functionalized MWCNTs on creep of epoxy at the concrete-FRP interface is investigated. In general, little to no effect is observed with the use of pristine MWCNTs. However, functionalized MWCNTs were able to limit shear creep of epoxy significantly. The use of

www.manaraa.com

functionalized MWCNTs at the 0.1% level (per weight of epoxy) out-performed all other MWCNTs loadings and resulted in 54% reduction in normalized creep compliance. These observations indicate the importance of chemical functionalization of MWCNTs in reducing shear creep strains of epoxy nanocomposite. In addition, the effect of the functionalized MWCNTs on the creep of adhesives is simulated by rheological modeling. Two modified rheological models are suggested to simulate creep behavior of MWCNTS reinforced epoxy nanocomposite. The functionalized MWCNTs increased the viscosity coefficients significantly. The effect of MWCNTs as described by the suggested models agrees well with experimental results. These rheological models would be beneficial for simulating creep behavior of epoxy in numerical models for FRP-concrete interface under sustained loads. A conference article is published and a journal article is accepted for publication from this work (Soliman *et al.*, 2011c, Soliman *et al.*, 2011a).

CHAPTER 6. CARBON NANOTUBES FOR SHORTENING FRP LAP SPLICE

6.1 Introduction

Lap splices of fiber reinforced polymer (FRP) composites have been widely used while strengthening infrastructures. Adequate lap spli ces are required in order to continuously transfer the load among multiple FRP plies. Some of the situations where splicing composite plates is needed include: 1) the inability to continuously access the structural element on the site; 2) strengthening long spans where the use of single FRP plate is impractical (ASTMD7616/D7616M, 2011); 3) wrapping RC columns or beam-column joints with FRP jackets especially for seismic applications. In a lap splice, the shear strength of the adhesive and the bond strength between the adhesive and the FRP substrate should allow stress transfer among multiple FRP plies in order to avoid premature failure. Therefore, the length of the lap splices or the bonded area is a critical parameter in the strengthening systems (ACI440.2R, 2006). Few studies have investigated the critical length of lap splice for infrastructure applications. (Yang & Nanni, 2002) investigated the fatigue performance of spliced CFRP laminates and purposed appropriate lengths for lap splices for quasi static and fatigue tests. (Dawood et al., 2007) investigated two configurations of double lap joint; square and reverse tapered and recommended using the later type for strengthening steel girders.

Over the last decade, the shear behavior and bond strength of lap splices are examined from three perspectives. The first perspective emphasized in understanding and

158

characterizing the behavior of these joints analytically. For instance, (Markolefas & Papathanassiou, 2009) studied the stress redistribution of elastic-plastic double lap joint under cyclic loading. (Zhao et al., 2011) performed elastic analysis to develop a closed form solution for single lap joints. (Khalili et al., 2008) performed numerical study to investigate the effect of fiber orientation and normal pressure on the behavior of single lap joint. A good review for finite element analysis on lap joints can be found elsewhere (He, 2011). In the second perspective, focus is placed on the geometrical properties of the lap joints. (Oterkus et al., 2006, Vallee & Keller, 2006) investigated the effect of tapered edges and chamfers on the behavior of bonded lap joints respectively. (Fessel et al., 2007) investigated the behavior of wavy and reverse bent joints. (Reis et al., 2007) investigated the effect of adherend rigidity on the behavior of single lap joint. The third group concerned about examining the bond strength of different materials. Many studies were performed to improve the bond strength to metals substrates while few studies are performed to with composite substrates. (Suhr et al., 2005) examined the viscoelastic behavior of single walled CNTs-epoxy nanocomposites through single lap joint test and they found significant improvement in loss modulus. In this study, we report experimental investigation for single and double lap shear test for adhesives bonded to FRP substrate. The main goal is to improve the adhesive bond strength by incorporating nanotubes in the bond line.

159

6.2 Single Lap Joint

6.2.1 Bond Line Fabrication and Test Setup

The single lap shear test was performed according to (ASTMD5868, 2008). This ASTM standard is intended to examine the lap shear adhesion for FRP composites. Two cases were examined for the epoxy. The first case was neat epoxy with no CNTs while the second case was epoxy with 0.5 % pristine CNTs by weight. The specimens were made of two substrates each of 63.5 mm long × 76.2 mm wide × 1.5 mm thick five-plies woven fabric CFRP composites attached together using CNTs-epoxy nanocomposite adhesive lap joint. Five plies were chosen in order to avoid a failure in the adherend substrates. The two parts of CFRP composite were fabricated according to the method described in Chapter 4 and thickened with CFRP tabs at the ends afterwards to account for the tension-gripping zone during the test and to minimize the eccentricity.

The lap surface was 12.7 mm × 12.7 mm prepared by grinding the CFRP composite surface with Grit 80 first coat drywall sand paper. 0.71 mm diameter glass beads, provided by Mo-Sci Corporation, were added to the CFRP lap surface in order to control the CNTs-epoxy composite thickness as recommended by ASTM standard. The dispersion of CNTs in epoxy resin was performed using the methods reported in Chapter 3. The prepared CNTs-epoxy nanocomposite was cast on the lap surface using syringe pump to avoid any formation for voids and the excess of epoxy was carefully removed. A proper pressure was applied using clamps and the CNTs-epoxy nanocomposite was cured for one day. After curing, the CFRP plates were cut into 12.7 mm wide strips. Figure 116 shows the fabrication of lap shear specimens. The specimens were tensioned up to failure using displacement-controlled mode with rate of 1.0 mm/minute. It is important to report

160

that the ASTM standards propose a rate of loading of 12.7 mm/minute, which in this case would fail the fabricated specimens within few seconds. Therefore, the rate of loading of 1.0 mm/minute was used for the tension test according to the (ASTMD3039/D3039M, 2008). Figure 117 shows the test setup for the single lap shear specimens.

(a) Clamping the lap shear joint and the end tabs

(b) Lap shear specimens are marked in strips

(c) Specimens are cut in strips and ready for testing
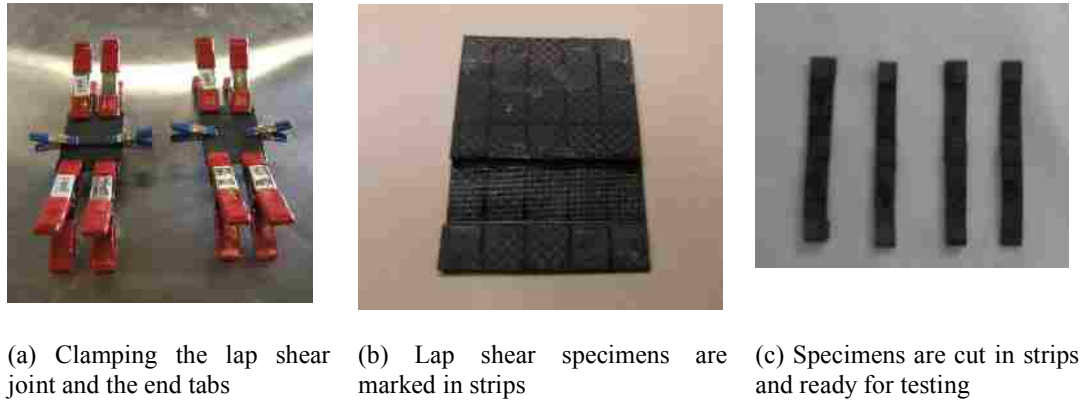
Figure 116. Fabrication of single lap shear test specimens
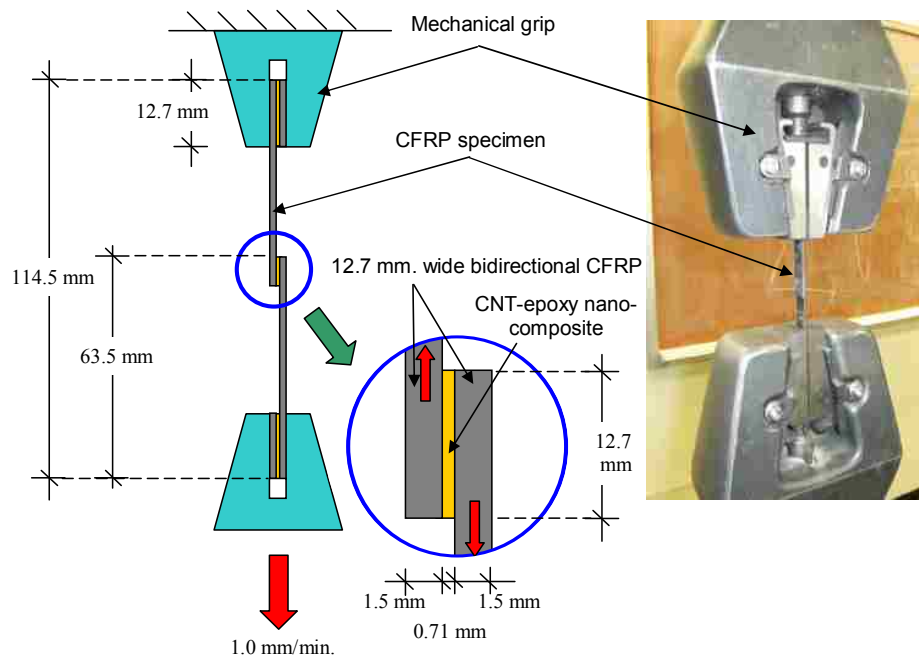
Figure 117. Single lap shear test specimen test setup

6.2.2 Results and Discussion

The stress strain behavior for the two cases is shown in Figure 118. The shear stress τ and shear strain γ are computed as follows:

$$\tau = \frac{P}{b \times l} \tag{6.1}$$

$$\gamma = \frac{\Delta L}{h} \tag{6.2}$$

where P is the applied load, b and l are the width and the length of the lap shear joint, respectively, h is the thickness of the bond line (0.71 mm), and ΔL is the extension in the loading direction. In general, significant enhancement in stress-strain behavior was obtained with the addition of 0.5% pristine CNTs. This enhancement is reflected in various mechanical properties as summarized in Table 6. The highest enhancement was observed in toughness and was equal to 70%. These enhancements are high relative to other tests reported in previous chapters. Although it is an ASTM standards, the stability and accuracy of the single lap shear test in computing the shear properties is questionable and should be analyzed carefully as demonstrated in the following section.

162
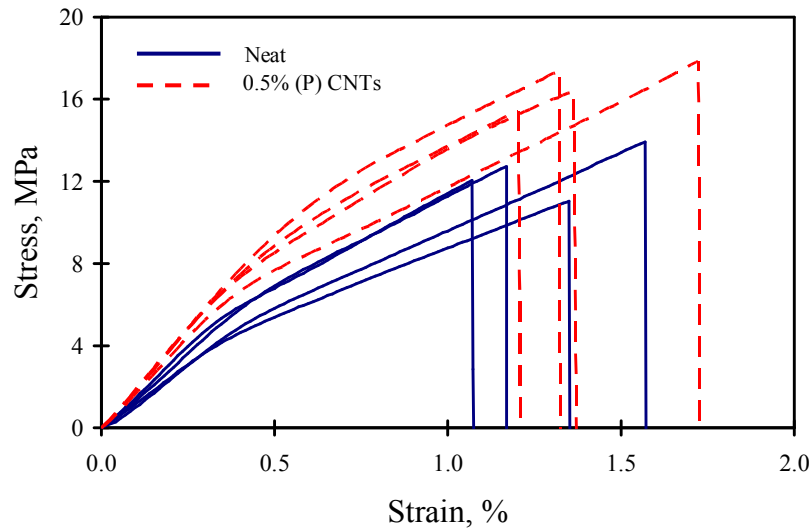
Figure 118. Stress-strain curves of single lap shear test

Table 6. Mechanical properties of single lap shear test

	Shear Strength, MPa	Shear Strain, %	Toughness, kPa	Young's Modulus, MPa
0%	12.4	1.1	77.9	1431.9
0.5% (P) CNTs	16.9	1.3	133.1	1920.3
% Increase	36%	19%	70%	25%

6.2.3 Challenges with the Single Lap Shear Test

There are several proposed ASTM standards for testing single lap shear specimens in order to obtain adhesive shear properties. Examples of these standards are (ASTMD1002, 2010, ASTMD3163, 2008, ASTMD3165, 2007, ASTMD5868, 2008). The major difference between them is the material type of the substrate. Metal, composites, and rigid plastic are used in ASTM D 1002, D 5868, and D 3163

163

respectively. However, all of them share similar challenges when obtaining accurate shear properties. It is observed that single lap shear joints rotate when subjected to uni-axial tension. The rotation of the joint causes bending and peel or cleavage stresses in addition to the pure shear stresses. This observation is reported by (ASTMD4896, 2008, Boone, 2002). In addition, a finite element model exhibited same deformation behavior as shown in Figure 119. In this context, (ASTMD4896, 2008) distinguished between apparent and true shear strengths. Apparent shear strength is the nominal shear stress at failure regardless of the effect of geometry or materials. The true shear strength is the maximum uniform shear stress a material can sustain in the absence of normal stresses. It is important to mention that the shear stress distribution varies across the width and along the length of single lap joint with highest values near the edges due to discontinuity regions.
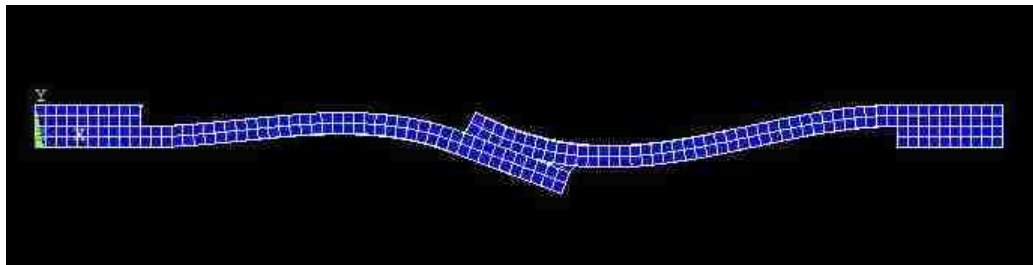
Figure 119. Rotation of single lap shear joint subjected to tension force

Based on other ASTM standards related to shear properties of adhesives, there are two methods to overcome the secondary deformations. First, the use of thick adherend specimens as proposed by (ASTMD3983, 2011, ASTMD5656, 2010) as shown in Figure 120. In this case, the rigidity of the substrates will limit the rotation of the lap joint. The thick adherend sections should be greater than 6.36 mm in thickness as recommended by

164

the two ASTM standards. The second method is to use double lap shear joint for thin adherend as proposed by (ASTMD3528, 2008). The ASTM standard proposes two configurations for the double lap shear test as shown in Figure 121. According to the clearance restriction in our grips system, we propose the second method as more accurate alternative to the single lap shear test in estimating the shear properties of CNTs-epoxy nanocomposites.
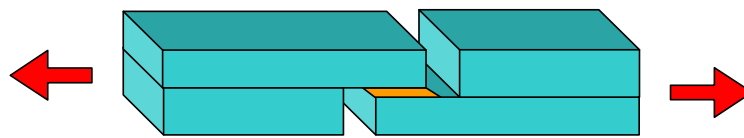
Figure 120. Single lap shear test for thick adherend
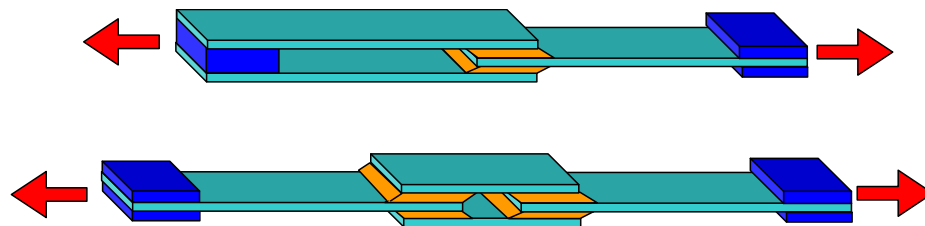
Figure 121. Double lap shear test

6.3   Double Lap Joint

6.3.1   Bond Line Fabrication and Test Setup

The fabrication and testing procedures of the double lap joint specimens were similar to that of the single lap joint specimens. However, the functionalized MWCNTs is used in this case. Three levels of MWCNTs loading are examined: 0.5, 1.0, and 1.5% by weight. Figure 122 shows the fabricated double lap joint specimens. Five specimens were tested for each MWCNTs loading and the statistical analysis using student t-test was perfomed with 95% level of confidence. All specimens are left to cure for 14 days before testing. The lap joint test was performed using MTS® Bionix servo hydraulic system and

165

extensometer is used to record the deformations at the joint (Figure 122). The epoxy shear strain γ for the double lap joint is computed, similar to the single lap joint, using Eqn. (6.2). The shear slip ΔL is measured by the extensometer. However, the shear stress τ acting on the double lap shear joint is half the single lap joint as follows:

$$\tau = P/2A \tag{6.3}$$

where A = the area of the lap joint and P = applied load.

166
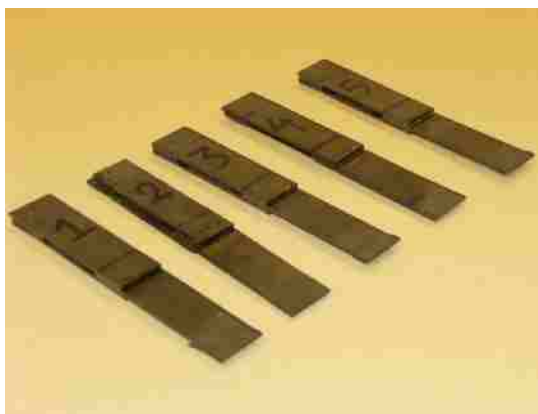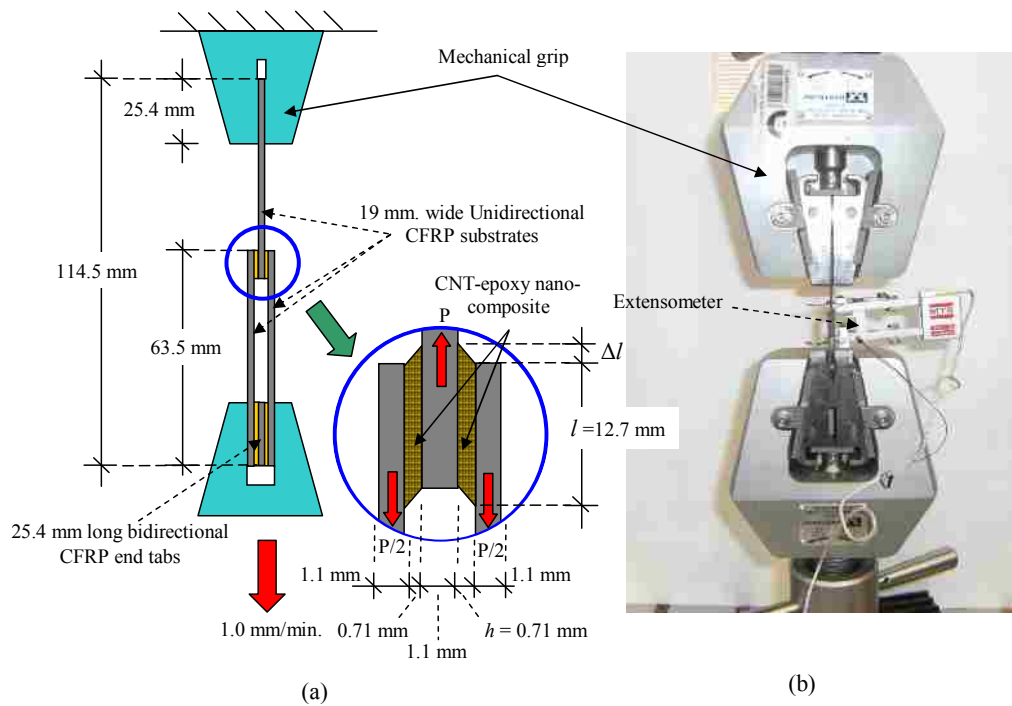
Figure 122. Double lap joint test setup (a) joint dimensions, (b) extensometer attached to the joint, (c) five specimens ready for testing, and (d) close view for the lap joint

167

6.3.2 Results and Discussion

All specimens failed at the epoxy-FRP interface and the two sides of the double lap joint failed simultaneously (Figure 123). The test results are therefore adequate to evaluate the bond strength for various epoxy nanocomposites. The shear stress-strain curves for the lap joint tests are shown in Figure 124. Only two specimens from each COOH-MWCNTs loading are shown however, the statistical analysis is performed in five specimens and its results are reported in Table 7. The figure shows that when neat epoxy or 0.5% MWCNTs is used to splice the FRP strips, the behavior of the joint is linear until failure. However, the lap joints with 1.0 and 1.5% MWCNTs loadings showed nonlinear behavior. The difference in the behavior between the specimens can be attributed to the significance of high MWCNTs contents: 1.0 and 1.5%. High contents of the MWCNTs were able to produce nonlinear shear behavior of FRP lap splice providing enhancement in failure shear strain and energy absorption to failure.

(a) Neat

(b) 1.0% COOH-MWCNTs

(c) Simultaneous Failure

Figure 123. Bond failure for double lap joint specimens

169
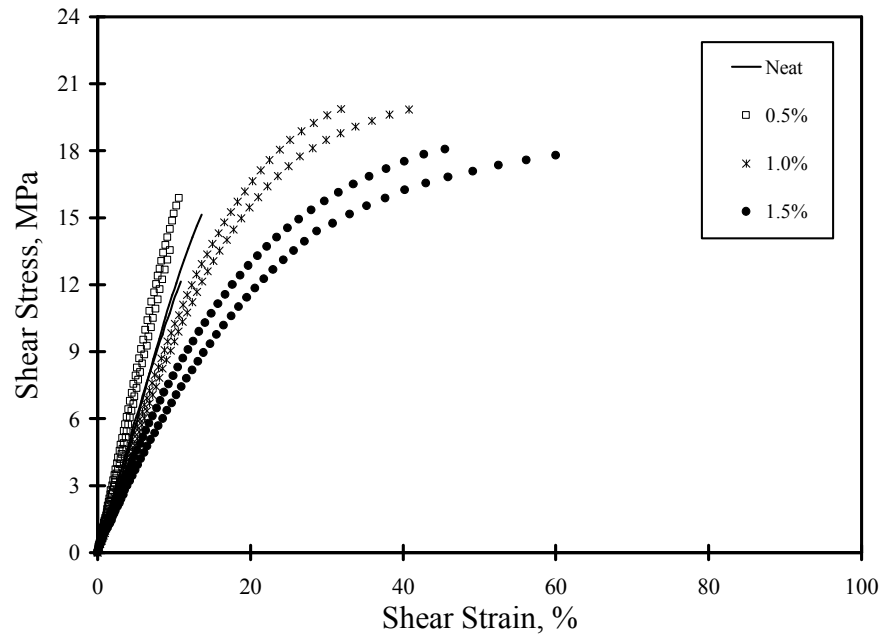
Figure 124. Shear stress strain response of the lap joint with various functionalized MWCNTs loadings

Table 7. Statistical analyses for off-axis test coupons

		Young's modulus, MPa	Bond strength, MPa	Failure strain, %	Toughness, MPa
Neat	Mean	141	11.8	9.21	0.4
	COV, %†	46	33	55	21
0.5% (F*)	Mean	173	14	8.6	0.67
	COV, %	15.9	15.4	6.6	21.2
	% Increase	22	21	-6	67
1.0% (F)	Mean	123	17.6	26.5	3.15
	COV, %	32.9	15.7	53.13	74.59
	% Increase	-12.8	49.1	187.6	693.2
1.5% (F)	Mean	92.71	16.16	42.32	4.9
	COV, %	7.8	15.76	28.6	46.3
	% Increase	-34	36	359	1130

*F: Functionalized, †COV: coefficient of variation, ‡% Increase: percentage of increase

The average shear moduli were 141 ± 65, 173 ± 27, 109 ± 40, and 92 ± 7 MPa for the 0, 0.5, 1.0, and 1.5% MWCNTs-epoxy nanocomposites respectively. The statistical

170

analyses using student t-test indicate that there is no significant statistical difference in the shear moduli among all cases. In addition, the bond strengths for the four cases were 11.8 ± 3.9, 14.3 ± 2.2, 15.1 ± 2.77, and 16.2 ± 2.6 MPa respectively. It was found that there is no statistical difference in the bond strength between the neat and 0.5% MWCNTs cases. However, there is significant difference between the neat epoxy and epoxy nanocomposite incorporating 1.0 or 1.5% MWCNTs. The bond strength increased by 49% and 37% with the addition of 1.0 and 1.5% MWCNTs. Figure 125 shows that the optimal content of the MWCNTs for improving the bond strength is 1.0%. The mechanism of improving the bond strength is attributed to that the CNTs become part of the epoxy microstructure and therefore contribute in shear load carrying capacity and enhance the matrix shear strain at failure.

Furthermore, the failure strains were 9.2, 8.6, 26, and 42% due to the addition of 0, 0.5, 1.0, and 1.5% functionalized MWCNTs respectively. Similar to the bond strength, the statistical analyses showed significant difference in failure strains only between the neat epoxy and the 1.0 or 1.5% MWCNTs cases. The enhancement in failure strains reached 187 and 360% with 1.0 and 1.5% COOH-MWCNTs respectively (Figure 126). A previous experimental study showed that MWCNTs are known to have high tensile elongation of 12% (Yu et al., 2000) or 20% (Tang et al., 2009) which could explain the significant increase in failure strain. Since the toughness can be measured by the area under the stress-strain curve (Dowling, 2007), the enhancement in toughness combines the improvements in both the stress and strain levels. In this study, the enhancement in toughness reached 700 and 1130 % for the case of 1.0 and 1.5% functionalized MWCNTs (Figure 127). Given that the MWCNTs contents are very small, the reported

enhancements are significant and can benefit the industrial applications of the epoxy systems and FRP composites.
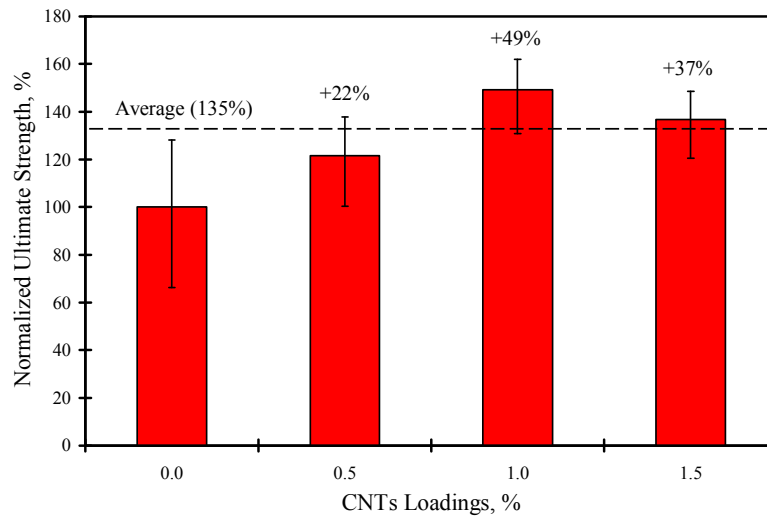
Figure 125. Comparison of shear strength among different COOH-MWCNTs epoxy nanocomposites
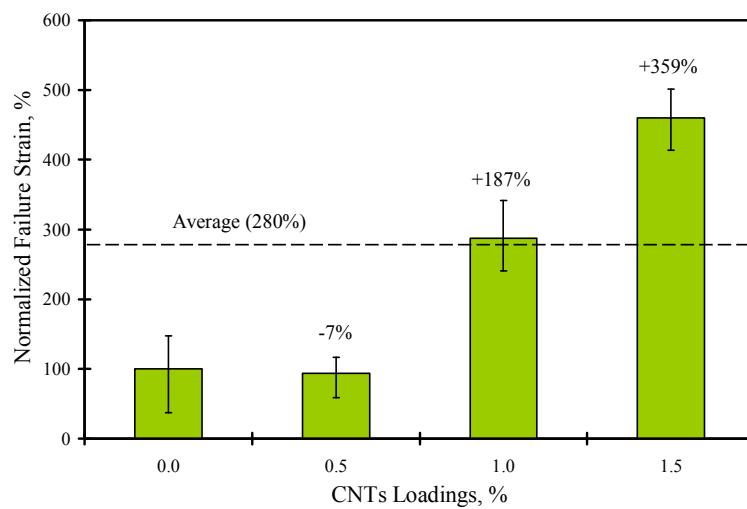
Figure 126. Comparison of failure strain among different COOH-MWCNTs epoxy nanocomposites

172
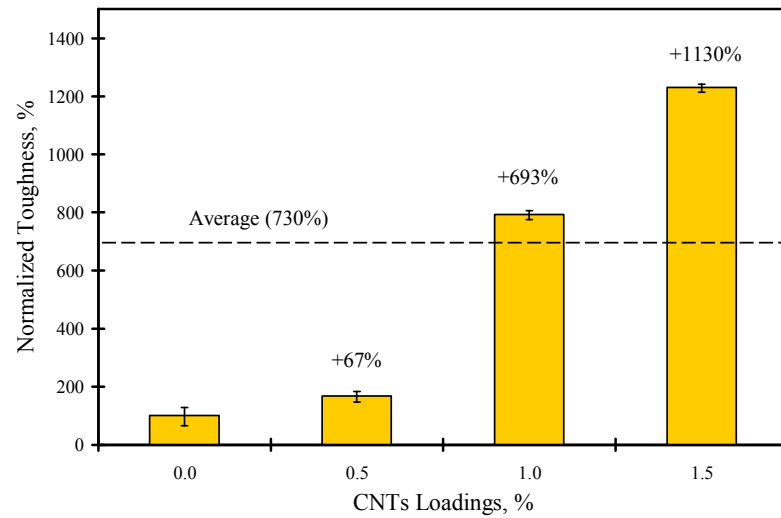
Figure 127. Comparison of the toughness among different COOH-MWCNTs epoxy nanocomposites

Finally, the ACI 440.2R for external strengthening RC structures with FRPs does not provide direct methods for computing lap splice length. The provisions instead refer to the manufacturers' specifications and experimental testing to determine the appropriate lap splice length. This might be attributed to the variability in the FRP and adhesive material properties and/or because there is not enough experimental data to establish consistent design requirements for FRP lap splice length. In general, the lap splice should be long enough to transfer the stresses among the spliced FRP laminates. Since 1% MWCNTs can obviously improve the bond strength in FRP lap splice by about 50%, CNTs can provide promising technique to shorten FRP lap splice length or the bonded area to one half. This technique would be beneficial where the strengthened area is of limited space such as in seismic retrofit of RC beam–column joints. More interestingly is the strain capacity and toughness, which are strongly required for seismic retrofit. The

173

relatively small loadings of CNTs needed to achieve such enhancements in FRP lap splice make it attractive to use CNTs in such applications.

6.4   Summary

Single and double lap joint tests for FRP composite substrates were performed to examine the performance of epoxy adhesive with carbon nanotubes. The results for single lap joint test were inconsistent because of the rotation of the joint which causes normal stresses. For the double lap joint test, three loadings of functionalized MWCNTs were examined and compared with the neat epoxy case; 0.5, 1.0, and 1.5% by wt. The experiments showed a significant nonlinearity in the stress-strain response of FRP lap splices incorporating CNTs. The use of MWCNTs results in enhancing the bond strength by 50% with 1.0% MWCNTs, Furthermore, enhancements in shear strain capacity and toughness reached about 700 and 1,100% respectively with 1.5% CNTs. The results suggest that CNTs can be used in shortening FRP lap splices or for enhancing energy absorption of FRP lap splices used in seismic retrofit of beam-column joints.

CHAPTER 7.   INTERLAMINAR FRACTURE TOUGHNESS OF WOVEN CARBON FABRIC COMPOSITES REINFORCED BY MWCNTS

7.1   Introduction

The double cantilever beam (DCB) test involves the determination of the opening mode-I interlaminar critical energy release rate (G_{Ic}). This test has been widely used to characterize the delamination failure of polymer matrix composites (PMC). It is well known that delamination has been one of the major limiting factors for composite design. The delamination is usually initiated due to transverse, cyclic loads or thermal stresses. In many occasions, delamination can form during the composites lay-up fabrication process (Adams *et al.*, 2003). The DCB delamination occurs due to interlaminar fracture of composites and therefore, it can be used to examine fracture toughness of the resin matrix.

Previous research associated with DCB fracture toughness of PMC includes experimental, analytical and numerical investigations. Experimentally, DCB have been used to examine different types of PMCs including unidirectional, multi-directional, trans-laminar reinforced and woven fabric composites (Alif *et al.*, 1997, Nicholls & Gallagher, 1983, Robinson & Song, 1992, Shi *et al.*, 1993, Tamuzs et al., 2003). Previous research showed that the use of tougher resins (known as thermoplastic interleaves) would increase the fracture toughness significantly. The thickness of the resin film has a significant effect on the fracture toughness (Ozdil & Carlsson, 1992). Crack growth of

vulcanized natural rubber is also examined using modified DCB (South *et al.*, 2002). The main objective from this study is to examine the effect of incorporating various loadings of functionalized MWCNTs on the fracture toughness of the woven fabric composite. This Chapter is divided into two main sections. In the first section, the experimental investigation is presented while a finite element (FE) model is developed and discussed in the second section.

7.2   Experimental Details

7.2.1   Test Setup

The DCB specimens dimensions and test setup is shown in Figure 128. The test is performed according to (ASTMD5528, 2007). The test specimen consists of 3.6 mm thick 12-layer composite plate with release film inserted at the mid thickness. The carbon fabrics are impregnated with various loadings of MWCNTs-epoxy nanocomposite. The length of the insert (32 mm) is considered as the initial crack or delamination length a_o. Once the load is applied in a displacement controlled mode with rate of 0.5 mm/minute, the load P, the opening displacement δ, and delamination length *a* are recorded by the MTS$^®$ load cell, contact extensometer, and in-situ optical microscope respectively. The function of the piano hinge is to maintain the loading direction normal to the crack plane throughout the test so that no significant shear stress is developed at the interface plan and thus mode II crack propagation would not occur.

176
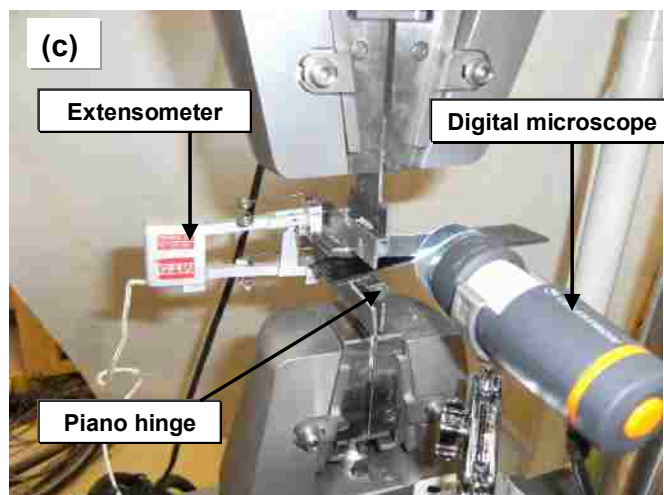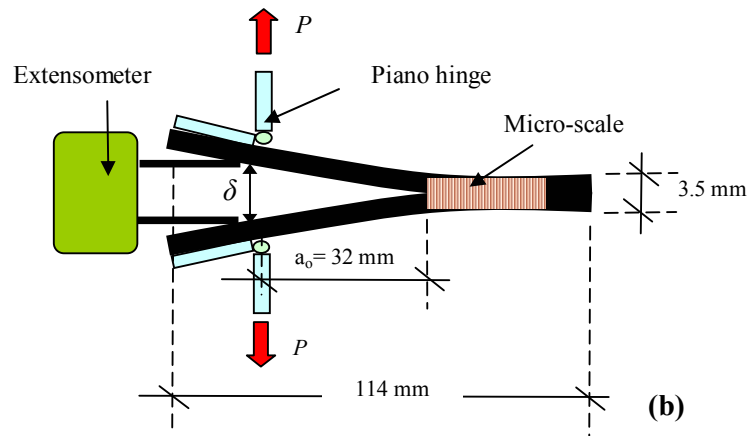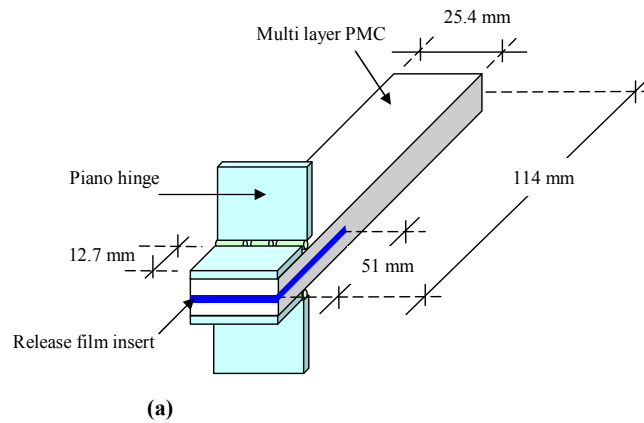
Figure 128. Test setup of DCB (a) dimensions, (b) schematic for deformed specimen, and (c) in-situ optical microscope used to record delamination length

Schematic of the load-displacement response for DCB is shown in Figure 129-(a). The onset of delamination can be determined by the onset of curve non-linearity. It can also be determined visually using the microscope. The mode I critical energy release rate, G_{Ic}, can be computed using modified beam theory (MBT) as given in Eqn 7.1. The MBT assumes that linear elastic fracture mechanics (LEFM) applies because the size of the fracture process zone is much less than the thickness of the specimens. A schematic of the resistance curve (R-curve) for composites is depicted in [Figure 129-(b)]. As the displacement increases, the delamination grow until steady-state growth is obtained. The steady-state delamination growth corresponds to constant critical energy release rate.

$$G_{Ic} = \frac{3P\delta}{2b(a + \Delta)} \tag{7.1}$$

where P is the applied load, b is the specimen width, a is the delamination or crack length, δ is the opening displacement in DCB test, and Δ is a correction for the delamination length.
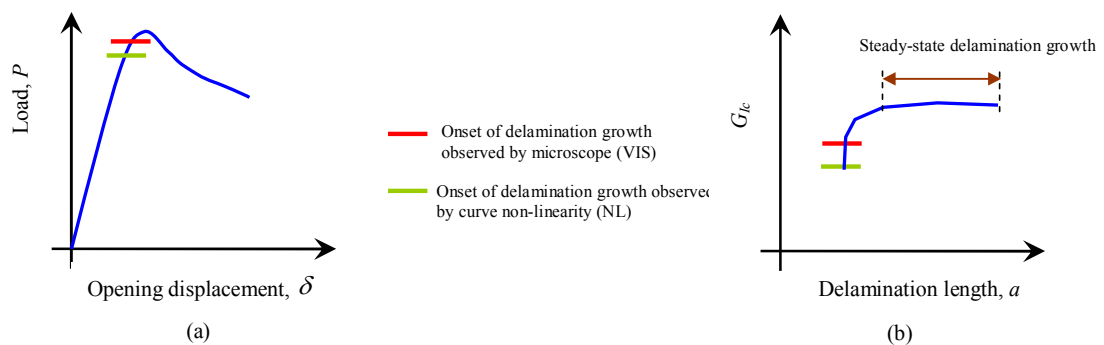
Figure 129. Schematic representation showing delamination behavior (a) Load-displacement response, and (b) R-curve

178

7.2.2   Results and Discussion

Three loadings of MWCNTs are examined in addition to the neat epoxy composite: 0.5%, 1.0%, and 1.5% by wt. Three specimens were tested for each MWCNTs loading level and two specimens for each MWCNTs loading are presented. It is important to report is that the thickness of the composite slightly increases as the MWCNTs loadings increases. For instance, the average thicknesses were 3.47, 3.58, 3.71, 3.80 mm for 0, 0.5, 1.0, and 1.5% MWCNTs-epoxy FRP composites respectively. The increase in thickness approached 10% with the addition of 1.5%. This increase is attributed to the increase in the viscosity of the epoxy nanocomposite. Based on Eqn 7.1, this slight change is expected to affect the stiffness of the specimens and have limited or no effect on the fracture toughness.

Figure 130, Figure 132, Figure 134, and Figure 136 present microscopic images for the crack (delamination) tip for 0, 0.5, 1.0, and 1.5% MWCNTs at various steps during the test. The corresponding load-displacement responses are depicted in Figure 131, Figure 133, Figure 135, and Figure 137. Each figure presents the results of two specimens for the same MWCNTs loading. In these figures, point (a) represents approximately the onset of delamination growth observed by load-displacement curve non-linearity (NL). In addition, point (b) represents the onset of delamination growth observed by microscope (VIS). Table 8 reports the mean load P, mean displacement δ, and their product for NL and VIS points between composites with various MWCNTs loadings. The load-displacement product, P.δ, is the critical parameter in delamination growth because it represents energy that is directly proportional to G_{Ic} according to Eqn 7.1. The initial critical energy release rate is calculated from the NL data. The table

179

shows that P.δ product for NL and VIS slightly increase as the MWCNTs loading increases. With the addition of 1.5% MWCNTs, the limited increase in P.δ product approaches 18% and 29% for the NL and VIS, respectively. This increase in P.δ indicates that the initial critical energy release rate increases as the MWCNTs loadings increases as shown in Table 8. The increase in the initial energy release rate approaches 18% with the addition of 1.5% MWCNTs. However, the increase in initial energy release rate is limited when compared to the maximum energy release rate. A comparison between the load-displacement curves of FRP composites with various MWCNTs is depicted in Figure 145. The figure shows that there is apparent change in the stiffness of composite specimens due to the differences in thickness. The thickness difference is attributed to the addition of MWCNTs, which results in an increase of the nanocomposites viscosity. In addition, the figure shows that there is increase in the peak force and the corresponding displacement with the addition of MWCNTs. This increase is expected to affect the fracture toughness of the FRP composites as explained below.

Table 8. Comparison between various MWCNTs loading in terms of onset of delamination growth

	NL*			VIS§			
	δ (mm)	P (N)	P.δ (N.mm)	δ (mm)	P (N)	P.δ (N.mm)	G_{Ic} (kJ/mm^2)
Neat	5.74	55.6	319	7.32	67.6	498	0.65
0.5%-MWCNTs	5.16	61.0	315	7.20	77.8	561	0.62
1.0%-MWCNTs	5.69	63.7	363	8.00	80.6	649	0.75
1.5%-MWCNTs	5.50	68.5	377	7.44	86.3	642	0.77

*NL: Onset of delamination growth observed by load-displacement curve non linearity
§VIS: the onset of delamination growth observed by microscope

The resistance curve (R-curve) shows the critical energy release rate G_{Ic} as a function of delamination length (a) in Figure 138. The critical energy release rate is computed according to Eqn 7.1. The data obtained from each MWCNTs loading is predicted using polynomial fit for three specimens and the maximum critical energy release rate are compared in Figure 139. It is obvious that there is a significant effect of adding MWCNTs on the mode I critical energy release rate G_{Ic} of the woven fabric composites. As the MWCNTs loading increases, critical energy release rate increases. The highest enhancement in critical energy release rate approached 160% with the addition of 1.5% MWCNTs. The enhancements are attributed to the ability of functionalized MWCNTs to enhance the tensile strength of the epoxy resin by bridging the micro and nano cracks in the epoxy matrix. As a result, the pull out or rupture of the

181

MWCNTs provide a mechanism of energy consumption at the crack tip that enables increasing the critical energy release rate. Functionalization plays an important role in the pull out strength of the functionalized MWCNTs when compared to pristine MWCNTs. Further studies at the microscale will be needed to examine which is the dominant mechanism and its relation to MWCNTs length, diameter, and surface treatment.

Furthermore, it is noted that the addition of MWCNTs have an effect for the profile of the R-curve. In case of FRP composites with neat epoxy, the critical energy release rate tends to approach a steady state limit as explained earlier in Figure 129. This profile justifies the use of LEFM for predicting fracture toughness where the epoxy at the interface behaves in a brittle fashion during the delamination growth. On the other hand, the FRP with MWCNTs epoxy nanocomposites does not approach a clear steady state limit for the critical energy release rate. In particular, the critical energy release rate tends to increase with the increase of delamination growth therefore; the R-curve becomes non-linear. This observation can be further understood by comparing the values of the initial and the maximum critical energy release rates as shown in Figure 139. The slight change in the initial critical release energy rate is attributed to that the epoxy governs the initial delamination growth. As the crack propagates, the critical energy release rate increases proportional to the content of the MWCNTs. For instance, the increase in the critical energy release rate was 77% with the use of neat epoxy while the increase approached 182, 193, and 290% with the addition of 0.5, 1.0, and 1.5% MWCNTs. The difference in the increase of the critical energy release rate confirms the bridging effect of the MWCNTs. As the content of the MWCNTs increases, the bridging effect increases and the energy consumed to propagate the crack increases. The two observations raise a

182

question regarding the applicability of LEFM when MWCNTs are incorporated. The profile of the R-curves with MWCNTs suggest that the deformations and the energy consumption at the crack tip can be accurately predicted if quasi brittle fracture mechanics (QBFM) or elastic plastic fracture mechanics (EPFM) is considered.

(i) Specimen-1   (ii) Specimen-2
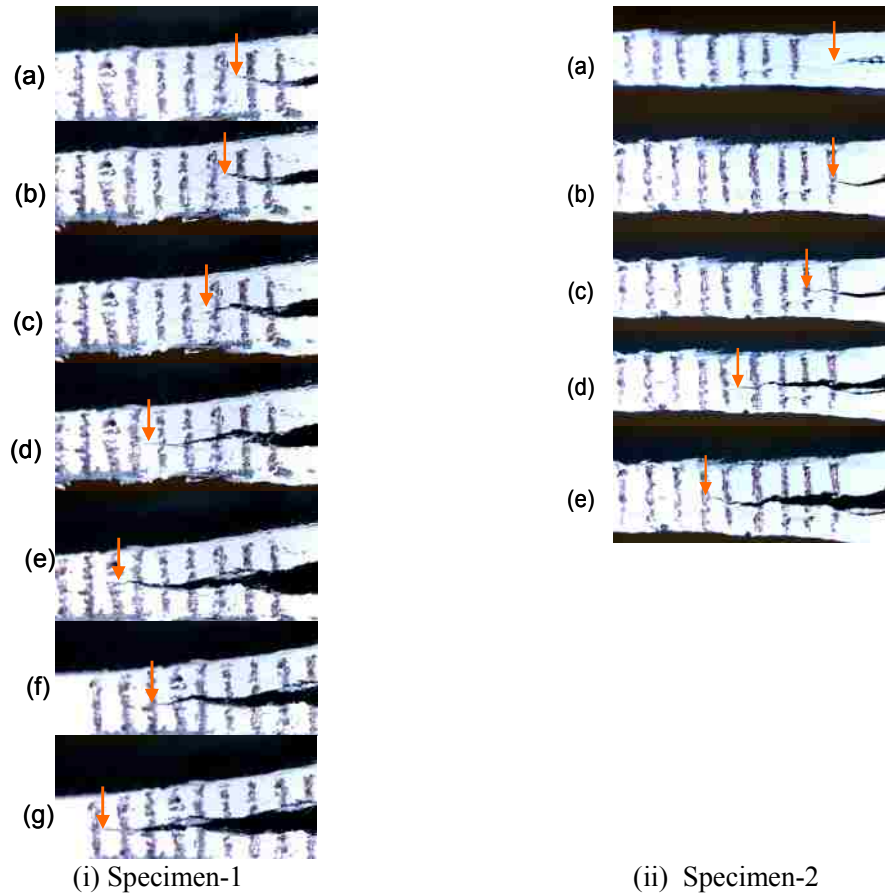
Figure 130. Crack propagation for neat-epoxy FRP composites
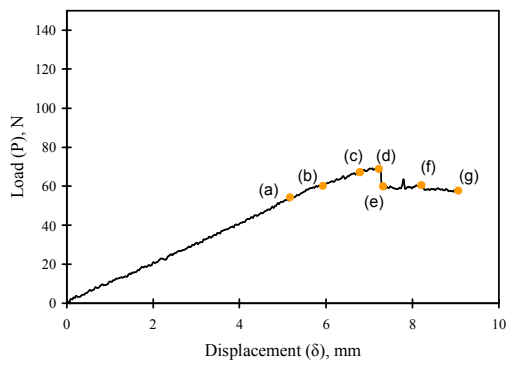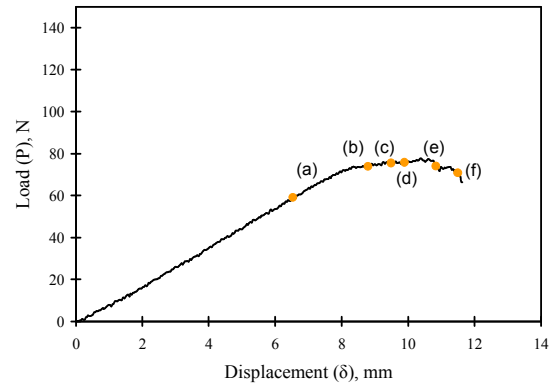
(i) Specimen-1   (ii) Specimen-2

Figure 131. Load-displacement responses for the neat-epoxy FRP composites
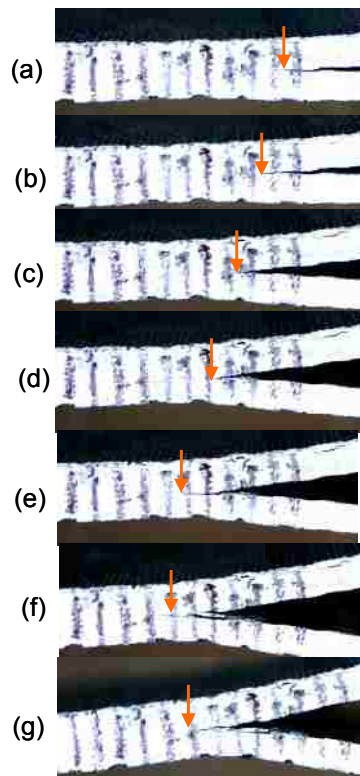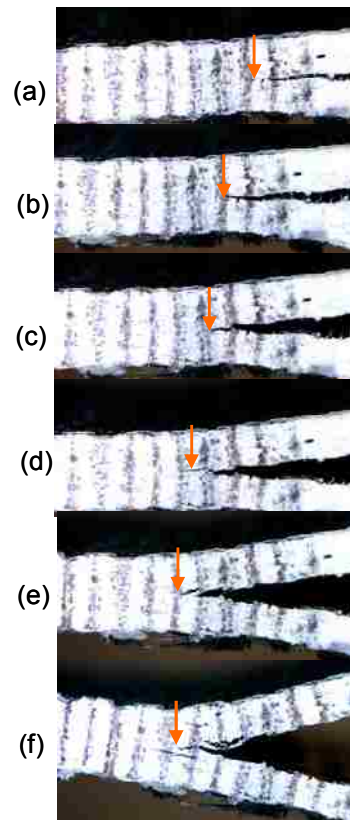
(i) Specimen-1   (ii) Specimen-2

Figure 132. Crack propagation for the 0.5% COOH-MWCNTs-epoxy FRP

composites

184
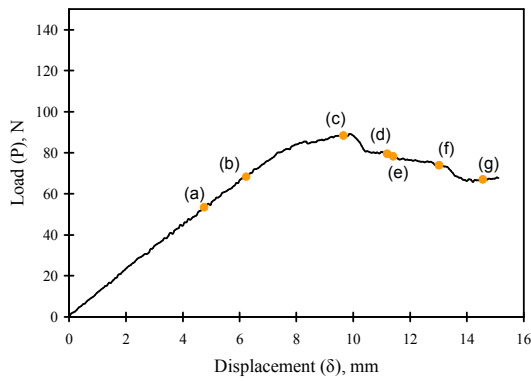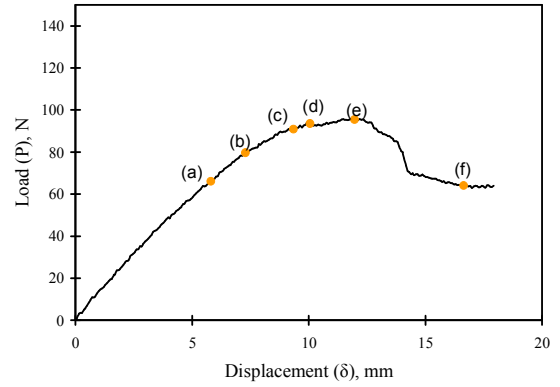
(i) Specimen-1   (ii) Specimen-2

Figure 133. Load-displacement responses for the 0.5% COOH-MWCNTs-epoxy
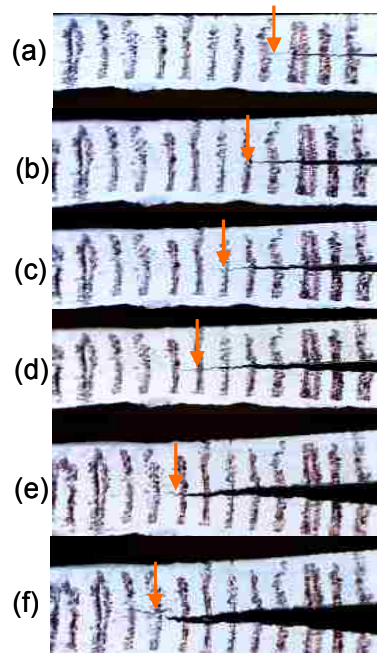
FRP composites
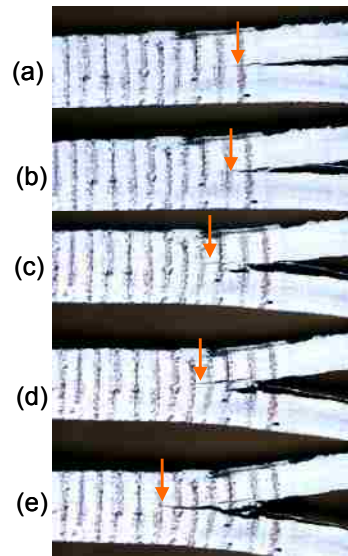
(i) Specimen-1   (ii) Specimen-2

Figure 134. Crack propagation for the 1.0% COOH-MWCNTs-epoxy FRP

composites

(i) Specimen-1   (ii) Specimen-2
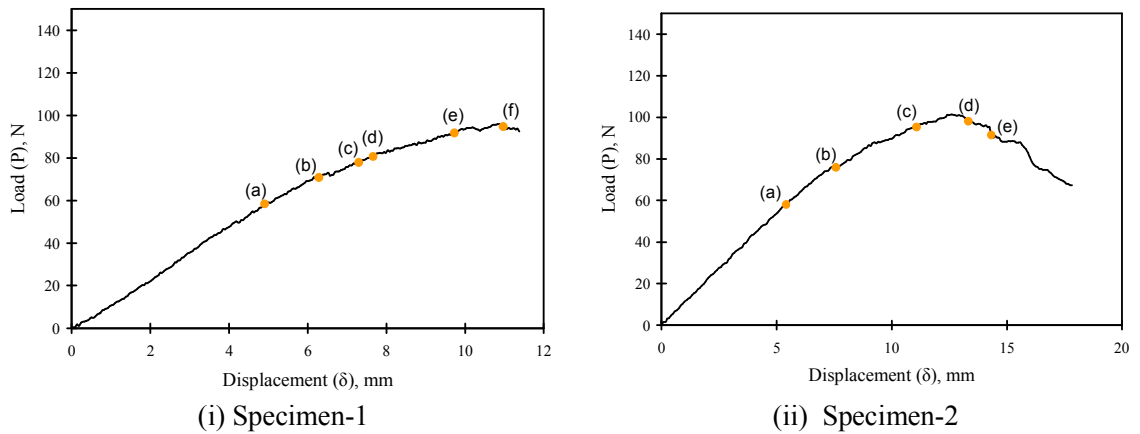
Figure 135. Load-displacement responses for the 1.0% COOH-MWCNTs-epoxy

FRP composites

(i) Specimen-1   (ii) Specimen-2
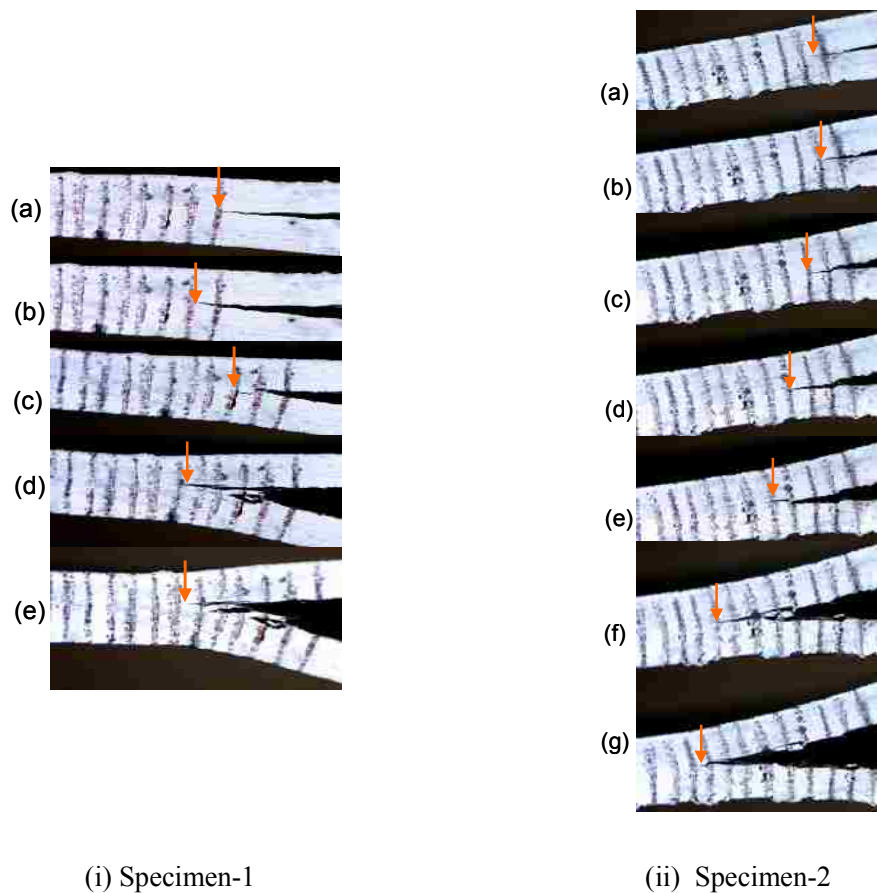
Figure 136. Crack propagation for the 1.5% COOH-MWCNTs-epoxy FRP

composites

186

(i) Specimen-1   (ii) Specimen-2
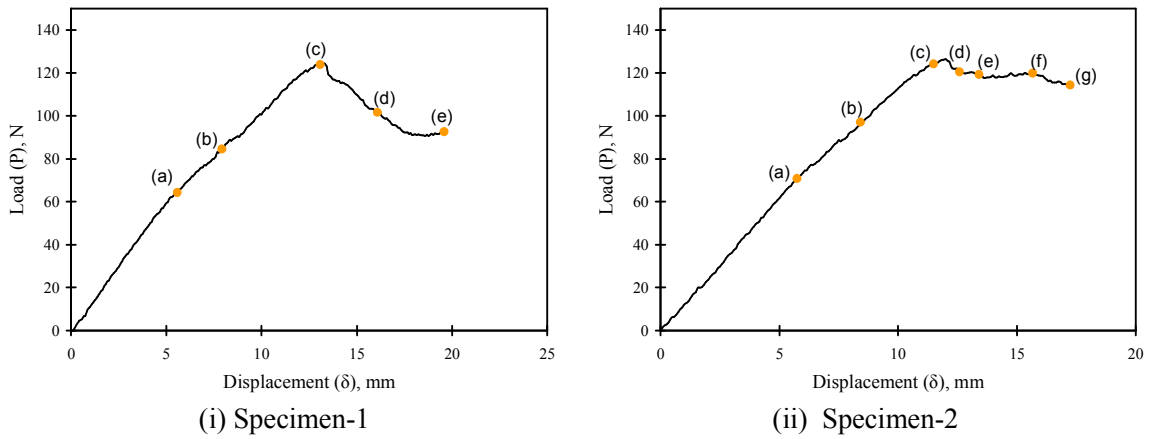
Figure 137. Load-displacement responses for the 1.5% COOH-MWCNTs-epoxy

FRP composites
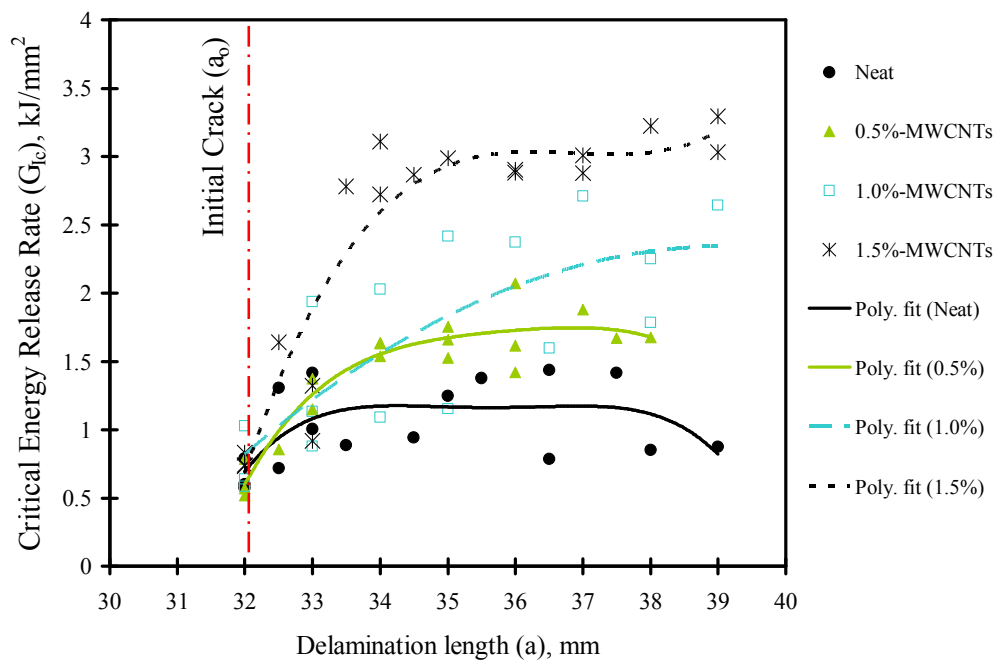
Figure 138. Resistance curve (R-curve) for various MWCNTs loadings
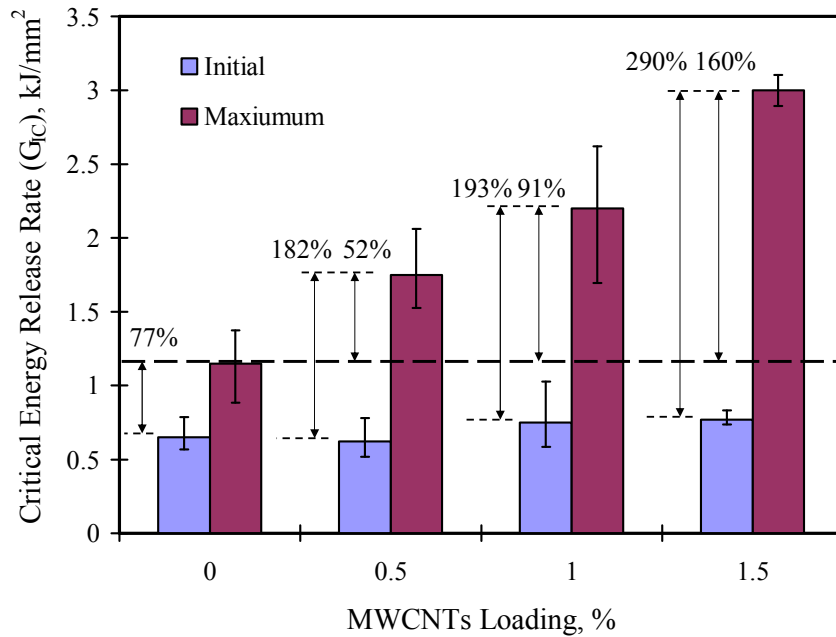
Figure 139. Comparison for the critical energy release rate corresponding to 6 mm delamination growth

It is observed that a flexure failure occurs to some DCB specimens after the delamination grow for few millimeters (Figure 140). The main cause of a flexure failure is the thickness of the FRP composite cantilevers. The thinner the specimens, the lower the flexure rigidity and the earlier the flexure failure would occur. This is because as the delamination grows, the lever arm for the two cantilevers increases and the bending moment at the crack tip increases. Once flexure failure occurs, the load remains constant as shown in Figure 133 (ii). The important point is to approach the steady state critical energy release rate before flexure failure occurs. ASTM D 5528 recommends testing 3 to 5 mm thick composites. However, this suggestion is based on the unidirectional FRP composites where the flexure rigidity is usually higher than that of the woven fabric

composites. The average thickness of the composite specimens in this study was about 3.6 mm and it was enough to reach the stead-state delamination growth as explained later.

Figure 140. Flexure failure of DCB specimens

7.3   Finite Element Simulation

7.3.1   Model Details

The DCB specimens were modeled using finite element (FE) package ANSYS®. The main purpose of the FE model is to extract more information about the stresses and deformations of the epoxy adhesives at the interface. The models are also used to better understand the effect of incorporating the MWCNTs on the governing stress-displacement relationship and fracture toughness at the interface. For that purpose, two different relationships are examined in this study after (Alfano & Crisfield, 2001, Xu & Needleman, 1994). The former relationship represents an exponential behavior while the latter one represents a bilinear behavior. The model dimensions are similar to the experimental specimens as shown in Figure 141.

189

SOLID 45-layered elements are assigned to the composite substrates. The carbon fiber composite cantilevers are assumed linear elastic with modulus of elasticity and poisson's ratio of 35 GPa and 0.30 respectively. The boundary conditions are depicted in Figure 141. A pinned support is assigned to the bottom cantilever at a distance of 12.5 mm from the left end and a vertical displacement of 20 mm is applied to the top cantilever at the same vertical plan. This boundary condition simulates the piano hinge, which allows free rotation of the composite structure and avoids introducing shear stresses at the interface to prevent mode II delamination growth.

In order to reduce the computation time, the model was divided into three regions along its length. The first region, 51 mm long, is the initial delamination created in the experiment by using a release film insert. In this region, no interaction between the top and bottom cantilevers is defined. The element size in this region is relatively coarse (2.5 mm). The second region, 20 mm long, is the region where delamination would occur during the simulation. The length of that region was chosen larger than the maximum delamination length observed in the experiment. In addition, a fine mesh with small the element size of 0.5 mm is used to obtain accurate simulation for the delamination growth. In the second region, the cohesive zone material (CZM) model is defined between the top and bottom cantilevers after the two models explained later. The third region, 39 mm long, represents the remaining part of the specimens where no delamination is expected to occur according to the experiment as a result of the applied displacement. Therefore, the top and bottom cantilevers are rigidly bonded at the third region. The element size for this region is chosen relatively large (4 mm) for its insignificance on the simulation.

190

In general, there are two relationships required to completely define the cohesive relationship at the interface: the normal traction-opening displacement and the shear stress-slip relationships. In the case of exponential model, INTER 205 elements are assigned at the second region on the interface. In the case of bilinear behavior, contact pair (Contact 174 & Target 170 elements) is used to represent the second region at the interface. A major difference between the exponential and bilinear models is that the normal traction and shear stress relationships are coupled in the case of exponential approach with interface elements. This means that the shear slip affects the normal traction relationship and vise versa. The coupling, although is not of interest in the DCB tests, is more realistic than the uncoupled relationship. On the other hand, in the bilinear approach with contact elements, the two relationships are uncoupled which implies that the shear slip does not affect the normal traction relationship. The exponential normal traction T_n-opening displacement δ_n relationship follows Eq. 7.2 and presented in Figure 142 (a) after (Xu & Needleman, 1994).

$$T_n = e.\sigma_{max}\Delta_n.e^{-\Delta_n}.e^{-\Delta_t^2} \tag{7.2}$$

where σ_{max} is the maximum normal traction, $\Delta_n = \dfrac{\delta_n}{\overline{\delta_n}}$ is the normalized opening displacement, $\overline{\delta_n}$ is the opening displacement corresponds to the maximum normal traction, $\Delta_t = \dfrac{\delta_t}{\overline{\delta_t}}$ is the normalized shear slip, and δ_t is the shear slip. Since the shear stresses are minimized at the interface in the DCB test, the normalized shear slip Δ_t would approach zero. It is also important to mention that in ANSYS®, there are two input

191

parameters that characterize the exponential relationship. The characteristic parameters are the maximum traction $\sigma_{\max}$ and its corresponding displacement $\overline{\delta_n}$. The fracture energy release rate or critical energy release rate G_{Ic} represents the area under the normal traction-opening displacement T_n - δ_n relationship and can be obtained by Eqn. 7.3.

$$G_{Ic} = e.\sigma_{\max}\overline{\delta_n} \tag{7.3}$$

On the other hand, the normal traction-opening displacement T_n - δ_n relationship in the bilinear model is computed from Eqn. 7.4 and depicted in Figure 142 (b) after (Alfano & Crisfield, 2001).

$$T_n = K_n\delta_n\left(1-d_n\right) \tag{7.4}$$

where K_n is the normal contact stiffness and d_n is debonding parameter. The later changes from 0 to 1.0 based on the damage intensity and it can be computed as follows:

$$d_n \begin{cases} = 0 & \text{if } T_n \leq \sigma_{\max} \\[2ex] = \left(\dfrac{\delta_n - \overline{\delta_n}}{\delta_n}\right)\left(\dfrac{\delta_n^c}{\delta_n^c - \overline{\delta_n}}\right) & \text{if } T_n \leq \sigma_{\max} \\[2ex] = 1.0 & \text{if } T_n \leq \sigma_{\max} \end{cases} \tag{7.5}$$

where $\sigma_{\max}$ is the maximum normal traction, δ_n is opening displacement, $\overline{\delta_n}$ is opening displacement corresponds to the maximum normal traction, and δ_n^c is the opening displacement at the completion of the debonding. It is worth reporting that one of the advantages of using the debonding parameter d_n is that once damage occurs beyond the

192

elastic limit ($\sigma_{max}, \overline{\delta_n}$), the contact stiffness reduces accordingly. Three characteristic

parameters are required to completely define the bilinear relationship. They are either

($\sigma_{max}, G_{Ic}, K_n$) or ($\sigma_{max}, \delta_n^c, K_n$). The critical energy release rate G_{Ic} represents the area

under the normal traction-opening displacement T_n - δ_n relationship and can be obtained

by Eqn. 7.6.

$$G_{Ic} = \frac{1}{2}\sigma_{max}\delta_n^c \qquad (7.6)$$
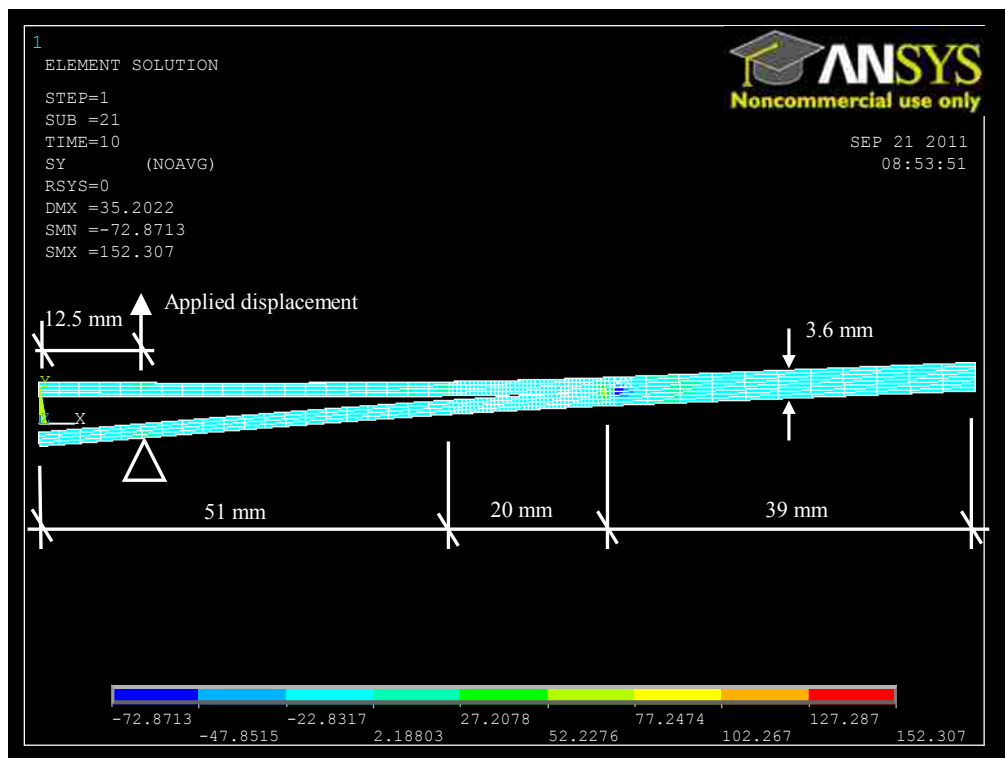
Figure 141. Finite element model for DCB test

(a) Exponential (b) Bilinear
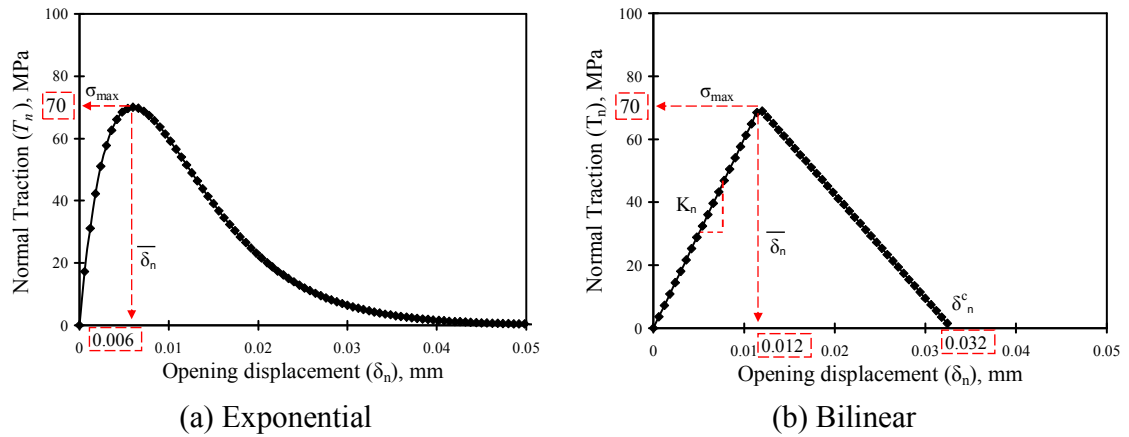
Figure 142. The governing normal traction-opening displacement - relationship at the interface

The two models are evaluated based on the experimental results obtained for the neat epoxy FRP composite. The delamination growth behavior is evaluated based on the load-displacement P-δ relationship, the load-delamination length P-a, and on the displacement-delamination length δ-a. The former relationship is critical for the global response of the DCB specimens while the latter is critical for the delamination growth. In the FE simulation, it is assumed that the maximum normal traction σ_{max} equals to the tensile strength of the neat epoxy (70 MPa). In addition, the critical energy release rate G_{Ic} is obtained directly from the maximum energy release rate obtained experimentally as shown in Figure 143. Given the aforementioned assumptions, the opening displacement $\overline{\delta_n}$ corresponds to the maximum normal traction and the opening displacement at the completion of the debonding δ_n^c are obtained for the exponential and bilinear models using Eqns. 7.3 and 7.6, respectively. Furthermore, the contact stiffness K_n of the bilinear model is altered to fit the global load-displacement response of DCB specimen.

194
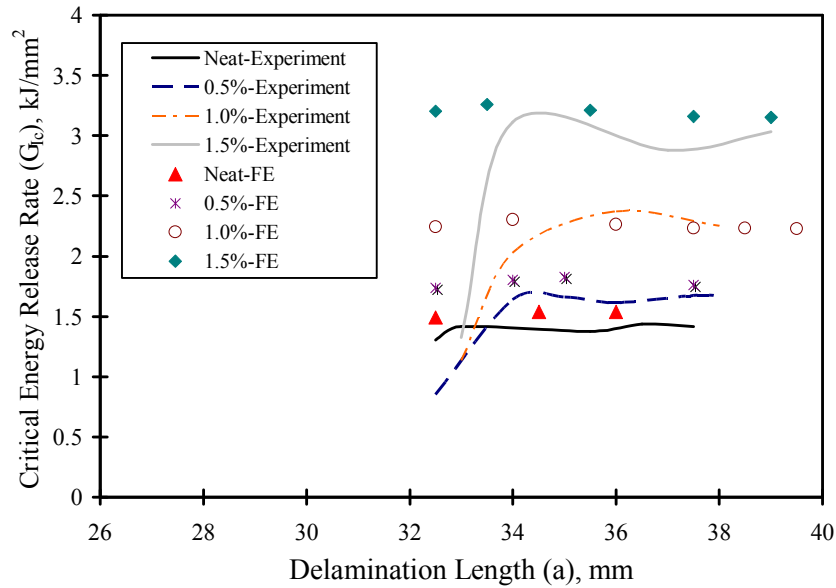
Figure 143. R-curves for experimental and numerical delamination growth for FRP composites reinforced by different MWCNTs loadings

7.3.2 Results and Discussion

Similar to the experimental tests, Figure 144 shows the delamination growth for the exponential and bilinear models. The figure shows contour plots for vertical normal stresses, which cause the crack propagation. The crack tip is determined adjacent to the tensile stress singularity. The crack images is used later to compare the delamination growth obtained from FE models with that of the experimental results. Figure 145 shows a comparison of the load-displacement responses for the neat epoxy FRP composites between the numerical and experimental investigations. The figure shows that the bilinear model overestimates the load P by 28%. On the other hand, the exponential model accurately estimates the load-displacement response. These observations are further verified in Figure 146, which represents the delamination growth as a function of the load

195

P [Figure 146 (a)] and displacement δ [Figure 146 (b)]. Figure 146 (b) shows that the bilinear model overestimates the displacements associated with the delamination growth. The overestimation in the load and displacement with the use of bilinear might be attributed to the use of contact elements. It is known that contact elements experience difficulties in convergence when penetration is considered. The region behind the crack tip usually exhibits large compressive stresses due to the curvature of the two cantilevers as observed from the contour plots in Figure 144. This compressive stresses would cause penetration to occur between the two cantilevers. In general, the exponential model with interface elements shows more accurate prediction for the delamination growth behavior than the bilinear model using contact elements.

196
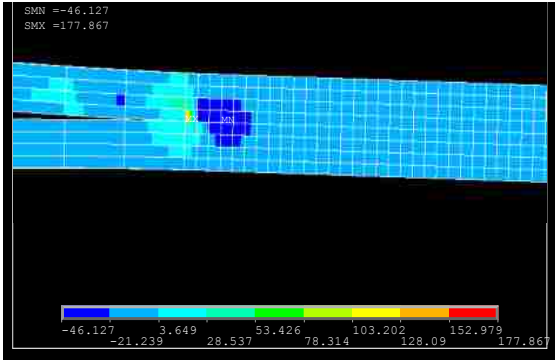
(a) P = 71 N, δ = 8 mm, a = 32 mm
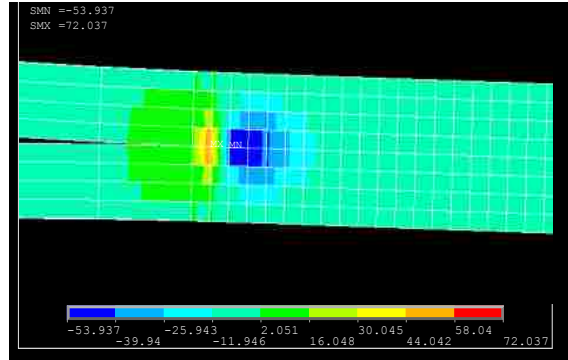
(e) P = 73 N, δ = 8 mm, a = 32 mm
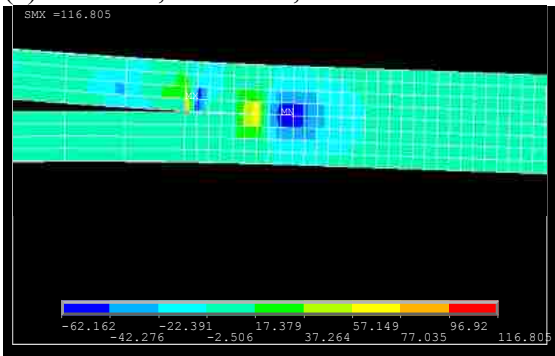
(b) P = 79 N, δ = 9.33 mm, a = 32.5 mm
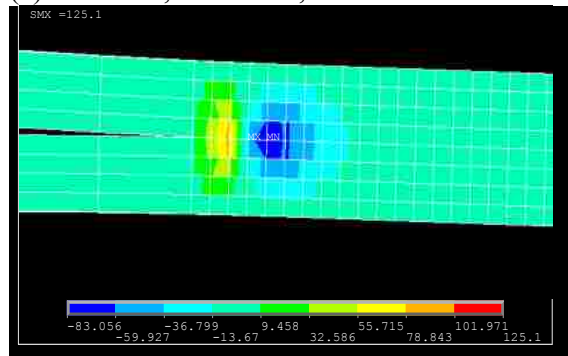
(f) P = 90.8 N, δ = 10.67 mm, a = 33 mm
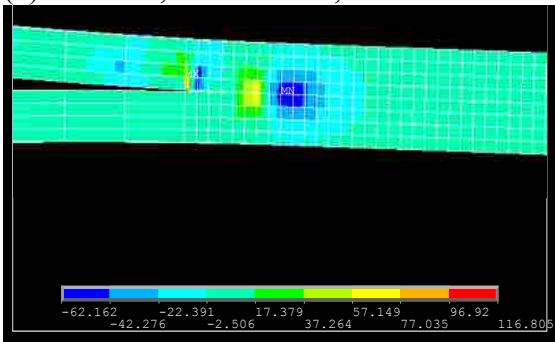
(c) P= 76 N, δ = 10.67 mm, a = 34.5 mm
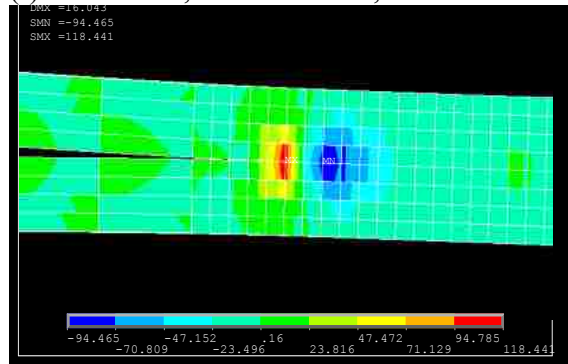
(g) P = 91.57 N, δ = 12.19 mm, a = 34.5 mm
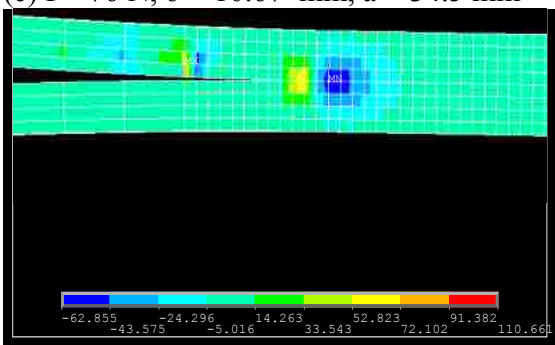
(d) P= 72.6 N, δ = 11.67 mm, a = 36 mm
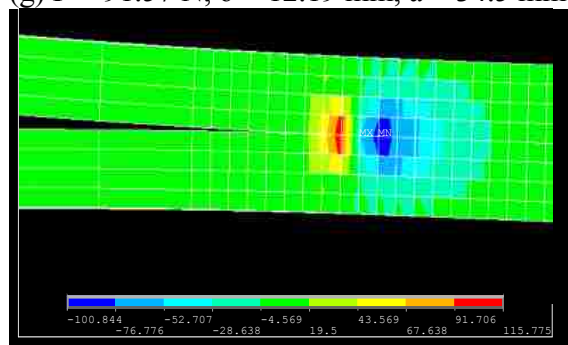
(h) P= 92.49 N, δ = 12.92 mm, a = 36 mm

Figure 144. Delamination growth for (a-d) exponential and (e-h) bilinear models

197
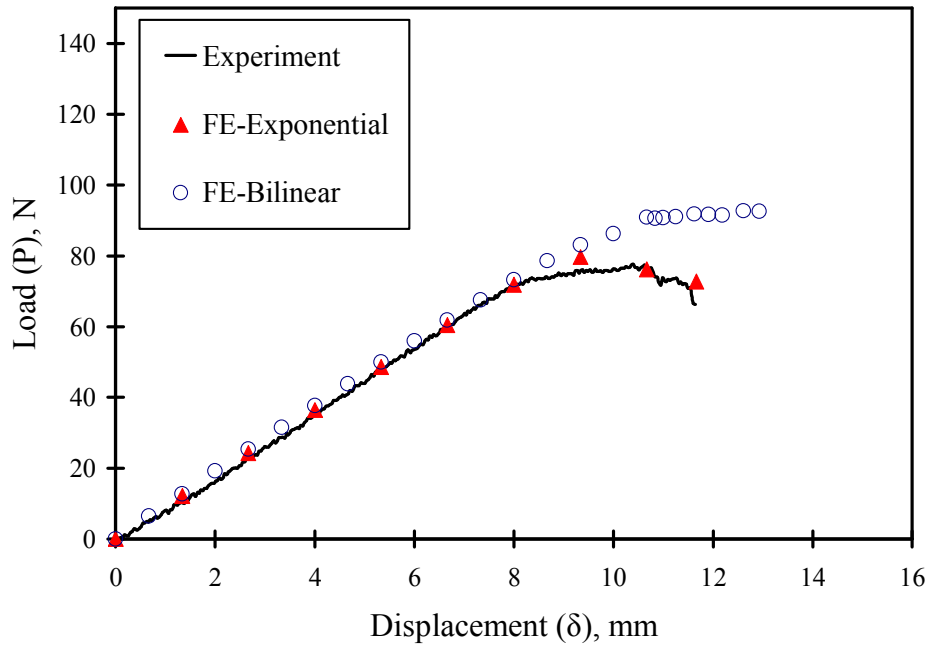
Figure 145. Comparison between experimental and numerical load-displacement response for the FRP composites with neat epoxy

(a) Load   (b) Displacement
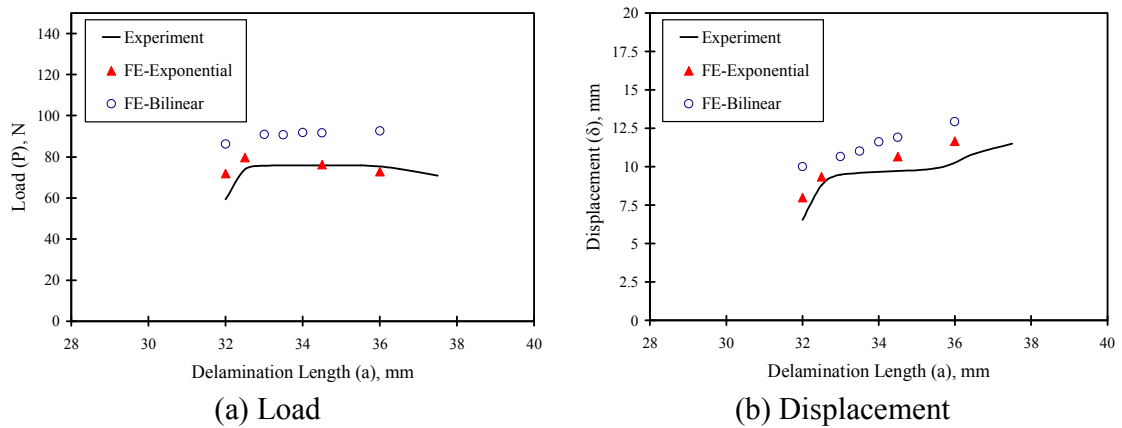
Figure 146. Comparison between experimental and numerical delamination growth for the FRP composites with neat epoxy

The exponential model is used further to predict the behavior of DCB specimens with various MWCNTS loadings. Model characteristic parameters ($\sigma_{max}, \overline{\delta_n}$) are altered

198

to closely match the load-displacement and delamination growth response observed experimentally. In addition, the area under the normal traction-opening displacement T_n - δ_n relationship is maintained as the maximum energy release rate obtained experimentally as discussed earlier. The load-displacement comparison between the experimental and numerical investigations for various MWCNTs loadings is shown in Figure 147. The figure shows that the exponential model is capable of properly predicting the load-displacement response for DCB with different MWCNTs loadings. Furthermore, the behavior of delamination growth, predicted in Figure 148 shows that the numerical analysis fails to predict the delamination growth behavior at the early stages while it closely predicts the behavior towards the maximum energy release rate. To understand this observation, one can look at the comparison between the experimental and numerical investigations in term of the resistance curve (R-curve) shown early in Figure 143. While the numerical investigation shows constant critical energy release rate, the experimental results show increased critical energy release rate. The mismatch in the values of the critical energy release rate at early stages explains the difference in the delamination growth. Therefore, it is suggested that the values for the critical energy release rate should vary along the length of the specimens according to the R-curve obtained experimentally.

The normal traction-opening displacement T_n - δ_n relationships for different MWCNTs loadings are depicted in Figure 149. The relationship shows that the characteristic parameters, the maximum normal traction T_n and its corresponding opening displacement $\overline{\delta_n}$, increases with the addition of MWCNTs. Figure 150 also

199

demonstrates that the increase in the opening displacement is higher than that of the maximum traction. For instance, the increase in the displacement and traction with the addition of 1.5% MWCNTs approached 100% and 15% respectively. This observation confirms other observations reported in Chapter 4 for the off-axis tension test results and Chapter 6 for the lap shear joint test. It was shown that MWCNTs have the ability to enhance the strain capacity over the strength.
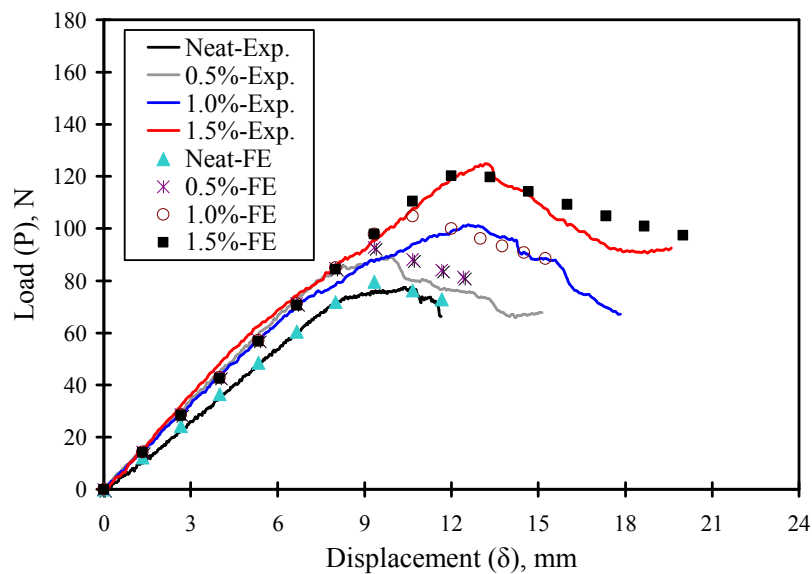
Figure 147. Comparison between experimental and numerical load-displacement response for FRP composites reinforced by different MWCNTs loadings
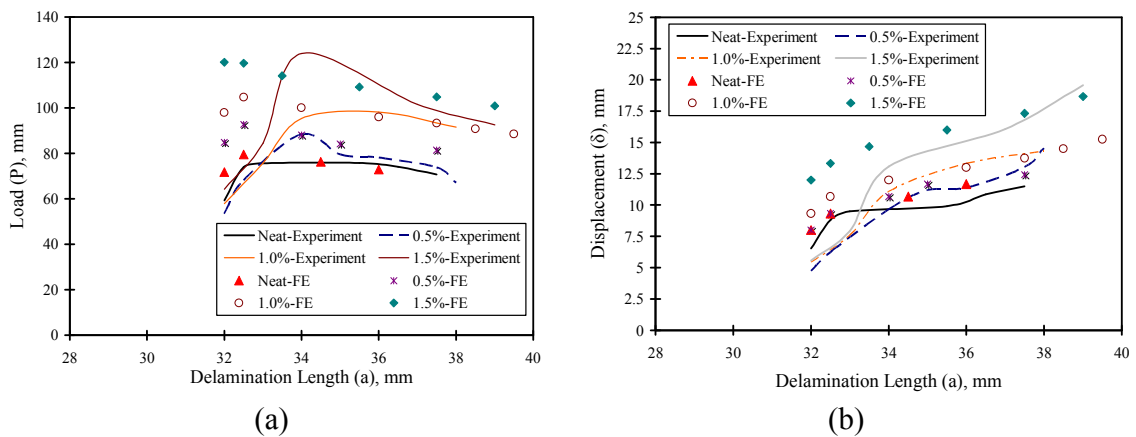
Figure 148. Comparison between experimental and numerical delamination growth for FRP composites reinforced by different MWCNTs loadings
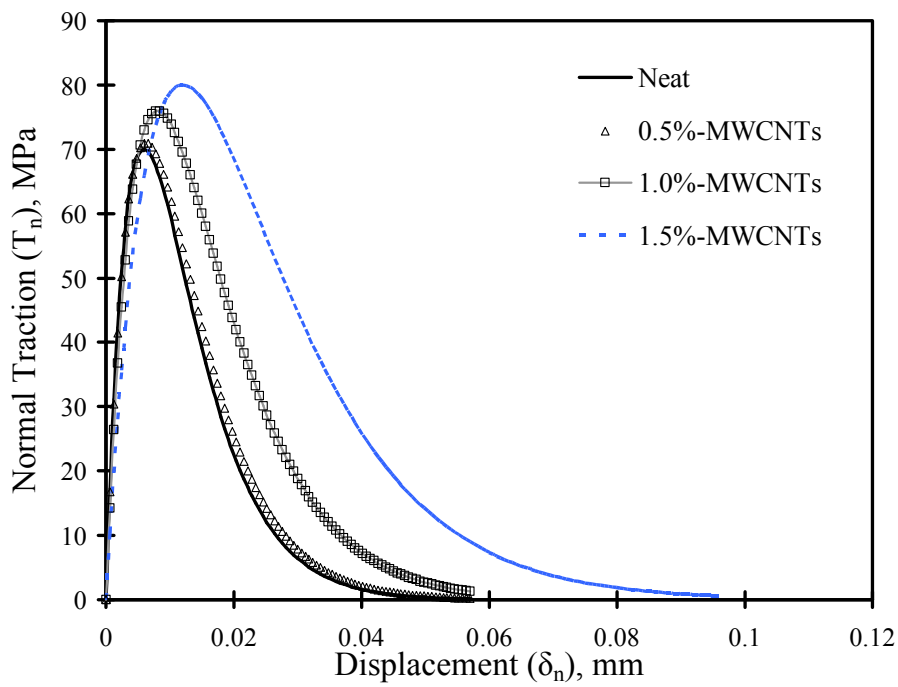
Figure 149. Normal traction-opening displacement relationships for various MWCNTs loadings
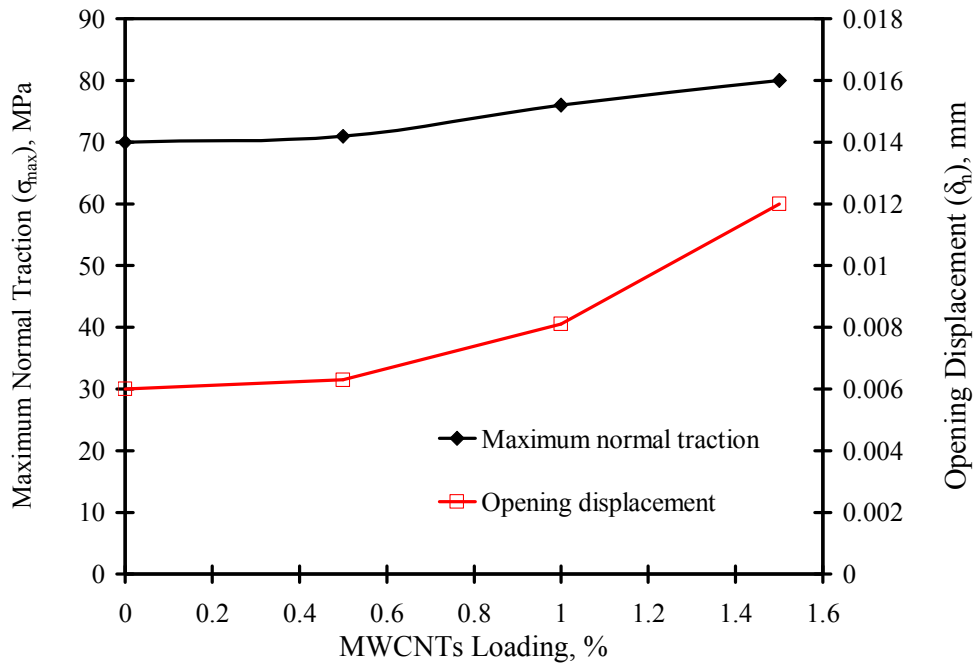
Figure 150. Effect of MWCNTs on the maximum normal traction and its corresponding opening displacement

7.4   Summary

Double cantilever beam (DCB) tests were performed on woven carbon fabric composites to determine the fracture toughness of MWCNTs-epoxy nanocomopsites with various loadings of MWCNTs. The results show 52, 91, and 160% increase in maximum critical energy release rate with the addition of 0.5, 1.0, and 1.5% MWCNTs, respectively. These improvements would have a significant impact on the delamination of composites. Moreover, finite element models are developed to extract more information about the delamination growth of different cases. The simulations show that the use of exponential relationship via interface element is more accurate in predicting the delamination behavior than using the bilinear relationship via contact element. The

202

predicted stress-displacement relationships show that the addition of the MWCNTs has a significant effect on the deformation of the epoxy at the interface.

203

CHAPTER 8. LOW-VELOCITY AND BALLISTIC IMPACT OF THIN WOVEN CARBON FABRIC COMPOSITES INCORPORATING CARBON NANOTUBES.

8.1 Introduction

Over the last century, fiber reinforced polymer (FRP) composites have been widely used in structural components subjected to quasi static loading due to their superior specific strength and stiffness (Reid & Zhou, 2000). However, in many occasions, the composite structures used in aerospace, pipelines, and military applications are prone to high strain rate loadings through their life span such as impact and blast (Abrate, 1994). In this regard, the performance of composite components is usually poor and brittle when compared to other ductile materials such as metals. One of the major causes of such brittle fracture is the premature failure of composites due to matrix transverse cracking or fiber/matrix interface debonding. The poor interlaminar shear strength (ILSS) and toughness of composites have been limiting their use in such applications. As a result, many studies addressed the behavior of composite structures subjected to impact loadings. These investigations studied various types of composites including laminated (Aktas *et al.*, 2009, Shyr & Pan, 2003, Yokozeki *et al.*, 2010), sandwich (Villanueva & Cantwell, 2004), and woven fabric structures (Naik *et al.*, 2000, Zhang *et al.*, 2009).

204

More emphasis is placed on the woven fabric composite due to higher impact resistance (Tan & Ching, 2006). The impact response of woven fabric composites have been widely investigated experimentally (Chocron *et al.*, 2009, Karahan *et al.*, 2008, Tan *et al.*, 2003), numerically (Barauskas & Abraitiene, 2007, Rao *et al.*, 2009, Tan & Ching, 2006) and analytically (Gu, 2003, Naik *et al.*, 2006). For instance, (Tan et al., 2003) investigated the perforation of various shapes of projectiles on the woven fabric composites. They found that the shape of the projectile has significant influence on the ballistic limit. The ballistic performance of woven aramid fabric protection panels is investigated (Karahan et al., 2008). It is reported that the number of plies and stitching type have great influence on the depth and diameter of the trauma. (Chocron et al., 2009) used embedded nichrome wires to measure the strain in the fabric during impact event. Moreover, the effect of fabrication process of the composite fabric is evaluated (Zhang et al., 2009). They concluded that composites cured with Quickstep technique resulted in less damage than those cured using Autoclave technique.

(Tan & Ching, 2006) introduced a simplified orthotropic finite element (FE) model to simulate the behavior of woven fabric composite. In this model, the unique properties of woven fabric such as viscoelastic nature of the yarns, the crimping of the yarns, and the sliding contact between yarns are simulated using a set of viscoelastic bar elements. Detailed procedures of modeling multi-layer woven fabric composites in LSDYNA$^®$ are presented by (Barauskas & Abraitiene, 2007). (Rao et al., 2009) studied the effect of yarn properties on the ballistic impact of plain weave fabric. They found that the friction between yarns has great influence on the impact resistance. In addition, the stiffness and strength of yarns affect the projectile declaration and failure duration. (Naik

205

et al., 2006) introduced analytical formulation for the ballistic impact of woven fabric composites. They showed the major energy absorption mechanisms during impact are the tension in the primary yarns and the deformation of the secondary yarns. In general, the ballistic impact of woven fabric composite plates is fairly studied over the last decade.

Few studies examined the use of nanoparticles to improve the ballistic impact of FRP composites. (Hosur *et al.*, 2007) examined the impact response of woven carbon/epoxy–nanoclay nanocomposites and observed no change in the impact response with the addition of nanoclay. However, a reduction in the damage size was reported. These observations were confirmed later by (Iqbal *et al.*, 2009) upon testing carbon fiber reinforced polymer (CFRP) laminates reinforced with nanoclay. (Avila *et al.*, 2007) studied the behavior of nanoclay GFRP laminated plates under low velocity impact. With the addition of nanoclays, 48% and 4% increase in the absorbed energy were reported when low and high velocity impact tests are performed respectively. A constitution model for the impact response of CNTs/poly-vinyl-ester-epoxy/E-glass fiber composites was developed and small improvements in the ballistic performance were observed (Grujicic *et al.*, 2008). (Kostopoulos *et al.*, 2010) investigated the impact response of quasi-isotropic CFRP laminates enhanced with 0.5% by wt. pristine MWCNTs and reported no effect on the absorbed energy or delamination area.

In general, the nanoparticles limited the damage size in many studies however; they did not improve the mechanical response. In addition, the use of MWCNTs did not enhance the impact response as expected. The ballistic impact response needs further investigations when nanotubes are used. This Chapter further examines the use of carbon nanotubes to improve the low-velocity and ballistic impact response of FRP composites.

It is well established that the low-velocity impact involves the non-penetrating impact tests while the ballistic impact involves a penetrating impact tests (Abrate, 1998). In this study, the use of wide range of functionalized MWCNTs loadings in epoxy carbon woven fabric composites is examined.

8.2   Testing Setup and Procedures

Two different treatments for epoxy were produced to fabricate the epoxy adhesive bond lines in this study. The first type was neat epoxy prepared by mixing the resin with the hardener and applying the mixture during the fabrication of the CFRP woven fabric composites. The second type was prepared by reinforcing the epoxy with functionalized carbon nanotubes (COOH-MWCNTs). The fabrication is performed following the procedures reported in Chapter 4. Ten fabric layers (0-90°) were used to fabricate all specimens. The composite plate average thickness was 2.7 ± 0.15 mm and the epoxy weight fraction ranged between 30–33 %.

CEAST® 9350-drop tower high velocity impact tester, supplied by Instron®, is used to conduct the biaxial testing on the woven fabric composites (Figure 151). The test is performed by dropping a 12.7 mm diameter hemispherical striker carrying a total weight of 14.93 kg on the composite specimens from various heights and investigating the dynamic response (Figure 152). The total weight includes a carriage weight of 4.3 kg, a striker weight of 0.63 kg, and 10 kg additional weights. The sampling rate and the striker load capacity are 800 kHz and 21 kN respectively. In addition to the neat epoxy, three different COOH-MWCNTs loadings are examined; 0.5, 1.0, and 1.5% by wt. of

207

epoxy. Five levels of energy are applied to the composites; 15, 24, 30, 60, and 120 J. The incident (initial) velocities for the five levels were 1.42, 1.8, 2.0, 2.85, and 4 m/sec and drop heights were 102.8, 165.2, 203.9, 414.1, and 815.7 mm respectively. The testing system is capable of measuring the time history for the force $F(t)$ using the instrumented striker. The system is also equipped with a laser system to measure the incident velocity v_i. The applied energy E and the drop height H are computed using Eqns 8.1 and 8.2 respectively.

$$E = \frac{m v_i^2}{2} \tag{8.1}$$

$$H = \frac{E}{mg} \tag{8.2}$$

where v_i is the initial velocity, m is the applied mass, and g is the gravity. The following responses are then calculated through the time domain after (ASTMD7136/D7136M, 2007).

$$v(t) = v_i + gt - \int_0^t \frac{F(t)}{m} dt \tag{8.3}$$

$$\delta(t) = \delta_i + v_i t + \frac{gt^2}{2} - \int_0^t \left(\int_0^t \frac{F(t)}{m} dt \right) dt \tag{8.4}$$

$$E(t) = \frac{m\left[v_i^2 - v(t)^2 \right]}{2} + mg\delta(t) \tag{8.5}$$

where t is the time, δ_i is the initial location, $v(t)$ is the velocity, $\delta(t)$ is the displacement, and $E(t)$ is the absorbed energy.

208

In order to further explain the results of the impact test, static flexure tests were performed on composite specimens produced from the same batch used to make the impact specimens. Two types of flexure tests were conducted; on and off-axis tests. In the on-axis test, the fibers orientation is aligned in the same direction as the span direction while in the off-axis test the fibers are aligned at a 45°angle with respect to the span direction (Figure 153). The flexure specimens were 32 mm long 19 mm wide and 2.5 mm thick and they were tested in displacement controlled (1.0 mm/min) three-point bending according to (ASTMD790, 2010) using MTS$^®$ Bionix servo hydraulic system with load capacity of 25 kN and a maximum stroke of 130 mm.

(a)   (b)
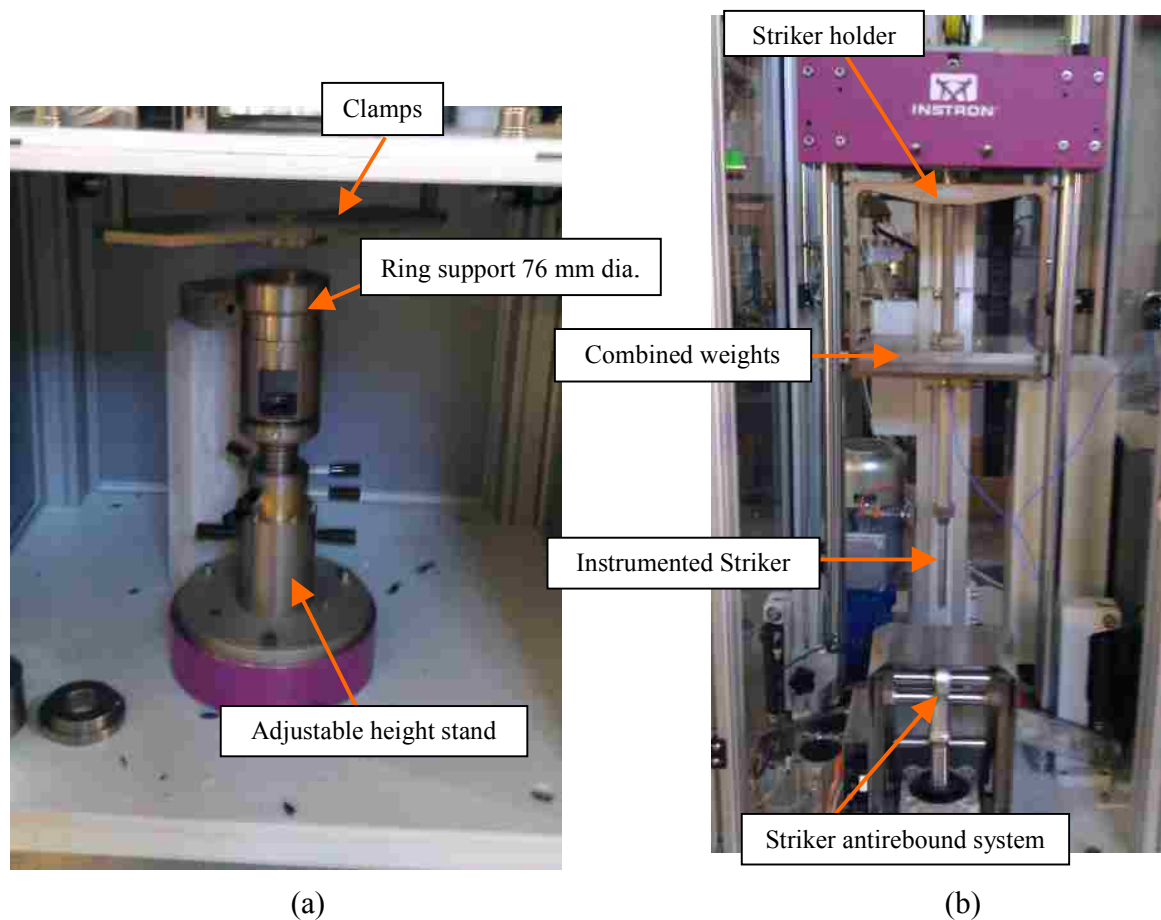
Figure 151. CEAST® 9350 impact tester (a) test chamber, and (b) turret
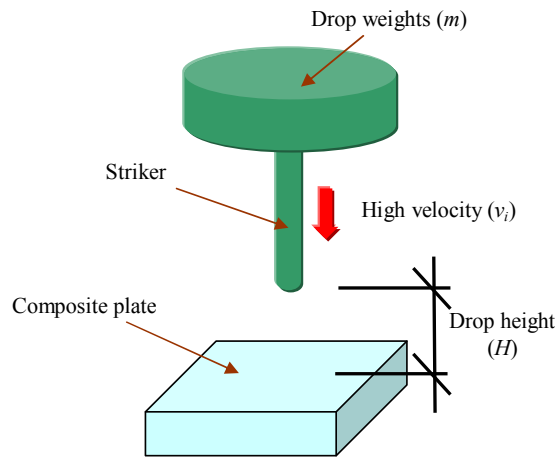
Figure 152. Schematic of impact test

(a)
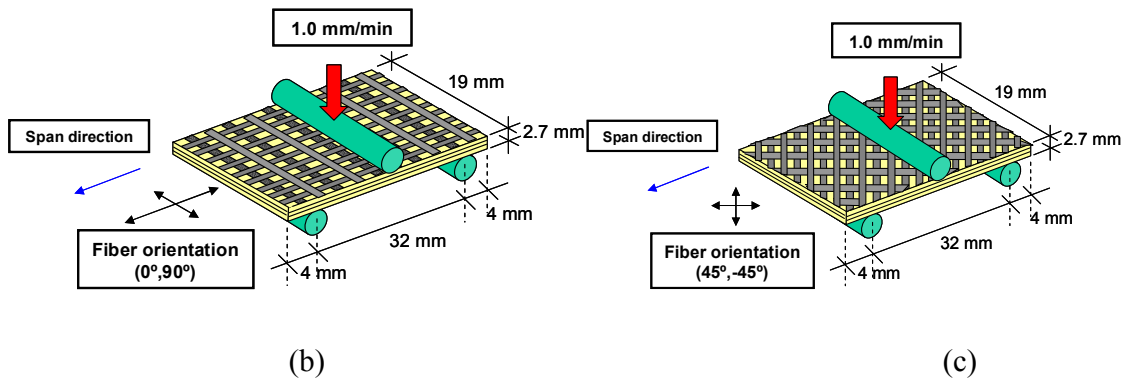
(b)   (c)

Figure 153. Flexure test (a) Test setup (b) Schematic for on-axis, and (c) Schematic for off-axis

210

8.3 Results and Discussion

8.3.1 Load-Displacement Response

Examples of load-displacement responses for different COOH-MWCNTs loadings subjected to various levels of energy are shown in Figure 154. The striker did not penetrate all composite specimens when energy of 15 J is applied. Upon applying 24 J, the striker penetrated only the neat-epoxy composite plates while it rebounded from the composite plates reinforced by COOH-MWCNTs. Moreover, the striker penetrated all composite specimens when energy of 30 J or above is applied. Based on statistical analysis using student t-test with 95% level of confidence, no significant difference in peak force was observed between the different cases. This observation is attributed to the fact that fibers govern the load capacity of the composites. In addition, in the neat epoxy composite, the load drops abruptly upon reaching the maximum or peak force while in the COOH-MWCNTs epoxy cases the load remains constant to form a yield like plateau. Contradictory to most of the previous studies, the functionalized nanotubes improved the mechanical response of the composite plates under impact significantly. The effect of COOH-MWCNTs loadings on the bounce and puncture displacements are investigated in Figure 155. The bounce point, defined only below the ballistic limit, is the point at which the striker's velocity approaches zero [Figure 154 (a)]. The puncture point, defined only above the ballistic limit, is the point at which the force drops to 50% of the maximum or peak force (ISO6603-2, 2000) [Figure 154 (d)].

It is observed that the bounce displacement decreased significantly (about 20%) as the COOH-MWCNTs loadings increased [Figure 155(a)]. Given that the bounce displacement is typically an indication for the damage of the composite plates, the

addition of COOH-MWCNTs reduced the damage significantly. On the other hand, the puncture displacement increased as the nanotubes loadings increased by 20% as shown in Figure 155 (b). The puncture displacement is an indication for the deformation (strain) capacity of the composites. The COOH-MWCNTs are therefore capable of increasing the strain capacity of the composite plates prior to fracture.

8.3.2 Energy-Time Response

An example of energy-time responses for various loadings of nanotubes is shown in Figure 156 (a) for the case of 30 J. An average of 50 % improvement in perforation energy is observed by adding 1.0 or 1.5 % COOH-MWCNTs. The statistical analyses reported in Table 9 for the energy and other responses show that 50 % improvement in perforation energy is achieved by adding 1.0 or 1.5 % COOH-MWCNTs. The coefficients of variation (COV) were relatively low for all cases and the majority of COVs were below 5%. In Figure 156 (b), the energy-time response for 1.0% COOH-MWCNTs FRP composite plates subjected to various energy levels. The rate of energy absorption increases with the increase of the applied energy. Moreover, the bar chart in Figure 156 (c) shows that the perforation energy (E_p), determined from the energy levels above the ballistic limit, does not depend on the applied energy since it is a material property.

212

(a) 15 J

(b) 24 J

(c) 30 J

(d) 60 J

(e) 120 J
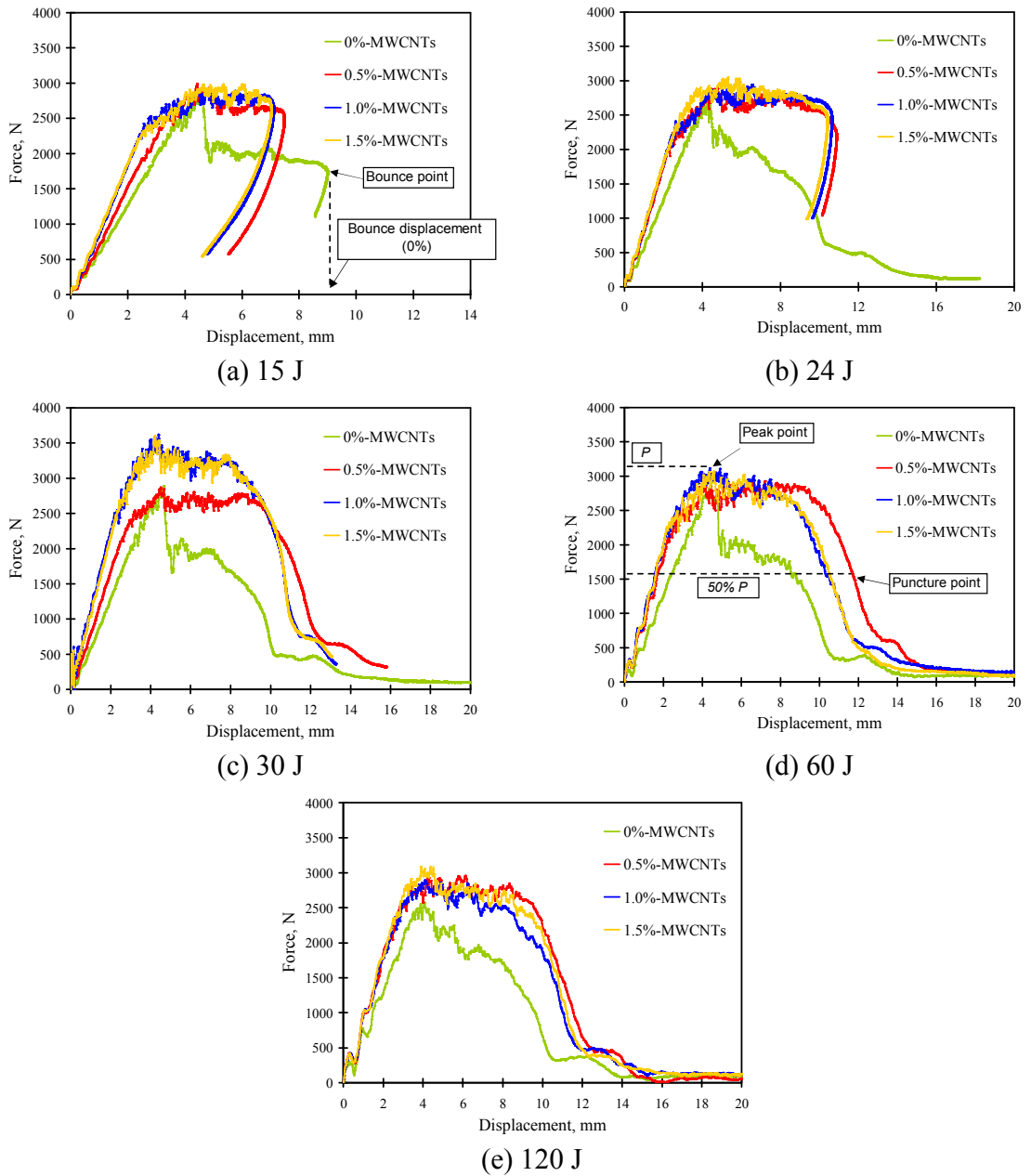
Figure 154. Load-displacement response for various COOH-MWCNTs composite plates subjected to different levels of energy
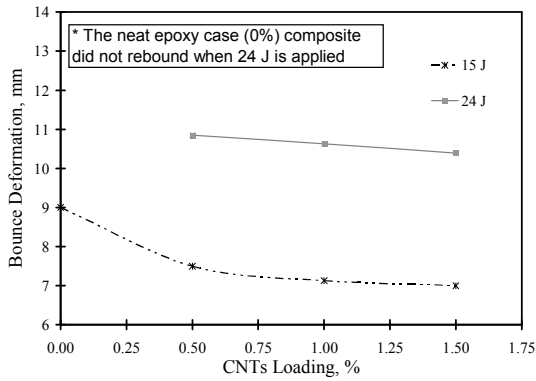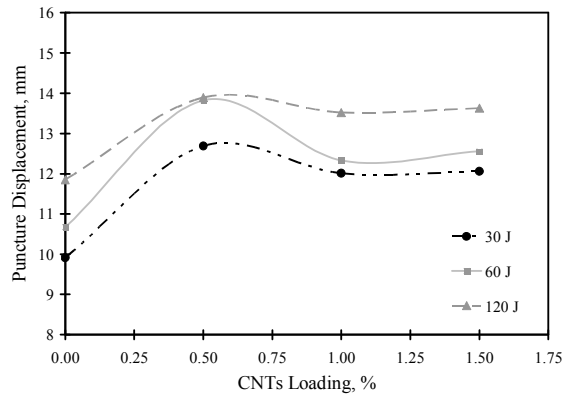
(a) Bounce   (b) Puncture

Figure 155. Effect of COOH-MWCNTs loadings on the bounce and puncture

displacement
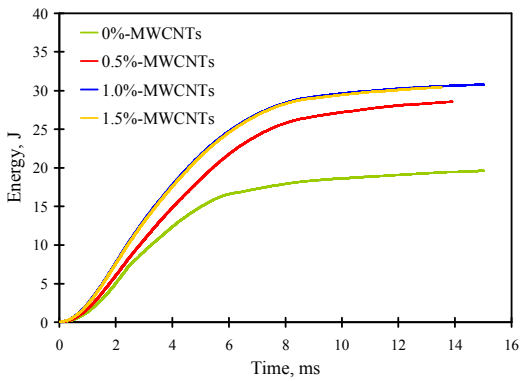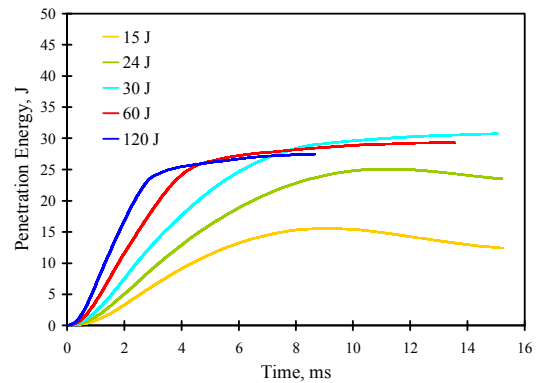
(a) 30 J   (b) 1.0% COOH-MWCNTs
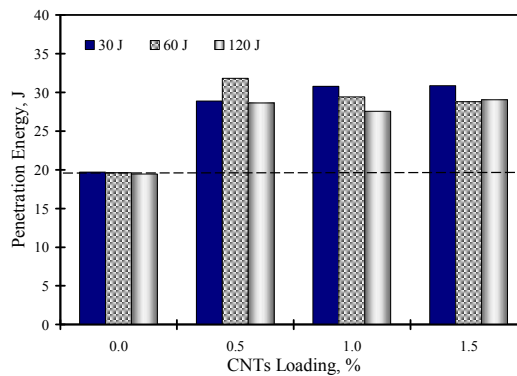
(c) Perforation Energy

Figure 156. Energy-time response of COOH-MWCNTs FRP composite plates

214

8.3.3 Velocity-Time Response

Figure 157 shows examples for the time history of the velocity during the impact test below [Figure 157 (a-b)] and above [Figure 157(c)] the ballistic limit. The positive values for the velocity represent downward motion for the striker while the negative values represent upward motion due to striker rebound. In general, the rate of change in velocity (deceleration) increases with the addition of nanotubes due to the increase in the stiffness of the composite plate. Below the ballistic limit, the bounce time and upward velocity depend also on the stiffness of the tested specimens. The bounce time is defined in this study as the time at which the striker's velocity approaches zero [see Figure 157 (b)]. The upward velocity is the final velocity at the end of the impact event. The addition of nanotubes decreased the bounce time and increased the upward velocity of the composite plates. Figure 157 (d) shows a 25% decrease in bounce time with the addition of 1.5% COOH-MWCNTs. Moreover, the bounce time increased by 20% as the applied energy increased from 15 to 24 J. This observation indicates that the nanotubes are capable of increasing the stiffness of the composite plates under impact loading.

Table 9. Response and statistical analysis for various COOH-MWCNTs FRP composites subjected to 30 J

		Max. Force, N	Perforation Energy, J	Ballistic Limit, m/s
Neat	Test-1	2942	19.68	0.67
	Test-2	2693	19.11	0.64
	Test-3	2905	20.63	0.71
	Mean	2846	19.81	0.67
	COV*, %	4.72	3.88	5.22
0.5%	Test-1	2913	28.9	1.35
	Test-2	3040	30.18	1.53
	Test-3	3091	30.70	1.73
	Mean	3014	29.93	1.54
	COV, %	3.04	3.10	12.37
1.0%	Test-1	3658	30.81	1.70
	Test-2	3563	29.56	1.45
	Test-3	3592	30.90	1.73
	Mean	3604	30.42	1.63
	COV, %	1.35	2.46	9.42
1.5%	Test-1	3638	30.69	1.66
	Test-2	3471	30.49	1.62
	Test-3	3595	30.87	1.87
	Mean	3568	30.68	1.72
	COV, %	2.43	0.62	7.82

* COV: Coefficient of variation

The ballistic limit, obtained from the difference between the initial and residual velocities, is compared in Figure 158. The bar chart shows that as the nanotubes loading increases, the ballistic limit increases. 200-300% increase in ballistic limit was observed with the addition of 1.5% COOH-MWCNTs. Moreover, as the applied energy increases, the ballistic limit decreases. The change in ballistic limit as a function of the applied energy is nonlinear and can be understood from Eqn. (8.6) based on the principle of energy conservation.

$$\frac{1}{2}mv_i^2 = E_p + \frac{1}{2}mv_r^2 \qquad (8.6)$$

where v_i is the incident (initial) velocity, v_r is the residual velocity, E_p is the perforation (penetration) energy. In Eqn. (8.4), the perforation energy E_p is almost constant and independent on the applied energy as reported in section 3.2. The second-degree term $\left(\frac{1}{2}mv_i^2\right)$ represents the applied energy, which therefore is non-linearly related to the initial v_i or residual v_r velocities. The second degree relationship between the applied energy and the velocities is the cause of non linear change in ballistic limit.

(a) 15 J
(b) 24 J
(c) 30 J
(d) Ballistic limit
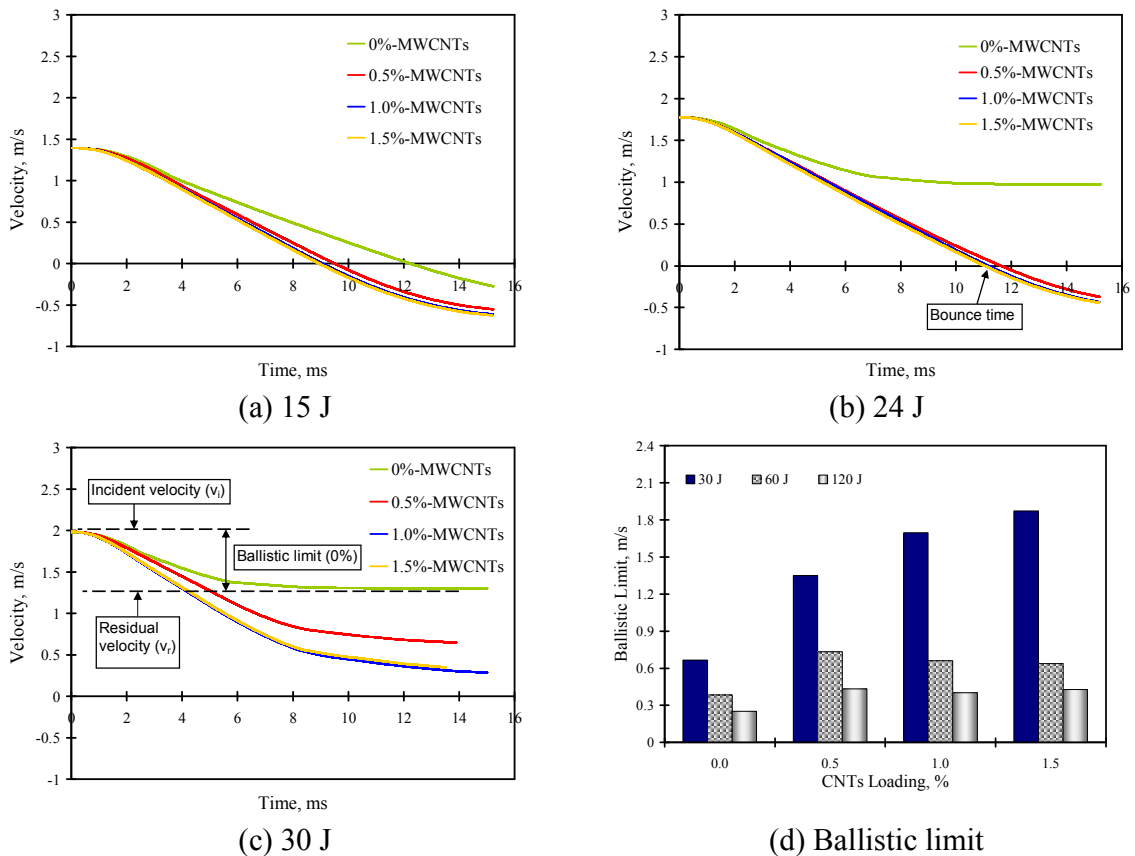
Figure 157. Velocity-time response for various COOH-MWCNTs composite plates subjected to different levels of energy

217
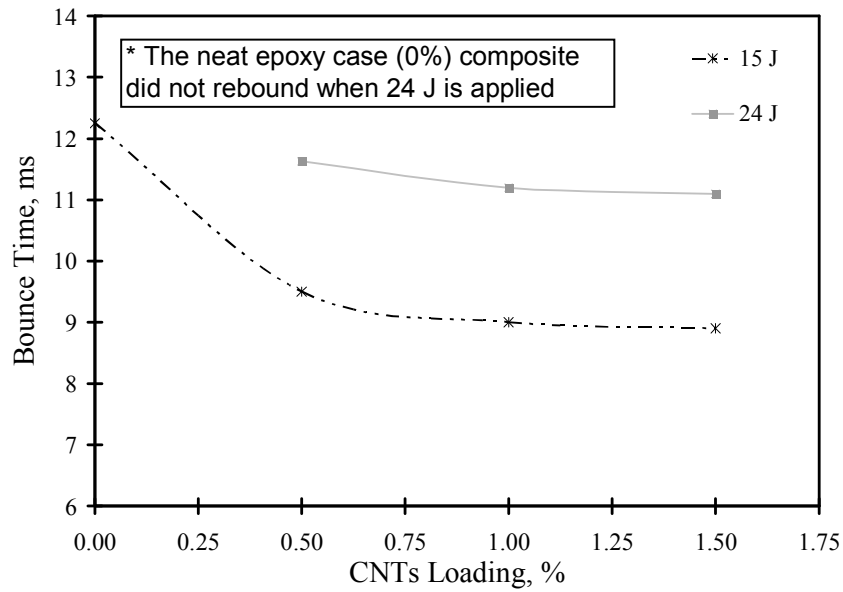
Figure 158. Effect of COOH-MWCNTs loadings on the bounce time and puncture velocity

8.3.4 Damage Evolution

Figure 159 shows the typical failure of all composite plates. The four-sided pyramidal (tetrahedral) fracture is attributed to the bi-directional layup of the woven fabric composite plates. The fracture of the composite plates involves fiber and matrix fractures. The damage size was evaluated by measuring the backplane plastic deformations of the pyramidal fracture. In particular, the plastic height h_p and plastic diagonal d_p are measured for each case (Figure 159). Examples for the measurements of the plastic deformations for different cases are shown in Figure 160.

From the figures, it is observed that the nanotubes have significant effect on plastic deformation below the ballistic limit. For instance, in the case of 15 J, the plastic heights were 3.2, 1.5, 0.8, and 0.8 mm due to the addition of 0, 0.5, 1.0, and 1.5% COOH-MWCNTs respectively. This yields 75% decrease in plastic height with the

218

addition of 1.5% COOH-MWCNTs. The significance of COOH-MWCNTs on the plastic height is shown in Figure 161. In addition, for the same applied energy, the plastic diagonals were 19, 16.7, 15.9, and 15.1 mm due to the addition of 0, 0.5, 1.0, and 1.5% COOH-MWCNTs respectively. A decrease of 20% in the plastic diagonals is observed with the addition of 1.5% COOH-MWCNTs. Obviously; the nanotubes reduced the damage size significantly when composite plates are loaded below the ballistic limit.

On the other hand, the effect of nanotubes on the plastic deformations is negligible above the ballistic limit as observed in Figure 162. Similar plastic heights were observed with various nanotubes loadings when energy of 30 J or above is applied. However, the plastic diagonals for the fracture of the composite plates above the Ballistic limit increased with the addition of nanotubes. For instance, the plastic diagonals associated with energy of 120 J were 20.6, 23, 22.2, and 22.2 mm due to the addition of 0, 0.5, 1.0, and 1.5% COOH-MWCNTs respectively. This increase could be attributed to that the composites with nanotubes absorb more energy (perforation energy) than the neat epoxy composites. The higher energy absorption causes more damage and therefore increases the plastic diagonals.

219
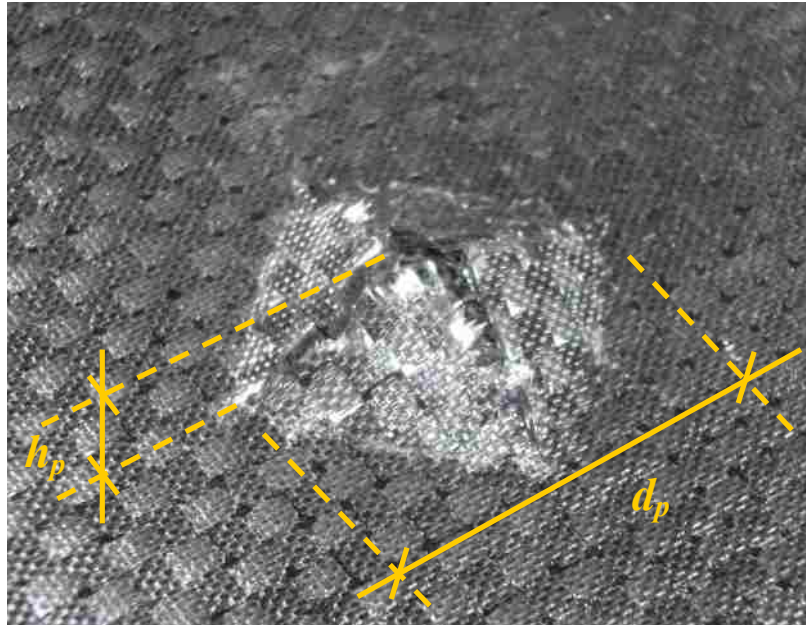
Figure 159. Four-sided pyramidal fracture of the woven fabric composite
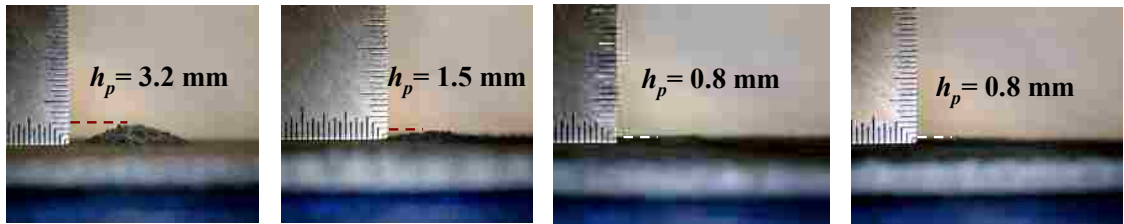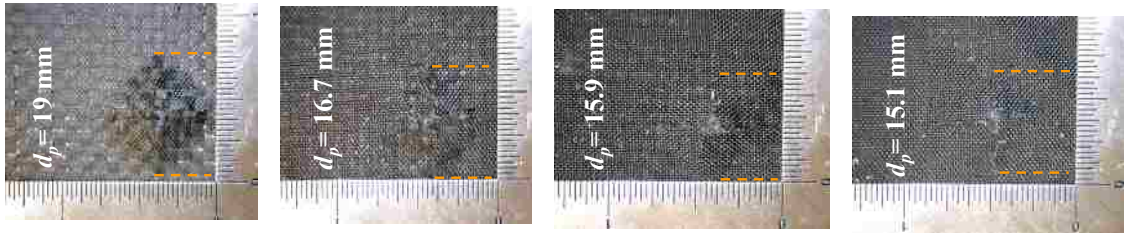
(a) Neat   (b) 0.5%   (c) 1.0%   (d) 1.5%

(e) Neat   (f) 0.5%   (g) 1.0%   (h) 1.5%

221

(i) Neat   (j) 0.5%   (k) 1.0%   (l) 1.5%
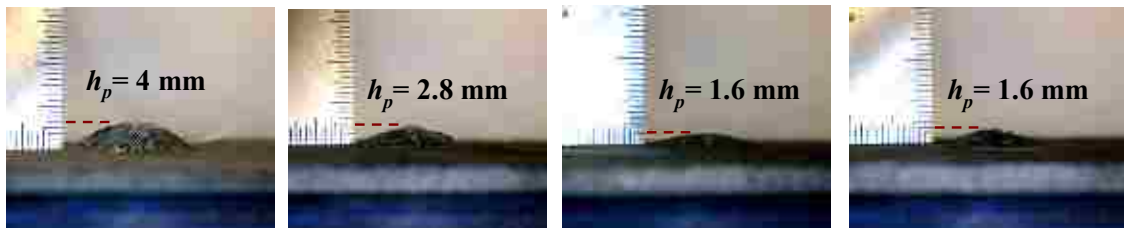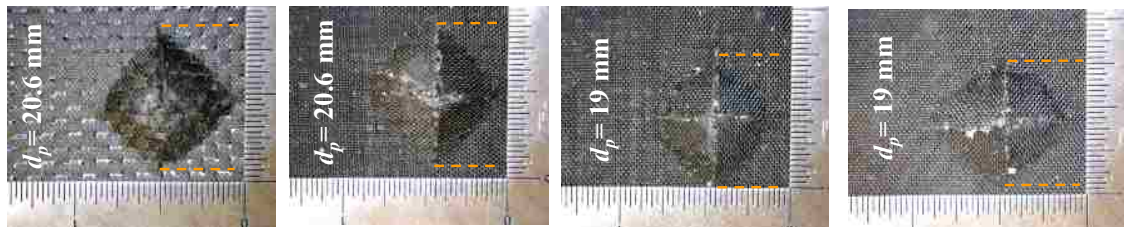
(m) Neat   (n) 0.5%   (o) 1.0%   (p) 1.5%
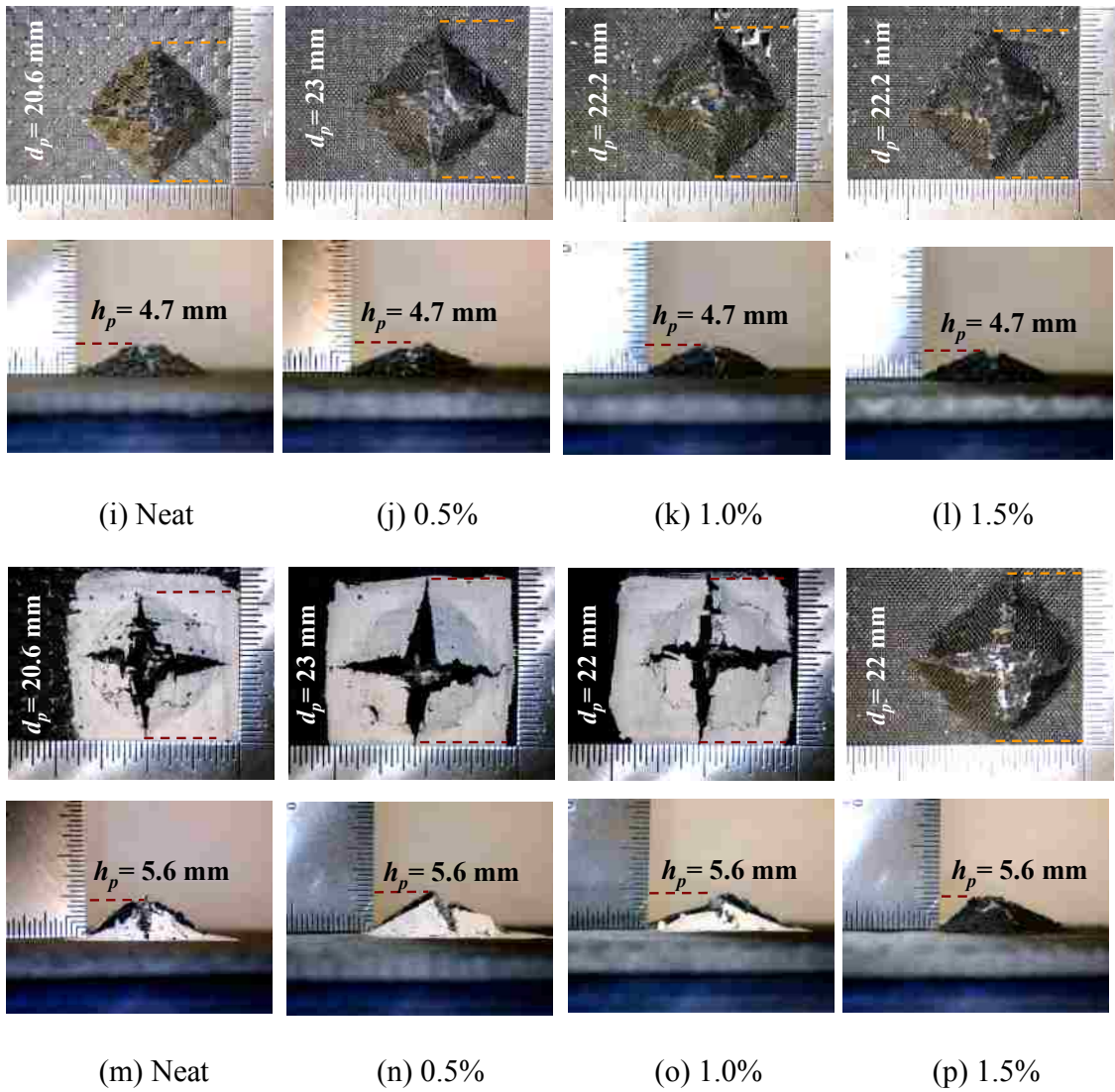
Figure 160. Plastic deformations of FRP composites subjected to various levels of energy (a-d) 15 J, (e-h) 24 J, (i-l) 30 J, and (m-p) 120 J
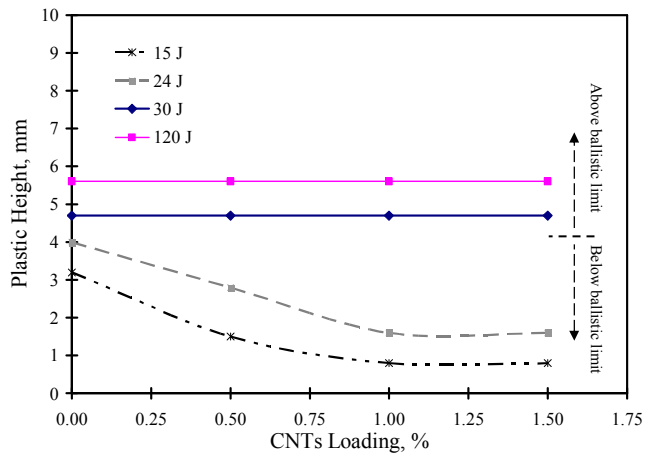
Figure 161. Effect of COOH-MWCNTs loadings on plastic height

(a) Diagonal

(b) Height
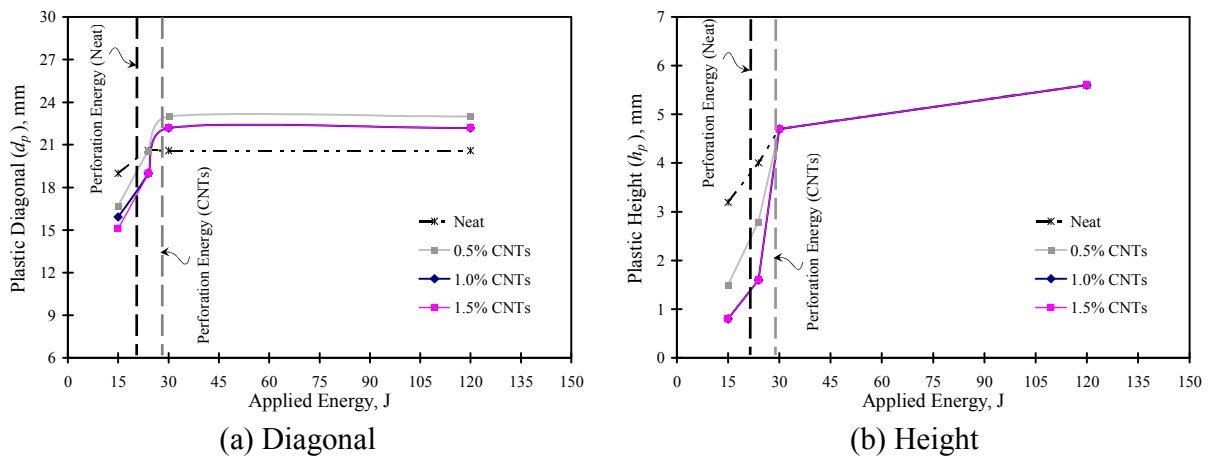
Figure 162. Effect of applied energy level on damage size

223

8.3.5 Static Flexure Test

Figure 163 (a) and (b) shows the deformed shape for the on and off axis flexure tests respectively. In can be noted that the off axis specimens deformed more than the on axis specimens. In addition, close views for the failed specimens show that the failure occurred in the compression zone [Figure 163(c) and (d)]. This is expected because FRP composites are stronger in tension than compression. The stress-strain curves for the on and off-axis flexure tests are depicted in Figure 164. Based on student t-test, there is no significant statistical difference in the on-axis flexure strength and modulus between composite plates with various COOH-MWCNTs loadings. This observation is attributed to that the on-axis flexure behavior of the composite plates is dominated by the carbon fibers. On the contrary, there is significant statistical difference in the flexure strength and modulus associated with the off-axis flexure test. The improvements in modulus and strength with the addition of 1.5% COOH-MWCNTs reached 19 and 28% respectively as shown in Figure 165. The off-axis test is dominated by matrix cracking thus the effect of the nanotubes is evident. Similar findings were observed in Chapter 4 for the on and off-axis tension test of composite coupons with nanotubes. The flexure test results show that the improvement in the ballistic impact is attributed to the contribution of the COOH-MWCNTs on the off-axis fracture of epoxy matrix. This improvement can be of significant value for many composite applications such as defense, aerospace, and offshore structures where impact or blast response is a critical parameter in design.

In general, the impact test results showed that below ballistic limit, same peak force and 50% improvement in perforation energy are observed using 1.5% COOH-MWCNTs by weight of epoxy. Above the ballistic limit, the perforation energy remains

224

the same regardless of the applied energy while the ballistic limit decreases as the applied energy increases. It is also noted that the content of MWCNTs has significant effect on the damage size only below the ballistic limit. The significance of MWCNTs can be attributed to their ability to enhance the off-axis strength and stiffness of the biaxial woven composites. The use of functionalized MWCNTs significantly limited the damage size and improved the mechanical response of the biaxial woven composite plates under impact.

(a) On-axis

(b) Off-axis

(c)

(d)

Figure 163. Flexure stress-strain curves for composite plates

(a) On-axis	(b) Off-axis
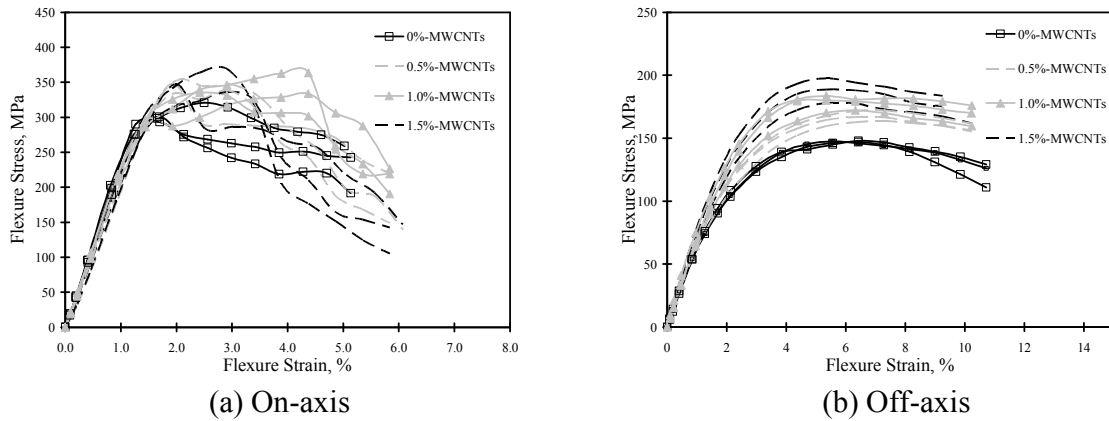
Figure 164. Flexure stress-strain curves for composite plates

(a) Flexure modulus	(b) Flexure strength
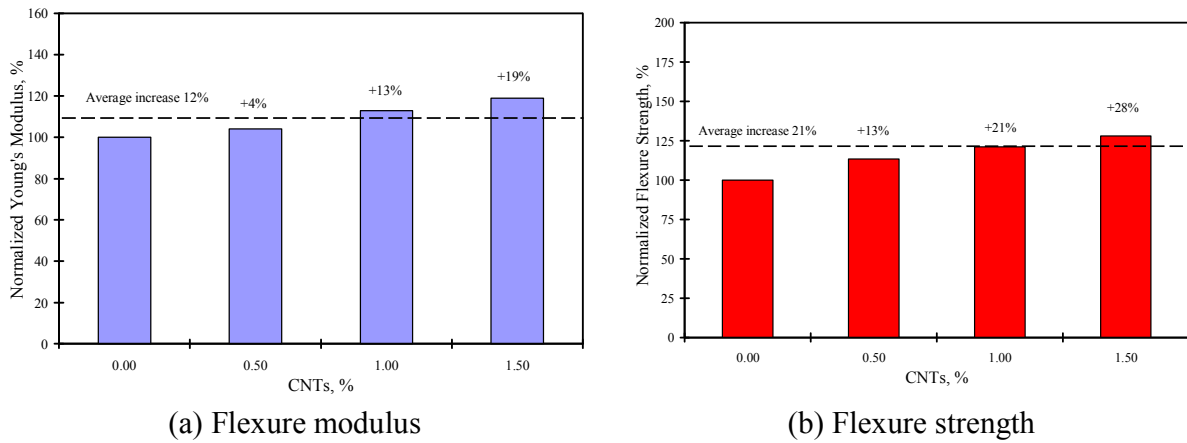
Figure 165. Comparison of the flexure mechanical properties between various

loadings of COOH-MWCNTs

8.4   Summary

Experimental investigation of impact tests of biaxial woven carbon fabric composites is conducted with various loadings of functionalized multi-walled carbon nanotubes (0, 0.5, 1.0, and 1.5% by wt. of epoxy). The composite plates were subjected to five different levels of energy; 15, 24, 30, 60, and 120 J. The results showed that below ballistic limit, same peak force and 50% improvement in perforation energy are observed using 1.5% COOH-MWCNTs by weight of epoxy. Above the ballistic limit, the

226

perforation energy remains the same regardless of the applied energy while the ballistic limit decreases as the applied energy increases. It is also noted that the content of MWCNTs has significant effect on the damage size only below the ballistic limit. The significance of MWCNTs can be attributed to their ability to enhance the off-axis strength and stiffness of the biaxial woven composites. The use of functionalized MWCNTs significantly limited the damage size and improved the mechanical response of the biaxial woven composite plates under impact. A journal article is submitted for review from this research work (Soliman *et al.*, 2011e).

CHAPTER 9. CONCLUSIONS AND RECOMMENDATIONS

Experimental study was conducted in order to investigate the benefits of reinforcing FRP structural composites with carbon nanotubes (CNTs). The MWCNTs nanocomposites were first fabricated and characterized before using them in FRP composites. All composites were made from bidirectional woven carbon fabrics using vacuum assisted wet layup technique. The new FRP composites are characterized through different structural tests such as tension, flexure, creep, lap shear joint, fracture toughness, and impact. This chapter is divided into three sections. The first section presents the findings and the conclusions obtained from the experimental investigation while the second section provides the recommendations for industrial application. The third section suggests research work that can be performed for future investigations.

9.1 Findings and Conclusions

9.1.1 CNTs-Epoxy Nanocomposites

Three types of MWCNTs treatment were used to fabricate MWCNTs-epoxy nanocomposite: pristine, functionalized, and surfactant treated. The functionalization and surfactant assistant are performed via carboxyl groups (COOH) and Triton X-100 respectively. The thermal stability, mechanical response, and microstructure were evaluated by differential scanning calorimetry (DSC), thermogravimetric analysis (TGA),

flexure, dynamic shear rheometer (DSR), and scanning electron microscope (SEM). The following main conclusions are drawn:

1. The pristine MWCNTs had reasonable effect on the flexure modulus (29%) and no effect on flexure strength (1.0%). However, the functionalized COOH-MWCNTs improved both the flexure modulus (40%) and flexure strength (43%) significantly. The improved mechanical properties of the functionalized MWCNTs are attributed to the strong interfacial bond between the MWCNTs and the surrounding polymer matrix. On the other hand, noticeable reduction in flexure modulus (-14%) and flexure strength (-25%) associated with the addition of surfactant. The degradation, observed with the use of surfactant, can be attributed to the large concentrations of surfactant (10 CMC) which form micelles of surfactants. The DSR test is an appealing test for polymer nanocomposites which can determine many shear properties. The DSR results for pristine MWCNTs nanocomposites shows limited improvement in the static, dynamic and time dependant shear properties.

2. The thermal stability tests via TGA and DSC show that the solvent used during the process of dispersing the MWCNTs. In particular, the heat flow and weight loss for the MWCNTs nanocomposites did not differ significantly from the neat epoxy nanocomposites. The two tests also show that the MWCNTs are very stable thermally since they did not experience a significant weight loss up to 1000°C (-5% only) and they experienced relatively high heat flow (4.85 mW/mg at 200°C) with respect to the epoxy nanocomposites. It is important to report that there is 9°C increase in T-50 (the temperature at which 50% of the weight

229

diminishes) with the use of 1.0% functionalized MWCNTs. The improvement in T-50 is limited due to the low loading of the MWCNTs.

3. Microstructural investigation using SEM shed light on the efficiency of dispersion techniques used in this study. The combination of ultrasonication and magnetic stirring seems to effectively disperse the MWCNTs when low contents are used such as 0.5% by wt. However, SEM images show agglomerations of MWCNTs when 1.5% MWCNTs by wt is added. The difficulties in identifying the MWCNTs with the use of large concentration of surfactant suggested that micelles of surfactant are formed and caused microstructural phase separation between the surfactant and the polymer matrix.

9.1.2 Tension Behavior of FRP Composites Reinforced with MWCNTs

Two approaches are presented to discuss the use of MWCNTs to improve the tension behavior of FRP composites. The first approach is performed by growing the MWCNTs on the surface of the fabric via graphitic structures by design (GSD) technique. This approach is evaluated by conducting on-axis tension test on carbon and glass fabrics. The second approach is performed by using the nanocomposites produced in Chapter 3 during the impregnation of the fabric. The second approach is evaluated by conducting on- and off-axis tension test on carbon fabric. The following conclusions are drawn:

1. In general, the removal of the polymer coating "sizing" by burning had adverse effect on the tension properties of the carbon and glass fibers. The carbon and glass fiber composites experienced a reduction in strength of 25% and 50% with

230

removing the sizing at 500°C. However, the reduction in the mechanical properties is sensitive to the level of temperature and the type of fibers. For instance, 250°C degraded the glass fiber fabric and did not affect the carbon fiber fabric while 500°C degraded both the glass and carbon fiber. The strength reduced further by 25% for both with the carbon filaments growth at 700°C.

2. No statistical difference is observed when CFRP composites with pristine or functionalized MWCNTs epoxy nanocomposites are tested on-axis tension. This is attributed to the fact that the fibers dominate the tension behavior when they are oriented in the loading direction. However, this type of nanocomposite had significant effect on the off-axis tension behavior. This is because the inter fiber fracture (IFF) governs the in plane shear behavior of the FRP composites. A reduction in the strength (-24%) was associated with the use of 1.0% surfactant treated MWCNTs. However, increase in the failure strain was observed with the use of 1.0% pristine (29%) and functionalized (19%) MWCNTs. Furthermore, the 1.0% functionalized improved the strength by 20%. These observations confirm the results obtained in Chapter 3 for the mechanical response of the epoxy nanocomposites. In general, the functionalized MWCNTs seem to be useful in enhancing the shear strength of the FRP composites.

9.1.3   Creep of MWCNTs-Epoxy Adhesive at the FRP-Concrete Interface

Nine double lap shear specimens were fabricated and tested to observe the shear creep behavior of the pristine or functionalized MWCNTs epoxy nanocomposites with different MWCNTs loadings. Four loadings are examined for each treatment of MWCNTs: 0.1, 0.5, 1.0, and 1.5% by wt of epoxy. All the specimens are loaded with

231

25% of the bond strength for one month and the deformations are reported. In addition, rheological models were developed to investigate the effect of the addition of MWCNTs on creep characteristic parameters. The following conclusions are drawn:

1. The experiment shows that there is little to no effect on the shear creep with the use of different loadings of pristine MWCNTs in epoxy adhesives. However, functionalized MWCNTs were able to limit shear creep of epoxy significantly. For example, the use of 0.1% functionalized MWCNTs out-performed all other MWCNTs loadings and resulted in 54% reduction in normalized creep compliance. Close reductions in creep were also observed with 1.0 and 1.5% functionalized MWCNTs. These observations indicate the importance of improving the interfacial bond between the MWCNTs and the surrounding matrix through chemical functionalization in order to reduce shear creep deformations of epoxy nanocomposites. The use of 1.0 and 1.5% MWCNTs can reduce the lap splice length significantly and can provide significant enhancement in ductility which is needed in seismic retrofit.

2. Three parameters' rheological models are sufficient to describe the shear creep behavior of MWCNTs-epoxy nanocomposites with different loadings. Examples of three parameters' rheological models, which agree well with experimental results, are Ross and modified Maxwell models. The two models are modified in order to describe the effect of using MWCNTs. The effect of MWCNTs on the viscosity or modulus coefficients can be simulated by second or third order degree polynomials.

232

9.1.4 Lap Shear Joint Bonded with MWCNTs-Epoxy Nanocomposites

Single and double lap joint tests for FRP composite substrates were performed to examine the performance of epoxy adhesive reinforced by functionalized MWCNTs. Three loadings for functionalized MWCNTs are examined in addition to the neat epoxy: 0.5, 1.0, and 1.5% by wt. The results for single lap joint test were inconsistent because of the joint asymmetry which causes rotation and normal stresses in addition to the shear stresses. For the double lap joint tests, the experiments showed a linear elastic response for the neat epoxy while they showed a non-linear stress-strain response of FRP lap splices reinforced with relatively high loadings of functionalized MWCNTs (1.0 and 1.5%). The use of 1.0% MWCNTs results in enhancing the bond strength by 50%. Furthermore, enhancements in shear strain capacity and toughness reached about 700 and 1,100% respectively with 1.5% MWCNTs. The improvements in strain capacity were higher than the bond strength because the latter is usually governed by the FRP-epoxy interface while the former is governed by the entire joint. In general, the level of improvements from this test is very significant and justifies the use of the low loadings of MWCNTs in structural applications.

9.1.5 Fracture Toughness of FRP Composites Reinforced by MWCNTs

Double cantilever beam (DCB) tests were performed on woven carbon fabric composites to determine the fracture toughness of MWCNTs-epoxy nano-comopsites with various loadings of functionalized MWCNTs. Four loadings of MWCNTs are examined: 0, 0.5, 1.0, and 1.5% by wt of epoxy. Three specimens are tested for each loading of MWCNTs. In addition, a finite element model is developed to simulate the

233

delamination growth process and better understand the effect of MWCNTs on that process. The following conclusions are drawn:

1. The experimental results show a significant effect of the MWCNTs on the fracture toughness represented by the R-curve of CFRP composites. Limited effect is observed on the initial critical energy release rate (~18%) with the addition of 1.5% MWCNTs while significant effect was observed on the maximum critical energy release rate (~160%). Moreover, the results also show that the improvements in maximum critical energy release rate increases with the increase of MWCNTs content. For example, 52, 91, and 160% increase in maximum critical energy release rate is observed with the addition of 0.5, 1.0, and 1.5% MWCNTs, respectively. In addition, the nonlinearity of the R-curve and significant change in the critical energy release rate from the initial to the maximum value with the addition of MWCNTs suggests that LEFM does not apply and the use of QBFM or EPFM might be more appropriate when MWCNTs are added to epoxy. The nonlinearity is attributed to additional energy consumption mechanisms such as MWCNTs pull out of epoxy matrix or rupture which result from the MWCNTs' bridging effect.

2. Finite element simulations show that the use of exponential relationship via interface element is more accurate in predicting the delamination behavior of FRP than the use of bilinear relationship via contact element. Mismatch between the experiment and the numerical results at early stages in the R-curve are observed because of the change in the experimental critical energy release rate which is not considered in the FE model. The predicted stress-displacement relationships show

234

that the addition of the MWCNTs has more effect on the deformation of the epoxy at the interface when compared with the strength.

9.1.6 Ballistic Impact of FRP Composites Reinforced by MWCNTs

Experimental investigation for impact tests of FRP composites is conducted with various loadings of functionalized MWCNTs (0, 0.5, 1.0, and 1.5% by wt. of epoxy). 10-layer bidirectional thin woven carbon fabric composites are tested below and above their ballistic limits. The composite plates were subjected to five different levels of energy; 15, 24, 30, 60, and 120 J. In addition, static flexure tests are performed to explain the results of the impact tests. The following conclusions are drawn:

1. The results showed that below ballistic limit, the functionalized MWCNTs limit the damage size characterized by the diagonal and height of the impact imprint. The rebound deformations were also reduced with the addition of MWCNTs. Significant effect takes place between the neat and the 0.5% MWCNTs while little effect occurs above 0.5% MWCNTs. Furthermore, the on and off-axis flexure tests show that the significance of MWCNTs can be attributed to their ability to enhance the off-axis strength and stiffness of the biaxial woven composites.

2. Above the ballistic limit, same peak force and 50% improvement in perforation energy are observed using 1.5% COOH-MWCNTs. The addition of MWCNTs to the FRP composites produces a yield like plateau on the load displacement response when compared to the FRP composites with neat epoxy. The perforation energy remains approximately constant regardless of the applied energy while the ballistic limit decreases as the applied energy increases following a second order

235

polynomial relationship with the applied energy. It is also noted that no effect from the MWCNTs is observed on the damage size above the ballistic limit.

9.2 Recommendations for Industrial Implementations

The findings from this research project can improve the design of structural composites in the following applications:

1. Improving the mechanical response of composite structures that are prone to inter fiber fracture or delamination such as 1) composite laminates loaded in many directions where some of the layers will be loaded off axis; 2) Reinforced concrete columns wrapped with FRP sheets or composite gas pipelines where hoop stress is in a 35-45° angle with respect to the fiber direction; 3) Pultruded sections, FRP shear studs, or FRP bolts which are governed by the weak shear strength of the matrix.

2. The improved bond strength can be utilized to shorten the lap splices for the FRP strengthening plates. In addition, the embedded length for dowels and anchors used in structural rehabilitation in buildings and bridges can be shortened. The reduced creep deformations of the MWCNTs-epoxy adhesives would allow using FRP strengthening systems for strengthening structures against sustained loads. In addition, the high strain capacity and toughness of the new FRP structural composites can benefit the seismic retrofitting for existing buildings.

3. The enhanced impact resistance and perforation energy is beneficial in composite materials used in armored vehicles subjected to blast or aircraft components and off shore composite structures subjected to impact loads.

الفنارة للاستشارات

www.manaraa.com

9.3 Future Work

The following issues require further investigations and are expected to benefit more applications:

1. It is recommended to examine the use other types and dimensions of carbon nanotubes such as SWCNTs or short MWCNTs and to improve the dispersing techniques by using probe sonication or calendering. This will allow not only better dispersion but also incorporating larger contents of MWCNTs. In addition, the use of low contents of surfactant (i.e 2 to 3 CMC) would avoid forming micelles and improve the dispersion of the carbon nanotubes. The use of other functional groups such as NH_2 or the use of hybrid functional groups (NH_2 and COOH) would allow dispersing the nanotubes in both the resin and the hardener prior to mixing and the curing.

2. It would be more efficient to examine the effect of using MWCNTs-epoxy nanocomposites with glass fiber because they are more prone to inter fiber fracture (IFF). In addition, examining the delamination of unidirectional composites reinforced by MWCNTs might be of interest because fracture toughness of unidirectional composites is typically lower than that of the woven fabric composites.

3. It is worth examining the fatigue and freeze and thaw resistance of the new FRP composites incorporating MWCNTs. Typical FRP composites experience

237

reduction in stiffness due to matrix micro-cracks when they are subjected to cyclic loadings or freeze and thaw cycles. The MWCNTs is expected to limit the matrix micro cracks thus improve the resistance of composites to fatigue or environmental conditions. It is also important to manufacture thick composite plates in order to examine inter laminar shear strength (ILSS) and mode II fracture toughness by conducting short beam strength (SBS) and end notched flexure (ENF) tests respectively.

4. Conducting nanoindentation experiments will enable nano-characterization of different nanocomposites. In particular, material properties such as hardness, reduced modulus, elastic energy, plastic energy, and creep compliance can be obtained and compared. Furthermore, the dynamic shear rheometer (DSR) can be used to obtain the creep compliance at the macro-scale and compare it with the one obtained from the nanoindentation. Furthermore, performing the dynamic mechanical analysis (DMA) test will also yield viscoelastic and dynamic properties of different nanocomposites.

5. Modeling of the experiments reported in this dissertation can be performed using multi continuum theory (MCT) simulations. The advantage of this technique is that the failure analyses are performed on each composite constituent (fibers or matrix) individually. This advantage allows the algorithm to capture and graphically present the progressive failure due to inter fiber fracture. This technique also allows modeling multi-scale FRP composites (micro-to-macro scales). Therefore, this approach can show the effect of improving the matrix in the mechanical response of structural composites.

238

APPENDIX A. MANUFACTURING OF FRP COMPOSITES

Manufacturing of thermoset FRP composites consists of two stages: fabrication and processing. The fabrications step involves shaping the fiber reinforcement and the polymer matrix into the desired shape using steel or aluminum molds. This step is independent on the types of the fibers or the matrices. The processing step involves curing of the matrix around the fiber reinforcements while the cross-linking is taking place. The main challenge in the second step is to minimize the formation of air voids in the composites by applying adequate scheme of temperature and pressure over time such. Over the years, many techniques were developed for manufacturing best quality composites. Examples of these techniques are autoclave molding, resin transfer molding (RTM), vacuum assisted resin transfer molding (VARTM), automated tape laying (ATL), filament winding, and automated tow placement (ATP).

Two types of FRPs were manufactured in this chapter; carbon and glass fibers. The fabrication of the CFRP composite was performed in accordance to ASTM D5687 standards (ASTMD5687/D5687M, 2007). The vacuum assisted hand lay-up technique was implemented to fabricate CFRP composite. In this study, plain-woven fabrics are used over other types of fabric (i.e twill or satin). The woven fabrics are used because it yields better quality composite when hand lay-up technique is used without significant fiber weaving as in the case of unidirectional composites. The plain weaves provides the highest number of interlaces between the wrap and filling yarns. Several types of layers are used during the manufacturing process as shown in Figure A.1. The function of the release films is to separate the FRP composite from the surrounding layers and plates.

239

The peel ply is usually placed in order to facilitate peeling the composite after the curing of epoxy and to protect the composite from contamination. The breather ply has two functions; first it provides the air bath towards the vacuum port when the Naylon bag is vacuumed. Second is to absorb the excess of the matrix (Hyer, 1997).
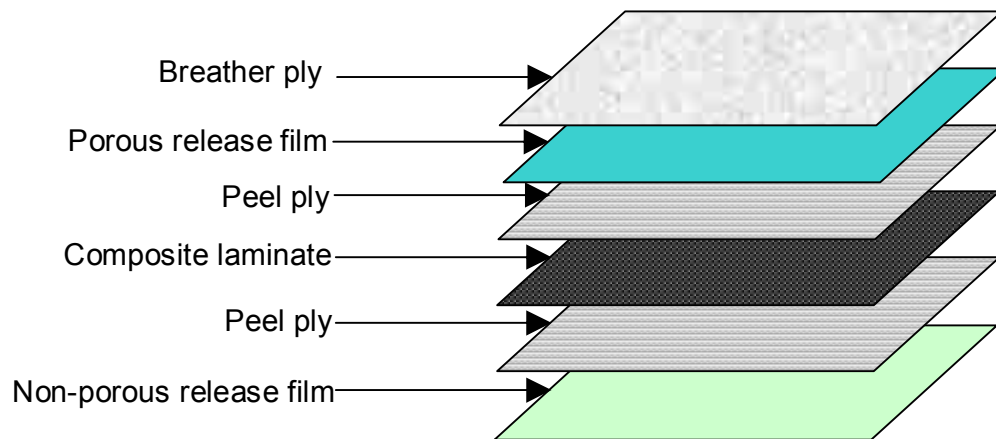
Figure A.1 Layered materials used in the manufacturing process

In the manufacturing process of two-layer composite, the non-porous release film was attached over an aluminum plate and a peel ply was placed over the release film. The use of aluminum plate ensures straight composite after the fabrication. Woven carbon fiber fabric was placed and the epoxy was applied using a roller. The second layer was placed over the first layer and more epoxy was added to the second layer. A roller was used to compact the fabric layers together in order to ensure adequate impregnation of the epoxy around the carbon fibers. The epoxy used in the fabrication process is either neat epoxy, dispersed, or functionalized CNTs reinforced epoxy. It is important to note that the addition of CNTs increased the viscosity of the epoxy during the fabrication, therefore 1.5% CNts by weight was the highest CNTs content examined in this study.

240

After the impregnation of the carbon fiber with epoxy took place, another peel ply was placed over the fabric. A porous release film was placed over the peel ply, which allows for the suction of air bubbles. A breather ply was placed over the film to form the vacuum path to the composite. The entire system was covered with a Naylon bag and sealed by a sealant tape. The various layers used in the fabrication are supplied by Aerospace Composite products, Inc. The vacuum pump was connected to the nylon bag through a vacuum port. A pressure level of 2.3×10^{-2} Torr was applied and maintained for one day to ensure full curing of the epoxy in the absence of air bubbles. The vacuum bag was checked from any leakage. Figures A.2 and A.3 show schematics and pictures for the manufacturing process respectively.
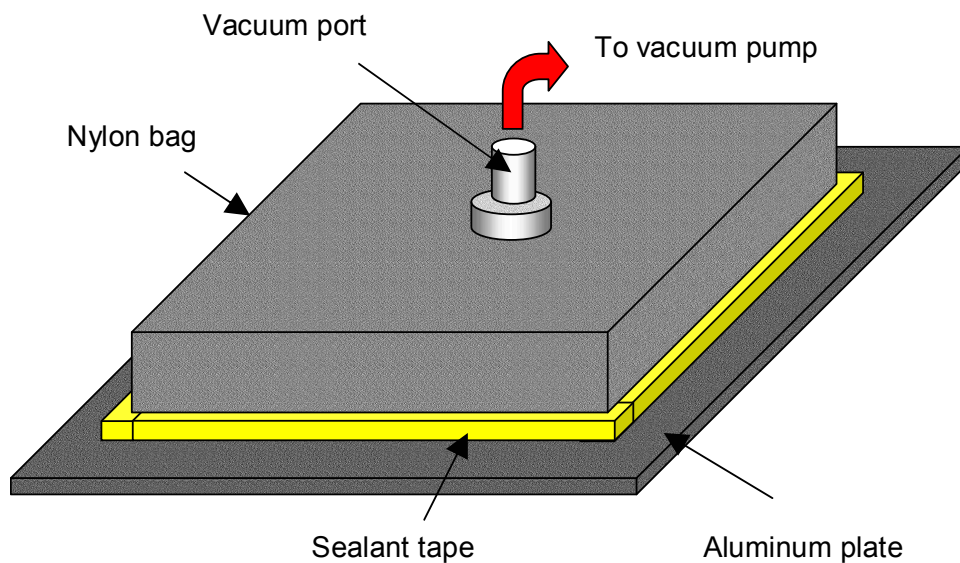
Figure A.2 Schematic for vacuum bag system

(a) Bottom peel ply is ready for fabric
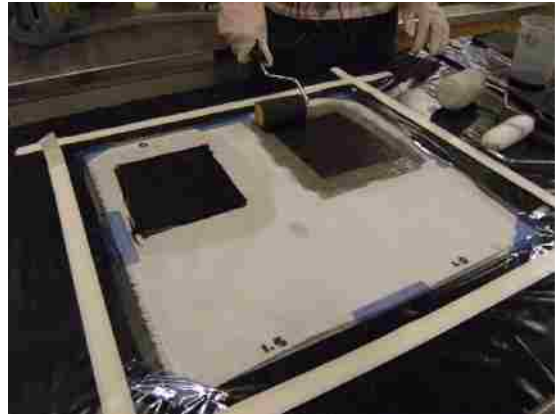
(b) Compacting carbon fabric using roller

(c) Epoxy impregnated in carbon fabric
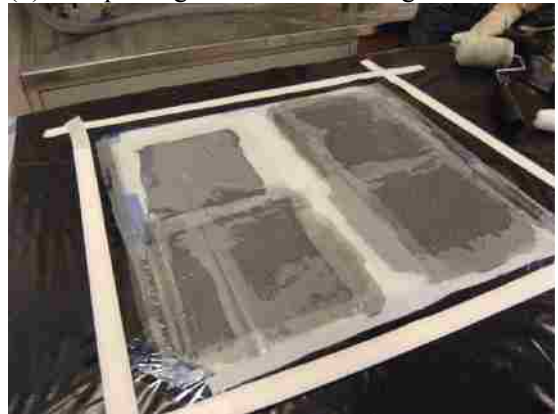
(d) Placement of top peel ply and release film

(e) Placement of breather ply
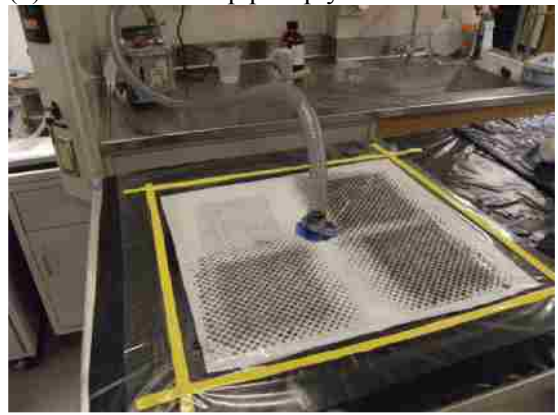
(f) Vacuum bag system connected to pump

Figure A.3 Step-by-step manufacturing process of composite plate using vacuum bag

APPENDIX B. MODIFIED MAXWELL RHEOLOGICAL MODEL

In Figure B.1, from strain compatibility, the total strain can be computed as

$$\varepsilon(t) = \varepsilon_{R_2} = \varepsilon_{\mu_1} + \varepsilon_{R_1} \tag{B.1}$$

By differentiation Eqn. (A.1) with respect to time and considering spring and dashpot relations then

$$\frac{\partial \varepsilon(t)}{\partial t} = \frac{1}{R_1} \frac{\partial \sigma_1(t)}{\partial t} + \frac{\sigma_1(t)}{\mu_1} \tag{B.2}$$

From stress equilibrium $\sigma_0 = \sigma_1(t) + \sigma_2(t)$ results in

$$\frac{\partial}{\partial t}[\varepsilon(t)] = \frac{1}{R_1} \frac{\partial \sigma_0}{\partial t} - \frac{1}{R_1} \frac{\partial[\sigma_2(t)]}{\partial t} + \frac{\sigma_0 - \sigma_2(t)}{\mu_1} \tag{B.3}$$

Since constant stress condition and spring Hooke's law imply $\dfrac{\partial \sigma_0}{\partial t} = 0$ and $\sigma_2(t) = R_2 \varepsilon(t)$

then

$$\int \frac{d\varepsilon(t)}{\sigma_0 - R_2 \varepsilon(t)} = \int \frac{dt}{\mu_1 \left(1 + \dfrac{R_2}{R_1}\right)} \tag{B.4}$$

By integrating Eqn. (A.4), then the total strain becomes

$$\varepsilon(t) = \frac{\sigma}{R_2} - \exp\left(\frac{-t}{\mu_1 \left(1 + \dfrac{R_2}{R_1}\right)} + C\right) \tag{B.5}$$

Considering the initial conditions $t = 0 \Rightarrow \varepsilon(t) = \varepsilon_0$

243

$$C = \ln\left(\frac{\sigma}{R_2} - \varepsilon_0\right) \text{ and } \varepsilon(t) = \frac{\sigma_0}{R_2} - \left(\frac{\sigma_0}{R_2} - \varepsilon_0\right)\exp\left(\frac{-t}{\mu_1\left(1 + \frac{R_2}{R_1}\right)}\right) \tag{B.6}$$

Since the total compliance is $J(t) = \dfrac{\varepsilon(t)}{\sigma_0}$, the elastic compliance is $J(0) = \dfrac{\varepsilon_0}{\sigma_0}$, and the

normalized creep compliance is $J_n(t) = \dfrac{J(t)}{J(0)}$, the normalized creep compliance becomes:

$$J_n(t) = \frac{1}{\varepsilon_0}\left[\frac{\sigma_0}{R_2} - \left(\frac{\sigma_0}{R_2} - \varepsilon_0\right)\exp\left(\frac{-t}{\mu_2\left(1 + R_2/R_1\right)}\right)\right] \tag{B.7}$$
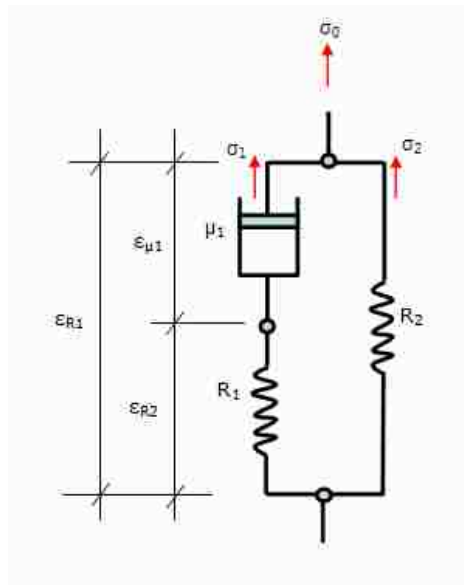
Figure B.1 Modified Maxwell Model for predicting creep

244

REFERENCES

Abrate, S., 1994: Impact on laminated composites: recent advances. *Applied Mechanics Review,* **47,** 517-544.

Abrate, S., 1998: *Impact on composite structures.* Cambridge University Press, New York.

ACI440.2R, 2006: Guide for the design and construction of concrete reinforced with FRP rebars. In: 1R-06 (ed.). ACI Committee 440, Farmington Hills.

Adams, D. F., L. A. Carlsson and R. B. Pipes, 2003: *Experimental characterization for advanced composite materials.* CRC Press, New York.

Advani, S. and Z. Fan, 2007: Dispersion, bonding and orientation of carbon nanotubes in polymer matrices. In: S. Advani (ed.), *Processing and Properties of Nanocomposites.* World Scientific Publishing Co. Pte. Ltd., Hackensack, NJ.

Aktas, M., C. Atas, B. M. Icten and R. Karakuzu, 2009: An experimental investigation of the impact response of composite laminates. *Compos Struct,* **87,** 307-313.

Alexandre, M. and P. Dubois, 2000: Polymer-layered silicate nanocomposites: preparation, properties and uses of a new class of materials. *Mat Sci Eng R,* **28,** 1-63.

Alfano, G. and M. A. Crisfield, 2001: Finite element interface models for the delamination analysis of laminated composites: Mechanical and computational issues. *Int J Numer Meth Eng,* **50,** 1701-1736.

Alif, N., L. A. Carlsson and J. W. Gillespie, 1997: Mode I, mode II, and mixed mode interlaminar fracture of woven fabric carbon/epoxy. *ASTM Special Technical Publication,* **1242,** 82–106.

Aslan, Z. and M. Sahin, 2009: Buckling behavior and compressive failure of composite laminates containing multiple large delaminations. *Compos Struct,* **89,** 382-390.

ASTMD790, 2010: Standard Test Methods for Flexural Properties of Unreinforced and Reinforced Plastics and Electrical Insulating Materials. *ASTM International: PA.* ASTM.

ASTMD1002, 2010: Standard Test Method for Apparent Shear Strength of Single-Lap-Joint Adhesively Bonded Metal Specimens by Tension Loading (Metal-to-Metal). *ASTM International: PA.* ASTM.

ASTMD3039/D3039M, 2008: Standard Test Method for Tensile Properties of Polymer Matrix Composite Materials. *ASTM International: PA.* ASTM.

ASTMD3163, 2008: Standard Test Method for Determining Strength of Adhesively Bonded Rigid Plastic Lap-Shear Joints in Shear by Tension Loading. *ASTM International: PA.* ASTM.

ASTMD3165, 2007: Standard Test Method for Strength Properties of Adhesives in Shear by Tension Loading of Single-Lap-Joint Laminated Assemblies. *ASTM International: PA.* ASTM.

ASTMD3518/D3518M, 2007: Standard Test Method for In-Plane Shear Response of Polymer Matrix Composite Materials by Tensile Test of a ±45 Laminate. *ASTM International: PA.* ASTM.

ASTMD3528, 2008: Standard Test Method for Strength Properties of Double Lap Shear Adhesive Joints by Tension Loading. *ASTM International: PA.* ASTM.

ASTMD3983, 2011: Standard Test Method for Measuring Strength and Shear Modulus of Nonrigid Adhesives by the Thick-Adherend Tensile-Lap Specimen. *ASTM International: PA.* ASTM.

ASTMD4896, 2008: Standard Guide for Use of Adhesive-Bonded Single Lap-Joint Specimen Test Results. *ASTM International: PA.* ASTM.

ASTMD5528, 2007: Standard Guide for Testing Polymer Matrix Composite Materials. *ASTM International: PA.* ASTM.

ASTMD5656, 2010: Standard Test Method for Thick-Adherend Metal Lap-Shear Joints for Determination of the Stress-Strain Behavior of Adhesives in Shear by Tension Loading. *ASTM International: PA.* ASTM.

ASTMD5687/D5687M, 2007: Standard Guide for Preparation of Flat Composite Panels with Processing Guidelines for Specimen Preparation. *ASTM International: PA.* ASTM.

ASTMD5868, 2008: Standard Test Method for Lap Shear Adhesion for Fiber Reinforced Plastic (FRP) Bonding. *ASTM International: PA.* ASTM.

ASTMD6272, 2010: Standard Test Method for Flexural Properties of Unreinforced and Reinforced Plastics and Electrical Insulating Materials by Four-Point Bending. *ASTM International: PA.* ASTM.

ASTMD7136/D7136M, 2007: Standard Test Method for Measuring the Damage Resistance of a Fiber-Reinforced Polymer Matrix Composite to a Drop-Weight Impact Event. *ASTM International: PA.* ASTM.

ASTMD7175, 2008: Standard Test Method for Determining the Rheological Properties of Asphalt Binder Using a Dynamic Shear Rheometer. *ASTM International: PA.* ASTM.

ASTMD7616/D7616M, 2011: Standard test method for determining apparent overlap splice shear strength properties of wet lay-up fiber-reinforced polymer matrix composites used for strengthening civil structures. *ASTM International: PA.* ASTM.

Avila, A. F., M. I. Soares and A. S. Neto, 2007: A study on nanostructured laminated plates behavior under low-velocity impact loadings. *Int J Impact Eng,* **34,** 28-41.

Bacon, R., 1960: Growth, Structure, and Properties of Graphite Whiskers. *J Appl Phys,* **31,** 283-290.

Barauskas, R. and A. Abraitiene, 2007: Computational analysis of impact of a bullet against the multilayer fabrics in LS-DYNA. *Int J Impact Eng,* **34,** 1286-1305.

Becher, P., 1966: Emulsions: Theory and Practice Reinhold Publishing, New York.

Benyoucef, S., A. Tounsi, E. A. A. Bedia and S. A. Meftah, 2007: Creep and shrinkage effect on adhesive stresses in RC beams strengthened with composite laminates. *Compos Sci Technol,* **67,** 933-942.

Boone, M., 2002: mechanical testing of epoxy adhesives for naval applications. The University of Maine.

Breton, Y., G. Desarmot, J. P. Salvetat, S. Delpeux, C. Sinturel, F. Beguin and S. Bonnamy, 2004: Mechanical properties of multiwall carbon nanotubes/epoxy composites: influence of network morphology. *Carbon,* **42,** 1027-1030.

Chandra, N., 2002: Evaluation of interfacial fracture toughness using cohesive zone model. *Compos Part a-Appl S,* **33,** 1433-1447.

Chandrasekaran, V. C. S., S. G. Advani and M. H. Santare, 2010: Role of processing on interlaminar shear strength enhancement of epoxy/glass fiber/multi-walled carbon nanotube hybrid composites. *Carbon,* **48,** 3692-3699.

Chocron, S., K. R. Samant, A. E. Nicholls, E. Figueroa, C. E. Weiss, J. D. Walker and C. E. Anderson, 2009: Measurement of strain in fabrics under ballistic impact using embedded nichrome wires. Part I: Technique. *Int J Impact Eng,* **36,** 1296-1302.

Coleman, J. N., U. Khan, W. J. Blau and Y. K. Gun'ko, 2006: Small but strong: A review of the mechanical properties of carbon nanotube-polymer composites. *Carbon,* **44,** 1624-1652.

Dai, J., E. Soliman, M. Safdari, M. Al-Haik and M. M. Reda Taha, 2010: *Effect of carbon nanotube growth conditions on strength and stiffness of carbon and glass fiber polymer composites, Orlando, FL*.

Davies, J. T., A quantitative kinetic theory of emulsion type, I. Physical chemistry of the emulsifying agent,Gas/Liquid and Liquid/Liquid Interface. in Proceedings of the Proceedings of the International Congress of Surface Activity, 1957, p. 426.

Dawood, M., M. Guddati and S. Rizkalla, Bond behavior of a CFRP strengthening system for steel structures. in Proceedings of the Smith ST. Proceedings of the Asia-Pacific Conference on FRP in Structures (APFIS), Hong Kong, 2007.

Dominguez, A., A. Fernandez, N. Gonzalez, E. Iglesias and L. Montenegro, 1997: Determination of critical micelle concentration of some surfactants by three techniques. *J Chem Educ,* **74,** 1227-1231.

Dowling, N., 2007: *Mechanical behavior of materials: engineering methods for deformation, fracture, and fatigue*. Pearson Education Inc., New Jersy.

Eklund, P., P. Ajayan, R. Blackmon, A. J. Hart, J. Kong, B. Pradhan, A. Rao and A. Rinzler, 2007: *International assessment of research and development of carbon nanotube manufacturing and applications: final report*. World Technology Evaluation Center (WTEC), Inc., Baltimore, Maryland.

Feng, C. W., C. W. Keong, Y. P. Hsueh, Y. Y. Wang and H. J. Sue, 2005: Modeling of long-term creep behavior of structural epoxy adhesives. *International Journal of Adhesion and Adhesives,* **25,** 427-436.

Ferrier, E. and P. Hamelin, 2002: Long-time concrete-composite interface characterization for reliability prediction of RC beam strengthened with FRP. *Mater Struct,* **35,** 564-572.

Ferrier, E., L. Michel, B. Jurkiewiez and P. Hamelin, 2011: Creep behavior of adhesives used for external FRP strengthening of RC structures. *Constr Build Mater,* **25,** 461-467.

Fessel, G., J. G. Broughton, N. A. Fellows and J. F. Durodola, 2007: Evaluation of different lap-shear joint geometries for automotive applications. *International Journal of Adhesion and Adhesives,* **27,** 574-583.

Feynman, R., 1992: There's Plenty of Room at the Bottom. *Journal of Microeleciromechanical Systems,* **1,** 60-66.

Findley, W. N., J. S. Lai and K. Onaran, 1989: *Creep and Relaxation of Nonlinear Viscoelastic Materials*. Dover Publications Inc., New York.

Fukushima, T., A. Kosaka, Y. Ishimura, T. Yamamoto, T. Takigawa, N. Ishii and T. Aida, 2003: Molecular ordering of organic molten salts triggered by single-walled carbon nanotubes. *Science,* **300,** 2072-2074.

Gabriel, G., G. Sauthier, J. Fraxedas, M. Moreno-Manas, M. T. Martinez, C. Miravitlles and J. Casabo, 2006: Preparation and characterisation of single-walled carbon nanotubes functionalised with amines. *Carbon,* **44,** 1891-1897.

Gasman, L., 2006: *Nanotechnology applications and markets*. Artech House, Inc., Norwood, MA.

Geng, Y., M. Y. Liu, J. Li, X. M. Shi and J. K. Kim, 2008: Effects of surfactant treatment on mechanical and electrical properties of CNT/epoxy nanocomposites. *Compos Part a-Appl S,* **39,** 1876-1883.

Gojny, F. H., M. H. G. Wichmann, B. Fiedler and K. Schulte, 2005: Influence of different carbon nanotubes on the mechanical properties of epoxy matrix composites - A comparative study. *Compos Sci Technol,* **65,** 2300-2313.

Gong, X. Y., J. Liu, S. Baskaran, R. D. Voise and J. S. Young, 2000: Surfactant-assisted processing of carbon nanotube/polymer composites. *Chem Mater,* **12,** 1049-1052.

Griffin, W. C., 1949: Classification of surface-active agents by HLB. *Journal of the Society of Cosmetic Chemists,* **1,** 311-326.

Griffin, W. C., 1954: Calculation of HLB values of non-iIonic surfactants. *Journal of the Society of Cosmetic Chemists,* **5,** 249-235.

Grossiord, N., J. Loos, O. Regev and C. E. Koning, 2006: Toolbox for dispersing carbon nanotubes into polymers to get conductive nanocomposites. *Chem Mater,* **18,** 1089-1099.

Grujicic, M., W. C. Bell, L. L. Thompson, K. L. Koudela and B. A. Cheeseman, 2008: Ballistic-protection performance of carbon-nanotube-doped poly-vinyl-ester-epoxy matrix composite armor reinforced with E-glass fiber mats. *Mat Sci Eng a-Struct,* **479,** 10-22.

Gu, B. H., 2003: Analytical modeling for the ballistic perforation of planar plain-woven fabric target by projectile. *Compos Part B-Eng,* **34,** 361-371.

Hamed, E. and M. A. Bradford, 2010: Creep in concrete beams strengthened with composite materials. *Eur J Mech a-Solid,* **29,** 951-965.

He, X. C., 2011: A review of finite element analysis of adhesively bonded joints. *International Journal of Adhesion and Adhesives,* **31,** 248-264.

Hinton, M. J., A. S. Kaddour and P. D. Soden, 2004: *Failure criteria in fibre reinforced polymer composites: the world-wide failure exercise*. Elsevier, New York.

Hobbiebrunken, T., M. Hojo, T. Adachi, C. De Jong and B. Fiedler, 2006: Evaluation of interfacial strength in CF/epoxies using FEM and in-situ experiments. *Compos Part a-Appl S,* **37,** 2248-2256.

Hobbiebrunken, T., M. Hojo, K. K. Jin and S. K. Ha, 2008: Influence of non-uniform fiber arrangement on microscopic stress and failure initiation in thermally and transversely loaded CF/epoxy laminated composites. *Compos Sci Technol,* **68,** 3107-3113.

Hosur, M. V., F. Chowdhury and S. Jeelani, 2007: Low-velocity impact response and ultrasonic NDE of woven carbon/epoxy-nanoclay nanocomposites. *J Compos Mater,* **41,** 2195-2212.

Hu, N., Y. Zemba, T. Okabe, C. Yan, H. Fukunaga and A. M. Elmarakbi, 2008: A new cohesive model for simulating delamination propagation in composite laminates under transverse loads. *Mech Mater,* **40,** 920-935.

248

Hyer, M. W., 1997: *Stress analysis of fiber-reinforced composite materials*. McGraw-Hill, New York.

Iijima, S., 1991: Helical Microtubules of Graphitic Carbon. *Nature,* **354,** 56-58.

Iijima, S. and T. Ichihashi, 1993: Single-Shell Carbon Nanotubes of 1-Nm Diameter. *Nature,* **363,** 603-605.

Iqbal, K., S. U. Khan, A. Munir and J. K. Kim, 2009: Impact damage resistance of CFRP with nanoclay-filled epoxy matrix. *Compos Sci Technol,* **69,** 1949-1957.

Islam, M. F., E. Rojas, D. M. Bergey, A. T. Johnson and A. G. Yodh, 2003: High weight fraction surfactant solubilization of single-wall carbon nanotubes in water. *Nano Lett,* **3,** 269-273.

ISO6603-2, 2000: Plastics -- Determination of puncture impact behaviour of rigid plastics -- Part 2: Instrumented impact testing. In: N. S. A. o. Ireland (ed.)*.* International Organization for Standardization, Dublin, Ireland.

Karahan, M., A. Kus and R. Eren, 2008: An investigation into ballistic performance and energy absorption capabilities of woven aramid fabrics. *Int J Impact Eng,* **35,** 499-510.

Katerelos, D. T. G., M. Kashtalyan, C. Soutis and C. Galiotis, 2008: Matrix cracking in polymeric composites laminates: Modelling and experiments. *Compos Sci Technol,* **68,** 2310-2317.

Kelly, G. and S. Hallstrom, 2005: Strength and failure mechanisms of composite laminates subject to localised transverse loading. *Compos Struct,* **69,** 301-314.

Khalili, S. M. R., S. Khalili, M. R. Pirouzhashemi, A. Shokuhfar and R. K. Mittal, 2008: Numerical study of lap joints with composite adhesives and composite adherends subjected to in-plane and transverse loads. *International Journal of Adhesion and Adhesives,* **28,** 411-418.

Khan, M. U., V. G. Gomes and I. S. Altarawneh, 2010: Synthesizing polystyrene/carbon nanotube composites by emulsion polymerization with non-covalent and covalent functionalization. *Carbon,* **48,** 2925-2933.

Kim, J. A., D. G. Seong, T. J. Kang and J. R. Youn, 2006: Effects of surface modification on rheological and mechanical properties of CNT/epoxy composites. *Carbon,* **44,** 1898-1905.

Kim, T. H., C. Doe, S. R. Kline and S. M. Choi, 2007: Water-redispersible isolated single-walled carbon nanotubes fabricated by in situ polymerization of micelles. *Adv Mater,* **19,** 929-+.

Kim, Y. J., T. S. Shin, H. D. Choi, J. H. Kwon, Y. C. Chung and H. G. Yoon, 2005: Electrical conductivity of chemically modified multiwalled carbon nanotube/epoxy composites. *Carbon,* **43,** 23-30.

Knops, M., 2008: *Analysis of failure of fiber reinforced polymer laminates*. Springer, New York.

Knops, M. and C. Bogle, 2006: Gradual failure in fibre/polymer laminates. *Compos Sci Technol,* **66,** 616-625.

Kostopoulos, V., A. Baltopoulos, P. Karapappas, A. Vavouliotis and A. Paipetis, 2010: Impact and after-impact properties of carbon fibre reinforced composites enhanced with multi-wall carbon nanotubes. *Compos Sci Technol,* **70,** 553-563.

Lau, K. T., C. Gu and D. Hui, 2006: A critical review on nanotube and nanotube/nanoclay related polymer composite materials. *Compos Part B-Eng,* **37,** 425-436.

Lee, Y. S., T. H. Cho, B. K. Lee, J. S. Rho, K. H. An and Y. H. Lee, 2003: Surface properties of fluorinated single-walled carbon nanotubes. *J Fluorine Chem,* **120,** 99-104.

Li, Y. L., I. A. Kinloch and A. H. Windle, 2004: Direct spinning of carbon nanotube fibers from chemical vapor deposition synthesis. *Science,* **304,** 276-278.

Loiseau, A., A. Launois, P. Petit, S. Roche and J. P. Salvetat, 2006: *Understanding Carbon Nanotubes: From Basics to Applications.* Springer, Berlin Heidelberg.

Luhrs, C. C., D. Garcia, M. Tehrani, M. Al-Haik, M. R. Taha and J. Phillips, 2009: Generation of carbon nanofilaments on carbon fibers at 550 degrees C. *Carbon,* **47,** 3071-3078.

Ma, P. C., J. K. Kim and B. Z. Tang, 2006: Functionalization of carbon nanotubes using a silane coupling agent. *Carbon,* **44,** 3232-3238.

Majda, P. and J. Skrodzewicz, 2009: A modified creep model of epoxy adhesive at ambient temperature. *International Journal of Adhesion and Adhesives,* **29,** 396-404.

Markolefas, S. I. and T. K. Papathanassiou, 2009: Stress redistributions in adhesively bonded double-lap joints, with elastic-perfectly plastic adhesive behavior, subjected to axial lap-shear cyclic loading. *International Journal of Adhesion and Adhesives,* **29,** 737-744.

Mazumdar, S., 2002: *Composites manufacturing: materials, products, and process engineering.* CRC Press.

Meshgin, P., K. K. Choi and M. M. R. Taha, 2009: Experimental and analytical investigations of creep of epoxy adhesive at the concrete-FRP interfaces. *International Journal of Adhesion and Adhesives,* **29,** 56-66.

Misonix®, S., *Ultrasonic Cleaners Models 50, 75, 150, 250, 550: Operator's Manual.* QSonica, LLC, Newtown, CT.

Naik, N. K., Y. C. Sekher and S. Meduri, 2000: Damage in woven-fabric composites subjected to low-velocity impact. *Compos Sci Technol,* **60,** 731-744.

Naik, N. K., P. S. Shembekar and M. V. Hosur, 1991: Failure Behavior of Woven Fabric Composites. *J Compos Tech Res,* **13,** 107-116.

Naik, N. K., P. Shrirao and B. C. K. Reddy, 2006: Ballistic impact behaviour of woven fabric composites: Formulation. *Int J Impact Eng,* **32,** 1521-1552.

Nairn, J. A., 2000: Matrix Microcracking in Composites. In: A. Kelly and C. Zweben (eds.), *Comprehensive Composite Materials.* Elsevier.

Nanni, A., FRP Reinforcement for Bridge Structures. in Proceedings of the Structural Engineering Conference, The University of Kansas, Lawrence, KS, 2000.

Nicholls, D. J. and J. P. Gallagher, 1983: Determination of GIc in angle-ply composites using a cantilever beam test method. *Journal of Reinforced Plastics and Composites,* **2,** 2-17.

O'Connell, M., 2006: *Carbon Nanotubes: Properties and Applications.* CRC Press, Boca Raton, FL.

Oberlin, A., M. Endo and T. Koyama, 1976: Adhesion of graphite fibers to epoxy matrices, I. The role of fiber surface treatment. *Journal of Crystal Growth,* **32,** 335-349.

Osorio, A. G., I. C. L. Silveira, V. L. Bueno and C. P. Bergmann, 2008: H(2)SO(4)/HNO(3)/HCl-Functionalization and its effect on dispersion of carbon nanotubes in aqueous media. *Appl Surf Sci,* **255,** 2485-2489.

Oterkus, E., A. Barut, E. Madenci, S. S. Smeltzer and D. R. Ambur, 2006: Bonded lap joints of composite laminates with tapered edges. *Int J Solids Struct,* **43,** 1459-1489.

Ozdil, F. and L. A. Carlsson, 1992: Mode-I Interlaminar Fracture of Interleaved Graphite Epoxy. *J Compos Mater,* **26,** 432-459.

Pagano, N. J. and G. A. Schoeppner, 2000: Delamination of polymer matrix composites, problems and assessment. In: A. Kelly and C. Zweben (eds.), *Comprehensive Composite Materials.* Elsevier.

Park, K. C., T. Hayashi, H. Tomiyasu, M. Endo and M. S. Dresselhaus, 2005: Progressive and invasive functionalization of carbon nanotube sidewalls by diluted nitric acid under supercritical conditions. *J Mater Chem,* **15,** 407-411.

Phillips, J., T. Shiina, M. Nemer and K. Lester, 2006: Graphitic structures by design. *Langmuir,* **22,** 9694-9703.

Puck, A. and H. Schurmann, 1998: Failure analysis of FRP laminates by means of physically based phenomenological models. *Compos Sci Technol,* **58,** 1045-1067.

Qiu, J. J., C. Zhang, B. Wang and R. Liang, 2007: Carbon nanotube integrated multifunctional multiscale composites. *Nanotechnology,* **18**.

Rao, M. P., Y. Duan, M. Keefe, B. M. Powers and T. A. Bogetti, 2009: Modeling the effects of yarn material properties and friction on the ballistic impact of a plain-weave fabric. *Compos Struct,* **89,** 556-566.

Rebiere, J. L. and D. Gamby, 2008: A decomposition of the strain energy release rate associated with the initiation of transverse cracking, longitudinal cracking and delamination in cross-ply laminates. *Compos Struct,* **84,** 186-197.

Reda Taha, M., E. Tromposch, G. Tadros, A. Mufti and C. Klowak, 2003: Performance Based Design for FRP Strengthening of the Roof Panels of Calgary Saddledome. *American Concrete Institute: Special Publications,* **215,** 385-398.

Reid, S. G. and G. Zhou, 2000: *Impact behaviour of fibre-reinforced composite materials and structures*. CRC Press Boca Raton, FL.

Reis, P., J. Ferreira and F. Antunes, 2007: Effect of adherend's rigidity on the shear strength of single lap adhesive joints. *International Journal of Adhesion and Adhesives***,** In press.

Robinson, P. and D. Q. Song, 1992: A Modified Dcb Specimen for Mode-I Testing of Multidirectional Laminates. *J Compos Mater,* **26,** 1554-1577.

Sahoo, N. G., S. Rana, J. W. Cho, L. Li and S. H. Chan, 2010: Polymer nanocomposites based on functionalized carbon nanotubes. *Prog Polym Sci,* **35,** 837-867.

Seo, M. K., S. J. Park and S. K. Lee, 2005: Influence of atmospheric plasma on physicochemical properties of vapor-grown graphite nanofibers. *J Colloid Interf Sci,* **285,** 306-313.

Seyhan, A. T., M. Tanoglu and K. Schulte, 2008: Mode I and mode II fracture toughness of E-glass non-crimp fabric/carbon nanotube (CNT) modified polymer based composites. *Eng Fract Mech,* **75,** 5151-5162.

Shaffer, M. and J. Sandler, 2007: Carbon Nanotube/Nanofibre Polymer Composites. In: S. Advani (ed.), *Processing and Properties of Nanocomposites.* World Scientific Publishing Co. Pte. Ltd., Hackensack, NJ.

Sham, M. L. and J. K. Kim, 2006: Surface functionalities of multi-wall carbon nanotubes after UV/Ozone and TETA treatments. *Carbon,* **44,** 768-777.

Shi, Y. B., D. Hull and J. N. Price, 1993: Mode-Ii Fracture of +Theta -Theta Angled Laminate Interfaces. *Compos Sci Technol,* **47,** 173-184.

Shyr, T. W. and Y. H. Pan, 2003: Impact resistance and damage characteristics of composite laminates. *Compos Struct,* **62,** 193-203.

Soliman, E. M., U. F. Kandil and M. M. Reda Taha, Creep of fiber reinforced polymer epoxy-concrete interface incorporating carbon nanotubes. in Proceedings of the Assessment and Rehabilitation of Civil Structures, Dubai, UAE, 2011a.

Soliman, E. M., U. F. Kandil and M. M. Reda Taha, 2011b: A new latex modified mortar incorporating carbon nanotubes: preliminary investigations. *American Concrete Institute: Special Publications*.

Soliman, E. M., U. F. Kandil and M. M. Reda Taha, 2011c: Shear creep of epoxy adhesive incorporating carbon nanotubes at the FRP-concrete interface. *International Journal for Adhesion and Adhesives***,** Accepted.

Soliman, E. M., U. F. Kandil and M. M. Reda Taha, 2011d: The significance of carbon nanotubes on styrene butadiene rubber (SBR) and SBR modified mortar. *Mater Struct***,** Accepted.

Soliman, E. M., M. P. Shyka and M. M. Reda Taha, 2011e: Ballistic impact of thin woven carbon fabric composites incorporating carbon nanotubes. *Int J Impact Eng***,** Submitted.

Soliman, M., M. Al-Haik and M. M. Reda Taha, 2011f: On and off-axis tension behaviour of fiber reinforced polymer (FRP) composites incorporating multi-walled carbon nanotubes. *J Compos Mater***,** Accepted.

South, J. T., S. W. Case and K. L. Reifsnider, 2002: Crack growth of natural rubber using a modified double cantilever beam. *Mech Mater,* **34,** 451-458.

Suhr, J., N. Koratkar, P. Keblinski and P. Ajayan, 2005: Viscoelasticity in carbon nanotube composites. *Nat Mater,* **4,** 134-137.

Taha, M. M. R., M. J. Masia, K. K. Choi, P. L. Shrive and N. G. Shrive, 2010: Creep Effects in Plain and Fiber-Reinforced Polymer-Strengthened Reinforced Concrete Beams. *Aci Struct J,* **107,** 627-635.

Tamuzs, V., S. Tarasovs and U. Vilks, 2003: Delamination properties of translaminar-reinforced composites. *Compos Sci Technol,* **63,** 1423-1431.

Tan, V. B. C. and T. W. Ching, 2006: Computational simulation of fabric armour subjected to ballistic impacts. *Int J Impact Eng,* **32,** 1737-1751.

Tan, V. B. C., C. T. Lim and C. H. Cheong, 2003: Perforation of high-strength fabric by projectiles of different geometry. *Int J Impact Eng,* **28,** 207-222.

Tang, C., W. L. Guo and C. F. Chen, 2009: Molecular dynamics simulation of tensile elongation of carbon nanotubes: Temperature and size effects. *Phys Rev B,* **79**.

Thess, A., R. Lee, P. Nikolaev, H. J. Dai, P. Petit, J. Robert, C. H. Xu, Y. H. Lee, S. G. Kim, A. G. Rinzler, D. T. Colbert, G. E. Scuseria, D. Tomanek, J. E. Fischer and R. E. Smalley, 1996: Crystalline ropes of metallic carbon nanotubes. *Science,* **273,** 483-487.

Tillier, D. L., J. Meuldijk and C. E. Koning, 2003: Production of colloidally stable latices from low molecular weight ethylene-propylene-diene copolymers. *Polymer,* **44,** 7883-7890.

Vaisman, L., H. D. Wagner and G. Marom, 2006: The role of surfactants in dispersion of carbon nanotubes. *Adv Colloid Interfac,* **128,** 37-46.

Vallee, T. and T. Keller, 2006: Adhesively bonded lap joints from pultruded GFRP profiles. Part III: Effects of chamfers. *Compos Part B-Eng,* **37,** 328-336.

Villanueva, G. R. and W. J. Cantwell, 2004: The high velocity impact response of composite and FML-reinforced sandwich structures. *Compos Sci Technol,* **64,** 35-54.

Wang, J. L., 2007: Cohesive zone model of FRP-concrete interface debonding under mixed-mode loading. *Int J Solids Struct,* **44,** 6551-6568.

Wu, Z. S. and H. Diab, 2007: Constitutive model for time-dependent Behavior of FRP-concrete interface. *J Compos Constr,* **11,** 477-486.

Xiao, J. R., B. A. Gama and J. W. Gillespie, 2007: Progressive damage and delamination in plain weave S-2 glass/SC-15 composites under quasi-static punch-shear loading. *Compos Struct,* **78,** 182-196.

Xu, X. P. and A. Needleman, 1994: Numerical Simulations of Fast Crack-Growth in Brittle Solids. *J Mech Phys Solids,* **42,** 1397-&.

Yang, X. B. and A. Nanni, 2002: Lap splice length and fatigue performance of fiber-reinforced polymer laminates. *Aci Mater J,* **99,** 386-392.

Ye, L., 1989: Characterization of Delamination Resistance in Composite Laminates. *Composites,* **20,** 275-281.

Yesil, S., C. Winkelrnann, G. Bayram and V. La Saponara, 2010: Surfactant-modified multiscale composites for improved tensile fatigue and impact damage sensing. *Mat Sci Eng a-Struct,* **527,** 7340-7352.

Yokozeki, T., A. Kuroda, A. Yoshimura, T. Ogasawara and T. Aoki, 2010: Damage characterization in thin-ply composite laminates under out-of-plane transverse loadings. *Compos Struct,* **93,** 49-57.

Yu, M. F., O. Lourie, M. J. Dyer, K. Moloni, T. F. Kelly and R. S. Ruoff, 2000: Strength and breaking mechanism of multiwalled carbon nanotubes under tensile load. *Science,* **287,** 637-640.

Zhang, J., B. L. Fox, D. Gao and A. W. Stevenson, 2009: Inspection of Drop-weight Impact Damage in Woven CFRP Laminates Fabricated by Different Processes. *J Compos Mater,* **43,** 1939-1946.

Zhao, B., Z. H. Lu and Y. N. Lu, 2011: Closed-form solutions for elastic stress-strain analysis in unbalanced adhesive single-lap joints considering adherend deformations and bond thickness. *International Journal of Adhesion and Adhesives,* **31,** 434-445.

Zhu, J., J. D. Kim, H. Q. Peng, J. L. Margrave, V. N. Khabashesku and E. V. Barrera, 2003: Improving the dispersion and integration of single-walled carbon nanotubes in epoxy composites through functionalization. *Nano Lett,* **3,** 1107-1113.